

Aptamer-Based Electrochemical Biosensors for Protein Detection: Integrating Immobilization Strategies, Plasma Surface Engineering, and Enzymatic Amplification

by

Sina Ardalan

Master of Science (Analytical Chemistry, Chemistry and Chemical Engineering Research
Center of Iran, 2020)

Bachelor of Science (Applied Chemistry, Sharif University of Technology, 2017)

A Dissertation Submitted in Partial Fulfillment
of the Requirements for the Degree of

Doctor of Philosophy

in the Graduate Academic Unit of Chemistry

Supervisor: Anna Ignaszak, PhD, Chemistry

Examining Board: Yang Qu, PhD, Chemistry

C. Adam Dyker, PhD, Chemistry

Shawn R MacLellan, PhD, Biology

External Examiner: Vicki Meli, PhD, Chemistry and Biochemistry, Mount Allison
University

This dissertation is accepted by the Dean of Graduate Studies.

THE UNIVERSITY OF NEW BRUNSWICK

March, 2026

© Sina Ardalan, 2026

Abstract

Biosensors have been an integral part of medical diagnosis and biochemical monitoring. The capture probe of biosensors has undergone modifications from isolated enzymes and antibodies to artificial biorecognition elements. Aptamers have emerged as a novel artificial capture probe with a similar affinity detection mechanism to naturally occurring antibodies. This thesis investigates aptamer-based sensor (aptasensor) fabrication to detect two protein targets: SARS-CoV-2 spike protein and, at a greater depth, a coagulation cascade protein, thrombin.

The high demand for accessible tools for coronavirus disease 2019 diagnostics was the first project's motif as demonstrated in chapter 2, in which an aptasensor based on self-assembled monolayer formation (SAM) of thiol-modified single-stranded DNA on a gold screen-printed electrode (SPE) was developed. The aptamer binding to the spike protein was observed by Electrochemical Impedance Spectroscopy (EIS). However, due to the rapid mutations of SARS-CoV-2 and the complexity of the aptamer redesign, this project was discontinued.

In chapter 3, we introduced a regeneration strategy for recycling gold SPE wastes by using an air plasma cleaning method, resulting in enhanced electrochemical properties and immobilization efficiency of a thrombin-binding aptamer. Surface chemistry studies confirmed that the air plasma created a hydrophilic surface, improved the electron transfer kinetics, and increased surface roughness.

In chapter 4, we utilized a plasma-enhanced chemical vapor deposition method, known as plasma-activated coating (PAC), to covalently tether the thrombin-binding aptamer to a printed carbon electrode. X-ray photoelectron spectroscopy of surface phosphorus signals

increased by 6-fold, and surface nitrogen increased by 5-fold after aptamer immobilization on a PAC-modified surface compared to the unmodified electrodes.

In chapter 5, we showed that EIS can be used for binding analysis of the thrombin aptamer, but with limited sensitivity. Therefore, thrombin's enzymatic cleavage was measured electrochemically by an electrogenic substrate that was cleaved by thrombin to liberate para-nitroaniline. Square-wave voltammetry enabled real-time monitoring of the liberated para-nitroaniline at 0.12 V, producing a 90-fold greater signal than EIS under identical conditions.

Our work provides the experimental knowledge for the development of sensitive biosensors for protein detection, with applications in biomedical devices for point-of-care coagulation health monitoring.

Dedication

To my father for encouraging me never to stop trying.

To my mother for her endless kindness and sacrifices.

To my sister who let me share the hard times.

To my aunts for their tremendous support.

Acknowledgements

I am truly grateful to my supervisor, Professor Ignaszak, for her guidance, encouragement, and moral support. I greatly appreciate her kind generosity throughout these years. During the pandemic, despite the many challenges with traveling, she provided immense support. Even when there were delays, she continually showed patience, trust, and kindness, assisting me with all the hurdles of moving, traveling, and settling as an international student in Canada.

I owe special thanks to my supervisors at the University of Sydney, particularly Professor Bilek for her support and collaboration, to Dr. Tran for her immense help in plasma systems and our collaborative projects and to Dr. Fraser for his insights and encouragement.

I greatly appreciate my committee members, Professor Burns and Professor Dyker, for their advice, guidance, and providing thorough evaluation. I am grateful for having received such valuable and constructive feedback from them throughout my PhD Journey.

I truly appreciate my examining boards, Professor Meli, Dr. MacLellan Dr. Qu, and Professor Dyker for their effort and consideration evaluating my thesis and providing constructive feedback.

I would like to thank my colleagues in the Ignaszak lab, particularly Hamidreza Parsimehr, Chun Keat Khor, and Nigel Patterson for supporting a culture of teamwork, sharing their passion for learning, and their friendly guidance in the lab. There are so many wonderful people I wish I could thank here far more than I can possibly name, especially my family and friends. A very special thanks goes to my partner, Sarah-Jane Parker for her kind support and encouragement in all aspects of life beyond the lab.

Table of Contents

Abstract.....	ii
Dedication.....	iv
Acknowledgements.....	v
Table of Contents.....	vi
List of Tables.....	xiv
List of Figures.....	xvii
List of Abbreviations.....	xxv
List of Symbols.....	xxvii
1. Chapter 1: Introduction.....	1
1.1. Overview of introduction to biosensors.....	1
1.2. Biosensors.....	2
1.3. The need for broader biosensing capabilities.....	3
1.4. Antibodies and aptamers as affinity-based biorecognition elements.....	4
1.5. History of aptamers.....	4
1.6. Electrochemical aptasensors.....	6
1.7. Theory of EIS.....	8
1.7.1. EIS circuit and plot analysis.....	13
1.7.2. EIS-based electrochemical aptamer biosensors for protein detection.....	16

1.8. Bottlenecks in the stability and performance of aptasensors	17
1.8.1. Electrode pre-treatment can lead to undesired defects	18
1.8.2. Redox molecules can change the surface properties of aptasensors.....	19
1.8.3. Aptamers detach from the electrode during electrochemical measurement	21
1.8.4. Elevated temperature leads to monolayer solubilization	21
1.8.5. Enzymes can degrade aptamers	22
1.8.6. Biofouling reduces electron-transfer rates	22
1.9. Addressing the constraints in aptasensor stability	22
1.9.1. Plasma treatment is a highly effective electrode cleaning technique	23
1.9.2. Tuning electrochemical test parameters reduce electric field induced aptamer desorption.....	23
1.9.3. Optimizing the alkylthiolates length chain may increase the stability of aptamers	24
1.9.4. Nanocomposite electrodes and hydrogel membranes reduce biofouling	25
1.10. Thesis structure	25
1.10.1. Electrochemical detection of SARS-CoV-2 spike protein.....	27
1.10.2. Air plasma regeneration of screen-printed gold electrodes	27
1.10.3. Plasma-activated coating of carbon electrodes for one-step reagent free aptamer immobilization.....	28
1.10.4. Electrochemical detection of thrombin.....	28

2. Detection of SARS-CoV-2 via an aptamer-modified electrochemical sensor.....	31
2.1. Abstract.....	31
2.2. Introduction.....	31
2.3. Literature review.....	33
2.3.1. Electrochemical immunosensors	33
2.3.2. Artificial bioreceptors	34
2.3.3. Commercial products	37
2.4. Project scope	38
2.5. Experimental.....	39
2.5.1. Materials	39
2.5.2. Methods.....	39
2.6. Results and discussion	44
2.6.1. Fe ²⁺ /Fe ³⁺ optical study.....	44
2.6.2. Characterization of gold SPEs	45
2.6.3. Isolated SARS-CoV-2 spike protein.....	47
2.6.4. Electrochemical characterization of aptasensors	49
2.7. Conclusion	52
2.8. Study limitations	53
2.9. Author contributions	53

2.10. Acknowledgement	54
2.11. Conflict of interest	54
3. Sustainable air plasma regeneration of screen-printed gold electrodes with enhanced electroactive surface area and biosensing performance.....	55
3.1. Abstract.....	55
3.2. Introduction.....	56
3.3. Experimental.....	63
3.3.1. Materials	63
3.3.2. Methods.....	66
3.4. Results and discussions.....	68
3.4.1. Influence of air plasma cleaning parameters on gold SPEs.....	68
3.4.2. Determination of electrochemically active surface area.....	71
3.4.3. Electrode characterization by electrochemical impedance spectroscopy	73
3.4.4. Electrochemical impedance spectroscopy analysis of gold SPE	74
3.4.5. Mass transfer diffusion of redox active species.....	75
3.4.6. Surface chemistry analysis by XPS and water contact angle	78
3.4.7. Aptasensor performance of regenerated gold SPE	84
3.4.8. Effects of repeated cycles of plasma cleaning on gold SPE.....	88
3.5. Conclusion	89
3.6. Study limitations.....	91

3.7. Future work.....	91
3.8. Author contributions.....	92
3.9. Acknowledgements.....	92
3.10. Conflict of interest.....	92
4. Towards sustainable and reagentless electrochemical biosensor fabrication: immobilization of linker-free DNA aptamer on carbon electrodes by plasma enhanced chemical vapor deposition.....	93
4.1. Abstract.....	93
4.2. Introduction.....	93
4.3. Experimental.....	96
4.3.1. Materials.....	96
4.3.2. Methods.....	98
4.4. Results and discussion.....	100
4.4.1. XPS characterization.....	100
4.4.2. Electrochemical characterization.....	101
4.4.3. Thrombin biosensing on the PAC-modified electrodes.....	106
4.5. Conclusion.....	109
4.6. Study limitations.....	110
4.7. Future work.....	110
4.8. Author contributions.....	111

4.9. Acknowledgements.....	111
4.10. Conflict of interest	111
5. Revisiting a classical aptamer-based biosensor for electrochemical enzymatic detection of thrombin.....	112
5.1. Abstract.....	112
5.2. Introduction.....	113
5.3. Literature review.....	114
5.4. Study novelties.....	116
5.5. Materials and methods	118
5.5.1. Chemicals and buffers.....	118
5.5.2. Thrombin binding aptamer preparation	119
5.5.3. Protein solutions preparation	119
5.5.4. Thrombin substrate preparation	119
5.5.5. Screen-printed gold electrode preparation	119
5.5.6. Electrochemical measurement unit.....	120
5.5.7. Scanning Electron Microscopy (SEM).....	120
5.5.8. Aptasensing procedure.....	120
5.5.9. Enzymatic sensing procedure	121
5.5.10. Data analysis.....	121
5.6. Results and discussion	121

5.6.1. Electroactive surface area calculations	121
5.6.2. Electrode characterization by electrochemical impedance spectroscopy	124
5.6.3. Effect of repeated EIS scans on the charge transfer and capacitance	125
5.6.4. Effect of $[\text{Fe}(\text{CN})_6]^{4-/3}$ on gold voltammogram	126
5.6.5. Effect of experimental variables on immobilization of thiolated aptamers	127
5.6.6. Effect of glycerin as solvent on gold	128
5.6.7. Thrombin and human serum albumin (HSA) adsorption on gold	129
5.6.8. DNA quantification by chronocoulometry	132
5.6.9. Diffusion and kinetics of electron transfer.....	137
5.6.10. Aptasensor fabrication and characterization.....	140
5.6.11. Effect of TCEP on immobilization efficiency and aptasensor performance	143
5.6.12. MCH:aptamer co-immobilization.....	148
5.6.13. Sandwich aptamer assay	149
5.6.14. Capacitive/non-faradaic EIS analysis of the aptasensor	150
5.6.15. Chromogenic and amperogenic thrombin assays	152
5.6.16. Square Wave Voltammetry (SWV) monitoring of thrombin enzymatic cleavage activity.....	154
5.6.17. Enzymatic activity of immobilized thrombin on gold.....	156
5.6.18. Kinetics of thrombin enzymatic cleavage of pNA from H-D-Phe-Pip-Arg-pNA	158

5.6.19. Analytical performance of electrochemical enzymatic thrombin sensing and aptasensing.....	160
5.6.20. Selectivity tests	163
5.7. Conclusion	164
5.8. Study limitations	166
5.9. Future work.....	166
5.10. Authorship contribution	167
5.11. Acknowledgements.....	167
5.12. Conflict of interest	167
6. Summary and future work	168
6.1. Summary	168
6.2. Future work.....	173
Bibliography	176
Curriculum Vitae	

List of Tables

Table 1.1. Comparative analysis of enzyme, antibody, and aptamer as common biorecognition elements in biosensors.[11]	7
Table 3.1. CV parameters of gold SPEs with different modifications. Oxidation current significantly increased upon plasma cleaning with a smaller peak-to-peak separation....	71
Table 3.2. Electrode surface area characteristics calculated from the reduction peak of gold in 0.5 M H ₂ SO ₄	73
Table 3.3. Faradaic EIS characterization of gold SPE with different modifications using equivalent Randles circuit.....	75
Table 3.4. Fixed parameter values for the Randel-Sevcik and Warburg impedance equations for diffusion calculations.	77
Table 3.5. Warburg Impedance coefficient (σ) derived form faradaic EIS tests for electrodes treated under two conditions.....	77
Table 3.6. Diffusion coefficient (D_0) of gold SPE with and without plasma cleaning derived from two electrochemical techniques based on CV and EIS	79
Table 3.7. Charge transfer resistance (R_{ct}), Water Contact Angle (WCA) and atomic percentage analysis results from XPS of three gold SPEs are reported based on the average value \pm absolute error for three gold SPEs.	80
Table 4.1. Peak characteristics in CV experiments conducted on electrodes that have undergone different surface treatments.....	105
Table 4.2. EIS parameters of SPCE at different modification stages.	106

Table 4.3. Electrochemical impedance spectroscopy parameters of PAC-modified SPCE-based thrombin biosensor at different modification stages.....	109
Table 5.1. Commercial Thrombin enzymatic substrates used in TGA or PT-INR instruments.....	114
Table 5.2. Gold SPE surface area characteristics calculated from reduction peak of gold in 0.5 M sulfuric acid. RSD is provided based on the voltammogram data of three individual gold SPEs.....	123
Table 5.3. Effect of different electrode modifications on charge transfer resistance (R_{ct}). The RSD is provided to represent the variability in the data collected from three individual gold SPEs for each condition.....	131
Table 5.4. Relative nonspecific protein adsorption on gold electrodes. The RSD is provided to represent the variability in the data collected from three individual gold SPEs.....	133
Table 5.5. CC results to measure the amount of aptamer per cm^2 (Γ) of the electrode..	137
Table 5.6. Calculated diffusion coefficient (D_0) using the Randles-Sevick equation with the CV technique, Warburg impedance analysis via the EIS technique, and the resulting heterogeneous electron transfer rates (k^0) for each stage of the fabrication process.....	140
Table 5.7. Fitted average R_{ct} and C values for thrombin aptasensor without TCEP reduction ($n = 3$) on gold SPE and its regeneration by KCl 3M incubation. Thrombin binding increases R_{ct} but does not change C significantly.....	142
Table 5.8. The effect of buffer stability and negative control test (50 μ M HSA) on Aptamer/MCH modified gold SPE show minimal nonspecific response.....	143

Table 5.9. Effect of experimental variables, TCEP reduction and thrombin pipetting on sensor response. The RSD is provided to represent the variability in the data collected from three different gold SPEs for each condition.	144
Table 5.10. Aptasensor binding analysis by faradaic EIS. R_{ct} increases in each step of modification and further increases by thrombin-aptamer binding due to steric hindrance of charge transfer and electrostatic repulsion of the redox couple.	147
Table 5.11. Quantitative fitted circuit analysis of non-faradaic EIS of aptasensors.	151
Table 5.12. Peak current SWV of thrombin aptasensing coupled with enzymatic reaction shows high sensitivity attributed to the cleaved pNA oxidation.	156
Table 5.13. Analytical figures of merit for thrombin detection using the developed aptasensor and enzymatic sensor.	162

List of Figures

Figure 1.1. SELEX process: A) bind oligonucleotide library and discard non-binders, B) elute oligonucleotides that bind desired target, C) perform PCR to amplify eluted binders, and D) repeat steps A through C using enriched oligonucleotide pool. Reproduced with permission from ref [22].	6
Figure 1.2. Schematic representation of electrochemical biosensors based on different biorecognition elements including a) antibody, b) enzyme, c) aptamer.[11] Created with BioRender.com.	9
Figure 1.3. Randles circuit utilizing CPE as a non-ideal double layer capacitance. Adapted from [37].	13
Figure 1.4. Nyquist plot of a Randles equivalent circuit over a wide frequency range. Reproduced with permission from ref [37].	17
Figure 2.1. UV-Vis absorbance spectra of 1 mM ferri/ferrocyanide solution in 1X PBS exposed to bright LED light for 1 and 3 days.	45
Figure 2.2. Experimental setup: a commercial gold SPE (Metrohm DropSens, C223BT) [95] connected to a potentiostat (PalmSens4).[96]	46
Figure 2.3. CV of gold SPE in 0.5 M sulfuric acid (electropolishing).	46
Figure 2.4. A) SEM image and B) EDS map of the C223BT gold working electrode.	47
Figure 2.5. EDS quantitative analysis of the C223BT gold working electrode.	47
Figure 2.6. Electrostatic binding of SARS-CoV-2 isolated S protein to ion exchange chromatography beads to positively charged Q Sepharose, and repulsion by negatively	

charged Sp Sepharose. Reproduced with permission from Crawford, M. 2021. INVESTIGATING THE USE OF ION-EXCHANGE CHROMATOGRAPHY FOR PURIFICATION OF THE SARS-COV-2 SPIKE PROTEIN. Honours Thesis, Department of Biology, University of New Brunswick. 48

Figure 2.7. CV characterization of aptasensor in each step of incubation..... 50

Figure 2.8. Modified Randles circuit: Equivalent electrical circuit of the aptasensor..... 50

Figure 2.9. Nyquist plot obtained from the EIS technique. The increase in the semi-circle represents a higher charge transfer resistance of redox molecules. 51

Figure 2.10. Relative R_{ct} signal changes of aptasensors after exposure to spike protein (SP) and non-specific proteins. Error bars represent the variability in the data collected from three individual gold SPEs for each condition..... 52

Figure 3.1. Schematic of an RF discharge plasma cleaner. 61

Figure 3.2. Schematics of the incubation chamber in Autodesk Tinkercad, dimensions are provided in millimetres: A) front view, B) top view, and C) Digital image..... 65

Figure 3.3. Effect of different plasma treatment time and power on R_{ct} provided by faradaic EIS. Used gold SPEs exhibited a high $R_{ct} \approx 8 \text{ k}\Omega$ compared to new SPEs with $R_{ct} \approx 1 \text{ k}\Omega$. After 10 minutes of air plasma cleaning at high power, R_{ct} reduced to below $1 \text{ k}\Omega$ by the removal of insulating (bio)layers. Error bars are included to represent the variability in the data collected from three different gold SPEs for each condition, with the measurements taken after a single cleaning of the sensors..... 69

Figure 3.4. A) Nyquist plots and B) CV of a used, plasma cleaned, and a new gold SPE. R_{ct} significantly reduced after plasma cleaning, while ΔE_{peak} decreased to 0.11 V , closer to

a reversible Nernstian behaviour of $1 e^-$ transfer. Potential values are vs screen-printed Ag/AgCl reference electrode in the measurement buffer solution. 70

Figure 3.5. Cyclic voltammogram of gold SPE in 0.5 M H_2SO_4 (E-polishing) reduces all gold atoms. Plasma cleaned electrodes depict a sharper peak due to a higher surface area. 72

Figure 3.6. Cyclic voltammograms of A)E-polished and B) plasma cleaned/E-polished gold SPE in 2 mM ferric/ferrocyanide in 1X TBS and 1 mM $MgCl_2$ at scan rates 25–150 mV/s..... 79

Figure 3.7. Water contact angle of A) new, B) used and C) 10 minutes air plasma cleaned gold SPE..... 80

Figure 3.8. Overlaid photoelectron spectra of A) Au4f: Plasma cleaned electrodes exhibited higher intensity through effective surface removal of contaminants, B) C1s: Plasma cleaned electrodes exhibited lower intensity through effective surface removal of excess pasting binders, and C) N1s: Plasma cleaned electrodes exhibited lower intensity through effective surface removal of immobilized biomolecules (aptamers, proteins). D) O1s: The presence of oxygen was mostly related to the organic binders and the bound gold oxide film generated due to air plasma cleaning. 82

Figure 3.9. Nyquist plot (A) and Bode plot (B) of a new and plasma regenerated electrodes after E-polish. Nyquist plot of plasma regenerated electrode exhibits a straight line and Bode plot exhibits no phase shift peak showing facile electron transfer kinetics. Equivalent Randles circuit of a new electrode (C) and plasma regenerated electrode after electropolish (D). In case of plasma regenerated electrode, due to very fast kinetics of electron transfer,

current is only limited by mass transfer and the circuit is simplified to R_u in series with Z_w .
..... 85

Figure 3.10. Aptamer load efficiency and aptasensor performance of electrodes undergoing different treatments based on the change in charge transfer resistance (ΔR_{ct}). Electrodes undergoing plasma cleaning, coupled with E-polishing, exhibit the highest aptamer load and aptasensor performance due to effective surface regeneration. Error bars are based on three individually tested gold SPEs for each condition. 86

Figure 3.11. Nyquist plots of gold SPE-based aptasensor (5 μ M aptamer, 50 nM Thrombin). Air plasma-treated electrodes exhibit significant charge transfer resistance upon thrombin incubation. 87

Figure 3.12. R_{ct} measurements after repeated formation and removal of MCH SAM by air plasma. Error bars are based on three individually tested gold SPEs for each condition. 89

Figure 3.13. SEM images of the working gold electrode A) without, B) 1 cycle, C) 2 cycles, and D) 3 cycles of air plasma cleaning reveals no morphological/structural changes in the printed gold microparticles. 90

Figure 4.1. Plasma Activated Coating (PAC) treatment of carbon electrodes. 99

Figure 4.2. Overlaid high-resolution XPS spectra of (A) P2p, (B) N1s, (C) O1s, and (D) C1s regions for surfaces with different treatments on SPCEs. 102

Figure 4.3. Bar chart comparing atomic percentage of aptamer-immobilized electrodes from XPS analysis; A) N1s: nitrogen and B) P2p: phosphorus of electrodes without and with PAC modification. Error bars are based on the XPS analysis of three individual SPCEs. 103

Figure 4.4. Cyclic voltammograms (CV) of SPCE with different surface modifications. The overlay demonstrates the enhancement of electrochemical response with PAC treatment and the subsequent decrease in peak currents following aptamer immobilization. Potential values are vs Ag/AgCl paste reference electrode in the measurement buffer solution (TBS 1X, 1 mM Mg²⁺, and 2 mM Fe(CN)₆^{3-/4-})..... 104

Figure 4.5. EIS analysis of SPCE electrodes at different modification stages. (A) Nyquist plots and (B) Bode phase angle plots of PAC-treated electrodes. 108

Figure 4.6. The resulted (A) Nyquist plot and (B) Bode plot faradaic EIS detection of thrombin using immobilized aptamer on PAC modified SPCE. 109

Figure 5.1. Electropolishing gold SPE in 0.5 M sulfuric acid provides a sharp gold reduction peak at ≈ 0.6 V which is used to calculate true surface area and roughness factor. 122

Figure 5.2. SEM image of an electropolished Italsens screen printed gold electrode showing micron-sized gold particles. 123

Figure 5.3. A) Modified Randles circuit for faradaic EIS modeling. B) Simplified equivalent circuit of a non-faradaic EIS test. 124

Figure 5.4. A) Decrease in R_{ct} and B) increase in effective capacitance of bare gold electrodes caused by $[\text{Fe}(\text{CN})_6]^{4-/3-}$ surface etching during repeated faradaic EIS scans. Error bars are included to represent the variability in the data collected from three different gold SPEs for each condition. 126

Figure 5.5. A) Treatment of the electrode with the redox-active buffer. B) Treatment of the electrode with the folding buffer..... 127

Figure 5.6. The effect of experimental conditions of thiol-modified aptamer SAMs on gold SPE. Control sample is related to electrodes without any aptamer modification (bare electrode). Error bars are included to represent the variability in the data collected from three different gold SPEs for each condition.	128
Figure 5.7. A) Nyquist plot and B) complex capacitance plot of gold electrode anti-biofouling by MCH.....	130
Figure 5.8. A) Nyquist plot and B) complex plane of thrombin adsorption on the gold SPE.	132
Figure 5.9. Anson plot response of aptasensors in absence (black curve) and presence (grey curve) of RuHex. A constant potential of -0.5 V is applied for 0.25 seconds, resulting in a significant charge increase with RuHex due to electrostatic binding, while the absence of RuHex shows minimal charge increase from ion adsorption. From 0.5 to 0.7 seconds, when the potential changes to +0.2 V, a drop in charge occurs if Ru ³⁺ was present, as they detach from the negatively charged aptamer.....	136
Figure 5.10. The slope of the $-Z''$ vs $\omega^{-1/2}$ provides the fitted σ value.	141
Figure 5.11. A) Nyquist plot and B) complex capacitance plot of a TCEP-reduced aptasensor.....	146
Figure 5.12. Nyquist plot of aptamer:MCH co-immobilization.	149
Figure 5.13. Sandwich assay using TBA15 as the homogenous assay pre-mixed with thrombin and incubated with TBA29 as the immobilized aptamer	150
Figure 5.14. Non-faradaic EIS A) Nyquist plot and B) complex capacitance plot of a thrombin aptasensor.	152

Figure 5.15. A) CV of pNA (100 μ M in 4.5% DMSO) and blank (without pNA) on an GCE. B) CV of pNA 100 and 200 μ M. C) Chronoamperometry (CA) response of varied concentration of pNA at -0.85 V for 10 s. D) CV of substrate with thrombin (1 μ M) and HSA control (50 μ M).....	153
Figure 5.16. A) Effect of reduction potential on signal generation. B) Direct enzymatic reaction measurement by SWV in the presence of varied amounts of thrombin (without aptamer). C) Aptasensor coupled with thrombin substrate for enhanced detection of thrombin by detecting the oxidative current of cleaved substrate. D) UV-Vis spectrophotometry of varied concentrations of thrombin in the presence of 100 μ M substrate vs control (50 μ M HSA).....	155
Figure 5.17. A) Oxidation current of 1 μ M tethered thrombin on gold electrode with or without MCH after 20 min in presence of 100 μ M substrate. B) The reproducibility of peak oxidation current was assessed through five repeated measurements of the same concentration of thrombin (1 μ M). C) Oxidation of substrate in absence of thrombin. D) SWV of pNA release from thrombin substrate in the presence of 1 μ M thrombin shows two-step reduction at -0.3 and -0.6 volts due to nitro to amine reduction.	159
Figure 5.18. Lineweaver–Burk plot of the enzymatic thrombin activity (100 nM) monitoring on Italsens gold SPE using varied amounts of H-D-Phe-Pip-Arg-pNA substrate. Reaction rate (v) was the slope of the pNA oxidation peak current in the first 60 seconds of thrombin introduction. Error bars shown for each point were based on the three replicates of each thrombin concentration on freshly prepared gold SPEs. RSD of calculated K_m found to be 5.7%.....	161

Figure 5.19. Calibration plots of thrombin biosensing on Italsens gold SPE; A) Enzymatic electrochemical thrombin assay: Substrate concentration was kept constant (200 μM) in all experiments. Reaction rate (v) was the slope of the pNA oxidation peak current in the first 60 seconds of thrombin introduction. B) Thrombin aptasensing using 10 $\text{ng}/\mu\text{L}$ aptamer and 1 mM MCH, both incubated for 1 hour. Error bars shown for each point were based on the three replicates of each thrombin concentration. 162

Figure 5.20. Selectivity tests of the developed biosensors for thrombin detection (Thr 100 nM) in the presence of interfering proteins, including prothrombin (Pthr, 0.7 μM) and fibrinogen (Fib 4.5 μM); A) Enzymatic sensor response, and B) aptasensor sensor response. Error bars are provided based on three replicates on Italsens gold SPE-based sensors..... 164

List of Abbreviations

Abbreviation	Full Form
AFM	Atomic Force Microscopy
CPE	Constant Phase Element
CV	Cyclic Voltammetry
DPV	Differential Pulse Voltammetry
ssDNA	Single Strand Deoxyribonucleic Acid
EAB	Electrochemical Aptamer-Based
EIS	Electrochemical Impedance Spectroscopy
E-Polish	Electropolish
MCH	Mercaptohexanol
OCP	Open Circuit Potential
PAC	Plasma Activated Coating
POC	Point Of Care
RF	Radio Frequency
RSD	Relative Standard Deviation
SAM	Self Assemble Monolayer
SEM	Scanning Electron Microscope
SPE	Screen Printed Electrode
SWV	Square Wave Voltammetry
TBA	Thrombin Binding Aptamer
TBS	Tris Buffer Saline

Abbreviation**Full Form**

WCA

Water Contact Angle

XPS

X-Ray Photoelectron Spectroscopy

List of Symbols

Symbol	Definition	Unit
A	Electrode Surface Area	cm ²
C	Capacitance	f
C ⁰	Bulk Concentration of Analyte	mol/cm ³
C _{dl}	Double Layer Capacitance	f
D	Thickness Of Attached Layers	cm
D	Diffusion Coefficient	cm ² /s
ΔE _{peak}	Peak-To-Peak Separation	v
E _{ox}	Oxidation Potential	v
E _{red}	Reduction Potential	v
F	Faraday Constant	C/mol
Γ _{ss}	Surface-Bound Species Concentration	mol/cm ²
I _{peak,Ox}	Oxidation Peak Current	a
K ^o	Heterogeneous Electron Transfer Rate Constant	s ⁻¹
K _{cat}	Catalytic Rate Constant	s ⁻¹
K _m	Michaelis Constant	s ⁻¹
M	Number Of Nucleotides In DNA	-
N	Exponent Of Constant Phase Element	-
N _A	Avogadro's Number	mol
Φ	Phase Angle	°

Symbol	Definition	Unit
n	Exponent of Constant Phase Element	-
N_A	Avogadro's Number	mol
φ	Phase Angle	$^\circ$
Q	Charge	C
Q^0	Constant Phase Element Admittance	S
Q_{dl}	Double Layer Capacitance Charge	μC
Q_{red}	Charge for Oxygen Electro-Desorption	μC
Q_{ss}	Surface-Bound Charge	μC
Q_{tot}	Total Charge	μC
r	Roughness Factor	-
R	Gas Constant	J/(mol.K)
R_{ct}	Charge Transfer Resistance	Ω
R_s	Solution Resistance	Ω
R_u	Uncompensated Resistance	Ω
S	Electrode Surface Area	cm^2
S_{geom}	Geometrical Electrode Surface Area	cm^2
S_{true}	True Electrode Surface Area	cm^2
T	Temperature	K

Symbol	Definition	Unit
v	Scan Rate	$V.s^{-1}$
W	Warburg Impedance Element	Ω
ω	Angular Frequency	$rad.s^{-1}$
Z'	Real Part of Impedance	Ω
Z''	Imaginary Part of Impedance	Ω
Z_W	Warburg Impedance	Ω
z	Charge of Redox Molecule	-
ε	Dielectric Constant	-
ε_0	Permittivity of Free Space	-
σ	Warburg Coefficient	$\Omega \cdot s^{1/2}$
Γ_{ss}	Surface-Bound Species Concentration	mol/cm^2

1. Chapter 1: Introduction

1.1. Overview of introduction to biosensors

This chapter provides the foundation for understanding the design, function, and significance of the electrochemical biosensors and aptasensors developed in this thesis. To guide the reader through the diverse and interconnected topics presented, this introductory chapter is organized as follows: Section 1.2 introduces the concept and historical development of biosensors, including their key components and classic examples that have shaped the field. Section 1.3 discusses the limitations of conventional biosensing technologies and highlights the demand for novel biosensors capable of detecting a wider range of targets. Section 1.4 compares antibodies and aptamers as selective biorecognition elements, describing their development, advantages, and the context of their use in biosensing applications. Section 1.5 explores the discovery and development of aptamers, their selection process, and their unique properties as biorecognition elements. Section 1.6 outlines the structure and working mechanisms of electrochemical aptasensors, with particular focus on the use of electrochemical impedance spectroscopy (EIS) as a detection technique. Section 1.7 describes the EIS method utilized for characterizing electrochemical aptasensors, outlining the relevant equations and mechanisms associated with EIS. Section 1.8 identifies common challenges in aptasensor development, including electrode surface defects, probe stability, and biofouling, among others. Section 1.9 presents strategies and technological innovations to overcome the identified limitations, ranging from electrode surface modifications to novel anti-biofouling techniques. Section 1.10 summarizes the specific research aims of the thesis, highlighting the target analytes (SARS-CoV-2 spike

protein and thrombin) and the innovative approaches—such as plasma surface engineering—investigated in this thesis.

1.2. Biosensors

The term "biosensor" was first coined by American biochemist Leland C. Clark Jr., renowned for inventing the oxygen electrode in 1956.[1] This electrode enabled the selective detection of oxygen, revolutionizing the measurement of dissolved oxygen in biological samples. Building upon this principle, Clark and then Updike developed the first enzymatic glucose biosensors, demonstrating the measurement of glucose concentrations in a solution containing glucose oxidase and oxygen.[2, 3] Using amperometric detection, a constant potential was applied to oxidize hydrogen peroxide generated during the enzymatic reaction. The resulting current was proportional to the glucose concentration, enabling quantitative analysis. The glucose biosensor marked a milestone in addressing a critical healthcare need: monitoring blood glucose levels for managing diabetes. With more than 800 million people diagnosed with diabetes, the disease remains a prevalent health concern.[4] Glucose levels fluctuate throughout the day, and improper regulation can lead to hypoglycemia or hyperglycemia, both of which pose severe risks, including coma and other life-threatening outcomes.[5]

In another realm of biosensing, lateral flow assays (LFAs) have gained prominence for their simplicity, portability, and ability to provide rapid diagnostics. Research on antibodies commonly used in LFAs dates back over eight decades and was developed by Berson and Yalow, earning them the Nobel Prize in Medicine in 1977.[6] Since its introduction, immunoassays have undergone significant evolution, becoming an established and commercialized technology. Rapid detection kits based on LFAs have become a well-

established solution for point-of-care (POC) detection of biochemicals and pathogens in non-clinical settings. LFAs were first introduced in the late 1980s for rapid pregnancy testing and later for the detection of sexually transmitted diseases.[7] Nowadays, they are commonly used for the detection of SARS-CoV-2 and drugs of abuse.[7] The mechanism of sensing in a conventional LFA is based on the selective affinity between the immobilized antibodies on gold nanoparticles, i.e., detection probes, and the target antigen forming an immune complex.[8] The immune complex wicks along a paper-based strip via capillary action into the detection zone where the antigen is sandwiched between the detection probe and a secondary antibody, i.e., capture probe, which consequently forms a line that can be visualized by naked eye.[8]

1.3. The need for broader biosensing capabilities

The demand for novel biosensors extends beyond traditional glucose monitoring or immune-responsive targets. Consider scenarios like biotechnology production facilities, where real-time monitoring of protein or antibody concentrations can significantly reduce costs and time compared to conventional, instrument-intensive analyses.[9] Alternatively, in underdeveloped regions with limited healthcare access, affordable and accessible POC biosensors could provide rapid diagnostics for various biomarkers.[10]

These two types of biosensors—enzyme-based glucose sensors and antibody-based lateral flow assays—are highly effective and dominate the field of biosensing.[10] However, what about targets that do not induce an immune reaction or lack enzymatic electroactivity? Are there analytes that are critical to measure in a POC setting but fall outside the capabilities of these conventional biosensors? In this case, artificially produced affinity capture probes,

such as aptamers, can be useful for targeting analytes that are not necessarily immune-responsive or do not undergo oxidation-reduction.[11]

1.4. Antibodies and aptamers as affinity-based biorecognition elements

Antibodies and aptamers are selective affinity-based biorecognition elements utilized in a range of research, diagnostic, and therapeutic contexts.[12] Although both antibodies and nucleic acids were discovered in the late 19th century, significant advancements in isolating and producing antibodies, DNA, and RNA occurred in the late 1950s.[6] However, successful antibody therapies have only emerged more recently, while the field of aptamer-based therapies continues to evolve. Developing methods for generating monoclonal antibodies and selecting DNA/RNA aptamers has taken many years. It was eleven years after the advancements in monoclonal antibody production that the first antibody drug received FDA approval, followed by another eleven years until the approval of the first humanized antibody in 1997, marking a significant success in antibody therapy.[13] It took an additional 15 years for the FDA to approve the first antibody-drug conjugate.[14] Meanwhile, aptamers were discovered in 1990, and the first therapeutic aptamer was approved in 2004, leading to anticipation for the next significant advancement in aptamer-based therapies.[15-17]

1.5. History of aptamers

The term “aptamer” was first coined by Andy Ellington and is derived from two Latin words: “aptus” which means to fit, and “meros” which means part.[15] Aptamers are short, single-stranded molecules of DNA or RNA (ssDNA or ssRNA) that can specifically bind to a variety of targets, including proteins, peptides, carbohydrates, small molecules, toxins, and even living cells.[17, 18] They can adopt different shapes due to their ability to form

helices and single-stranded loops.[19] Their versatility allows them to bind targets with high selectivity and specificity. Instead of being determined by their primary sequence, the binding affinity of aptamers is influenced by their secondary structure.[19] The recognition and binding to targets involve three-dimensional interactions that rely on shape as well as hydrophobic effects, base stacking, and intercalation.[18]

Aptamers that bind specifically to a target are identified from a vast library of oligonucleotides using a technique known as SELEX, which stands for Sequential Evolution of Ligands by Exponential Enrichment.[20] This method involves multiple iterations where aptamers that do not bind are eliminated, while those that do bind to the target are further amplified by Polymerase Chain Reaction (PCR). PCR involves a series of temperature cycles that enable the replication of DNA segments, making it possible to generate millions of copies of a target DNA region using a DNA polymerase enzyme.[21] After initial rounds of positive selection, negative selection is often conducted to improve the specificity of the resulting aptamer candidates (Figure 1.1). Several rounds of SELEX are carried out with progressively stricter conditions to enhance the concentration of the desired oligonucleotide.

Aptamers are used as an emerging biorecognition element with potential advantages over conventional biorecognition elements. Table 1.1 provides a comparison between antibody, enzyme, and aptamer as biorecognition elements in biosensors. Aptamers offer a potentially large target pool that can bind to non-immunogenic molecules. Their in vitro production can be cost-effective with higher stability and shelf life compared to antibodies.[12]

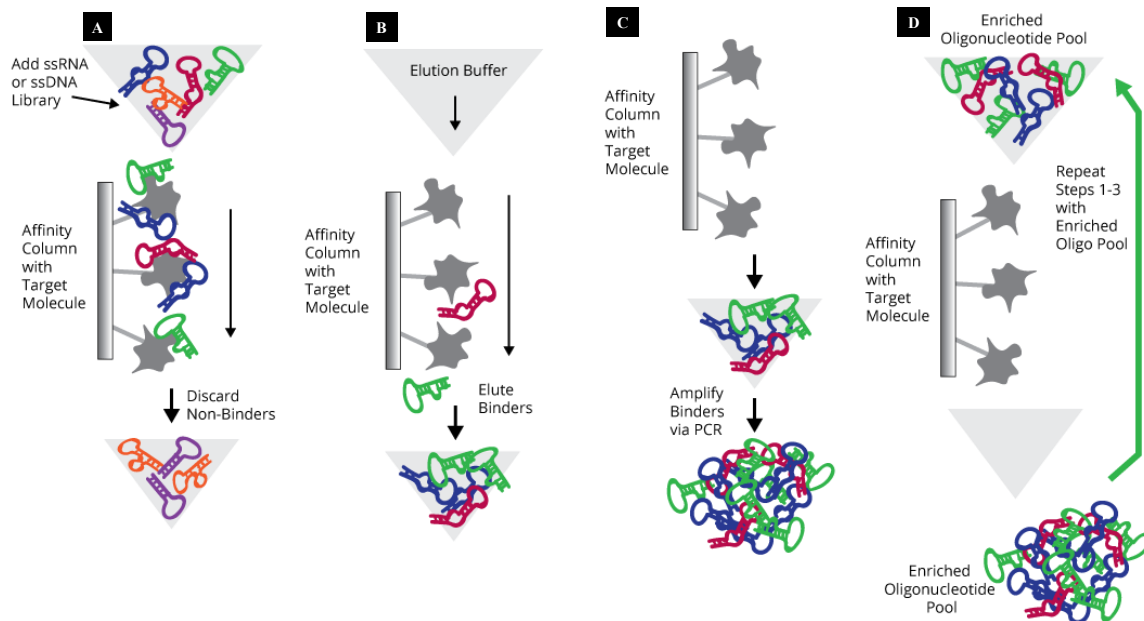


Figure 1.1. SELEX process: A) bind oligonucleotide library and discard non-binders, B) elute oligonucleotides that bind desired target, C) perform PCR to amplify eluted binders, and D) repeat steps A through C using enriched oligonucleotide pool. Reproduced with permission from ref [22].

1.6. Electrochemical aptasensors

Aptasensors typically consist of three major components: the aptamer, the electrode, and the signal transduction system.[23] The aptamer is immobilized on the surface of the electrode, which serves as the biorecognition element. The target molecule in the sample solution binds to the aptamer, causing a change in the electrochemical properties of the electrode surface. The signal transduction system, a potentiostat, detects and converts this change into a measurable electrical signal.[23] Herein, we focus on ssDNA aptamers. In an ssDNA, one or more phosphate groups are bonded to atom C3' or atom C5' of the five-carbon sugar group of an ssDNA (pentose) to form a 3'-nucleotide or a 5'-nucleotide, respectively.[24]

Table 1.1. Comparative analysis of enzyme, antibody, and aptamer as common biorecognition elements in biosensors.[11]

	Enzyme	Antibody	Aptamer
Stability	Temperature/pH induced degradation, inactivation by inhibitors[25]	Temperature/pH induced degradation[26]	High but prone to nuclease degradation[27]
Target pool	Limited to oxidoreductase reactions[27]	Limited to immunogenic compounds[12, 28]	Wide range but limited with hydrophobic/negatively charged targets[29, 30]
Average size	~3-7 nm[31]	~10-15 nm[32]	~1-2 nm[32]
Development process	<i>In vitro</i> by microbial fermentation <i>In vivo</i> by recombinant technologies[33]	<i>In vivo</i> , requires immune response and animals[28]	<i>In vitro</i> , SELEX[12]
Production time	Days to weeks[33]	Weeks to months[28]	Days to weeks[12]

In an electrochemical aptasensor, each end of an aptamer strand can be modified with a desired functional group for two primary purposes: a) chemical immobilization on an electrode by modifying the 5' end with thiol or amine groups and b) covalent attachment of a redox molecule such as methylene blue or ferrocene on the 3' end.[23] Figure 1.2 depicts the most common mechanisms of biosensing in the three types of introduced biorecognition elements, including a) antibody: in a label-free approach increase in the thickness of the biorecognition layer causes steric hindrance which reduces electron transfer rate of redox mediator. In a sandwich assay, the signals originate from the catalytic reaction of an enzyme molecule, designated as a signal tracer, with the detection antibody.

The electrode can then detect the electroactive products, b) enzyme: the substrate undergoes catalytic conversion into an electroactive product, which can be monitored using an amperometry technique. In labeled enzymatic sensors transfer of electron from enzyme to electrode needs an external chemical mediator, and c) aptamer: there are several mechanisms by which the binding event between the aptamer and the target can be transduced into an electrical signal. One common mechanism is based on using a redox-active probe, i.e., $[\text{Fe}(\text{CN})_6]^{3/4-}$ in the measurement solution.[34] In the presence of a target analyte, the aptamer-target complex would impede the redox molecules to migrate from the bulk solution to the electrode's surface; thus, a decrease in the produced current is anticipated, which can be monitored by direct current (DC) voltammetry techniques.[34] Electrochemical impedance spectroscopy (EIS) technique can also be used to measure the charge transfer resistance increase caused by spatial hindrance of the target-aptamer complex.[34, 35] Another mechanism is based on the use of redox probes that are covalently attached to the aptamer. The binding event between the aptamer and the target molecule can induce a conformational change, which causes the aptamer's end (either 3' or 5') to get closer or further to/from the electrode, therefore causing a shift in the redox activity and the produced current.[36]

1.7. Theory of EIS

In EIS characterization of an electrochemical sensor, the working electrode is perturbed by applying a small AC amplitude (V_0) along with a fixed direct potential, commonly open circuit potential (OCP), which is approximately equal to the formal potential over a wide range of frequencies.[37]

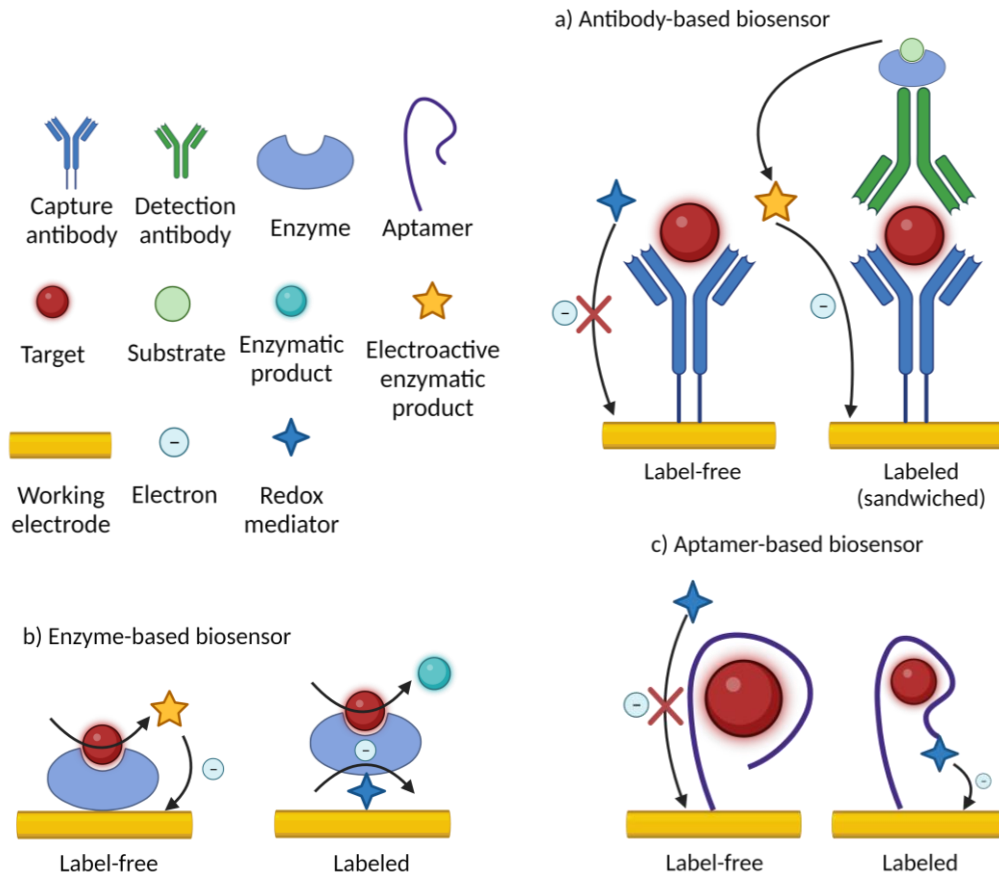


Figure 1.2. Schematic representation of electrochemical biosensors based on different biorecognition elements including a) antibody, b) enzyme, c) aptamer.[11] Created with BioRender.com.

The alternating voltage $v(t)$ applied to the electrode at a particular frequency (f) is defined as Equations 1.1 and 1.2.[37]

$$v(t) = V_0 \sin(\omega t) \quad 1.1$$

$$\omega = 2\pi f \quad 1.2$$

Where ω is angular frequency in rad/s and V_0 is AC amplitude. The applied voltage generates a current resulting from both faradaic processes (redox reactions) and non-

faradaic processes (charging and discharging of double-layer capacitance).[37] The resulting alternating current $i(t)$ at the same frequency is defined as Equation 1.3.[37]

$$i(t) = I_0 \sin(\omega t + \varphi) \quad 1.3$$

Where I_0 is the maximum current peak applied to the electrode and φ is the phase shift (in degrees) between current and voltage .[37] According to Ohm's law, the presence of current and potential implies resistance.[37] In EIS of an electrode in a solution containing redox-active species, the current flow is impeded by various factors. These include the direct current (DC) resistance arising from solution resistance and faradaic processes, which are governed by Ohm's law.[37] Additionally, the alternating current (AC) is impeded by non-faradaic processes. This opposition is termed reactance, which, unlike resistance, is frequency-dependent but still measured in Ohms.[37] In conclusion, impedance is the combined effect of both resistance and reactance in a system subjected to small amplitude AC voltages combined with a DC potential such as OCP at which the current flowing in the cell is zero.[37] The opposition to the current flow or impedance at a particular frequency is defined as Equations 1.4 to 1.10.[37]

$$Z(\omega) = |Z| e^{j\varphi} = |Z| (\cos(\varphi) + j \sin \varphi) = Z' + jZ'' \quad 1.4$$

$$|Z| = \sqrt{(Z')^2 + (Z'')^2} \quad 1.5$$

$$Z' = |Z| \cos \varphi \quad 1.6$$

$$Z'' = |Z| \sin \varphi \quad 1.7$$

$$\varphi = \omega t \quad 1.8$$

$$\tan(\varphi) = \frac{Z''}{Z'} \quad 1.9$$

$$\varphi = \tan^{-1} \frac{Z''}{Z'} \quad 1.10$$

Where $Z(\omega)$ is the total impedance at a certain frequency, $|Z|$ is the impedance magnitude, Z' is the real impedance representing resistance on the x-axis, Z'' is the imaginary impedance representing reactance on the y-axis, and φ is the phase in degrees, which is the angle between the voltage and current indicating the extent to which the current lags or leads the voltage.[37]

The producing current of an electrochemical sensor in a redox-active solution where it is perturbed by alternating current (i_{tot}) is defined as Equation 1.11.[37]

$$i_{tot} = i_F + i_C \quad 1.11$$

Where i_F expresses the faradaic current produced by redox couple charge transfer and i_C is current charging/discharging at the double layer capacitor.[37]

The total impedance (Z_{tot}) of an electrochemical system in a redox-active solution is defined as Equations 1.12 to 1.17.

$$Z_{tot} = R_u + Z_F + Z_{Cdl} \quad 1.12$$

$$Z_F = R_{ct} + Z_W \quad 1.13$$

$$Z_{cdl} = \frac{1}{C_{dl} j\omega} \quad 1.14$$

$$R_{ct} = \frac{RT}{k^0 n^2 F^2 A C_0} \quad 1.15$$

$$Z_w = R_w + C_w = [\sigma \omega^{-1/2} - j(\sigma \omega^{-1/2})] \quad 1.16$$

$$\sigma = \frac{2RT}{n^2 F^2 \sqrt{2} \sqrt{D} C_0} \quad 1.17$$

Where uncompensated resistance (R_u) is the ohmic resistance of the measurement buffer affected by the distance between the reference and working electrodes, ohmic resistance of connection cables/wirings, and the ohmic resistance of the working electrode. Faradaic impedance (Z_F) expresses the difficulty of charge transfer (R_{ct}) and mass transfer (Z_w) of redox couple to the electrode surface. Z_{cdl} is the charge/discharge impedance of double layer capacitor.

R_{ct} is related to the difficulty of heterogeneous electrochemical charge transfer from the redox couple to the working electrode. In the R_{ct} Equation 1.15, R is the gas constant (8.314 J mol⁻¹ K⁻¹), T is the temperature (K), k^0 is heterogeneous electron transfer rate (cm s⁻¹), n is number of electron transfer of the redox couple, F is Faraday's constant (96485 C mol⁻¹), A is the electroactive surface area of the working electrode (cm²), and C_0 is the concentration of the redox couple (mol L⁻¹).

At low frequencies, the electrode is depleted from the redox couple; thus, the electron transfer is limited to the diffusion of the redox couple from the bulk solution to the electrode's surface.[37] The opposition to this diffusion is known as the Warburg impedance (Z_w), described by a resistor (R_w) and a capacitor (C_w) in series, both of which

are inversely proportional to frequency. Thus, the lower the frequency, the higher the Warburg impedance and both the real and imaginary components of impedance increase equally with frequency in the Warburg region. [37]

1.7.1. EIS circuit and plot analysis

One of the most common representations of impedance spectroscopy results is through a Nyquist plot.[37] In a Nyquist plot, imaginary component of impedance ($-Z''$) is plotted against the real component of impedance (Z') over a wide range of excitation frequencies.[37] To analyze these results, an equivalent electrical circuit that models the electrochemical sensor can be defined. The Randles circuit is the most frequently used model, as it effectively represents charge transfer resistance, Warburg impedance, and double-layer capacitance (Figure 1.3). By fitting the impedance data to this equivalent circuit using appropriate modeling software, the values of each electrical component can be accurately calculated.[37]

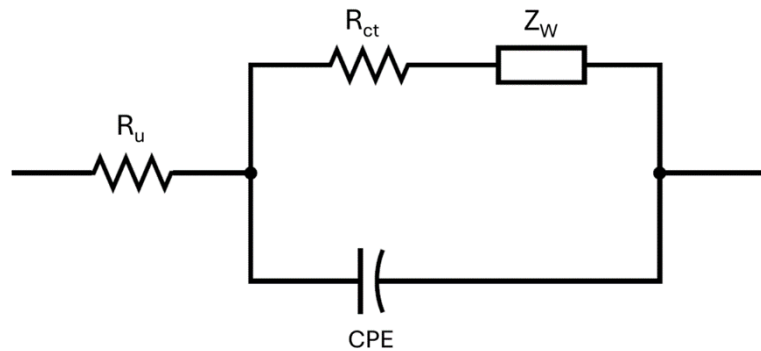


Figure 1.3. Randles circuit utilizing CPE as a non-ideal double layer capacitance. Adapted from [37].

In a Randles circuit of an electrochemical sensor, it is common to use constant phase element (CPE) instead of C_{dl} . CPE is a non-ideal capacitor in a real electrochemical system, which contributes to the charging/discharging of the electric double layer. One proposed

physical explanation for the non-ideal behaviour of double-layer capacitance is the roughness of the electrode.[38] Another theory suggests that it results from non-uniform reaction rates on a surface, which is observed in polycrystalline metal surfaces or carbon electrodes with varying activation energies across different active sites.[39] CPE is frequency-dependent, and its impedance is defined by the Equation 1.18.

$$Z_{CPE} = \frac{1}{Y_0(j\omega)^n} \quad 1.18$$

Where Y_0 is a numerical value of admittance ($1/|Z|$) at angular frequency $\omega=1$ rad/s with a dimension $F s^{n-1}$, and n is a constant phase exponent which is related to the deviation from a regular capacitor and is between zero and one. Hence, it has a similar dimension to capacitance and in an ideal double-layer capacitance where $n = 1$, $Y_0 = C_{dl}$. The phase shift φ of the Z_{CPE} is independent of frequency and has a value of $90n$ degrees. This gives the CPE its name.[40]

The Nyquist plot of a Randles circuit can be divided to four categories. This summary was adopted by the works of Chang, Wang and Lazanas et al.[37, 40, 41]

i) At the starting point of the plot, the frequency is very high (100 kHz). At high frequencies, the reactance of the C_{dl} is insignificant ($Z_{Cdl} \propto \omega^{-1} \approx 0$) and much smaller than charge transfer resistance ($Z_{Cdl} \ll R_{ct}$). Thus, the current (i_{tot}) goes through the least resistive pathway, which is through R_u and CPE and is defined as $i_{tot} = i_c$. Z_w is also insignificant since $Z_w \propto \omega^{-\frac{1}{2}}$. Moreover, the sinusoidal waveforms $V(t)$ and $i(t)$ are almost in-phase ($\varphi \approx 0$, $e^{j\varphi} = 1$, $\sin(\varphi) = 0$). Thus, the impedance is independent of the frequency and contains only the real component ($Z \approx Z'$). As a result, $Z_{tot} = R_u$

ii) As the frequency decreases, i_{tot} would split to both capacitive and faradaic pathways. Moreover, X_{Cdl} becomes significant to a point that Z'' reaches its maximum. The frequency

of this maximum is defined as $\omega = \frac{1}{R_{\text{ct}} C_{\text{dl}}}$.

iii) At low frequencies, the reactance of C_{dl} is very high ($X_{\text{Cdl}} \gg R_{\text{ct}} + Z_{\text{W}}$) and therefore the current passes through the faradic pathway, including R_{u} , R_{ct} , and Z_{W} . Thus, at both high and low frequencies, the Randles circuit behaves as a resistor, and its impedance is defined as R_{u} and $R_{\text{u}} + R_{\text{ct}}$, respectively.

iv) As the frequency decreases further, the current is constrained by mass transfer of the redox couple from the bulk solution to the electrode's surface. The low frequency region is a straight line with slope 1 ($\varphi \approx 45^\circ$), defined as Warburg impedance, with equal resistive ($\sigma\omega^{-\frac{1}{2}}$) and capacitive ($j(\sigma\omega^{-\frac{1}{2}})$) behaviour.

Overall, at both high frequencies ($\omega \rightarrow \infty$; $X_{\text{Cdl}} \rightarrow 0$; $Z = R_{\text{u}}$) and low frequencies ($\omega \rightarrow 0$; $X_{\text{Cdl}} \rightarrow \infty$; $Z = R_{\text{u}} + R_{\text{ct}}$) the circuit's behaviour is governed by resistors rather than the capacitor.

Another common impedimetric plot is known as the Bode plot. It consists of two curves: $\log |Z|$ vs f and $-\varphi$ vs f . The advantage of the Bode plot over the Nyquist plot is that it directly provides information about the total impedance and phase changes at each specific frequency. Moreover, impedance data over a wide range of frequencies is clearer since both $|Z|$ and frequency axes are on a logarithmic scale. The Bode plot of a Randles circuit can be divided into four categories.

- i. At the starting point $f \geq 100\text{KHz}$ and since $t = \frac{1}{f}$ hence $\varphi = \omega t \approx 0$. Moreover, the logarithmic change in $|Z|$ is small and does not increase significantly since most current passes through the low reactance C_{dl} .
- ii. As the frequency decreases, the impedance increases, and consequently, the phase shift increases until it reaches a maximum where the circuit's behavior is influenced by both resistive and capacitive elements.
- iii. After the maximum shift in phase, which is a transition between the circuit's capacitive and resistive behavior, the phase shift decreases, and the impedance becomes more dominated by resistors.
- iv. At low frequencies, impedance is governed by the difficulty of mass transfer diffusion, which involves both resistive and capacitive elements; thus, the phase shift would increase again.

1.7.2. EIS-based electrochemical aptamer biosensors for protein detection

The impedimetric aptasensor principle was first introduced in early 2005.[42-46] In short, the Nyquist plot obtained from the EIS analysis is modelled by a Randles circuit to calculate the R_{ct} of a redox couple. The R_{ct} increases after the aptamer is immobilized onto an electrode, as the aptamer's monolayer impedes the facile electron transfer between the charged redox couple and the electrode. This is related to the electrostatic repulsion between the negatively charged phosphate backbone of aptamers and redox couple, along with the densely packed SAMs that create a barrier to diffusion from the bulk solution to the electrode surface.[43]

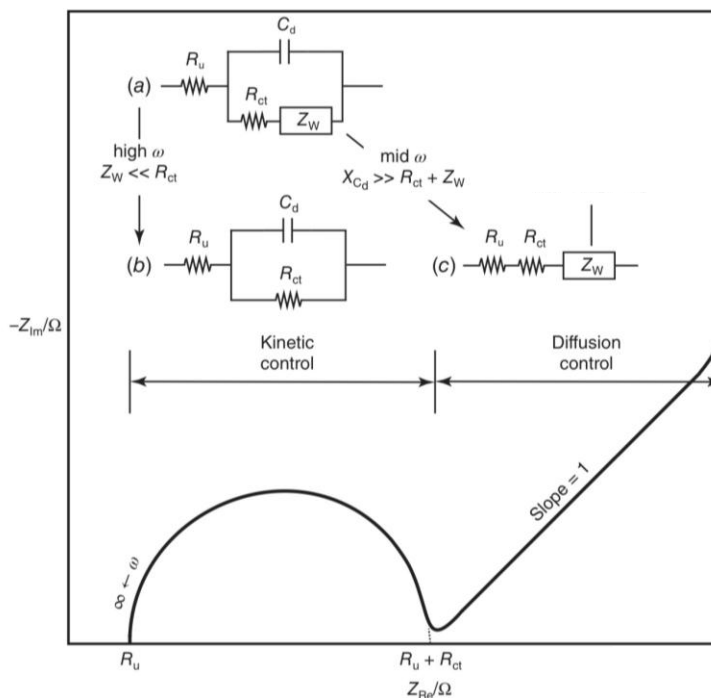


Figure 1.4. Nyquist plot of a Randles equivalent circuit over a wide frequency range. Reproduced with permission from ref [37].

After the aptamer is immobilized onto the electrode, the next step involves incubating the electrode with a sample containing the specific protein that the aptamer targets. This incubation allows for the selective binding of the protein to the aptamer. Once protein binds to the aptamer, R_{ct} increases significantly as the hydrophobic bulky protein layer disrupts electron transfer between the electrode and the redox couple.[45] The linear response between thrombin concentration and R_{ct} can be used as a signal to quantify protein concentration.

1.8. Bottlenecks in the stability and performance of aptasensors

Herein, technological bottlenecks in the performance of aptasensors, particularly gold electrode-based aptasensors, will be investigated including (1) electrode defects due to surface treatment methods,[47-50] (2) hampering effects of redox molecules,[51-54] (3)

electrical potential-induced aptamer detachment,[34, 55] (4) thermal-induced monolayer solubilization,[56, 57] (5) biochemical/enzymatic degradation,[27] (6) biofouling[27, 55]. The following subsections provide a detailed explanation of each bottleneck. Moreover, we proposed antidotes for the obstacles by applying novel surface treatment methods, adapting redox molecules, tuning electrochemical tests, tweaking backfilling agents, and anti-bio-fouling coatings as discussed in section 1.9.

1.8.1. Electrode pre-treatment can lead to undesired defects

The quality of self-assembled monolayers (SAMs) on polycrystalline gold is dependent on the reliable removal of inherent contaminants on ambient surfaces and exposure of a pristine gold surface.[58] In the past, an acidic piranha solution (a 3:1 concentrated sulfuric acid:30% hydrogen peroxide solution) was commonly used to remove organic contaminants during gold electrode production. However, piranha creates uncontrollable defects on the gold electrode, causing extensive etching and oxidation. As a safer alternative, sulfochromic acid was proposed to eliminate organic residues, but it causes permanent etch pits and is not recommended for repeated use.[59]

A comprehensive study evaluated different electrode pre-treatment methods, including chemical oxidation, ultraviolet (UV) and ozone treatment, and electrochemical treatment.[47] Dipping a gold electrode in 50 mM potassium hydroxide with 25% hydrogen peroxide and performing single linear sweep voltammetry from -0.2 to -1.2 V in 50 mM KOH resulted in the lowest contamination (from elemental carbon and oxygen sources) and the lowest charge transfer resistance.[47]

X-ray photoelectron spectroscopy (XPS) provided the surface elemental composition of gold electrodes treated with different methods.[60] Although all surface pre-treatment

methods significantly decreased contamination and increased SAMs coverage, they induced structural changes that affected functionalization characteristics. Different pre-treatment methods did not result in significant differences in surface area or molecule coverage. However, some induced structural changes to the gold surface, and affected the morphology of the thiolated molecule layer. Pre-treatment methods that contain chloride anions were found to cause changes to the gold surface structure, leading to surface redistribution and possible introduction of defects.[60]

Electrochemical technique parameters, such as cyclic voltammetry (CV), in which recurrent potential scans are performed between two potentials, also affect the preparation of gold electrodes.[49] Anion adsorption resulted in a passivating layer of Au_2SO_4 or AuCl , which is formed through a redox reaction on the gold electrode. It is recommended to avoid chloride leakage and platinum counter electrodes when preparing gold electrodes using CV. Surface roughness is another debated topic, as recent studies have shown that alkanethiolate monolayers on rough gold surfaces can act as stronger barriers to electron transfer than those on smooth surfaces.[36] However, the defects on smooth surfaces were larger than those on rough surfaces, leading to an increased rate of heterogeneous electron transfer.

1.8.2. Redox molecules can change the surface properties of aptasensors

Understanding electron transfer at electrode-electrolyte interfaces is crucial for probing biomolecular interactions on the surface of heterogeneous aptasensors. $[\text{Fe}(\text{CN})_6]^{3/4-}$ is a common redox probe to test the electron transfer on gold-based electrochemical aptasensors. However, the interaction between gold electrodes and $[\text{Fe}(\text{CN})_6]^{3/4-}$ often leads to unwanted reactions. Early studies have focused on measuring intermediate species and

by-products such as Prussian blue,[61] and recent studies show the evolution of $\text{Au}(\text{CN})_2^-$ on the gold electrode's surface during voltametric techniques such as CV.[51] Moreover, the surface of gold electrodes becomes rough and less reproducible after reacting with $[\text{Fe}(\text{CN})_6]^{3/4-}$ due to the etching effect of CN^- on the gold substrate.[54] Such a disruptive and reactive nature of $[\text{Fe}(\text{CN})_6]^{3/4-}$ could result in detachment of aptamers from the gold electrode, which significantly drifts the sensor's signals and reduces its performance over time. Other redox probes, such as covalently attached ferrocene and methylene blue, were introduced as alternative probes in analyzing electrochemical aptasensors.[36, 62] However, the synthesis of covalently attached redox tags is cumbersome and more expensive than conventional redox probes. Moreover, fluctuations in the charge transfer resistance in redox-tagged aptasensors are very common due to the inherent sensitivity of aptamers to their media as well as sensitivity of electrodes to the solution's ionic strength which can result in false positives during sensing experiments. Loss of thiolated nucleic acid probes during electrochemical tests can alter the two- and three-dimensional structures of the ssDNA probes, exacerbating signal changes.[34, 36]

In conclusion, the use of $[\text{Fe}(\text{CN})_6]^{3/4-}$ as a redox probe in electrochemical aptasensors can lead to unwanted reactions, negatively impacting the sensor's performance over time. While alternative redox probes have been introduced, they come with their own limitations and challenges. A comprehensive study is needed to develop more effective and reliable redox probes for analyzing biomolecular interactions on the surface of heterogeneous aptasensors.

1.8.3. Aptamers detach from the electrode during electrochemical measurement

Even though thiolated DNA SAMs are meant to form a robust covalent bond with a gold electrode, they can be detached from the surface during electrochemical tests. For instance, applying repeated electrochemical potentials (over 100 cycles) to thiol-modified immobilized aptamers on a gold electrode, more negative than -0.4 V (vs Ag/AgCl), or more positive than -0.1 V, led to oxidation of the thiol bonds, which desorbed them from the surface.[55] Moreover, SAMs are prone to desorption and structural change during multiple CV scans.[34] Thus, it is critical to define a safe potential window during electrochemical tests and avoid repeated CV scans to reduce SAM detachment.

1.8.4. Elevated temperature leads to monolayer solubilization

The thermal stability of DNA SAMs on gold surfaces is a critical parameter correlated with the sensor's lifetime. Thermal desorption of DNA SAMs is still a significant challenge, particularly for the monitoring of therapeutic drugs and metabolites.[27] DNA SAMs prepared without any potential control over the substrate (i.e., open circuit potential deposition or OCP_{dep}) tend to be less thermally stable with reduced mobility.[56] Meanwhile, the crystallography of the underlying surface is crucial for thermal stability. Square or rectangular surface structures (e.g., surfaces from 110 to 100) exhibited the highest thermal stability, while 111 and related surfaces were the least stable.[56] Moreover, there is a trade-off between sensitivity and stability in DNA SAMs. Stable surfaces may not be optimized for sensing, while good sensors may be thermally unstable using the current preparation procedure.[57]

1.8.5. Enzymes can degrade aptamers

DNA SAMs face significant challenges when introduced into the bloodstream. The presence of both endogenous nucleases and catalytic DNAzymes reduce the stability and integrity of aptasensors.[27, 55] Blood nucleases actively target extracellular DNA, including aptamers. These nucleases cleave phosphodiester bonds within the DNA backbone, leading to the fragmentation and degradation of aptamer molecules. DNAzymes, designed for specific catalytic activities, may inadvertently target DNA aptamers. If a DNAzyme recognizes a sequence within an aptamer as its substrate, it can initiate cleavage, resulting in the fragmentation of the aptamer's structure. [27, 55]

1.8.6. Biofouling reduces electron-transfer rates

One of the primary concern in aptasensors for long-term analyte monitoring is protein biofouling.[27, 55] Biofouling leads to an initial reduction in redox-tag current when scanned in protein-rich fluids like serum. The mechanism involves hydrophobic protein domains fouling at defect sites in the monolayer. Additionally, the reorganization of biofouled protein molecules and their interactions with immobilized aptamer molecules can impact sensor response over multiple days. Overall, protein biofouling has significant implications, affecting electron-transfer rates and limiting the freedom of mobility of aptamers.

1.9. Addressing the constraints in aptasensor stability

Herein, potential methods for addressing the stability of aptasensors are introduced. Each method is discussed in detail in the following subsections, including plasma surface

treatment methods, adapting redox molecules, tuning electrochemical tests, tweaking backfilling agents, aptamer chemical modification, and anti-biofouling coatings.

1.9.1. Plasma treatment is a highly effective electrode cleaning technique

Highly purified gold surfaces are essential for the successful formation of firmly attached SAMs on the electrode surface. Gold surfaces commonly capture impurities during post-processing, storage, and chip transportation. This contamination evidently impacts both the SAM's quality and the sensor's efficiency. [58] Plasma cleaning methods using H₂ and O₂ are more effective than electrochemical cleaning methods in removing contamination, resulting in a higher SAM density.[60, 63] SAMs could be completely removed by H₂ and O₂ plasma in less than 60 seconds. The downside of pure O₂ plasma cleaning is gold oxidation (Au₂O₃) and contaminated with oxidized sulfur species.[63] However, it was found that O₂ plasma followed by an ethanol rinsing reduced surface carbon contamination of gold electrodes to less than 5% and increases elemental surface gold composition to over 90% based on an XPS analysis without any significant surface oxidation. [60]

1.9.2. Tuning electrochemical test parameters reduce electric field induced aptamer desorption

Redox-tagged aptamers (such as methylene blue) at a narrow potential window (partial scans) reduce the electrochemical oxidation and desorption of thiolated SAMs.[27, 55] For instance, limiting the potential window of methylene blue tagged aptamers to -0.4 to -0.2 V resulted in only 5% signal loss after 1500 scans. In the case of label-free aptasensors, the EIS technique has a minimal effect on the surface density of SAMs due to the small potential biases used in this technique.[34] While repeated CV scans of gold electrodes in [Fe(CN)₆]^{3/4-} redox couple led to $\approx 50\%$ decrease in surface coverage of aptamer SAMs,

repeated EIS scans in the same redox couple solution led to only ≈ 2 -10% decrease in surface coverage. Moreover, to reduce the etching of gold electrodes caused by $[\text{Fe}(\text{CN})_6]^{3/4-}$ redox couple, the introduction of hexaammineruthenium (III), or RuHex, as an alternative redox-probe during EIS measurements, with the application of a DC-bias, has proven successful.[64] In contrast to the previous study [34] it was shown $[\text{Fe}(\text{CN})_6]^{3/4-}$ redox couple causes significant signal drift—up to $\pm 40\%$ —and visibly corroded the electrodes over time, while RuHex maintained remarkable stability with only $\pm 10\%$ signal variation and no signs of degradation.[64]

1.9.3. Optimizing the alkylthiolates length chain may increase the stability of aptamers

Conventional electrochemical aptamer sensors mostly utilize 6-mercapto-1-hexanol (MCH), a hydroxyl-terminated alkylthiolate, as the passivating blocking layer molecule.[65] A study by Watkins et al showed that extending the alkylthiolate chain length increases the intermolecular forces in self-assembled monolayers on gold substrates, leading to improved stability in buffer conditions. Longer-chain alkylthiolates offer enhanced stability due to increased van der Waals interactions, resulting in more orderly packed monolayers.[27] The signal loss of methylene blue-tagged aptamers modified with MCH in a buffer at 37 °C declined 80% over a week whereas 8-mercapto-1-octanol modified sensor response declined 40% in similar conditions. However, for electrochemical aptamer sensors, which rely on electron transfer, longer alkylthiolate chains present challenges. They increased the electron-tunneling distance and reduced defects in the monolayer, hindering efficient electron transfer. While attempts have been made to use longer alkylthiolate monolayers to improve stability, issues with impeded

electron transfer and potential toxicity arise.[66] For instance, signal gain drops from $\approx 70\%$ for C6 layers to $\approx 20\%$ for C11 layers.

1.9.4. Nanocomposite electrodes and hydrogel membranes reduce biofouling

Despite the alterations to sensor signalling properties caused by biofouling, implementing membrane protection and surface chemistry modifications can mitigate these adverse changes, thereby preserving sensor performance during extended, multiday operations.[27] Watkins et al. studied the protection of a zwitterionic polybetaine hydrogel and its impact on sensor performance over 3 days in undiluted bovine serum at 37 °C. It was observed that the hydrogel coating preserves nearly all of the initial sensor response over multiday operation. In contrast, unprotected sensors lose 33–62% of their maximum signal within 3 days under the same conditions.[27] Electrochemical protein biosensors capable of functioning in whole blood for an extended period, exceeding one month, are achieved through the utilization of composite electrodes comprising nanowires and bovine serum albumin.[67] It consists of a three-dimensional porous matrix of cross-linked bovine serum albumin supported by a network of conductive nanomaterials, including gold nanowires, gold nanoparticles, or carbon nanotubes. The composite retains $\approx 88\text{--}93\%$ of its original redox current after one month in 1% BSA, in human serum, or in human plasma at 4 °C. In contrast, bare gold electrodes were completely passivated within hours. However, unfolding or degradation of proteins was not studied under biological conditions, such as at 37 °C.

1.10. Thesis structure

In this thesis, four separate experimental works were conducted, all of which are centred around a common theme: electrochemical aptamer-based sensors. The first project was a

proof-of-concept work based on the high demand for rapid COVID-19 diagnostics. The research goal of the first project was to develop an easy-to-fabricate and user-friendly electrochemical tool for detecting SARS-CoV-2, with a concept similar to that of point-of-care blood glucose analyzers but utilizing aptamers as biorecognition elements and impedance spectroscopy as the signal transduction method. Due to the decrease in demand for this research, primarily resulting from adequate immunization through vaccination and a lack of investment in this specific field, the project direction was shifted towards understanding the basics of aptasensors and the experimental conditions affecting aptamer immobilization and target detection. For this reason, the widely studied aptamer, specifically the thrombin-binding aptamer, was chosen as a model for the second project. However, a local problem in our lab was the mass usage of one-time-use screen-printed gold electrodes, which were expensive and limited our ability to conduct large-scale experiments to evaluate experimental conditions on sensor response, reproducibility, calibration, and other factors. Based on a local need, the next project involved studying surface cleaning and regeneration of gold electrodes. Based on the literature background, plasma (ionized gas) surface treatment has the potential to be a highly effective treatment method. An air plasma cleaning method was proposed and studied in the second project as a sustainable and rapid method to clean gold electrodes for reuse. Amidst the second project, given the sharp increase in the price of gold electrodes, carbon-based electrode substrates were evaluated as an alternative surface for biosensor fabrication. Conventional research is based on wet chemical treatment of carbon-based electrodes for biosensor fabrication. Alternatively, for the third project, we conducted experiments using a plasma-enhanced chemical vapour deposition method as a surface treatment technique to provide

an active surface for aptamer immobilization and biosensor fabrication on a carbon electrode. The project on thrombin-binding aptamers on gold electrodes was continued in the fourth project. An alternative approach based on the enzymatic activity of thrombin was employed to measure thrombin activity, rather than directly measuring its binding to the immobilized aptamer.

1.10.1. Electrochemical detection of SARS-CoV-2 spike protein

This project demonstrates the selection of novel DNA aptamers with high specificity and affinity for binding to the SARS-CoV-2 spike glycoprotein. Using faradaic EIS, it was demonstrated that the SARS-CoV-2 spike protein N-terminal domain-binding aptamer effectively bonded to the spike protein. In section 2.2, the standard clinical diagnosis of COVID-19 is introduced. In section 2.3, a comprehensive literature background regarding the current advancements in electrochemical biosensors for the detection of SARS-CoV-2 is provided. Section 2.4, provides the objectives and goals of the project. Section 2.5, provides the experimental details, including materials and methods. Section 2.6, explains the experimental results regarding redox couple photostability, gold electrode electrochemical characterization, microscopy analysis, spike protein characterization, aptasensor fabrication, biosensing performance and selectivity.

1.10.2. Air plasma regeneration of screen-printed gold electrodes

This project studies an air plasma (ionized gas) technique for surface treatment and recycling of screen-printed gold electrodes. In section 3.2 data are provided regarding the screen-printed electrode market, highlighting its significant production and the need for sensor research along with a literature review regarding gold electrode regeneration techniques is provided. Section 3.3 includes experimental materials and methods, including

plasma cleaning, surface characterization and electrochemical tests. Section 3.4 presents the results and provides a discussion on the electrochemically active surface area, surface chemistry analysis by X-ray photoelectron spectroscopy, surface hydrophilicity, electrochemical analysis by voltammetry and impedance techniques, variations in diffusion coefficients, and the biosensing performance of a thrombin-binding aptamer on regenerated gold electrodes.

1.10.3. Plasma-activated coating of carbon electrodes for one-step reagent free aptamer immobilization

In this study, an alternative method for immobilizing aptamers on carbon electrodes based on plasma surface treatment was explored. Section 4.2 outlines the common surface treatment techniques for biorecognition element immobilization. We propose a plasma-activated coating technique involving energetic ion bombardment that enables covalent immobilization of an aptamer on a carbon electrode in the absence of other chemical reagents. Section 4.3 explains the experimental conditions regarding the plasma-activated coating treatment and characterization of screen-printed carbon electrodes. Section 4.4 describes each step of electrode modification through a combination of electrochemical and surface chemistry characterization techniques, including impedance spectroscopy to determine the electrode's capacitance, charge transfer resistance, mass transfer diffusion, and X-ray photoelectron spectroscopy to provide surface elemental analysis and chemical states of the covalent bonds.

1.10.4. Electrochemical detection of thrombin

The final project pivoted toward evaluating experimental conditions for detecting a specific protein target of high significance: thrombin. Section 5.2 describes thrombin, its function,

and current clinical diagnosis assays related to detecting its activity. Within New Brunswick, this project holds significance in addressing critical health research needs, particularly in the area of coagulation disorders and heart disease monitoring. Notably, ischemic heart disease (IHD) stands as the most prevalent cardiovascular disease in Canada.[68] In New Brunswick specifically, the incidence of IHD is notably high, with approximately one in ten individuals aged 20 and above affected.[69] Given the aging demographic of New Brunswick, this rate is anticipated to rise. Moreover, 22.7% of New Brunswick's population is aged 65 and above, surpassing the national average of 18.8%.[70] In addition, elevated thrombin levels can lead to heart failure with preserved ejection fraction (HFpEF) through their involvement in inflammation and microvascular dysfunction. In HFpEF, inflammation and endothelial dysfunction are key pathological mechanisms. Thrombin can exacerbate these conditions by promoting inflammatory pathways and contributing to endothelial dysfunction, which can lead to increased stiffness of the heart muscle and worsen HFpEF symptoms.[71, 72] HFpEF makes up half of all current heart failure cases and is particularly common in women from New Brunswick, often occurring after menopause. It is especially prevalent in the Maritimes and results in the loss of around 193 to 200 lives per 100,000 individuals.[73].. Section 5.3 outlines the literature background of thrombin biosensing and also commercial products that measure thrombin. Moreover, details regarding the thrombin substrates currently used in commercial products, such as thrombin generation assays and prothrombin time assays, are provided. Section 5.4 summarizes the specific novelties of this study regarding thrombin detection, including faradaic EIS aptasensing, enzymatic amplification, and biofouling experiments. Section 5.5 presents the experimental details of this work including solution

preparation, electrode preparation, and biosensing procedures. In section 5.6, we evaluated different chemical and electrochemical surface modification methods, and also aptasensing parameters such as using a reducing agent, tris(2-carboxyethyl)phosphine (TCEP), and anti-biofouling by mercaptohexanol (MCH). Moreover, the natural enzymatic activity of thrombin in cleaving an electrogenic reagent was evaluated, which showed significant signal amplification for rapid thrombin detection.

2. Detection of SARS-CoV-2 via an aptamer-modified electrochemical sensor

This chapter is based on a poster presented by Sina Ardalan at ChemCon 2023, Dalhousie University, Halifax, NS, Canada.

2.1. Abstract

Since the onset of the coronavirus disease 2019 (COVID-19) pandemic, preventive social paradigms and vaccine development have undergone fundamental renovations, which drastically reduced the viral spread and increased collective immunity. Although the technological advancements in diagnostic systems for severe acute respiratory syndrome coronavirus-2 (SARS-CoV-2) detection are groundbreaking, the lack of sensitive, robust, and consumer end point-of-care (POC) devices are conspicuously felt. The fabrication of an electrochemical aptasensor based on a thiol-terminated ssDNA aptamer self-assembled monolayer on screen-printed gold electrodes is demonstrated. Both DC and AC electrochemical detection mechanisms were employed to study the interactions of alkanethiolates, mercaptohexanol (as an anti-biofouling agent), and thiolated ssDNA aptamers with the N-terminal domain of the SARS-CoV-2 spike protein in the presence of common blood protein interferences.

2.2. Introduction

Timely detection of infectious diseases is crucial before they become a global threat. The COVID-19 pandemic has highlighted the importance of early diagnosis, which can drastically reduce viral spread and save lives. Bioanalytical techniques to detect viral infections and pathogens, such as Reverse Transcription Polymerase Chain Reaction (RT-PCR), have had a revolutionary impact on biotechnology and molecular diagnostics and

are commonly practiced as gold standard methods of molecular diagnostics in a clinical setting.[74] However, such advanced instrumental techniques are not suitable for rapid diagnostics in non-clinical settings, such as point-of-care (POC) platforms, due to their high cost, need for well-trained operators, large instrument size, and limited stability and shelf-life in non-clinical/non-sterilized environments.[75] The use of rapid detection kits based on lateral flow assays (LFAs) has emerged as a well-established solution for POC detection of biochemicals and pathogens in non-clinical settings.[7] LFAs were first introduced in the late 1980s for rapid pregnancy testing and later for the detection of sexually transmitted diseases.[76] Nowadays, they are commonly used for the detection of SARS-CoV-2 and drugs of abuse. However, the current challenges with LFAs in the rapid detection of SARS-CoV-2 are their lack of sensitivity, high rate of false negatives, and limited ability to provide quantitative information about viral load, particularly in the early stages of infection.[77]

One overlooked factor in COVID-19 diagnosis is the sampling method, still dominated by nasopharyngeal swab sampling. Though it is a non-invasive sampling, it still needs training and careful consideration as it may cause significant errors due to patient discomfort and reactions such as coughing and gagging, resulting in early swab removal from the nasopharyngeal area.[78] Altogether, the current monopolies of diagnostic methods from sampling (nasopharyngeal), imaging (CT-scan), and molecular detection (LFA, RT-PCR) require reconsideration and improvement. It is essential to develop and implement viable and comparable alternatives to improve the accuracy and efficiency of COVID-19 detection as well as for other emerging infectious diseases.

2.3. Literature review

2.3.1. Electrochemical immunosensors

Simply put, the concept of immunosensors is based on a transducer's response (commonly optical and electrochemical) due to the binding affinity between the biorecognition element (i.e., antibody) and the target. Electrochemical immunosensor fabrication starts with modifying an electrode's surface to produce proper surface chemistry to immobilize the antibody. This can be achieved through various approaches, such as chemisorption of thiolated antibodies on a gold electrode's surface or carbodiimide crosslinker chemistry to create an amide bond between carboxylated carbon electrodes, amine-terminated antibodies, and streptavidin-avidin affinity binding.[79] The antibodies act as a lock for specific keys (antigens); thus, by adding the target antigen to the modified electrode, a complex of antigen-antibody can be formed. Voltametric and impedimetric techniques are common electrochemical methods used to monitor complex formation.[80] Without the presence of a target, the redox reagent can be oxidized or reduced at the working electrode, thus creating a significant current analyzed by a potentiostat. Alternatively, target-receptor binding causes a spatial hindrance for the redox molecules to migrate from the bulk solution to the electrode surface, thus decreasing the amount of produced current.[80] The enzyme-linked electrochemical biosensors are another type of immunosensor commonly used in magnetic-assisted electrochemical assays.[81] In enzyme-linked methods, detection antibodies and capture antibodies are immobilized on the electrode surface and magnetic beads, respectively. Moreover, the magnetic beads' surface is modified with an enzyme, commonly horseradish peroxidase (HRP). Introducing the target antigen to the magnetic bead solution forms a complex with the capture antibody. Then, a sandwich

hybrid is formed after incubating the magnetic-bead-antigen complex with the immobilized detection antibodies on the electrode surface. Next, substrates (commonly 3,3',5,5'-tetramethylbenzidine (TMB)) are added to the sandwich complex, consequently oxidized by the HRP enzyme. The number of electrons generated by substrate oxidation can be monitored by amperometric techniques, commonly chronoamperometry.[82] In the absence of the antigen, no sandwich complex forms; consequently, magnetic beads with unbound capture antibodies are washed away, preventing any enzymatic reaction.

2.3.2. Artificial bioreceptors

Although antibody-based biorecognition elements offer high selectivity and sensitivity, their production cost and batch-to-batch structural difference might hinder their application in commercial IVD tools.[83] On the contrary, artificially-produced bioreceptors, namely aptamers and molecularly printed polymers (MIPs), can be produced cost-effectively with a consistent structural form.[83] Particularly, significant research has been conducted for aptamer development for SARS-CoV-2 detection.[84] Aptamers are short single-stranded DNA or RNA molecules (oligonucleotide) or short peptides produced in vitro by a process known as systematic evolution of ligands by exponential enrichment (SELEX) to bind to a target ligand specifically.[85] Electrochemical aptamer-based biosensors (aptasensors) have received tremendous attention due to the fast and cost-effective production of customized aptamers with higher stability than in vivo-produced antibodies.[86] Each end of an aptamer strand can be modified with a desired functional group for two primary purposes in oligonucleotide aptasensors: a) chemical immobilization on an electrode by modifying the 5' end with thiol or amine groups and b) covalent attachment of a redox molecule, such as (methylene blue), on the 3' end.[87]

The common mechanisms of aptasensing are based on a) spatial hindrance due to the formation of the aptamer-target complex or b) aptamer conformational change in the presence of its target.[86] In case of spatial hindrance, the aptamer-target complex would impede the redox molecules to migrate from the bulk solution to the electrode layer; thus, a decrease in the produced current is anticipated. In case of the induced conformational change, the aptamer's end (either 3' or 5') would get closer or further to/from the electrode, therefore causing a shift in the redox activity and the produced current.[86] For example, Zhang et al. designed a highly sensitive aptasensor based on dimeric DNA aptamers (DSA1N5) to detect salivary spike proteins.[35] The binding affinity of this dimeric aptamer against variants of SARS-CoV-2 was investigated. This aptamer, showed a selective affinity to the common variants with different dissociation constants of 120, 290, and 480 pM against wildtype, Alpha and Delta variants, respectively. The aptamer was designed based on multivalent ligation of two or more monomers to achieve picomolar sensitivity. This approach resulted in enhanced binding with spike proteins since each virus carries around 30 trimeric spike proteins on its surface with an average spacing distance of 13–15 nm between each other. The developed aptamer's length was more than 15 nm. Thus, it can surround and bind the spikes more significantly than monomeric aptamers. Moreover, a gold screen printed electrode (SPE) electrochemical aptasensor was fabricated to test spike proteins in saliva samples. The synthesized aptamer was thiolated at the 3' end to facilitate chemisorption on the gold working electrode. Also, tris(2-carboxyethyl)phosphine (TCEP) was mixed with the thiolated aptamer to reduce all the S-S bonds to S-H, which improves the chemisorption efficiency on the gold's surface. Then, the electrode was incubated with thiolated polyethylene glycol (Mw = 6000 Da) to reduce

the non-specific absorption of interfering biomolecules. The ferro/ferricyanide redox couple was utilized to study the electrochemical charge transfer on the modified gold electrode. In the presence of spike proteins, the complex between aptamers and spikes passivates the gold's surface, hindering the charge transfer of the redox-active molecules. Electrochemical impedance spectroscopy (EIS) technique was utilized to measure the charge transfer resistance of the redox reagents from the bulk solution to the electrode's surface, resulting in highly specific detection of viral proteins with 80.5% sensitivity.

In another report, Alafeef et al. designed four aptamers targeting N gene at four segments simultaneously.[88] The biosensor consisted of a paper substrate coated with graphene and then aptamer-capped gold nanoparticles (AuNPs). The aptamers were designed in the Soligo software with some constraints and considerations such as folding temperature and ionic strength to predict the binding energy (≤ -8 kcal/mol cutoff) of RNA-DNA hybridization. Also, the biosensor was integrated with a customized Arduino-based circuit board equipped with internet of things (IoT) modules, such as Bluetooth and Wi-Fi to provide a rapid and portable POC system.

There is a common problem in electrochemical biosensors known as biofouling due to the accumulations of biomolecules and particles on the sensing electrode. Li et al. addressed the biofouling issue by designing an electrochemical biosensor with enhanced antifouling property.[89] Bovin serum albumin (BSA), a relatively cheap and abundant protein for electrode blocking, was used to reduce the non-specific adsorption of biomaterials on the electrode surface.[89] The key point of this paper is that the BSA was covalently bounded to polymerized aniline nanowire (PANI-NW) to enhance the electrode blocking, reduce the BSA leaking, and mitigate BSA blocking effect on the electrode's conductivity.

Moreover, a commercial peptide aptamer against COVID-19 immunoglobulin G (IgG) was immobilized on BSA using 4-(N-Maleimidomethyl) cyclohexane-1-carboxylic acid 3-sulfoN-hydroxy-succinimide ester sodium salt (sulfo-SMCC) to covalently bond the amine groups of BSA and the aptamer's Cys-terminal thiols. Overall, this biosensor showed significant antifouling properties without diminishing the electron transfer of redox-active molecules at the electrode surface.

2.3.3. Commercial products

Most FDA-approved in vitro diagnostic devices are dominated by optical and RT-PCR techniques. However, two electrochemical-based medical devices, namely Sampinute™ and ePlex®, offer alternative approaches for SARS-CoV-2 diagnosis.[90] Sampinute™ analyzer is a magnetic force-assisted electrochemical sandwich immunoassay for the qualitative detection of spike proteins of SARS-CoV-2 within one hour (limit of detection or LOD = 30 TCID₅₀/mL). The analyzer is equipped with a cartridge that encompasses magnetic nanoparticles (MNPs) and an electrode, both coated with antibodies against spike proteins; hence, in case of the virus presence, it would be sandwiched between the MNPs and the electrode surface. Developed by GenMark, ePlex® SARS-CoV-2 assay consists of digital microfluidics for fluid handling/mixing, followed by an automated RT-PCR amplification, and finally electrochemical detection. The detection mechanism is based on DNA hybridization of the target's DNA and the capture's probe, determined by voltammetry. Antibody analysis is also of great importance as it provides valuable information on diagnostics, post-infection immunity, vaccine immunity, and health decisions. For instance, Roche Diagnostics has developed a rapid (18 min), high-throughput, and automated electrochemiluminescence immunoassay for total anti-SARS-

CoV-2 antibodies in the range of 0.4–250 U/mL.[91] Moreover, a handful of LFAs are listed on the FDA website for qualitative antibody detection, which are cheaper and can be available for POC use, particularly the fingerstick whole blood tests.[92]

2.4. Project scope

The objective of this study is to fabricate an electrochemical aptasensor for SARS-CoV-2 spike protein detection, serving as a proof of concept. By employing a newly discovered aptamer with high selectivity and sensitivity and a streamlined fabrication process, this work establishes a foundational framework for aptasensor development in our laboratory. Although the aptamer and EIS approach used here aligns with prior studies, the emphasis on a simple detection mechanism addresses the need for accessible diagnostic tools and research methods in resource-limited settings. This work complements existing research by adapting a newer aptamer and evaluating its performance under practical conditions, offering insights for further optimization. While the sensor's sensitivity and novelty are limited, this study lays the groundwork for future advancements in aptasensor design, focusing on improving sensitivity and specificity through material and methodological innovations.

This project investigates critical factors in the design and fabrication of electrochemical aptasensors for bioanalytical diagnostics. All investigations are analyzed with a variety of electrochemical methods (both AC and DC techniques) along with electron microscopic methods (scanning electron microscopy or SEM and electron energy dispersive X-ray spectroscopy or EDS).

2.5. Experimental

2.5.1. Materials

Oligonucleotide (Aptamer): RP-HPLC-purified aptamer was synthesized by Biomers GmbH (Ulm, Germany). This aptamer had been thoroughly studied and characterized towards its target, SARS-CoV-2 Spike (S) proteins.[93] The 5' end of the aptamer was modified with a six-carbon alkane chain (CH₂)₆ and a thiol functional group (SH) in the reduced state. Sequence:

5' - HS - (CH₂)₆ CGCGGTCATTGTGCATCCTGACTGACCCTAAGGTGCGAACAT
CGCCCGCG - 3'. Length: 50 nucleotides, Molecular Weight (MW): 15520 g/mol, Yield:
6.2 Optical Density (OD) at 260 nm, 12 nmol, Melting temperature: 89 °C.

6-mercapto-1-hexanol (MCH) 97%, phosphate buffer saline (PBS) 10X, tris (hydroxymethyl) aminomethane hydrochloride (Tris.HCl), potassium hexacyanoferrate (II) trihydrate (FeCN₆²⁻) and potassium hexacyanoferrate (III) (FeCN₆³⁻), magnesium chloride hexahydrate, and calcium chloride dihydrate were purchased from Sigma.

Gold screen-printed electrodes (SPE), model BT with low temperature curing ink (Metrohm DropSens, Spain, $\varnothing = 3\text{mm}$) were used for aptasensor fabrication. Double-distilled, 0.2 μm membrane-filtered water was used in all experiments.

2.5.2. Methods

The experimental workflow of this study is as follows: First, the gold SPEs were prepared for modification with the capture probe, which is the aptamer. The electrodes were first treated by electrochemical polishing (E-polish) and then subsequently analyzed using

electron microscopy techniques to evaluate their electrochemical characteristics and microscopic structure.

The objective is to test the aptasensor response with the target, which is the SARS-CoV-2 spike protein. Before conducting the aptasensor binding test with the target, the isolated spike protein was analyzed using dodecyl sulfate polyacrylamide gel electrophoresis (SDS-PAGE) to determine its molecular weight and net charge.

After characterizing the sensor and its target, the target (spike protein) was incubated with the aptasensor to obtain the binding response. The binding response is based on the EIS analysis to measure the change in charge transfer resistance (R_{ct}) due to target binding.

Electrochemical Analyzer: A compact, USB, and battery-powered electrochemical interface with wireless (Bluetooth) and wired (double shielded cell cable) connectivity was purchased from PalmSens4 (PalmSens, Netherlands) for electrochemical analysis of electrodes and biosensors.

Scanning Electron Microscope (SEM): SEM Images and EDS spectra were collected with a ThermoFisher Scientific Scios 2 electron microscope with an Oxford Ultim Max 170 EDS detector and Aztec software.

Electrochemical setup: All measurements were performed in a dark box. A Teflon cap was designed to slide the SPE inside the glass cell with two narrow holes for N_2 gas inlet and outlet. Before experiments, the solutions were purged for 15 minutes under a constant flow of N_2 at 10-15 Psi to remove dissolved oxygen. During experiments, N_2 was passed on top of the solution (N_2 blanket).

Screen-printed gold electrode preparation: Screen-printed gold electrode (gold SPE; \varnothing 3 mm working electrode) was purchased from Metrohm (BT model, Spain). Electrodes were pre-treated by three cyclic voltammetry (CV) scans in 0.5 M H₂SO₄ at a scan rate of 0.1 V/s from 0 V to 1.2 V (vs Ag/AgCl). This treatment is referred to as electropolishing (E-polish).

Aptamer preparation and incubation: The lyophilized aptamer was first centrifuged for about 20 seconds to detach particles from the walls of the microtube. Then, the aptamer was dispersed in a storage buffer (Tris.HCl 10 mM, pH 7.5 and EDTA 0.1 mM) and mixed by a vortex shaker to provide a stock solution of 100 μ M aptamer. The stock solution was kept in the fridge at 4 °C. A diluted aliquot of the aptamer stock solution was made (250 nM) in a folding buffer (Tris.HCl 10 mM, pH 7.5, NaCl 150 mM, KCl 50 mM, MgCl₂ 1 mM, CaCl₂: 2mM). The diluted aliquot was annealed in a dry bath heater at 90 °C for 5 min and then cooled slowly to reach room temperature. Then, 5 μ L of the diluted aptamer was drop-casted on the SPE working electrodes. The electrodes were inserted inside a humidity-saturated chamber and incubated at 25 °C overnight. Next, the electrodes were rinsed with ultra-pure water, then with the folding buffer. The electrodes, also known as aptasensors, were inserted inside the electrochemical cell, which contained a working buffer (Tris.HCl 10 mM pH 7.5, NaCl 150 mM, KCl: 50 mM, MgCl₂: 1 mM, CaCl₂: 2mM, [Fe(CN)₆]^{3/4-} 2mM each). The working buffer was first purged for 15 minutes under a constant flow of N₂ at 10-15 Psi to remove dissolved oxygen. During electrochemical characterization experiments, N₂ was passed on top of the solution (N₂ blanket).

Mercaptohexanol (MCH) preparation and incubation: A stock solution of MCH (10 mM) was prepared in ethanol under a fume hood. A diluted aliquot of MCH (100 μ M) was

prepared in the folding buffer, and 5 μ L of it was drop-casted on the aptasensors (previously dried with N_2 gas) and then incubated in the humidity chamber for 1 h at room temperature. Next, the aptasensors were rinsed with ultra-pure water and then with the folding buffer. The MCH-functionalized aptasensors were inserted inside the electrochemical cell, containing the working buffer. The working buffer was first purged for 15 minutes under a constant flow of N_2 at 10-15 Psi to remove dissolved oxygen. During electrochemical characterization experiments, N_2 was passed on top of the solution (N_2 blanket).

Proteins used in this study: The Spike (S) glycoprotein from the coronavirus 2 (SARS-CoV-2), Wuhan-Hu-1 was purified as a soluble protein (residues 1 to 1213) with a polybasic cleavage site deletion (RRAR to A; residues 682 to 685) and stabilizing mutations (K986P and V987P, wild type numbering) with a C-terminal thrombin cleavage site, a T4 foldon trimerization domain and a C-terminal hexa-histidine tag. The gene sequence was codon optimized for mammalian expression and was subcloned into the pCAGGS mammalian expression vector under control of the AG promoter. This plasmid was acquired from BEI Resources (product NR-52394).

The Spike Receptor Binding Domain (RBD) protein consists of Spike amino acids 319-541 fused to an N-terminal Spike signal sequence and a C-terminal hexa-histidine tag. The gene sequence was codon optimized for mammalian expression and was subcloned into the pCAGGS mammalian expression vector under control of the AG promoter. This plasmid was acquired from BEI Resources (product NR-52309).

Protein Expression: Proteins were expressed using the Gibco Expi293 Expression system following supplier (Thermofisher) guidelines. Cell density and viability was monitored using the Countess device and Ethidium Homodimer staining. After the recommended

schedule of passaging, ExpiF293 cells were adjusted to a final density of 3×10^6 viable cells/mL and transfected with 1 ug purified Spike or RBD gene plasmid DNA per ml cell culture. Three days post-transfection, cells (80-85% viability) were collected by centrifugation at 3000xg for 20 min, and the supernatant was filtered through a 0.22 um membrane. Cell-free supernatants were subjected to affinity chromatography immediately.

Protein Purification: Cell-free supernatant was supplemented to a final concentration of 5 mM imidazole (pH 8) and 300 mM NaCl, and adjusted to pH 8 using 10 M NaOH. Ni-NTA beads (Novagen) were washed 2x with Binding Buffer (50 mM phosphate buffer [pH 8], 5 mM imidazole, 300 mM NaCl). A 50% slurry of washed beads (4 ml drained bead volume) was added to 100 ml of amended cell-free supernatant and mixture was incubated at RT with slow rotation for 2 hrs. The beads were collected by centrifugation and added to a 5 ml disposable chromatography column. Unbound supernatant proteins were eluted with a 4 ml volume of Wash Buffer (50 mM phosphate buffer [pH 8], 20 mM imidazole, 300 mM NaCl) four times. Bound proteins were eluted from column using 7 ml of Elution Buffer (50 mM phosphate buffer [pH 8], 250 mM imidazole, 300 mM NaCl). Recombinant RBD and recombinant Spike proteins were concentrated using centrifugal filtration devices (Amicon) with 10 kDa and 50 kDa molecular weight cut-offs, respectively. In both cases, elution buffers were exchanged with phosphate buffered saline (10 mM Na_2HPO_4 , 1.8 mM KH_2PO_4 , 2.7 mM KCl, 137 mM NaCl) pH 7.4. Generally, Spike protein solution was concentrated to a final volume of 0.5 ml and RBD protein was concentrated to a final volume of 2 ml. Protein concentration was measured using the Biocinchoninic acid (BCA) assay (Pierce) with bovine serum albumin as a standard. Protein purity was assessed using 4-20% pre-cast TGX gels (Bio-Rad) under denaturing conditions followed by Coomassie

Blue R-250 staining. Immunoreactivity was assessed using anti-His primary antibody (Ab) conjugated to horseradish peroxidase (Santa Cruz Biotechnology), mouse anti-RBD primary Ab and mouse anti-S2 domain primary Ab and goat anti-mouse Ab conjugated to HRP. Immunoblots were developed using Pierce ECL Western Blotting Substrate (ThermoFisher). Purified proteins were stored at either -20°C or -80°C.

Spike (S) protein preparation and incubation

Stock solution of SARS-CoV-2 S protein (50 μ L of 100 μ g/mL in PBS 1X pH 7.4) was taken out from the freezer (-20 °C) and thawed to room temperature. A 50 μ L aliquot of diluted S protein sample (1 μ g/mL) was prepared in PBS 1X before the experiments. 5 μ L of the diluted protein sample was drop-casted on the aptasensors (previously dried with N₂ gas) and was further incubated in the humidity chamber for 1 h at room temperature. Then, the aptasensors were rinsed with ultra-pure water and then with the folding buffer. Next, the aptasensors were inserted into the electrochemical cell, containing the working buffer. The working buffer was first purged for 15 minutes under a constant flow of N₂ at 10-15 Psi to remove dissolved oxygen. During electrochemical characterization experiments, N₂ was passed on top of the solution (N₂ blanket).

2.6. Results and discussion

2.6.1. Fe²⁺/Fe³⁺ optical study

To evaluate the stability of redox molecules in the electrochemical measurement buffer, a study of the Fe²⁺/Fe³⁺ redox system was conducted. A 1 mM ferri/ferrocyanide solution in 1X PBS was prepared and exposed to bright LED light for 1 and 3 days to assess light sensitivity. UV-Vis absorbance measurements, as depicted in Figure 2.1 showed no

significant changes in the redox probe absorbance, indicating that meticulous light control was unnecessary for subsequent electrochemical tests.

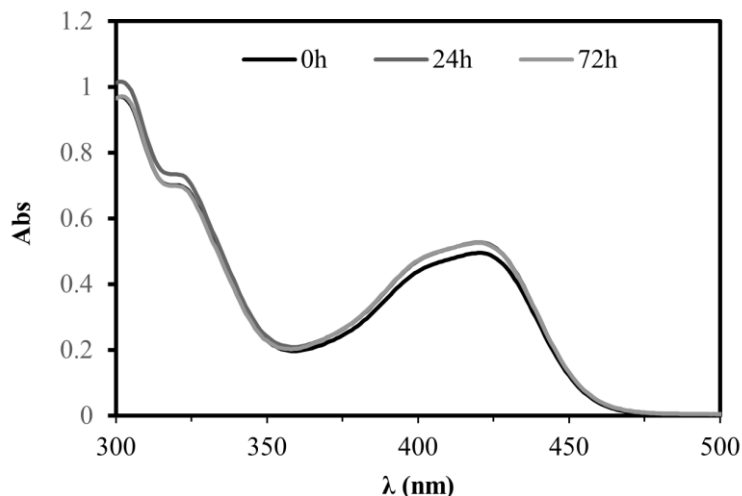


Figure 2.1. UV-Vis absorbance spectra of 1 mM ferri/ferrocyanide solution in 1X PBS exposed to bright LED light for 1 and 3 days.

2.6.2. Characterization of gold SPEs

Commercial gold SPEs were pre-treated by electropolishing (E-polish) with a potentiostat/impedance analyzer, PalmSens4 (Figure 2.2). Pre-treatment of a gold electrode is commonly done by CV in 0.5 M H_2SO_4 , providing a reduced state of gold atoms.[94] This process is known as electropolishing (E-polish). Figure 2.3 depicts the CV results from E-polishing an SPE in a sulfuric acid solution. The gold atoms were oxidized 0.9 V to 1.2 V and then reduced at ≈ 0.6 V (vs Ag/AgCl) during the 3 cycles in the sulfuric acid solution. The final potential of the CV test is set at 0 V to ensure surface gold atoms are in a homogenous reduced state.



Figure 2.2. Experimental setup: a commercial gold SPE (Metrohm DropSens, C223BT) [95] connected to a potentiostat (PalmSens4).[96]

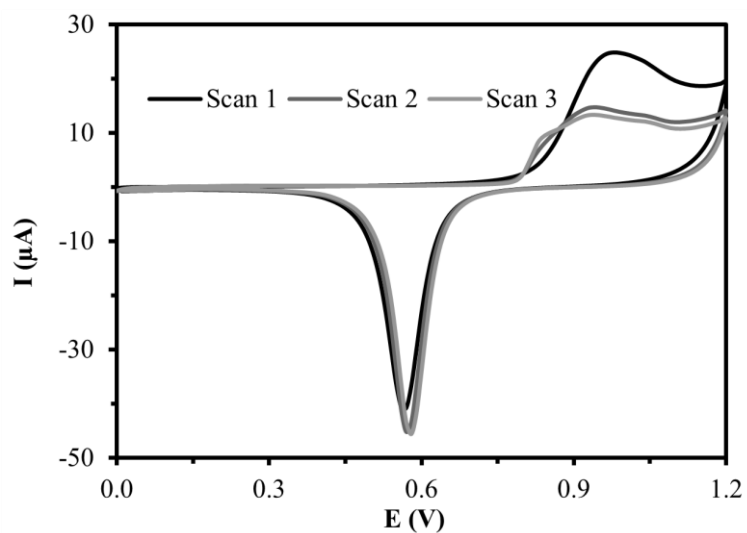


Figure 2.3. CV of gold SPE in 0.5 M sulfuric acid (electropolishing).

Figure 2.4.A presents the SEM image of the SPE, which shows micrometre-sized granular gold particles which provide a large and rough surface area.[97] Figure 2.4.B depicts the EDS map, showing surface atoms of the SPE gold, which is dominated by gold atoms (green) and modest amounts of carbon atoms (red), which are presumably related to the

organic binders between the ceramic substrate and the printed gold layer. Figure 2.5 provides a quantitative analysis to confirm the chemical composition of the surface atoms, which mainly contain gold, carbon and oxygen peaks from the pasting binder.

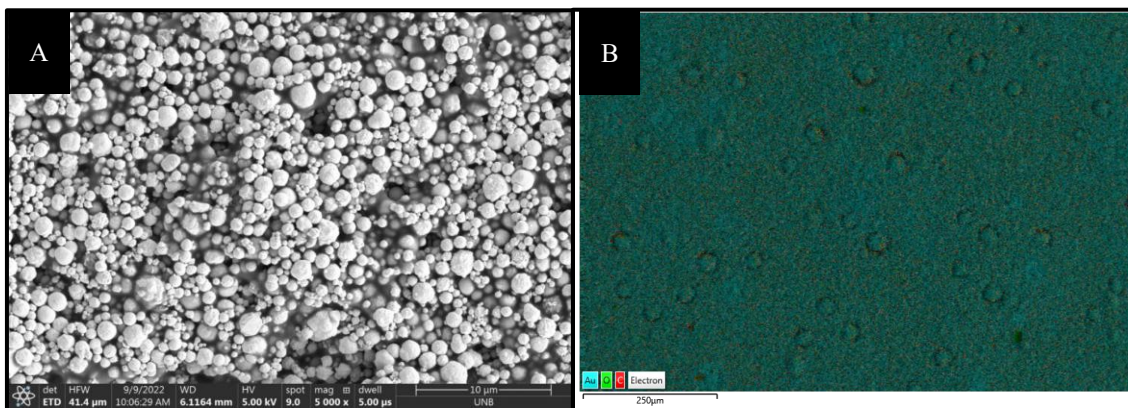


Figure 2.4. A) SEM image and B) EDS map of the C223BT gold working electrode.

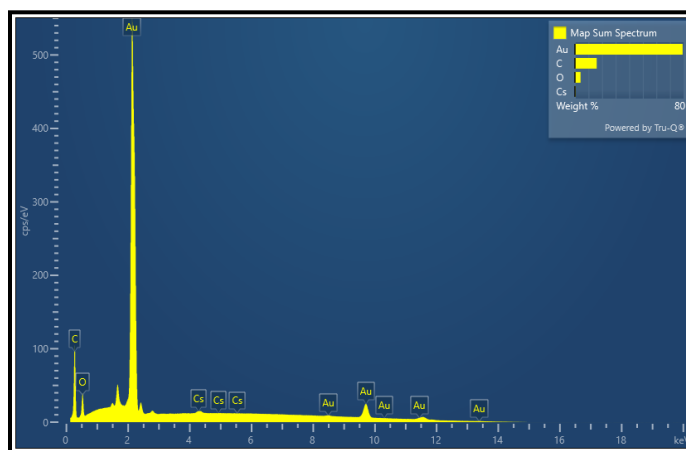


Figure 2.5. EDS quantitative analysis of the C223BT gold working electrode.

2.6.3. Isolated SARS-CoV-2 spike protein

Figure 2.6 provides the binding assay of isolated SARS-CoV-2 spike protein using SDS-PAGE. The spike protein (molecular weight of \approx 140 kDa, isoelectric point (pI) of 6.2.) eluted from the Q Sepharose column but not from the SP Sepharose column. Q Sepharose contains quaternary amine positively charged groups, acting as an anion-exchange resin

that binds to negatively charged proteins. Whereas SP Sepharose contains sulfopropyl groups with a negative charge, it is a cation-exchange resin that binds positively charged proteins. The presence of a prominent band at ≈ 200 kDa in lanes corresponding to Q Sepharose (lanes 2–4) and its absence in SP Sepharose lanes (lanes 5–7) indicated that the spike protein interacted with the anion exchanger, thus it carried a net negative charge under the experimental conditions with phosphate buffered saline, pH 7.4 ($\text{pH} > \text{pI}$). This is consistent with the protein's pI of 6.2, meaning that at the buffer pH, the protein is deprotonated and negatively charged. All proteins were tagged with a C-terminal hexahistidine tag to coordinate with nickel ions (Ni-NTA beads), as shown in lanes 8-10.

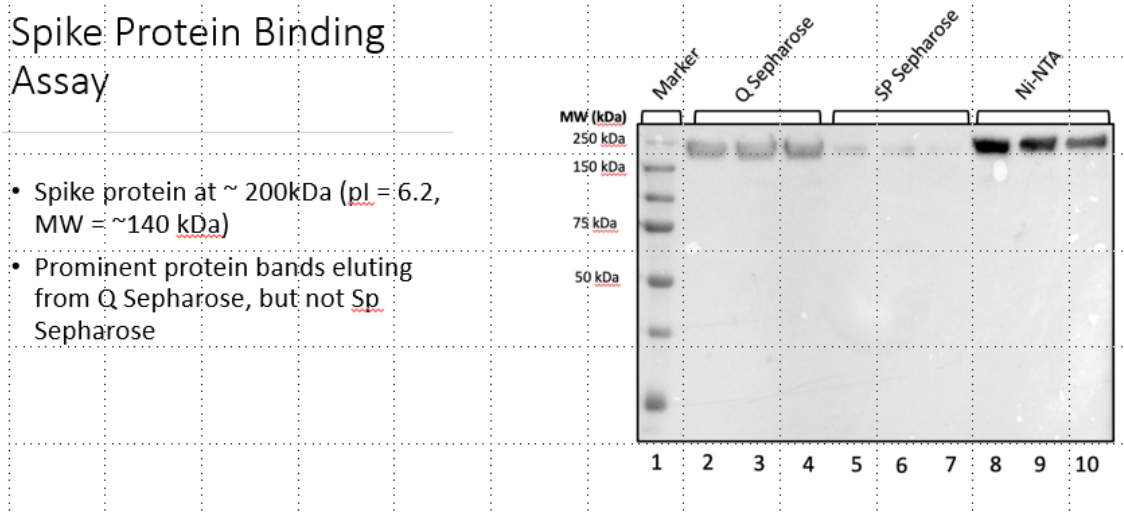


Figure 2.6. Electrostatic binding of SARS-CoV-2 isolated S protein to ion exchange chromatography beads to positively charged Q Sepharose, and repulsion by negatively charged Sp Sepharose. Reproduced with permission from Crawford, M. 2021. INVESTIGATING THE USE OF ION-EXCHANGE CHROMATOGRAPHY FOR PURIFICATION OF THE SARS-COV-2 SPIKE PROTEIN. Honours Thesis, Department of Biology, University of New Brunswick.

2.6.4. Electrochemical characterization of aptasensors

After E-polishing, the gold SPEs were characterized by CV and EIS techniques inside the measurement buffer solution containing $[\text{Fe}(\text{CN})_6]^{3/4-}$ redox couple. The objective was to understand how each modification step, such as aptamer and protein incubation, changed the electrochemical properties of the gold electrode. The redox couple $[\text{Fe}(\text{CN})_6]^{3/4-}$ has a reversible redox behavior that was observed by CV technique. Figure 2.7.A provides the voltammogram of the oxidation and reduction potentials of $[\text{Fe}(\text{CN})_6]^{3/4-}$ on the bare gold SPE (no modification), which were 0.2 V and 0.1 V (vs Ag/AgCl), respectively (black line). After the aptamer was immobilized on the gold SPE, the peak potentials were shifted and the peak current were slightly decreased, since the immobilized aptamer slightly hindered the electron transfer of $[\text{Fe}(\text{CN})_6]^{3/4-}$ redox couple as shown in the grey curve of Figure 2.7.A. After MCH immobilization on the aptamer-modified electrode (as shown in dotted black curve in Figure 2.7.B) oxidation and reduction peaks were broadened further, as MCH created a non-conductive organic film to reduce non-specific interactions.[98] Grey dotted curve in Figure 2.7.B shows that the redox reaction was almost diminished (disappearance of the redox peak potentials) after S protein incubation due to aptamer-protein binding, which hindered redox activity significantly. The results were further confirmed by the EIS technique. The Nyquist plot showed the resistance and diffusion of the charged molecules using an equivalent circuit based on a modified Randles circuit, depicted in Figure 2.8. We applied this circuit to fit the experimental data obtained from the EIS test, which provided the amount of charge transfer resistance (R_{ct}) of redox molecules in each step of incubation.

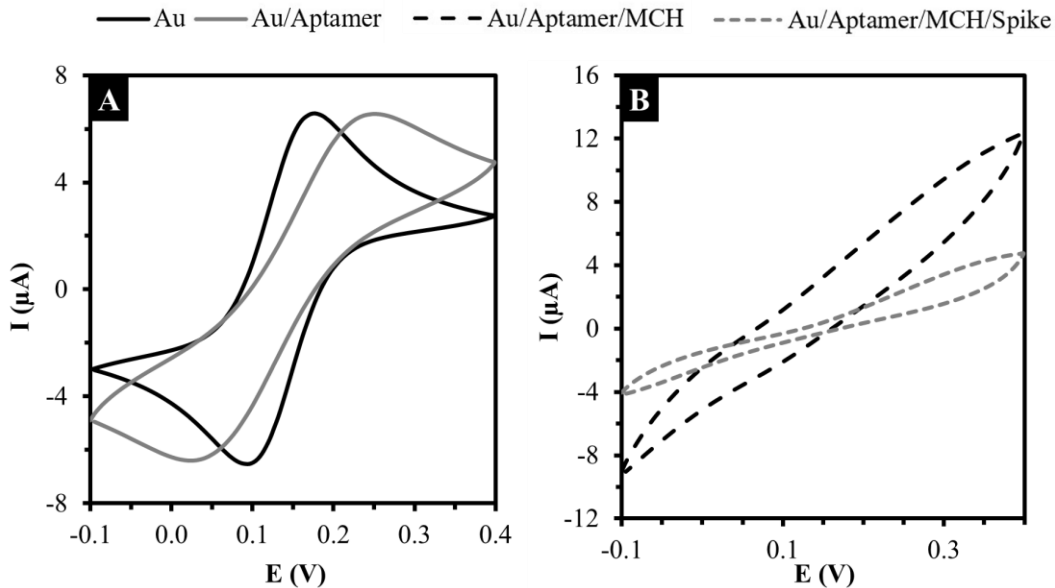


Figure 2.7. CV characterization of aptasensor in each step of incubation.

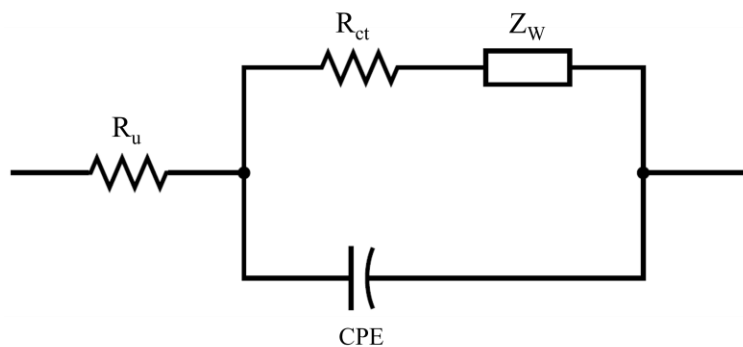


Figure 2.8. Modified Randles circuit: Equivalent electrical circuit of the aptasensor.

Figure 2.9 provides the Nyquist plot of each modification step. There was an increase in the semi-circle diameter after each step of modification, corresponding to the charge transfer resistance (R_{ct}). Charge transfer of the redox couple was hindered progressively due to the immobilization of the aptamer, blocking agent and the spike protein binding. Specifically, after spike protein ($1 \mu\text{g}/\text{mL}$) incubation, a remarkable increase in the R_{ct} was observed (from $9 \text{ k}\Omega$ to $12 \text{ k}\Omega$), which confirmed aptamer-protein binding. The relative

change in R_{ct} (Equation 2.1) was used as the sensor signal to determine the aptamer-target binding.[34]

$$Relative R_{ct} \text{ change} = \frac{R_{ct}(spike \text{ protein}) - R_{ct}(\text{aptamer/MCH})}{R_{ct}(\text{aptamer/MCH})} \quad 2.1$$

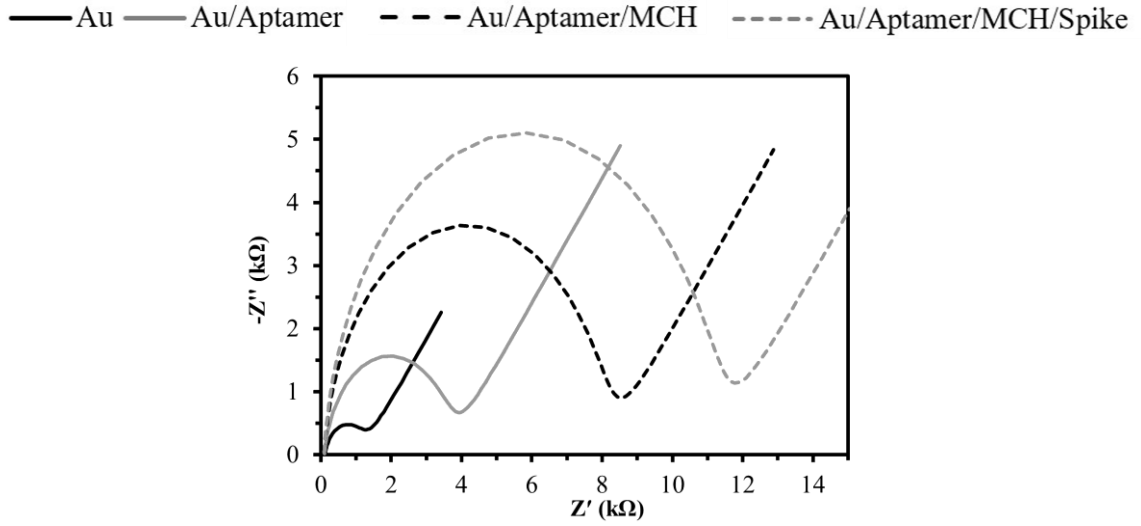


Figure 2.9. Nyquist plot obtained from the EIS technique. The increase in the semi-circle represents a higher charge transfer resistance of redox molecules.

Figure 2.10 provides sensor signal regarding aptamer's selectivity towards non-specific proteins, including Bovine Serum Albumin (BSA, 20 $\mu\text{g/mL}$), thrombin (Thr, 10 $\mu\text{g/mL}$), and immunoglobulin A (IgA, 10 $\mu\text{g/mL}$). The relative R_{ct} changes of all the tests are shown in a bar chart for a better depiction of signal change in the presence of the S protein (SP) and non-specific proteins, which indicate a selective response of the aptamer towards the SARS-CoV-2 S protein. The selectivity test involved incubating each non-specific protein with the aptasensor individually, and then measuring the R_{ct} change associated with the binding of each protein. The spike protein was also tested under similar conditions but not simultaneously mixed with the other proteins. Instead, each protein was introduced one after another to ensure that any observed changes in R_{ct} could be attributed directly to the

specific interactions between the aptamer and the proteins. The evaluation of the aptasensor's performance was based on measuring the changes in R_{ct} that occurred when the target protein bonded to the aptamer. In the experiment, a significant response was observed with the spike protein, showing ≈ 3.4 -fold increase in R_{ct} at a concentration of 1 $\mu\text{g}/\text{mL}$. This pronounced increase indicated that the aptasensor could differentiate from other proteins that were tested as potential interferents. In contrast, when other interfering proteins were introduced to the sensor, the observed changes in R_{ct} were much smaller, yielding increases in the range of ≈ 0.8 to 1.1-fold. This minimal response suggests that the aptasensor could effectively discriminate between the spike protein and other proteins.

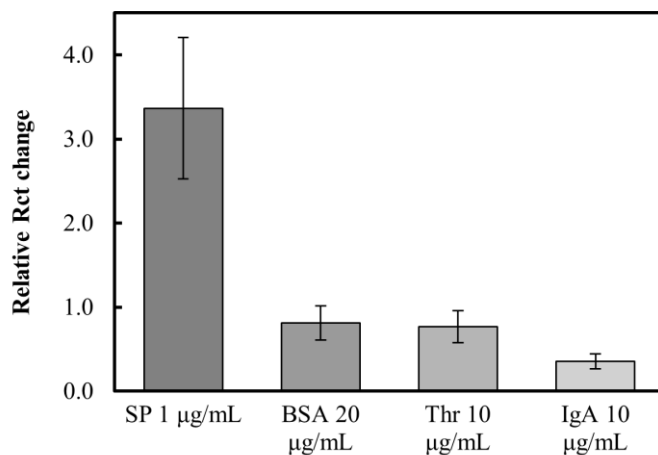


Figure 2.10. Relative R_{ct} signal changes of aptasensors after exposure to spike protein (SP) and non-specific proteins. Error bars represent the variability in the data collected from three individual gold SPEs for each condition.

2.7. Conclusion

The study describes the development and evaluation of an aptamer-based electrochemical biosensor for the detection of the SARS-CoV-2 spike protein. The electrochemical sensor consisted of a miniaturized three electrode system including a screen-printed gold working electrode. The surface chemistry of the gold electrode was characterized by

electrochemical and electron microscopy methodologies which showed micron-sized gold particles with effective and consistent electrochemically active surface area that allowed for immobilization of a thiol-modified aptamer through SAM formation. The binding between aptamer and its target, SARS-CoV-2 spike protein, resulted in a significant increase in charge transfer resistance characterized by the EIS technique. Our results showed that the EIS technique was selective in detecting the target spike protein compared to non-specific proteins. The combination of a portable electrochemical analyzer, disposable SPE, and a straightforward impedance analysis provides a potential POC platform for early detection of SARS-CoV-2.

2.8. Study limitations

A calibration curve to determine the correlation between the concentration of the SARS-CoV-2 spike protein and the sensor signal was not determined due to reproducibility issues at each stage. Additionally, complex matrices or clinical samples, such as whole blood, plasma, or saliva were not tested; instead, the experiments were conducted using isolated and purified proteins. This work provides a proof of concept to understand the electrochemical processes, particularly the impedance analysis of immobilized ssDNA and protein binding, rather than being a fully developed analytical bioassay. Spike proteins from other pathogens, such as Influenza, were not tested to assess selectivity against other pathogens.

2.9. Author contributions

All authors contributed to the preparation of this chapter. The work regarding protein preparation, expression, purification, and characterization was completed by Dr. Michael Duffy, Dr. Aurora Nedelcu, and Dr. Shawn MacLellan (Department of Biology, University

of New Brunswick). Figure 2.6 is from Crawford, M. 2021. INVESTIGATING THE USE OF ION-EXCHANGE CHROMATOGRAPHY FOR PURIFICATION OF THE SARS-COV-2 SPIKE PROTEIN. Honours Thesis, Department of Biology, University of New Brunswick. The specific contributions for this chapter are as follows: A.I. conceived of the original idea. S.A. and A.I. planned the experiments. S.A. and A.I. analyzed the data. S.A. conducted the experiments and wrote the chapter. S.A. and A.I. edited the chapter. A.I. supervised and acquired funding for the project. All authors discussed the results and contributed to the final chapter.

2.10. Acknowledgement

Financial supports from Canada Foundation for Innovation CFI-JELF (Project No. 36874) and the New Brunswick Innovation Foundation NBIF and New Brunswick Health Research Fund NBHRF (Project No. COV-0000000063) are greatly appreciated. We appreciate Crawford, M., Dr. Michael Duffy, Dr. Aurora Nedelcu, and Dr. Shawn MacLellan (Department of Biology, University of New Brunswick) regarding protein preparation, expression, purification, and characterization, funded by the grant (# COV2020-035 Production of COVID19 antigens for rapid and extensive NB community testing initiatives) to SM from the New Brunswick Innovation Foundation.

2.11. Conflict of interest

The authors declare no competing financial interest.

3. Sustainable air plasma regeneration of screen-printed gold electrodes with enhanced electroactive surface area and biosensing performance

S. Ardalan, C.T.H. Tran, S.T. Fraser, M. Bilek, A. Ignaszak. Submitted to RSC Sustainability, manuscript number SU-ART-02-2026-000113, Feb 23, 2026.

3.1. Abstract

Miniaturized electroanalytical devices paired with screen-printed electrodes (SPE) are gaining popularity due to their compact design and minimal analyte requirements. However, their single-use nature and non-degradable polymer substrates with printed precious metals like gold limit their sustainability as biosensing platforms. Disposing of each electrode after a single use is neither cost-effective nor sustainable. Herein, a green air plasma cleaning technique is introduced to regenerate multiple gold SPEs simultaneously within 10 minutes. Air plasma treatment results in surface hydrophilicity (water contact angle 33° vs control, 101°), significant reduction in surface nitrogen analyzed by X-ray photoelectron spectroscopy (0.5% vs 7.3% control), near-zero charge transfer resistance (vs $1.2\text{ k}\Omega$ control) with a simplified equivalent circuit only limiting charge transfer processes by redox mass diffusion characterized by Warburg impedance. Moreover, the regenerated electrode was reused to fabricate an EIS-based biosensor using a thiol-modified thrombin-binding aptamer. A ≈ 1.24 -fold increase in the electroactive surface area led to a ≈ 2 -fold increase in thiol-modified ssDNA aptamer immobilization towards 50 nM thrombin with ≈ 3 -fold increase in the sensor signal. Air plasma cleaning is a sustainable and facile technique to regenerate contaminated gold SPEs for biosensor fabrication with enhanced capture probe loading and biosensing sensitivity.

3.2. Introduction

As an integral part of biomedical diagnostics, biosensors have become invaluable tools for healthcare professionals to detect biomolecules, disease-related biomarkers, pathogens, and viral infections. They are readily deployed, not only in a clinical setting, such as diagnostic laboratories, but also at the point of care, where they can be self-administered by non-professionals, as seen in continuous glucose monitoring devices.[99] Screen-printed electrodes (SPEs) have emerged as cost-effective substrates for electrochemical biosensors, making them particularly valuable in healthcare and environmental monitoring.[100] SPEs are planar devices featuring three electrodes arranged on a plastic or ceramic substrate. The SPE market is projected to expand at a Compound Annual Growth Rate (CAGR) of approximately 8.5% over the forecast period, with the market size expected to reach USD 500 million in 2024 and grow to USD 898 million by 2033.[101] The increasing interest in SPE-based biosensors is reflected in scientific research outputs, with 1,014 research articles published since 2000; over half of these have emerged in the past five years. Significant growth is also noted in the number of granted patents, totalling 1,629, with 684 awarded in the last five years.[102] Among these innovations, screen-printed gold electrodes (gold SPEs) are in high demand for developing electrochemical biosensors.[103]

Gold SPEs provide a miniaturized platform that requires a minimal volume of analyte for the fabrication of electrochemical biosensors.[104] For instance, single-stranded DNA (ssDNA) aptamers are commonly used capture probes for the fabrication of electrochemical aptamer-based biosensors.[27, 34, 105-107] The rigorous experimental trials involved in biosensor development require substantial quantities of gold SPEs, which

are typically designed for single-use and disposed of after testing. This results in high consumption rates, especially when optimizing conditions or dealing with experimental errors such as contamination during handling and storage, as well as systematic human errors in electrode preparation, all of which can damage the electrodes.[97] The disposal of used gold SPEs, along with purchasing new ones, presents both economic and environmental challenges. For instance, gold SPEs from reputable manufacturers are priced between 6.4 and 8.2 USD per electrode. The repetitive cycle of designing, testing, and optimizing with gold SPEs leads to significant resource use. Additionally, the disposal of these electrodes poses environmental hazards due to their non-degradable nature and the presence of precious metals along with plastic or ceramic substrates.

Given the challenges associated with contamination and waste management in gold SPEs, developing effective cleaning and regeneration strategies becomes vital to enhance their usability and reduce environmental impact. Post-manufactured SPEs are markedly contaminated with pasting binders (e.g. ethyl cellulose, epoxy-based polymeric binders, polyester resin),[108] which partially blocks the working electrode and decreases electroactive surface area and surface coverage of biosensor capture molecules.[60] Previous research has primarily focused on pre-treating SPEs using electrochemical techniques, with a few studies investigating chemical and physical pre-treatment methods, such as plasma (ionized gas) modification.[60, 109-113] These methods effectively remove the contamination or extra binders, increase the surface area, and make the SPEs suitable for biosensor fabrication. While current research addresses the pre-modification of SPEs, more investigation is required regarding post-cleaning and regeneration of SPEs. One study examined the regeneration capacity of SPEs by a two-step cyclic voltammetry method

using sulfuric acid and ferricyanide.[114] It revealed that electrochemical recycling led to limited regeneration caused by the inherent heterogeneity and low robustness, resulting in a significant reduction in the gold layer thickness of the working electrode.[114] Considering the high consumption of SPEs, exploring an effective regeneration strategy could reduce the cost of SPE consumption and potentially minimize waste and environmental hazards.

Numerous studies have been conducted on cleaning protocols for the preparation of electrodes, especially gold.[36, 47, 49, 115-121] For molecular electronics or biosensor applications, the quality of self-assembled layers on polycrystalline gold depends on the reliable removal of inherent contaminants from ambient surfaces and the exposure of pristine gold surfaces. In the past, acidic piranha solution was commonly used to remove organic contaminants during gold electrode production.[59] However, piranha can create uncontrollable defects on the gold electrode, causing extensive etching and oxidation. As a safer alternative, sulfochromic acid was proposed to eliminate organic residues, but it causes permanent etch pits and is not recommended for repeated use.[59] A comprehensive study evaluated different electrode pre-treatment methods, including chemical oxidation, UV treatment, ozone treatment, and electrochemical treatment.[47] Dipping gold in 50 mM potassium hydroxide in 25% hydrogen peroxide with a single linear sweep voltammetry from -0.2 to -1.2 V in KOH 50 mM resulted in the lowest contamination (elemental carbon and oxygen sources) and lowest charge transfer resistance.[47] In a systematic study of cleaning photolithography gold on silicon wafers, X-ray photoelectron spectroscopy (XPS) provided the elemental composition of gold surfaces treated with different methods.[60] Although all surface pre-treatment methods significantly decreased contamination and

increased SAMs coverage, they induced structural changes that affected functionalization characteristics. Different pre-treatment methods did not result in significant differences in surface area or molecule coverage but induced structural changes to the gold surface and affected the morphology of the thiolated molecule layer. Pre-treatment methods which contain chloride anions were found to cause changes to the structure of the gold surface, leading to surface redistribution and possible introduction of defects.[60] Moreover, anion adsorption can result in a passivating layer of Au_2SO_4 or AuCl , which is formed through a redox reaction on the Au electrode.[49] It is recommended to prevent chloride leakage from the reference electrode during electrochemical treatment and avoid using platinum counter electrodes when preparing gold electrodes by electropolishing.[49] Surface roughness is another debated topic, as recent studies have shown that alkanethiolate monolayers on rough gold surfaces can act as stronger barriers to electron transfer than those on smooth surfaces.[36] However, the defects on smooth surfaces were larger compared to those on rough surfaces, leading to an increased rate of heterogeneous electron transfer. One study found that the electrochemical characteristics of DNA SAMs were mostly unaffected by different pre-treatments.[122] Despite these findings, it is still unclear how these treatment methods affect biosensor fabrication, especially for oligonucleotide or aptamer immobilization and their affinity towards their target.

Plasma is the fourth state of matter, and it forms when gas molecules lose electrons, resulting in a mixture of positive ions, free electrons, and neutral particles.[123] Plasma can be generated through several techniques, including thermal and radiation ionization. Plasma has numerous applications across various fields, such as surface treatment, thin film deposition, and sterilization.[124] One effective process is plasma cleaning, which

excels at removing organic contaminants, dust, grease, and other particulate matter. This method offers several advantages: it is highly efficient, non-contact (minimizing the risk of physical damage), eco-friendly (due to the absence of chemical solvents), and quick.[124] While mechanical polishing is commonly used to clean macroscopic and micrometre-sized electrodes, cleaning the surfaces of nanoelectrodes poses challenges due to their small size and fragility. Air plasma cleaning is highly compatible with nanoelectronics for non-destructive cleaning, as demonstrated by atomic force microscopy (AFM) images and electrochemical measurements.[125] Alkane thiolate groups, such as hexadecanethiolate SAMs, can be effectively detached by H₂ plasma in less than a minute, reducing the layer thickness from 22 Å to nearly zero.[63] Additionally, O₂ plasma followed by ethanol reduction can fully regenerate the photolithographic gold layer from a gold oxide layer. [60]

A commonly used commercial radio frequency (RF) discharge plasma cleaner consists of a coil wrapped around an insulating layer that houses a sealed chamber (Figure 3.1). An external RF power source energizes the cylindrical coil, creating a fluctuating magnetic field in its vicinity.[126] This magnetic field induces an alternating current in the working gas within the reaction chamber. Once the kinetic energy of the residual free electrons exceeds the ionization threshold of the gas molecules and atoms, ionization occurs resulting in the formation of positively charged ions and more free electrons.[126] Low-pressure air plasma cleaning effectively removes organic contaminants from large-aperture optical components in situ within inertial confinement fusion facilities. During this cleaning process, reactive species are formed, including C–O, C=C, C=O, and O–H bonds, with

C=O being the final product. The radicals O, HO₂, and O₃ are shown to be key components in breaking down contaminants.[127]

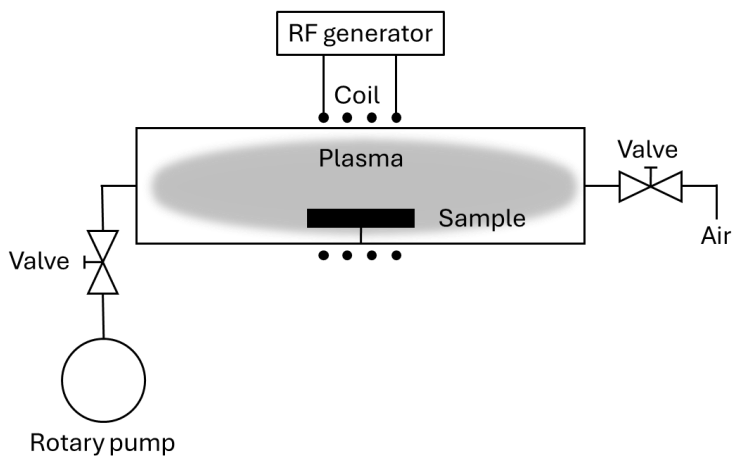


Figure 3.1. Schematic of an RF discharge plasma cleaner.

From these studies, one conclusion can be drawn that plasma treatment methods are another effective alternative for cleaning and recovering biosensor platforms. Unlike macroscopic disk-shaped electrodes, which can be easily cleaned through mechanical polishing, cleaning screen-printed surfaces is a significant challenge. Their fragility and incompatibility with organic solvents or chemical treatments complicate the replication of biosensor experiments. In the biosensing community, it is well recognized that rigorous experimental trials must be conducted from the initial idea to the final biosensing device to optimize analyte binding, capture probe immobilization, and improve analytical performance and reproducibility. The widespread use of such biosensing platforms is not sustainable and can lead to considerable research costs.

The objective of this study is to develop an air plasma cleaning protocol to regenerate the gold SPEs that had been used for binding analysis of a model target protein, thrombin. The used gold SPEs are referred to as electrodes on which a thiol-modified ssDNA aptamer

was immobilized through self-assembled monolayer (SAM) formation using thiol-gold chemisorption chemistry. They were then exposed to a thrombin solution for impedance-based binding analysis. Thrombin specifically binds to the aptamer through a high-affinity interaction (dissociation constant or $K_d \approx 5$ nM).[128] After the aptasensor is used for thrombin detection, it becomes coated with the covalently attached aptamer and the bound thrombin target. To reuse the same aptasensor for detecting a different thrombin sample or for conducting experiments under new conditions, the thrombin-aptamer complex can be disrupted by rinsing the electrode with a high salt concentration, which detaches the thrombin.[129] However, the aptamer remains tethered to the gold electrode, limiting its reusability for experiments that require variations in conditions, such as aptamer concentration, type, or immobilization conditions. To address this challenge, we propose an air plasma cleaning technique to effectively regenerate gold SPEs. This technique utilizes a cylindrical coil inductively coupled RF plasma cleaner (30 Watts at 0.7 torr). The effectiveness of plasma cleaning was assessed using electrochemical impedance spectroscopy (EIS), X-ray photoelectron spectroscopy (XPS), and contact angle (CA) measurements. This plasma cleaning process can simultaneously clean multiple electrodes within a brief ten-minute timeframe. It is environmentally friendly, does not involve toxic chemical treatments, and preserves the electrochemical performance of gold SPEs. We demonstrated this with a proof-of-concept faradaic EIS biosensor model based on the thrombin-binding aptamer as the capture probe. The regenerated gold SPEs can be reused for biosensor fabrication with enhanced immobilization efficiency of the aptamer probe and sensitivity for target detection.

3.3. Experimental

3.3.1. Materials

Potassium hexacyanoferrate(II) trihydrate ($\text{Fe}(\text{CN})_6^{4-}$; 98.5%), potassium hexacyanoferrate(III) ($\text{Fe}(\text{CN})_6^{3-}$; 99%), ethylenediaminetetraacetic acid (EDTA; 98.5%), tris(hydroxymethyl)aminomethane hydrochloride (Tris.HCl; >99%), mercaptohexanol (MCH; 99%) potassium chloride (KCl; 99%), sulfuric acid (H_2SO_4 ; 96%, p.a.), sodium hydroxide (NaOH; 98%, pellets), custom DNA oligo (aptamer; HPLC purified, 100 μM in TE buffer), and thrombin from human plasma (250 units, lyophilized powder, $\geq 2,000$ NIH units/mg) were purchased from Sigma Aldrich. Italsens gold Screen-Printed Electrode (gold SPE; \varnothing 3 mm working electrode) was purchased from Palmsens (Netherlands)

All solutions were prepared with Milli-Q water. Except for protein and aptamer solutions, which were purchased in purified, DNase/RNase- and protease-free form, all solutions were filtered using vacuum-driven filters (Stericup Quick Release, Sigma Aldrich). Aptamer and protein solutions were stored in low-binding tubes to reduce stickiness to the walls of the microtubes (DNA/Protein LoBind Tubes, Eppendorf). Low-retention pipette tips (ART, Thermo Fisher Scientific) were used for pipetting to minimize DNA/protein binding to pipette tips. All solutions, except $\text{Fe}(\text{CN})_6^{3-}$, $\text{Fe}(\text{CN})_6^{4-}$, H_2SO_4 , protein, and aptamer solutions, were sterilized by autoclaving at 121°C for 30 minutes, with a total cycle time of 1 hour.

A 10X stock solution of Tris-Buffered Saline (TBS) buffer was prepared by dissolving Tris.HCl and NaCl, then adjusting the pH to 7.4 with NaOH, with a final concentration of 200 mM Tris and 1500 mM NaCl. An electrochemical measurement buffer was prepared by mixing as-prepared TBS, Mg^{2+} and $\text{Fe}(\text{CN})_6^{3-/4-}$ stock solutions with the final

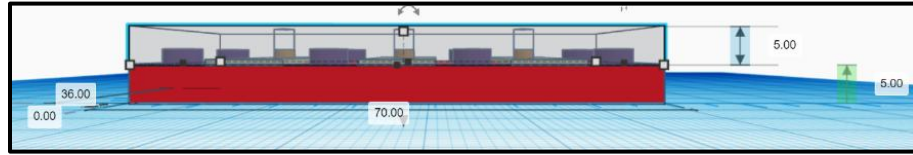
concentrations of 1X TBS, 1 mM Mg^{2+} , and 1 mM $Fe(CN)_6^{3-/4-}$. An incubation buffer was prepared by mixing as-prepared TBS and Mg^{2+} stock solutions with the final concentrations of 1X TBS and 1 mM Mg^{2+} . A 100 mM MCH stock solution was prepared by diluting MCH in water.

Aptamer solution. A 29-nucleotide single-stranded DNA aptamer against thrombin was chosen from the original research by Tasset et al.[130] HPLC-purified lyophilized aptamer was purchased from Sigma-Aldrich with the sequence of 5'-AGTCCGTGGTAGGGCAGGTTGGGGTGACT-3' and a C6 S-S thiol-modifier on the 5' end. Aliquots of a 5 μ M aptamer solution were prepared in LoBind DNA microtubes diluted with TE buffer 1X and stored at 4°C.

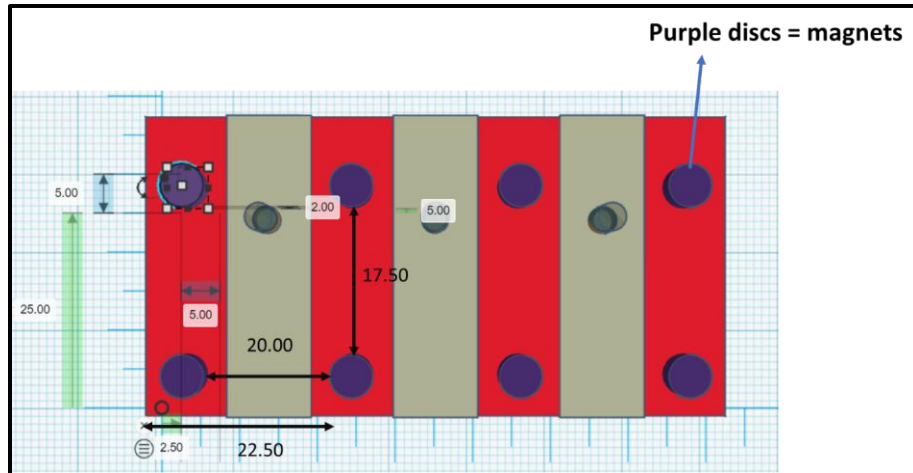
Protein solution. Thrombin (250 units) was purchased from Sigma Aldrich (>2000 units/mg). Each unit corresponds to 0.324 μ g, totalling 81 μ g of thrombin. The molecular weight (Mw) of thrombin is 37.4 kDa. To calculate protein concentration, the equation μ M = (μ g/mL) / Mw in kDa was used.[131] The glass vial containing thrombin was first centrifuged at 4°C at 3000 rpm to ensure complete settling of the thrombin. The thrombin-containing vial was then transferred to an ice bath, and thrombin was dissolved in cold Milli-Q water to a final concentration of 50 nM. The dissolved thrombin was then transferred to LoBind protein microtubes and stored in the freezer at -80°C.

Incubation cell. An incubation chamber was designed to sandwich the gold SPE between two Perspex layers to reduce droplet leakage between electrodes. The top layer had a hole drilled precisely to expose the WE to the immobilization droplet, while covering the RE and CE. To ensure a secure and tight fit, neodymium magnets were used to hold the Perspex layers together. Schematics of the incubation chamber are provided in Figure 3.2.

A)



B)



C)

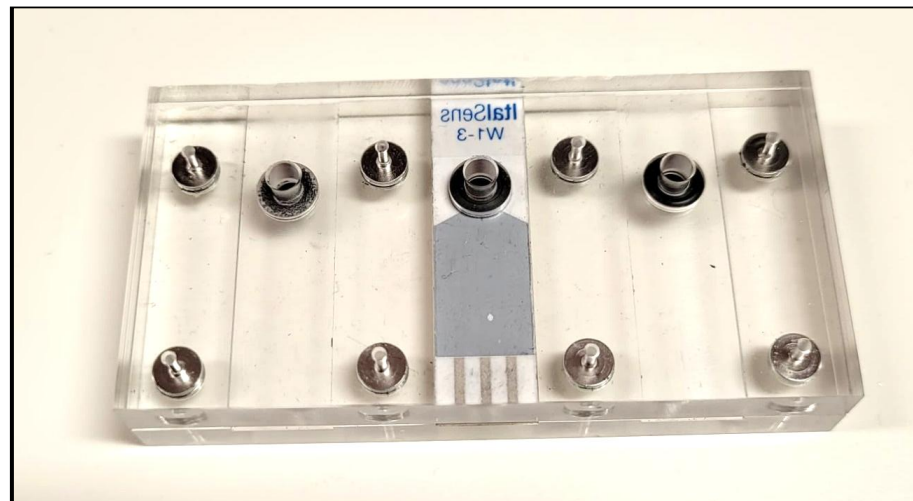


Figure 3.2. Schematics of the incubation chamber in Autodesk Tinkercad, dimensions are provided in millimetres: A) front view, B) top view, and C) Digital image.

3.3.2. Methods

Electrochemical characterization. A compact potentiostat (PalmSens4) was used for electrochemical analysis of gold SPEs. Results were analyzed by an electrochemical analysis software (PStrace, PalmSens). All measurements were performed in a dark box to minimize light exposure. A Teflon cap was designed to slide the gold SPE inside the glass cell with two narrow holes for the N₂ gas inlet and outlet. Electrochemical Impedance Spectroscopy (EIS) was performed to characterize charge transfer processes at the electrode interface by applying an alternating voltage of 5 mV and a biasing DC potential at the open circuit potential (OCP) vs Ag/AgCl reference electrode with a frequency range from 0.1 Hz to 100 kHz. Cyclic voltammetry (CV) was scanned twice in the measurement buffer solution to characterize the redox peaks within a potential window from -0.2 to 0.4 V (vs Ag/AgCl) at a scan rate of 50 mV/s and a step of 5 mV. For the determination of electrochemically active surface area, gold SPEs were scanned three times using CV in 0.5 M H₂SO₄ from 0 to 1.4 V with a scan rate of 0.1 V/s, 5 mV/step. This step is known as electropolishing (E-polish).

Aptamer immobilization. The 5 μM aptamer solution had a concentration of 40 μg/mL and an A260/A280 ratio of 1.81 as analyzed by a microvolume spectrophotometer (NanoDrop, Thermo Fisher Scientific). The aptamer's aliquot was annealed in a dry bath heater at 90 °C for 5 minutes and then cooled slowly to reach room temperature. Then, 5 μL of the co-immobilization aliquot was drop-casted on the electrodes. The incubation chamber was put inside a humidity chamber and incubated at 25 °C for 16 h. Next, the electrodes were rinsed with incubation buffer and dipped in the same buffer for 10 minutes.

Then, each electrode was rinsed with the measurement buffer and inserted into the electrochemical cell for electrochemical characterization.

Protein incubation. Thrombin's aliquot was taken out from the freezer (-80 °C) and thawed to room temperature. Gold SPEs were inserted into the incubation chamber. Then, 5 μ L of the aliquot was drop-casted on the electrodes in the incubation chamber. The incubation chamber was put inside a humidity chamber and incubated at room temperature for 30 minutes. Next, the electrodes were dipped in the incubation buffer for 10 minutes and then rinsed with the measurement buffer and inserted into the electrochemical cell for electrochemical characterization.

Plasma cleaning. A plasma cleaner (PDC-002 Expanded plasma cleaner, Harrick Plasma), equipped with a vacuum pump, was used for surface cleaning of gold SPEs. This system has three power levels applied to an RF coil, including low (7 W), medium (11 W) and high (30 W). The gold SPEs were affixed to two slides of polystyrene films using adhesive tape to ensure stability during the cleaning process. To expose only the working electrode to plasma while covering the rest of the electrode, a hole with a diameter of 3 mm, matching the size of the working electrode, was drilled into the top polymeric film. The plasma cleaning was conducted at approximately 0.7 Torr with a tolerance of ± 0.05 Torr.

Surface chemistry. An X-ray Photoelectron Spectroscopy (XPS) instrument (K-alpha⁺, Thermo Fisher Scientific) with a monochromatic Al K α X-ray source was used to characterize the surface chemistry of gold SPEs. Ten survey scans and five high-resolution scans of major elements (carbon, oxygen, nitrogen, and phosphorus) were taken on each sample for comparison. Element peak areas were divided by element-specific sensitivity

factors and converted to atomic percentage for each element. Results were analyzed by surface analysis software (Avantage Data System, Thermo Fisher Scientific)

Surface wettability. Water contact angle (WCA) measurements were performed on gold SPEs to evaluate the effect of plasma cleaning on surface wettability using a Theta tensiometer (Biolin Scientific). Results were averaged over 3 drops for each sample.

Surface morphology. Scanning electron microscopy (SEM) images were collected to analyze surface morphology and particle size on the gold SPE using an electron microscope (Scios 2, Oxford Ultim Max 170 EDS detector, Thermo Fisher Scientific) and were analyzed by microscopy analysis software (Aztec, Oxford Instruments).

3.4. Results and discussions

3.4.1. Influence of air plasma cleaning parameters on gold SPEs

The parameters of the plasma source, including power and treatment time, to regenerate gold SPEs were investigated. The "used gold SPEs" referred to those that were utilized for the fabrication of thrombin-binding aptasensors. They consisted of thiol-bonded, chemisorbed SAMs of the thrombin-binding aptamer, along with the bonded thrombin used for aptasensor fabrication and characterization. The used gold SPEs were exposed to an air plasma for different durations with two levels of power, and the results are shown in Figure 3.3. Pre-immobilized functional biomolecules partially blocked electron transfer processes on the electrode-solution interface. Therefore, the charge transfer resistance (R_{ct}) of the electrodes was measured using the faradaic EIS technique in the measurement buffer solution (containing ferro/ferricyanide redox couple) to evaluate the effectiveness of air plasma cleaning to remove the electron transfer barriers. Air plasma cleaning reduced the R_{ct} of used electrodes that had been utilized to fabricate thrombin-binding aptasensors. By

applying 10 minutes air plasma with 30 W power (\approx power density of 10 mW/cm^3) on the used electrodes, the barriers to charge transfer, including the SAMs of thiol-modified aptamers and the aptamer-thrombin complex, are removed. This removal resulted in a significant decrease in the R_{ct} values from $8.3 \text{ k}\Omega$ to $0.9 \text{ k}\Omega$ which is similar to that of new electrodes ($1.2 \text{ k}\Omega$). The resulting Nyquist plots and cyclic voltammograms (CV) of electrodes with and without plasma modification are shown in Figure 3.4. The semi-circle in the Nyquist plot representing the R_{ct} showed a significant reduction following plasma cleaning, since the surface was cleaned by removal of the immobilized biomolecules and excess binders.

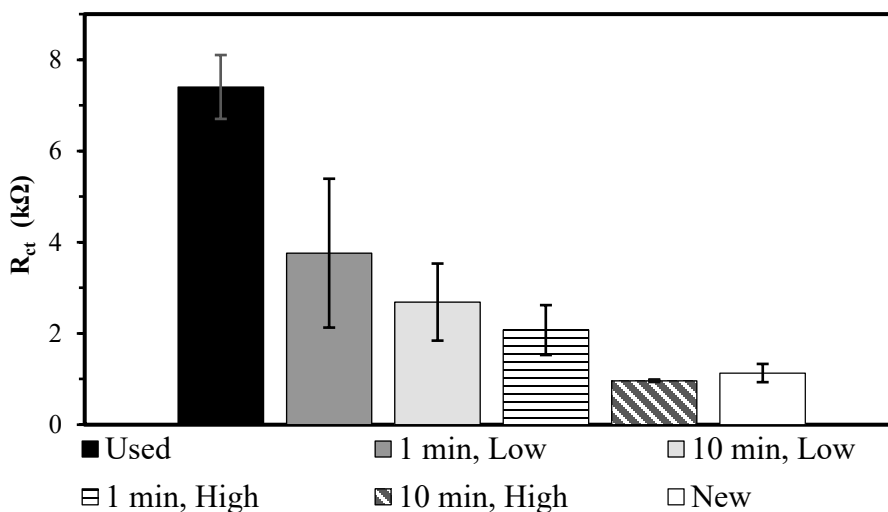


Figure 3.3. Effect of different plasma treatment time and power on R_{ct} provided by faradaic EIS. Used gold SPEs exhibited a high $R_{ct} \approx 8 \text{ k}\Omega$ compared to new SPEs with $R_{ct} \approx 1 \text{ k}\Omega$. After 10 minutes of air plasma cleaning at high power, R_{ct} reduced to below $1 \text{ k}\Omega$ by the removal of insulating (bio)layers. Error bars are included to represent the variability in the data collected from three different gold SPEs for each condition, with the measurements taken after a single cleaning of the sensors.

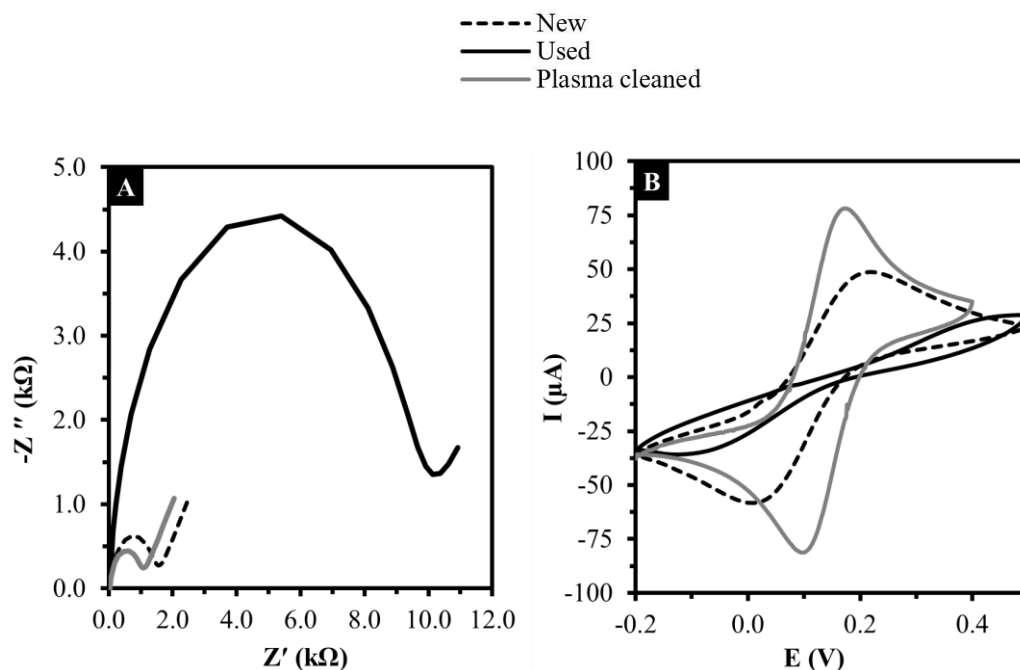


Figure 3.4. A) Nyquist plots and B) CV of a used, plasma cleaned, and a new gold SPE. R_{ct} significantly reduced after plasma cleaning, while ΔE_{peak} decreased to 0.11 V, closer to a reversible Nernstian behaviour of $1 e^-$ transfer. Potential values are vs screen-printed Ag/AgCl reference electrode in the measurement buffer solution.

The parameters from the CV were measured and depicted in Table 3.1. Though the new electrodes exhibited reversible redox peaks with distinct oxidation and reduction peaks, the plasma-cleaned electrode showed a smaller peak-to-peak separation ($\Delta E_{peak} \approx 0.11$ V) drawing closer to the ideal reversible Nernstian behavior associated with the transfer of a single electron from the $Fe(CN)_6^{4-/3-}$ redox probe. Meanwhile, the highest oxidation peak of $Fe(CN)_6^{4-}$ to $Fe(CN)_6^{3-}$ redox probe belonged to the plasma cleaned electrode (77.4 μA vs New 44.5 μA). In contrast, the used electrode poorly represented a reversible redox reaction; its response resembled that of a pure resistor, with the current increasing almost linearly with voltage, in accordance with Ohm's Law.

Table 3.1. CV parameters of gold SPEs with different modifications. Oxidation current significantly increased upon plasma cleaning with a smaller peak-to-peak separation.

Parameters	New	Used	Plasma cleaned
$I_{\text{peak}} (\mu\text{A})$	49.5	6.8	77.4
$E_{\text{ox}} (\text{V})$	0.2	0.39	0.16
$E_{\text{red}} (\text{V})$	0.02	-0.08	0.05
$\Delta E_{\text{peak}} (\text{V})$	0.18	0.47	0.11

3.4.2. Determination of electrochemically active surface area

Pre-treatment of a gold electrode is commonly done by CV in 0.5 M H₂SO₄, providing gold atoms in a reduced state. This process is known as electropolishing (E-polish) and is shown in Figure 3.5. Several parameters were calculated from the cathodic peak of gold, including the electrode's real surface area (S_{true}) and roughness factor (r). The integral from 0.5 V to 0.7 V of the cathodic (reduction) peak, which is the reduction of Au³⁺ to Au, is used to calculate the total charge (Q).[132] The integral from a current-potential (i-E) curve is the power ($i \times E$), and was divided by the scan rate (v) to get the charge according to Equation 3.1.

$$Q = \frac{\int_{V_1}^{V_2} I dv}{v} \quad 3.1$$

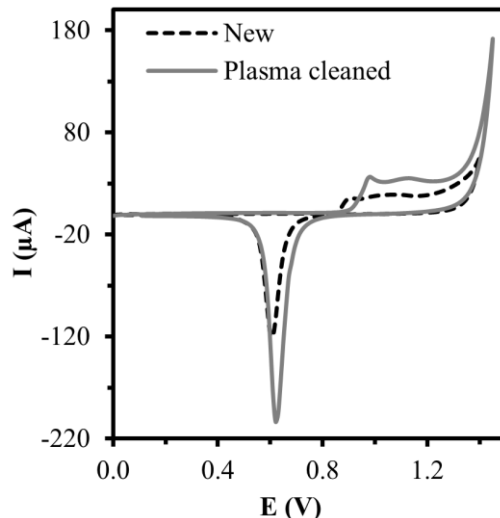


Figure 3.5. Cyclic voltammogram of gold SPE in 0.5 M H₂SO₄ (E-polishing) reduces all gold atoms. Plasma cleaned electrodes depict a sharper peak due to a higher surface area.

The working electrode roughness factor (r) was estimated based on a well-developed protocol for calculating the electrode's true surface from the charge in the range of oxygen reductive desorption.[133] The true electrode surface (S_{true}) was the actual reactive area, while the geometrical surface (S_{geom}) is based on the electrode surface area (πr^2). The charge (Q_{red}) for oxygen electro-desorption was divided by $400 \mu C/cm^2$, the charge needed to desorb an oxygen monolayer from $1 cm^2$ (Equation 3.2).[134] Roughness factor (r) was calculated based on the ratio of true electrode surface to its geometrical area (Equation 3.3).[134] The electrochemical surface analysis of the Italsens gold electrodes (Table 3.2) demonstrated the presence of rough, micron-sized gold particles.

$$S_{true} = \frac{Q_{red}(\mu C)}{400 (\mu C \cdot cm^{-2})} \quad 3.2$$

$$r = \frac{S_{true}}{S_{geom}} \quad 3.3$$

Table 3.2. Electrode surface area characteristics calculated from the reduction peak of gold in 0.5 M H₂SO₄.

Parameters	New electrode	Plasma cleaned
Average Q _{red} (μC)	84.5	103
S _{geom} (cm ²)	0.0707	0.0707
S _{true} (cm ²)	0.21	0.26
Roughness (f)	2.98	3.64

3.4.3. Electrode characterization by electrochemical impedance spectroscopy

In EIS characterization of an electrochemical sensor, the working electrode is perturbed by applying a small amplitude excitation alternating voltage (V_0) along with a fixed direct potential, commonly open circuit potential (OCP), which is approximately at the formal potential (E^0) of the over a wide range of frequencies.[37] The Randles circuit is the most frequently used model, as it effectively represents uncompensated resistance (R_u), charge transfer resistance (R_{ct}), Warburg impedance (Z_w), and double layer capacitance (C_{dl}). By fitting the impedance data to this equivalent circuit using appropriate modelling software, the values of each electrical component can be accurately calculated. The capacitance is explained by Equation 3.4.[37]

$$C = \epsilon\epsilon_0 \left(\frac{A}{d}\right) \quad 3.4$$

Where ϵ is the dielectric constant of the medium at the electrode/electrolyte interface, ϵ_0 is the permittivity of free space, A is the electrode's surface area, and d is the thickness of attached layers on the electrode's surface. In a non-ideal behavior of capacitance, the term constant phase element Q_0 is used. Q_0 has the numerical value of the admittance ($1/|Z|$) at $\omega = 1$ rad/s. n is the exponent in the CPE impedance equation. In the case of an ideal capacitor where $n = 1$, and $C = Q_0$; However, the capacitance element in the Randles circuit in electrochemical sensors is drifted from an ideal capacitance. When $n < 1$, the CPE represents a non-ideal capacitive behavior, often due to surface roughness and varying thickness or composition of coatings.[37] In a Randles circuit with semi-finite diffusion, the effective capacitance is given by Equation 3.5. [135, 136]

$$C = Q_0^n \left(\frac{1}{R_u} + \frac{1}{R_{ct}} \right)^{\frac{n-1}{n}} \quad 3.5$$

3.4.4. Electrochemical impedance spectroscopy analysis of gold SPE

The gold SPEs were characterized using the EIS technique in a solution containing the redox couple, ferro/ferricyanide and TBS buffer (pH 7.4) to measure the equivalent electrical component as explained in section 3.4.3. The EIS data presented in Table 3.3 reveal relationships between surface modifications and their resulting electrochemical properties. In Table 3.3, plasma-cleaned electrodes are related to the used electrodes that were cleaned by 10-minute air plasma cleaning at high power. The most significant trends emerge in the R_{ct} and effective capacitance (C) parameters. As mentioned earlier, the decrease in R_{ct} from 1132 Ω to 434 Ω is related to the removal of excess organic binders and post-manufacturing contamination, with a parallel increase in capacitance (plasma cleaned 3.19 μF vs control 1.33 μF). This increase was related to the decrease in dielectric

thickness and an increase in electrochemical surface area, as capacitance follows an inverse relationship with layer thickness and a direct relationship to surface area ($C \propto A/d$). However, the mass transfer diffusion defined by the Warburg coefficient (σ) increases from 819.9 to 1440 $\Omega \cdot s^{-1/2}$. The observation that the R_{ct} remains relatively low following plasma surface cleaning suggests that the electron transfer process at the electrode interface is not significantly limited by heterogeneous electron transfer kinetics but instead, predominantly governed by mass transfer impedance.

Table 3.3. Faradaic EIS characterization of gold SPE with different modifications using equivalent Randles circuit.

Electrode	R_s (Ω)	R_{ct} (Ω)	W (σ)	Q (μT)	n	C (μF)
New_No treatment	43.6	1132	819.9	4.98	0.865	1.33
New_E-polished	40.7	567	965.9	9.39	0.866	2.75
Plasma cleaned	55.5	434	1440	1.19	0.850	3.19
Plasma cleaned_E-polished	51.1	-	1611	-	-	-

3.4.5. Mass transfer diffusion of redox active species

To better understand the diffusion process, we investigated how the scan rate affects the peak current in cyclic voltammetry experiments. We used the Randles-Sevcik equation to derive the diffusion coefficient. Additionally, we conducted parallel diffusion calculations from EIS by analyzing the Warburg impedance. The Warburg impedance, denoted as Z_w , characterizes the challenges associated with the mass transport of redox species to the

electrode surface, considering a semi-infinite linear diffusion. Z_w acts like a series circuit composed of a resistance (R_w) and a capacitance (C_w), both of which vary with frequency defined by Equation 3.6.[37]

$$Z_w = R_w + C_w = \left[\sigma \omega^{-\frac{1}{2}} - j \left(\sigma \omega^{-\frac{1}{2}} \right) \right] \quad 3.6$$

Where Warburg coefficient σ is defined by Equation 3.7.[37]

$$\sigma = \frac{2RT}{n^2 F^2 A \sqrt{2} \sqrt{D_0} C_0} \quad 3.7$$

Rewriting Equation 3.7 to calculate diffusion coefficient D_0 is derived from Equation 3.8.

$$D_0 = \left(\frac{2RT}{\sigma n^2 F^2 A \sqrt{2} C_0} \right)^2 \quad 3.8$$

The diffusion coefficient (D_0) of the redox couple is assumed to be equal for both the oxidized (D_{ox}) and reduced (D_{red}) forms. The other symbols retain their previously defined meanings, and their values are shown in Table 3.4. The σ value was derived by plotting the imaginary impedance $-Z''$ vs $\omega^{-1/2}$, and the slope of this plot provided σ , which is shown in Table 3.5.

An alternative method to derive the diffusion coefficient (D_0) is based on the Randle-Sevcik method.[37] In processes involving electrochemically reversible electron transfer with freely diffusing redox species, the Randles–Sevcik equation (Equation 3.9) illustrates the peak current (A) correlates linearly with the square root of the scan rate v ($V.s^{-1}$).[137]

$$i_p = 0.446nFAC^0 \left(\frac{nFvD_0}{RT} \right)^{\frac{1}{2}}$$

Table 3.4. Fixed parameter values for the Randel-Sevcik and Warburg impedance equations for diffusion calculations.

Parameter	Value
A (cm ²)	0.21
C (mol/cm ³)	2×10 ⁻⁶
n	1
R (J/mol.K)	8.314
F C/mol	96,485
Constant	0.446
T (K)	295

Table 3.5. Warburg Impedance coefficient (σ) derived from faradaic EIS tests for electrodes treated under two conditions.

Parameter	E-polished	Plasma cleaned/E-polished
σ ($\Omega \cdot s^{-1/2}$)	1071	1461

In Randles–Sevcik equation, n represents the number of electrons involved in the redox reaction, A (cm²) denotes the electrode's surface area (typically regarded as the geometric area), D₀ (cm².s⁻¹) indicates the diffusion coefficient of the oxidized species, and C₀ (in mol.cm⁻³) refers to the bulk concentration of the analyte. Plasma cleaning increases roughness and area, lowering charge transfer resistance, but the complex surface can hinder effective diffusion, resulting in a lower apparent D₀.

Rewriting Equation 3.9 based on plotting the i_p vs ν provides the diffusion coefficient according to Equation 3.10.

$$D_0 = \left(\frac{\text{Slope } i_p \text{ vs } \nu}{0.446nFAC^0} \right)^2 \frac{RT}{nF} \quad 3.10$$

Figure 3.6 demonstrates the cyclic voltammograms of Randles–Sevcik experiments with plasma-cleaned/E-polished gold SPE in ferric/ferrocyanide solution. Diffusion coefficients were calculated using the Randles-Sevcik equation with parameters from Table 3.4. Both diffusion coefficients, calculated using the Randles-Sevcik equation from voltammetry tests and the EIS technique, showed a trend indicating that regenerated electrodes had lower diffusion coefficients, as presented in Table 3.6. The reasoning behind this phenomenon may be complex, but one study suggests that increased roughness can lead to a more tortuous diffusion path, which could potentially slow down diffusion and subsequently affect the measured diffusion coefficient.[138]

3.4.6. Surface chemistry analysis by XPS and water contact angle

The electrochemical tests discussed in the previous sections provided insights into the electron transfer processes, but they did not provide chemical information about the electrode's surface. XPS analysis could directly provide information about surface elemental composition. Table 3.7 provided the elemental surface composition of the electrodes with different treatments. Used electrodes showed the lowest Au% ($\approx 13.9\%$) and the highest C% ($\approx 54.9\%$), as a result of attached biomolecules and residual binder. New electrodes had a higher Au% ($\approx 20.1\%$) with a slight reduction in C% ($\approx 53.8\%$).

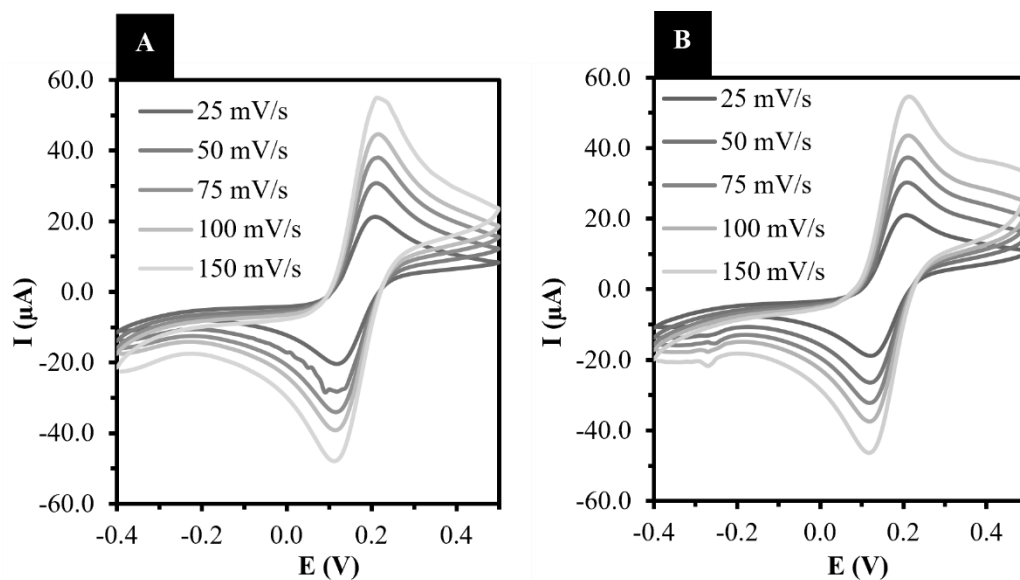


Figure 3.6. Cyclic voltammograms of A)E-polished and B) plasma cleaned/E-polished gold SPE in 2 mM ferric/ferrocyanide in 1X TBS and 1 mM MgCl₂ at scan rates 25–150 mV/s.

Table 3.6. Diffusion coefficient (D_0) of gold SPE with and without plasma cleaning derived from two electrochemical techniques based on CV and EIS

Electrode	$D_0 \text{ cm}^2 \text{ s}^{-1}$ (CV)	$D_0 \text{ cm}^2 \text{ s}^{-1}$ (EIS)
Au/E-polished	5.86×10^{-6}	6.84×10^{-7}
Au/Plasma-treated/E-polished	5.01×10^{-6}	3.68×10^{-7}

Plasma cleaning enhanced Au% ($\approx 22.5\%$) and significantly reduced C% ($\approx 43.6\%$). However, air plasma cleaning increased O% ($\approx 25.3\%$), which could be due to the binder oxidation.

Water Contact Angle (WCA) measurements indicated that new gold SPEs (Figure 3.7.A) show hydrophobic surfaces (101°), stemming from pasting binder and other post-manufacturing sources of contamination. This WCA decreased to approximately 76°

(Figure 3.7.B) after immobilizing water-soluble molecules like aptamers and proteins. Plasma-treated electrodes showed a significant decrease of WCA to 33° (Figure 3.7.C) by removing the excess binders and oxidation with more oxygen-containing groups.

Table 3.7. Charge transfer resistance (R_{ct}), Water Contact Angle (WCA) and atomic percentage analysis results from XPS of three gold SPEs are reported based on the average value \pm absolute error for three gold SPEs.

Gold SPE samples	R_{ct} (k Ω)	WCA°	Au%	C%	O%	N%
New	1.2 \pm 0.16	101 \pm 3.0	20.1 \pm 0.19	53.8 \pm 1.2	20.5 \pm 0.21	5.6 \pm 0.030
Used	8.3 \pm 1.1	76 \pm 7.6	13.9 \pm 0.13	54.9 \pm 0.48	20.7 \pm 0.040	10.5 \pm 0.30
Plasma cleaned	0.9 \pm 0.030	33 \pm 2.3	22.5 \pm 0.23	43.6 \pm 0.18	25.3 \pm 0.16	8.5 \pm 0.040

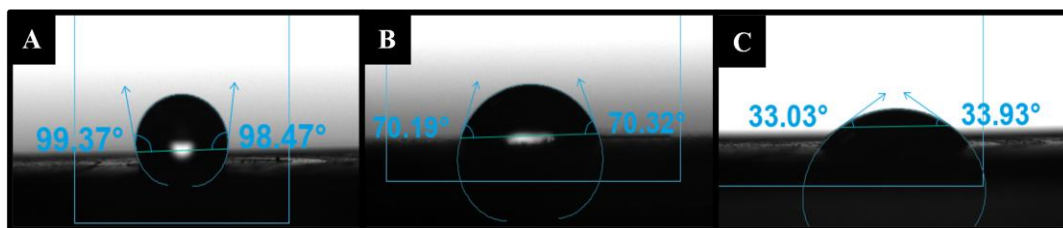


Figure 3.7. Water contact angle of A) new, B) used and C) 10 minutes air plasma cleaned gold SPE.

The Au4f core levels photoelectron spectra exhibited a doublet including the Au4f_{7/2} band at 84.02 eV and Au 4f_{5/2} band at 87.69 eV with spin-orbit splitting energy of $\Delta E = 3.7$ eV binding energy (BE) for the pure metallic gold (Au⁰) which corresponds to the reference (Figure 3.8.A).[139] Although previous studies showed that O₂ plasma resulted in gold oxidation as confirmed by 1 eV shift in the Au4f_{7/2} band, we did not observe such oxidation and shift in gold photoelectron spectra.[119, 140] [141] Moreover, new electrodes

exhibited significant surface carbon C1s peaks as a result of excess pasting binders and post-manufacturing contamination.[60] After plasma treatment, the intensity of the C1s peak decreases due to the removal of excess binders and tethered biomolecules (Figure 3.8.B). DNA-based aptamers and proteins contain amine-based functional groups, which resulted in a significant nitrogen peak from pre-attached biomolecules. The removal efficiency of these biomolecules is evaluated by the reduction of the N1s to the noise level, after plasma treatment (Figure 3.8.C). The reduction in the peak intensity for both carbon and nitrogen after air plasma treatment indicates the removal of excess organic binders and tethered biomolecules with slight oxidation as observed in the increased O1s peak (Figure 3.8.D). Having confirmed the effective removal of organic contaminants and biomolecules by plasma treatment, the electrodes were subsequently characterized in the measurement buffer using the electrochemical methods, CV and EIS. The CV technique identifies the redox peaks of $\text{Fe}(\text{CN})_6^{3-/4-}$, thereby validating the electrochemical process of a reversible redox active molecule and that the peaks occur at predictable potentials. However, CV was avoided in characterizing immobilized aptamer and protein as a result of the intrusive effects of CV in gold-thiol bonds.[34] Self-Assembled Monolayers (SAMs) of thiolated aptamers can detach from the gold surface during voltametric scans.[11] For instance, electrochemical potentials versus Ag/AgCl, more negative than -0.4 V and more positive than -0.1 , can oxidize the thiol bonds.[55] Moreover, SAMs are prone to desorption and structural change during multiple CV scans.[34]

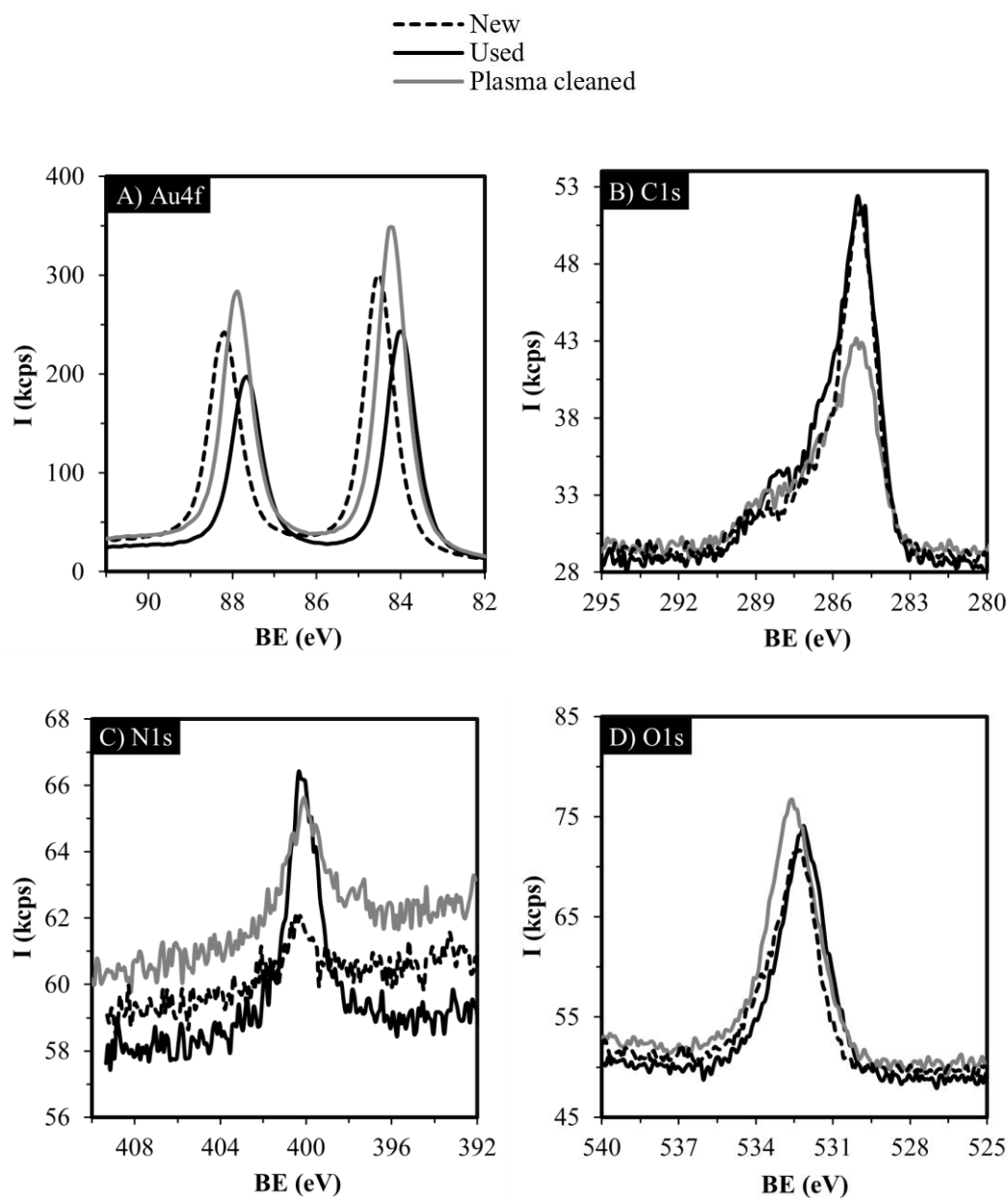


Figure 3.8. Overlaid photoelectron spectra of A) Au4f: Plasma cleaned electrodes exhibited higher intensity through effective surface removal of contaminants, B) C1s: Plasma cleaned electrodes exhibited lower intensity through effective surface removal of excess pasting binders, and C) N1s: Plasma cleaned electrodes exhibited lower intensity through effective surface removal of immobilized biomolecules (aptamers, proteins). D) O1s: The presence of oxygen was mostly related to the organic binders and the bound gold oxide film generated due to air plasma cleaning.

Therefore, to characterize the immobilized aptamers and proteins, EIS was utilized as the primary electrochemical interrogation method. By electropolishing the plasma-treated electrodes in sulfuric acid, the semi-circle in the Nyquist plot of the regenerated gold SPE diminished. In a Nyquist plot, the imaginary component of impedance ($-Z''$) is plotted against the real component of impedance (Z') over a wide range of excitation frequencies (Figure 3.9.A). In the case of electropolished and air plasma regenerated electrodes, the electron transfer was remarkably kinetically facile. In reversible electrochemical systems with fast kinetics, R_{ct} becomes negligible compared to the R_u , and the Z_w dominates across the entire frequency range.[37] In such kinetically facile systems, the current is primarily governed by mass transfer, led to a poorly defined semicircular region. The distinction between the kinetic and mass transfer regions depends on the relative magnitudes of R_{ct} and Z_w . Thus, in electropolished plasma cleaned electrodes, the current is only limited by mass transfer of redox couple,[37] and the semicircular region was not well-defined as depicted in Figure 3.9.A. Hence, the impedance of the regenerated electrode was mainly governed by the Warburg impedance, which was observed as a straight line at 45° on the abscissa. Moreover, the peak phase (ϕ) in the Bode plot was diminished since the impedance was mainly controlled by mass transfer.[37] The Bode plot (Figure 3.9.B) further clarified the frequency-dependent behavior of the regenerated electrodes. The $-\phi$ vs. frequency (Figure 3.9.B) curve showed a diminished phase shift, supporting the hypothesis of kinetically facile electron transfer. In contrast, for new electrodes, the phase shift increased until it reached a maximum, where both resistive and capacitive elements of the Randles circuit affected the system. To analyze these results, an equivalent electrical circuit based on a modified Randles circuit that modeled the electrochemical sensor was

defined (Figure 3.9.C). Consequently, the equivalent Randles circuit of the electrodes was simplified to a circuit consisting of uncompensated resistance (R_u) and Warburg impedance (Z_w) when they were treated with air plasma and electropolishing as shown in Figure 3.9.D. In summary, after plasma treatment and electropolishing, the electrodes exhibited remarkably fast electron transfer kinetics, resulting in negligible R_{ct} compared to R_u . This shift simplified the impedance response, as the interface was dominated by mass transfer processes rather than electron transfer rates. The diminished influence of the C_{dl} and R_{ct} eliminates the semicircular feature in Nyquist plots, leaving the Z_w as the primary determinant of the system's behavior. Consequently, the equivalent circuit reduced to a simple combination of R_u and Z_w , reflecting a kinetically facile and mass-transfer-limited system.

3.4.7. Aptasensor performance of regenerated gold SPE

After the-used gold SPEs were regenerated using plasma treatment, their potential for reuse as aptasensors was evaluated. Aptamer loading efficiency and thrombin binding (aptasensor performance) were assessed by fabricating the aptasensor on the gold SPEs with three modifications, including: 1) New, 2) plasma-regenerated, and 3) E-polished plasma-regenerated gold SPEs. The Nyquist plots obtained from the EIS analysis of the sensors were modelled by the Randles circuit to calculate the R_{ct} of the redox couple. R_{ct} increased upon aptamer immobilization since the aptamer's monolayer impeded the facile electron transfer from the charged redox couple to/from the electrode.[45] This was related to the electrostatic repulsion between the negatively charged phosphate backbone of aptamers and redox couple, along with the densely packed SAMs that create a barrier to diffusion from the bulk solution to the electrode surface.[43]

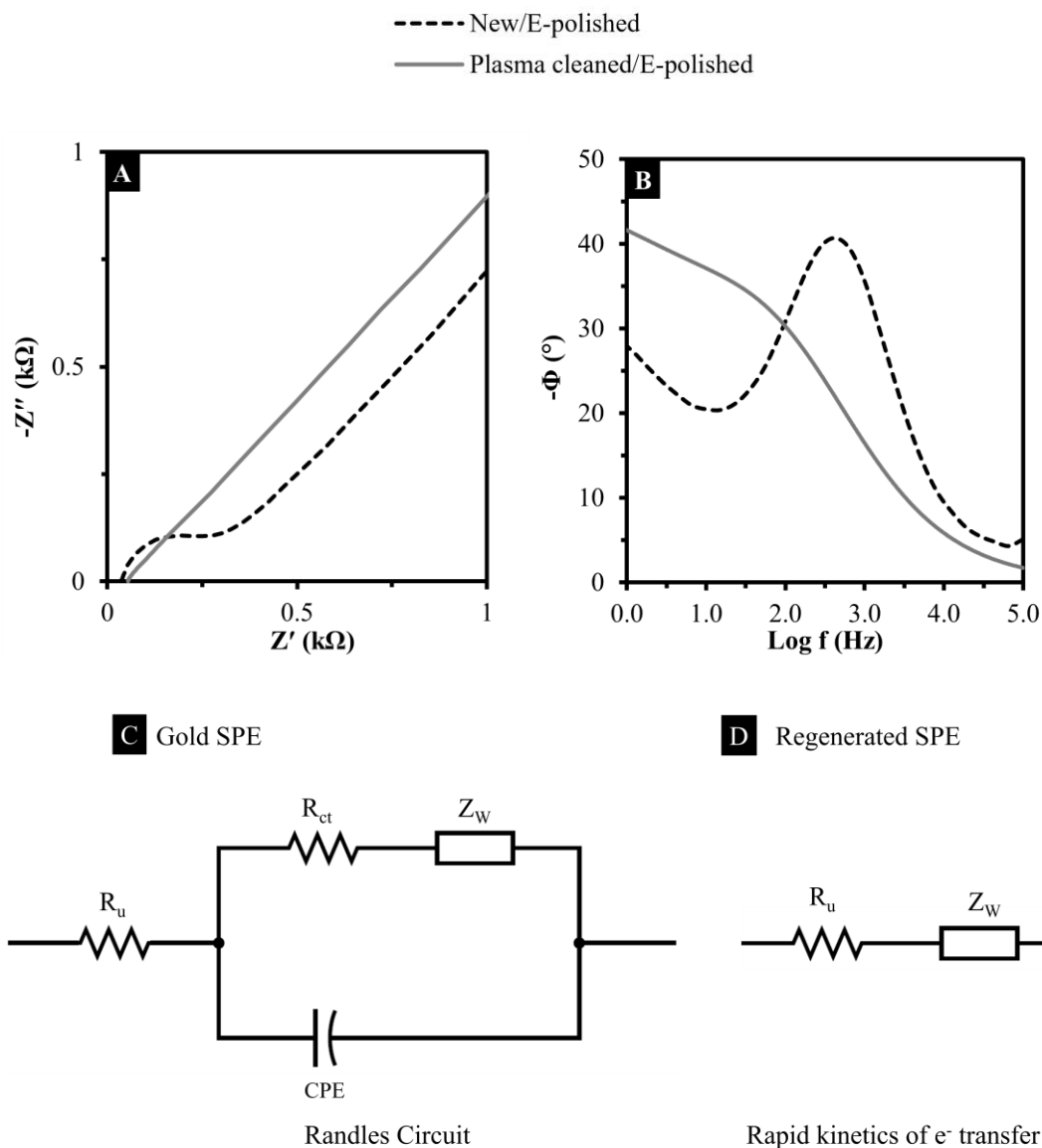


Figure 3.9. Nyquist plot (A) and Bode plot (B) of a new and plasma regenerated electrodes after E-polish. Nyquist plot of plasma regenerated electrode exhibits a straight line and Bode plot exhibits no phase shift peak showing facile electron transfer kinetics. Equivalent Randles circuit of a new electrode (C) and plasma regenerated electrode after electropolish (D). In case of plasma regenerated electrode, due to very fast kinetics of electron transfer, current is only limited by mass transfer and the circuit is simplified to R_u in series with Z_w .

Furthermore, R_{ct} increased significantly after thrombin binding since the bulky protein layer disrupted electron transfer between the electrode and the redox couple.[45] It was observed that the aptamer loading efficiency of the regenerated gold SPEs without E-polishing was lower than that of new gold SPEs as shown in Figure 3.10. Aptamer immobilization led to $3.4 \pm 0.4 \text{ k}\Omega$ for the new gold SPE versus 1.0 ± 0.3 for the plasma-regenerated gold SPEs, with corresponding thrombin binding R_{ct} responses of $7.3 \pm 0.5 \text{ k}\Omega$ and $4.1 \pm 0.9 \text{ k}\Omega$, respectively (see Figure 3.10).

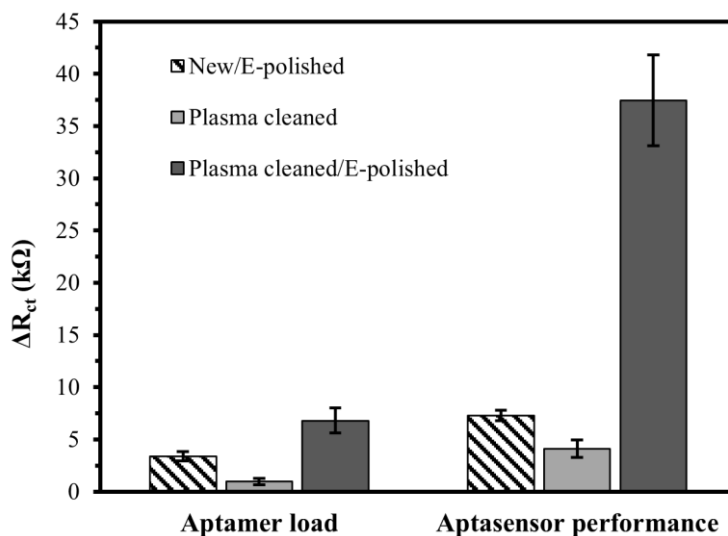


Figure 3.10. Aptamer load efficiency and aptasensor performance of electrodes undergoing different treatments based on the change in charge transfer resistance (ΔR_{ct}). Electrodes undergoing plasma cleaning, coupled with E-polishing, exhibit the highest aptamer load and aptasensor performance due to effective surface regeneration. Error bars are based on three individually tested gold SPEs for each condition.

Consequently, regenerated SPEs were E-polished by CV in H_2SO_4 to reduce the gold atoms and to improve thiol-gold self-assembled monolayer formation.[50, 60, 122] After E-polishing, aptamer immobilization and aptasensor performance improved substantially, with the E-polished plasma-regenerated SPEs increasing the R_{ct} to $6.8 \pm 1.2 \text{ k}\Omega$ by aptamer

immobilization and a significant increase in R_{ct} by thrombin binding to $37 \pm 4 \text{ k}\Omega$ (Figure 3.10). The enhancement in aptamer loading and thrombin binding was likely due to the strong regeneration and cleaning efficiency of air plasma, which effectively removes biomolecules and post-manufacturing surface contamination. The enhanced thrombin sensing performance was evident in the Nyquist plot of the electropolished plasma-regenerated electrodes, which showed a significantly larger semicircle compared to the new electrodes (Figure 3.11). In a previous study, similar improvements in electrochemical properties were observed in screen-printed carbon electrodes, where low-level oxygen plasma effectively removed the non-conductive binder covering the graphite grains on the electrode's surface.[142]

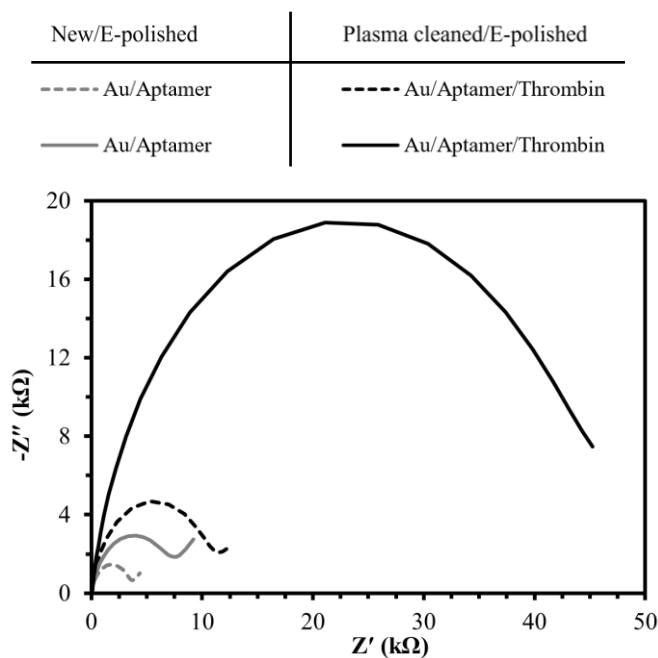


Figure 3.11. Nyquist plots of gold SPE-based aptasensor (5 μM aptamer, 50 nM Thrombin). Air plasma-treated electrodes exhibit significant charge transfer resistance upon thrombin incubation.

3.4.8. Effects of repeated cycles of plasma cleaning on gold SPE

Recycling the electrodes, even once, could reduce the environmental impact and cost of biosensor fabrication. We investigated whether the electrode remains integrated and functional after three cycles of air plasma cleaning. The impact of successive plasma cleaning cycles on the electrochemical properties of electrodes was investigated, with a particular focus on R_{ct} and immobilization efficiency. The process involved exposing the electrode to a 25 mM Mercaptohexanol (MCH), followed by air plasma cleaning and repeated E-polishing. We adapted the methodology from Raiber et al., where the removal of hexadecanethiolate by H_2 plasma from a gold electrode was evaluated by Ellipsometry.[63] In our method, we observed that the new electrodes showed a R_{ct} response of 0.37 ± 0.03 k Ω and, after MCH backfilling R_{ct} increased to 1.2 ± 0.7 k Ω . The high standard deviation observed in the R_{ct} following MCH immobilization, as reported for three electrodes, might be attributed to the fact that not all electrodes exhibit similar electrochemical behavior. This variability could stem from excess binder in the screen-printing process and contamination that occurred during manufacturing.[143] Additionally, the self-assembled monolayer (SAM) formation of MCH was performed for only 1 hour in a humidity chamber. Although it has been shown that SAMs can form almost immediately upon incubation, they may take over 24 hours to reorganize, leading to some variability in results.[144] The first plasma cycle reduced the R_{ct} to near-zero while the first plasma cycle followed by MCH increased the R_{ct} to 1.4 ± 0.3 k Ω . The second plasma cycle again showed near-zero R_{ct} and the second plasma cycle with MCH incubation increased the R_{ct} to 1.0 ± 0.1 k Ω . Same pattern was observed after the third plasma cycle with a near-zero R_{ct} of the plasma-cleaned electrodes (Figure 3.12). Improvements in the reproducibility of the

immobilization process were noted after each cycle, reflected in a decrease in the relative standard deviation (RSD) from 37% to 12%. This enhancement may be linked to the cleaned high surface area of the gold electrodes due to plasma cleaning, which facilitates MCH SAM formation compared to untreated electrodes. To further assess the structural and compositional integrity of the printed gold microparticles following plasma treatment, SEM imaging was conducted, which revealed no significant changes in the morphology or surface structure of the gold particles (Figure 3.13).

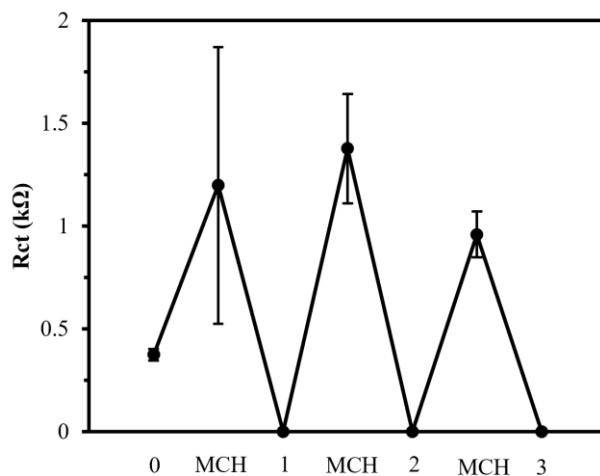


Figure 3.12. R_{ct} measurements after repeated formation and removal of MCH SAM by air plasma. Error bars are based on three individually tested gold SPEs for each condition.

3.5. Conclusion

Gold SPEs were regenerated by air plasma cleaning to remove surface-attached ssDNA-based aptamer and thrombin. XPS and WCA measurement results show that air plasma cleaning creates an oxidized surface with high hydrophilicity, while new electrodes have significant carbon contamination and are hydrophobic. When the plasma-regenerated surfaces are electropolished in sulfuric acid, surface oxide films are reduced.

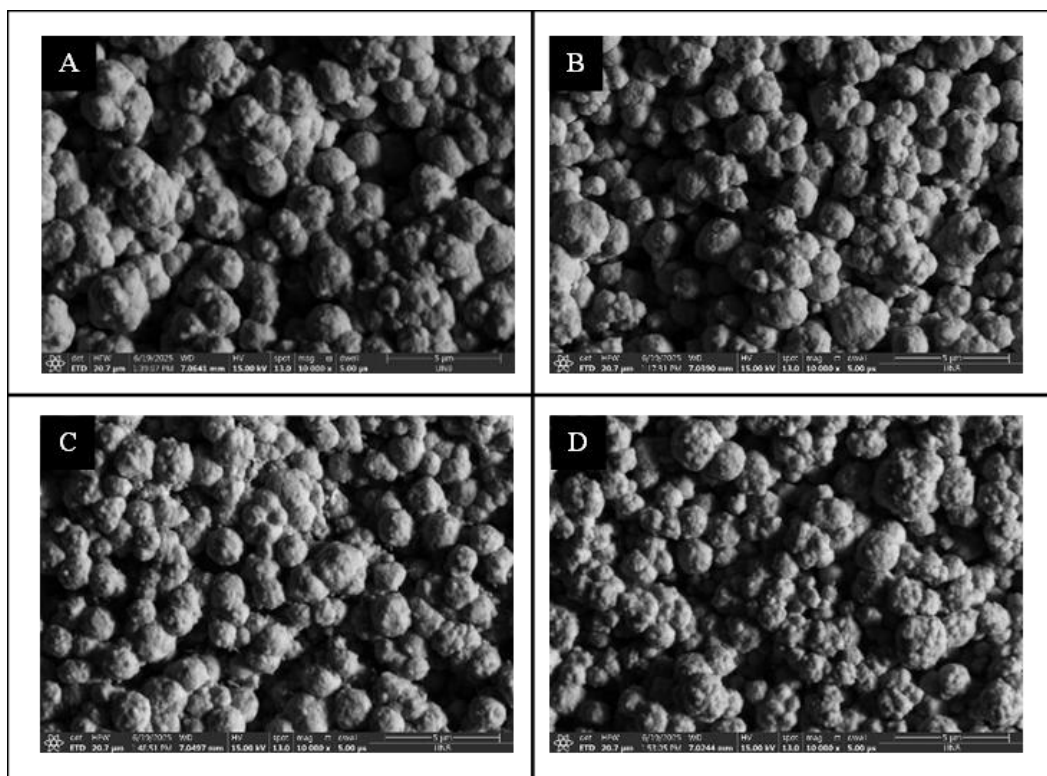


Figure 3.13. SEM images of the working gold electrode A) without, B) 1 cycle, C) 2 cycles, and D) 3 cycles of air plasma cleaning reveals no morphological/structural changes in the printed gold microparticles.

This process results in very efficient electron transfer kinetics, as evidenced by a straight-line Nyquist plot without a semi-circle and the absence of a peak phase in the Bode plot since the electron transfer is only limited by mass transfer diffusion. Additionally, air plasma-regenerated electrodes undergoing electropolishing exhibit higher aptamer load and improved aptasensor performance compared to new electrodes as a result of effective contaminant removal and a reduced gold surface. However, mass transfer diffusion decreases post-treatment, as shown by both Randles–Sevcik and Warburg impedance analyses. This suggests surface changes that hinder diffusion, warranting further investigation to understand and optimize this trade-off. Moreover, with each plasma treatment cycle, charge transfer resistance decreases to near-zero. However,

immobilization efficiency declines after the second cycle. In summary, air plasma cleaning enhances electrode performance through efficient contaminant removal and contributes to sustainable biosensor development by enabling gold SPE reuse.

3.6. Study limitations

This study utilized a single model of commercial screen-printed gold electrodes. As a result, the findings need to be validated with additional electrode types and suppliers. The analytical characterization was limited to a proof-of-concept demonstration of thrombin sensing, focusing on a fixed aptamer density and thrombin concentration. Comprehensive analytical performance metrics, such as the limit of detection, were not determined. Moreover, electrode stability was evaluated only after up to three plasma cleaning cycles, leaving long-term operational and storage stability untested.

3.7. Future work

Future research should validate plasma regeneration and sensing performance across a wider range of electrode materials, such as alternative gold electrodes, carbon, and indium tin oxide. Extended cycling studies are needed to assess the number of plasma regeneration cycles until electrode failure or significant degradation occurs. A comprehensive validation of thrombin sensing should include varying aptamer densities and analyte concentrations, along with selectivity testing against potential interferents and real sample matrices. Surface chemical characterization using XPS should focus on sulfur speciation and other relevant surface chemistries to correlate chemical changes with sensor performance. Lastly, it is essential to evaluate the immobilization and activity retention of other recognition elements and enzymes on plasma-regenerated electrodes for broader biosensing applications.

3.8. Author contributions

All authors contributed to the preparation of this manuscript. Specific contributions are as follows: S.A. conceived of the original idea. S.A. planned the experiments. S.A., C.T., analyzed the data. S.A. conducted the experiments and wrote the manuscript. S.A., C.T., S.F., M.B., and A.I. edited the manuscript. S.A., and A.I., and M.B. supervised and acquired funding for the project. All authors discussed the results and contributed to the final manuscript.

3.9. Acknowledgements

This work was carried out with financial support of the New Brunswick Innovation Foundation NBIF (Project No. EP-0000000155) & New Brunswick Health Research Fund NBHRF (Project No. 0000000045) and MITACS Globalink Research Award Application Ref. IT36728. We thank Professor Vicki Meli (Mount Allison University) for access to plasma equipment, Steven Cogswell (UNB) for SEM analysis, and Kostadinos Tsoutas (University of Sydney) for his valuable advice.

3.10. Conflict of interest

The authors declare no conflict of interest.

4. Towards sustainable and reagentless electrochemical biosensor fabrication: immobilization of linker-free DNA aptamer on carbon electrodes by plasma enhanced chemical vapor deposition

S. Ardalan, C.T.H. Tran, S.T. Fraser, M. Bilek, A. Ignaszak. Manuscript under review.

4.1. Abstract

A critical step in fabricating a heterogeneous biosensor is immobilizing the biorecognition element on the sensing substrate. This step is conventionally achieved through self-assembled monolayer formation from thiol-modified capture probes on precious metals or through chemical reactions using carbodiimide, glutaraldehyde crosslinking, or click chemistry. However, these methods all share a common characteristic: they involve wet chemical reactions that often require multiple steps. Is it feasible to attach the capture probe covalently without relying on such wet chemistries? We evaluated a plasma-enhanced chemical vapour deposition method that saturates a carbon electrode surface with long-lived radicals, allowing for the direct covalent tethering of linker-free DNA aptamers to the electrode without chemical coupling agents. The functionalized electrodes demonstrated binding specificity toward the model target protein, thrombin. Furthermore, the plasma-deposited layer preserved the electrode's conductivity and eliminated the requirement for additional chemical activation steps, thereby reducing reagent waste and processing time. This approach offers a reagent-free, scalable, and sustainable alternative for electrochemical biosensor fabrication.

4.2. Introduction

The evolution of electrochemical biosensors has been fundamentally shaped by advances in biomolecule immobilization techniques, which serve as the critical interface between biological recognition elements (capture probe) and transducer surfaces.[145, 146] From the pioneering glucose biosensors of the 1960s to contemporary nanoscale devices, immobilization chemistry has progressed through multiple generations of innovation, each addressing specific challenges related to stability, selectivity, and signal transduction efficiency.[147] The historical development of immobilization techniques in electrochemical biosensors reveals a continuous evolution from simple physical entrapment methods as seen in antibody adsorption in cellulosic substrates in Lateral Flow Assays (LFA) or on polystyrene microplates in Enzyme-Linked Immunosorbent Assay (ELISA) to sophisticated chemical and biological recognition systems.[8] Thiol self-assemble monolayer (SAM) formation on precious metals provides robust and versatile platforms for surface functionalization.[148] Carbodiimide crosslinker chemistry (EDC/NHS) offers precise control over protein conjugation with improved stability.[149] Glutaraldehyde crosslinking, despite its long history of use, continues to reveal new mechanistic insights that inform optimal reaction conditions.[146] The biotin-streptavidin system demonstrates the power of biological recognition while highlighting the importance of understanding interference mechanisms in practical applications.[150] While most commercial biosensors still utilize conventional immobilization strategies, there is increasing momentum toward adopting dry plasma techniques for covalent biomolecule attachment.[151-153] For instance, Gleize et al. studied two types of energetic ion plasma known as plasma immersion ion implantation (PIII) and plasma-activated coating (PAC)

on polystyrene microplates.[151] The introduced methods involved one-step linker-free activation of microplates by energetic ions from plasma for covalent immobilization of DNA and protein. They confirmed that the plasma treatment generated long-lived radical-activated surfaces, characterized by X-ray photoelectron spectroscopy (XPS) and electron spin resonance. Tran et al. conducted similar experiments on PAC-treated borosilicate glass to immobilize proteins.[153] Such dry plasma-enhanced chemical vapor deposition techniques offer a promising alternative, providing reagent-free, environmentally sustainable, and scalable solutions for next-generation biosensor fabrication.[154] PAC technology addresses this gap by enabling direct, reagent-free covalent attachment of biomolecules through plasma-generated surface radicals.[151-153]

To our knowledge, no studies have specifically examined the modification of conductive materials, particularly electrodes used in electrochemical setups, through the application of PAC treatment. In this work, we extend the application of PAC to electrochemical biosensors, using thrombin-binding aptamers as a conceptual model. Our approach demonstrates the feasibility and effectiveness of PAC for fabricating high-performance, reagent-free electrochemical sensors, potentially setting a new standard for bioreceptor immobilization in biosensing technologies. The main objective is one-step reagent-free covalent immobilization of a DNA capture probe via PAC modification on a screen-printed carbon electrode (SPCE). The capture probe is a single-stranded DNA (ssDNA) probe, i.e., aptamer, toward detecting a serine protease, i.e., thrombin. The objectives' breakdown is as follows: 1. PAC modification of SPCE using capacitively coupled radio frequency (RF) power and a negative pulsed bias generated by a pulse generator. This process involves two main steps. I) Surface activation by argon plasma to facilitate coating adhesion and

removal of surface contamination. II) PAC deposition of a reactive gas mixture of acetylene, nitrogen, and argon with plasma discharge and a negative bias voltage. 2. Immobilization of an ssDNA aptamer against thrombin with a poly adenine linker to promote DNA attachment to the plasma-treated surface with the correct orientation.[130, 155] 3. Thrombin incubation: The immobilized aptamer binds the heparin binding site of thrombin with high affinity which increases the electrode's charge transfer resistance.[45] The outcomes contribute significantly to biosensor technology and surface science by developing a novel, one-step, reagent-free method for covalent immobilization of DNA capture probes onto electrochemical substrates using PAC deposition.

4.3. Experimental

4.3.1. Materials

Potassium hexacyanoferrate(II) trihydrate ($\text{Fe}(\text{CN})_6^{4-}$; 98.5%), potassium hexacyanoferrate(III) ($\text{Fe}(\text{CN})_6^{3-}$; 99%), ethylenediaminetetraacetic acid (EDTA; 98.5%), tris(hydroxymethyl)aminomethane hydrochloride (Tris.HCl; >99%), sodium hydroxide (NaOH; 98%, pellets), custom DNA oligo (aptamer; HPLC purified), and thrombin from human plasma (250 units, lyophilized powder, $\geq 2,000$ NIH units/mg) were purchased from Sigma Aldrich. Screen Printed Carbon Electrode (SPCE, 3×4 mm working electrode) was purchased from Pine Research (USA).

All solutions were prepared with Milli-Q water. Except for protein and aptamer solutions, which were purchased in purified, DNase/RNase, and protease-free form, all solutions were filtered using vacuum driven filters (Stericup Quick Release, Sigma Aldrich). Aptamer and protein solutions were stored in low-binding tubes to reduce stickiness to the walls of the microtubes (DNA/Protein LoBind Tubes, Eppendorf). Low-retention pipette

tips (ART, Thermo Fisher Scientific) were used for pipetting to minimize DNA/protein binding to pipette tips. All solutions, except $\text{Fe}(\text{CN})_6^{3-}$, $\text{Fe}(\text{CN})_6^{4-}$, H_2SO_4 , protein, and aptamer solutions, were sterilized by autoclaving at 121°C for 30 minutes, with a total cycle time of 1 hour.

A 10X stock solution of tris-buffered saline (TBS) buffer was prepared by dissolving Tris.HCl and NaCl and adjusting the pH to 7.4 with NaOH with final concentration of 200 mM Tris and 1500 mM NaCl. An electrochemical measurement buffer was prepared by mixing as-prepared TBS, MgCl_2 and $\text{Fe}(\text{CN})_6^{3-/4-}$ stock solutions with the final concentrations of 1X TBS, 1 mM Mg^{2+} , and 2 mM $\text{Fe}(\text{CN})_6^{3-/4-}$. A folding buffer was prepared by mixing as-prepared TBS, and Mg^{2+} and $\text{Fe}(\text{CN})_6^{3-/4-}$ stock solutions with the final concentrations of 1X TBS and 1 mM MgCl_2 .

ssDNA Aptamer solution. A 29-nucleotide ssDNA thrombin binding aptamer was chosen from the original research by Tasset et al.[130] A 20-poly-Adenine tailed HPLC purified lyophilized aptamer was purchased from Sigma-Aldrich with the sequence of 5'-AAAAAAAAAAAAAAAAAAAAAAAAAGTCCGTGGTAGGGCAGGTTGGGGTGACT-3'. Aliquots of a 100 μM stock aptamer solutions were prepared in LoBind DNA microtubes, diluted with water and stored at -80°C . Prior to immobilization on electrodes, aptamer stock solution aliquot was thawed rapidly at 37°C and annealed at 90°C for 5 minutes and slowly cooled down to room temperature ≈ 30 minutes.

Protein solution. Thrombin (250 units) was purchased from Sigma Aldrich (>2000 units/mg). Each unit corresponds to 0.324 μg , totalling 81 μg of thrombin. The molecular weight (Mw) of thrombin is 37.4 kDa. To calculate protein concentration the equation $\mu\text{M} = (\mu\text{g}/\text{mL}) / \text{Mw in kDa}$ was used.[131] The glass vial containing thrombin was first

centrifuged at 4°C at 3000 rpm to ensure complete settling of the thrombin. The thrombin containing vial was then transferred to an ice bath and thrombin was dissolved in cold Milli-Q water to a final concentration of 1 μ M. The dissolved thrombin was then transferred to LoBind protein microtubes and stored in the freezer at -80°C. Prior to binding tests, thrombin stock solution aliquot was thawed rapidly at 37 °C and then left at room temperature for \approx 10 min. It was further diluted to 100 nM and 50 μ L of it was pipetted on the working electrode for 30 minutes at room temperature in a humidity chamber followed by 3 times 200 μ L rinsing by the folding buffer.

4.3.2. Methods

Electrochemical characterization. A compact potentiostat (PalmSens4) was used for electrochemical analysis of SPCEs. Results were analyzed by an electrochemical analysis software (PStrace, PalmSens). All measurements were performed in a dark box to minimize light exposure. A Teflon cap was designed to slide the SPCE inside the glass cell with two narrow holes for the N₂ gas inlet and outlet. Electrochemical Impedance Spectroscopy (EIS) was performed to characterize charge transfer processes at the electrode interface by applying an alternating voltage of 5 mV and a biased DC potential at the open circuit potential (OCP) vs Ag/AgCl reference electrode with a frequency range from 0.1 Hz to 100 kHz in the measurement buffer solution. Cyclic voltammetry (CV) was scanned twice in the measurement buffer solution to characterize the redox peaks within a potential window from -0.2 to 0.6 V at a scan rate of 50 mV.s⁻¹ and a step of 5 mV.

Plasma activated coating of SPCE. Electrodes were sandwiched between two polystyrene films leaving only the working electrode (WE) exposed to plasma. They were mounted on a stainless-steel sample holder and electrically connected to a pulsed bias

generator (RUP6, GBS Elektronik). The holder was loaded into a chamber of a capacitively coupled RF plasma system (13.56 MHz, Eni OEM-6), and the chamber was evacuated to 5×10^{-5} Torr using rotary and turbo pumps. An argon plasma pretreatment was applied to enhance coating adhesion (Ar at 37 sccm, 75–80 mTorr, 75 W RF power, -500 V pulsed bias at 3 kHz, 20 μ s pulse width) for 2 minutes. Following this, a gas mixture of acetylene (1 sccm), nitrogen (10 sccm), and argon (3 sccm) was introduced. After 5 minutes of gas stabilization, PAC deposition was performed for 15 minutes at 110 mTorr, 50 W RF power, and a -500 V pulsed bias. After sample removal, the chamber was cleaned with oxygen plasma (= O₂ at 50 sccm, 1.5×10^{-1} Torr, 100 W RF power, no bias) for 30 minutes. SPCEs were kept at ambient condition to allow surface radicals to react with atmospheric oxygen, completing the functionalization process. The images of each step of plasma treatment are depicted in Figure 4.1.

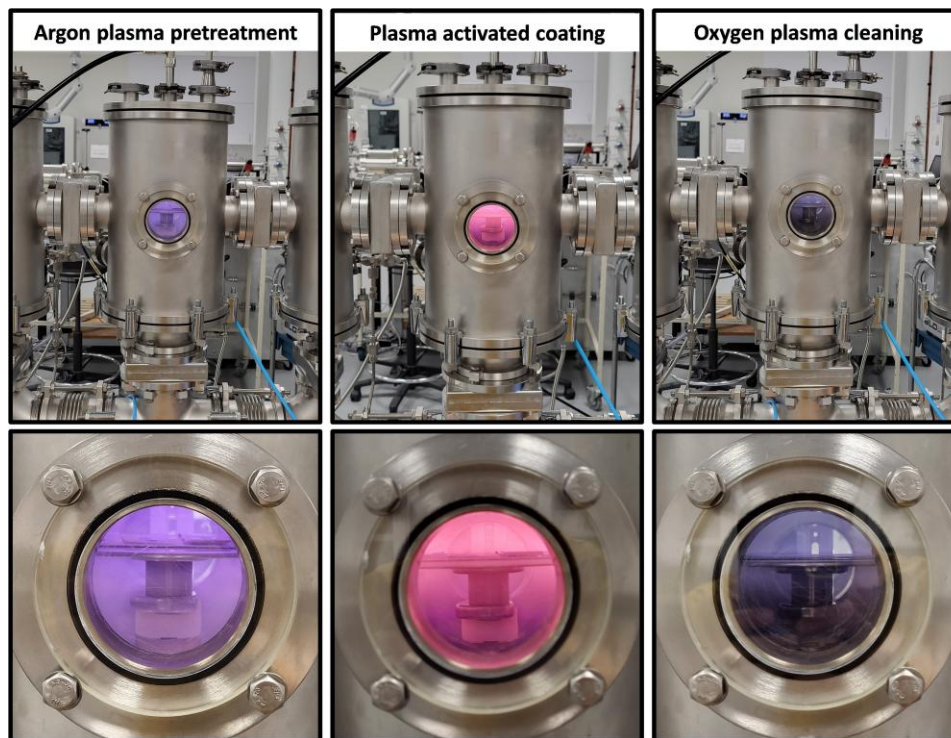


Figure 4.1. Plasma Activated Coating (PAC) treatment of carbon electrodes.

Surface chemistry. An X-ray Photoelectron Spectroscopy (XPS) instrument (K-alpha⁺, Thermo Fisher Scientific) with a monochromatic Al K α X-ray source was used to characterize the surface chemistry of SPCE. Ten survey scans and five high-resolution scans of major elements (carbon, oxygen, nitrogen, and phosphorus) were taken on each sample for comparison. Results were analyzed by surface analysis software (Avantage Data System, Thermo Fisher Scientific)

4.4. Results and discussion

4.4.1. XPS characterization

The amount of the ssDNA aptamer that is immobilized on PAC-treated carbon electrode depends on the surface chemistry and orientation of biomolecules on the treated surface. It has been shown PAC treatment deposits a polymer coating with a high concentration of long-lived radicals on surfaces resulting in a hydrogenated amorphous carbon nitride layer from a mixture of acetylene and nitrogen gases. [151] To determine the effect of PAC treatment on aptamer immobilization, the chemical properties of treated electrodes were studied using XPS. Specifically, to assess changes in key surface elements after different treatments, we analyzed XPS peak areas for phosphorus (P), nitrogen (N), oxygen (O), and carbon (C) as depicted in Figure 4.2. A-D, respectively. Phosphorus, tracked via the P2p peak, is a marker for ssDNA aptamer immobilization.[156] It was previously studied that a rich adenine spacer in an acidic medium enhances ssDNA immobilization on PAC-treated surfaces.[155] After a 1-hour aptamer incubation, the P2p signal on PAC-treated surfaces increased by \approx 6-fold compared to the SPCE/Aptamer control. This substantial rise confirms that PAC treatment greatly enhances ssDNA aptamer immobilization. For nitrogen (N1s), the unmodified SPCE baseline increased by \approx 1.2-fold after aptamer

immobilization, because of the DNA's nitrogen content.[157] Relative surface N1s atomic percentage of SPCEs increased \approx 4-fold after PAC treatment. Meanwhile, the %N1s of PAC/Aptamer electrodes reached a \approx 5.2-fold rise relative to the unmodified SPCE. This trend demonstrates that both PAC and aptamer contribute to nitrogen enrichment and the introduction of nitrogen-containing functional groups.[151] A bar chart as shown in Figure 4.3 provides a clear comparison of the surface atomic percentage values of surface nitrogen and phosphorus. Oxygen (O1s) content increased only slightly (\approx 1.0–1.3-fold) across treatments, with the highest values observed for PAC/Aptamer surfaces. These modest increases are attributed to the oxidation of PAC-treated electrodes. Upon exposure to air, radicals on the treated surfaces react with oxygen in the air to form oxygen-containing groups as reported elsewhere.[151]

4.4.2. Electrochemical characterization

To assess the electrochemical behavior of the modified electrodes, cyclic voltammetry (CV) was conducted in the measurement buffer solution containing TBS 1X, 1 mM Mg^{2+} , and 2 mM $\text{Fe}(\text{CN})_6^{3-/4-}$ on four surface conditions: unmodified SPCE, SPCE/Aptamer, PAC- treated SPCE (SPCE/PAC), and PAC-treated SPCE with aptamer immobilization (SPCE/PAC/Aptamer) and the results are shown in Figure 4.4. The key parameters including the oxidation peak current, oxidation potential, reduction potential, and peak-to-peak separation are shown in Table 4.1. The unmodified SPCE served as the baseline, exhibiting moderate redox activity. Upon aptamer immobilization, the SPCE/Aptamer electrode showed a 41.6% decrease in oxidation current and a 50.0% increase in peak-to-peak separation. These changes indicate that electron transfer was hindered due to the random adsorption of aptamers within the binder matrix, which introduces steric barriers.

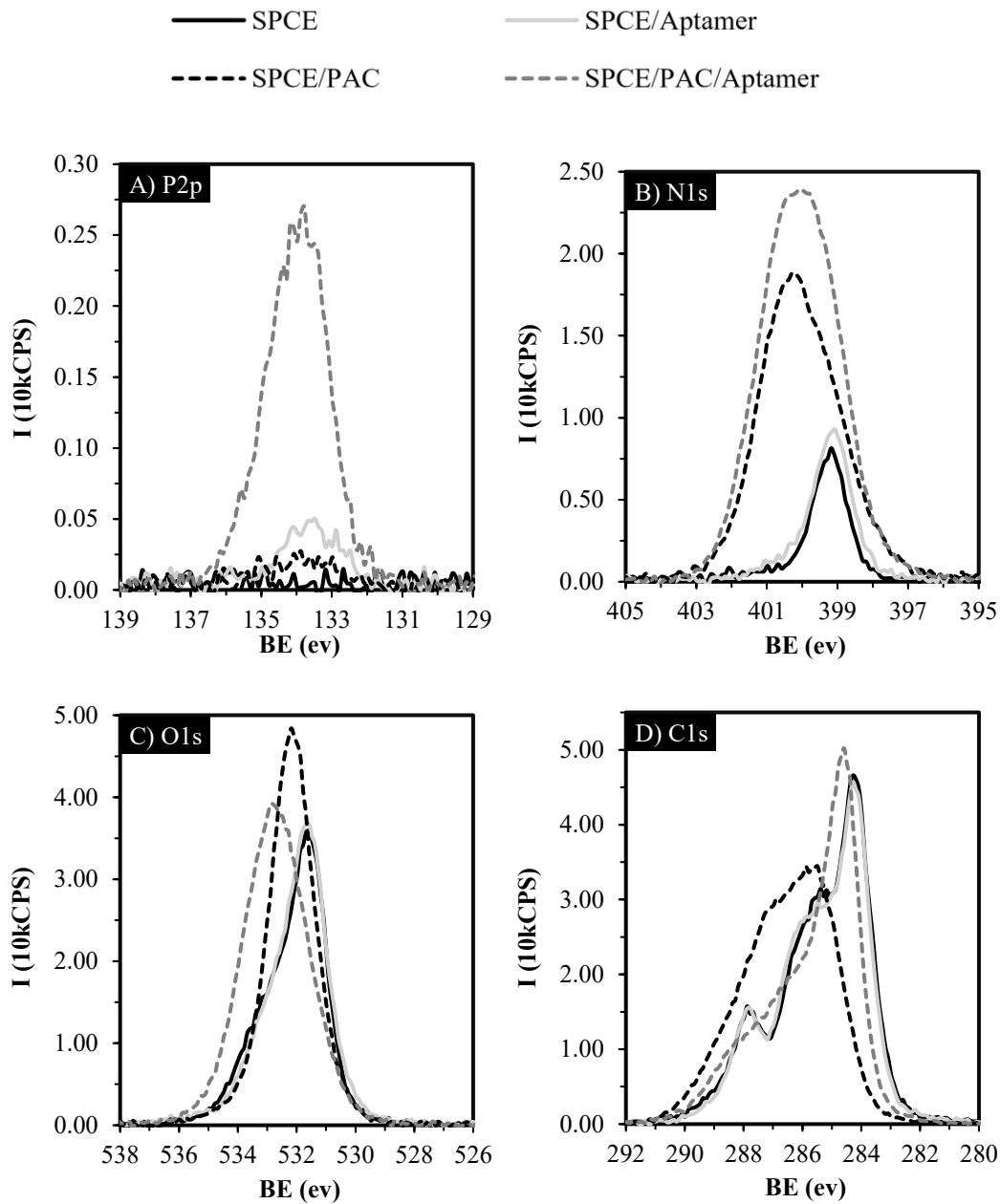


Figure 4.2. Overlaid high-resolution XPS spectra of (A) P2p, (B) N1s, (C) O1s, and (D) C1s regions for surfaces with different treatments on SPCEs.

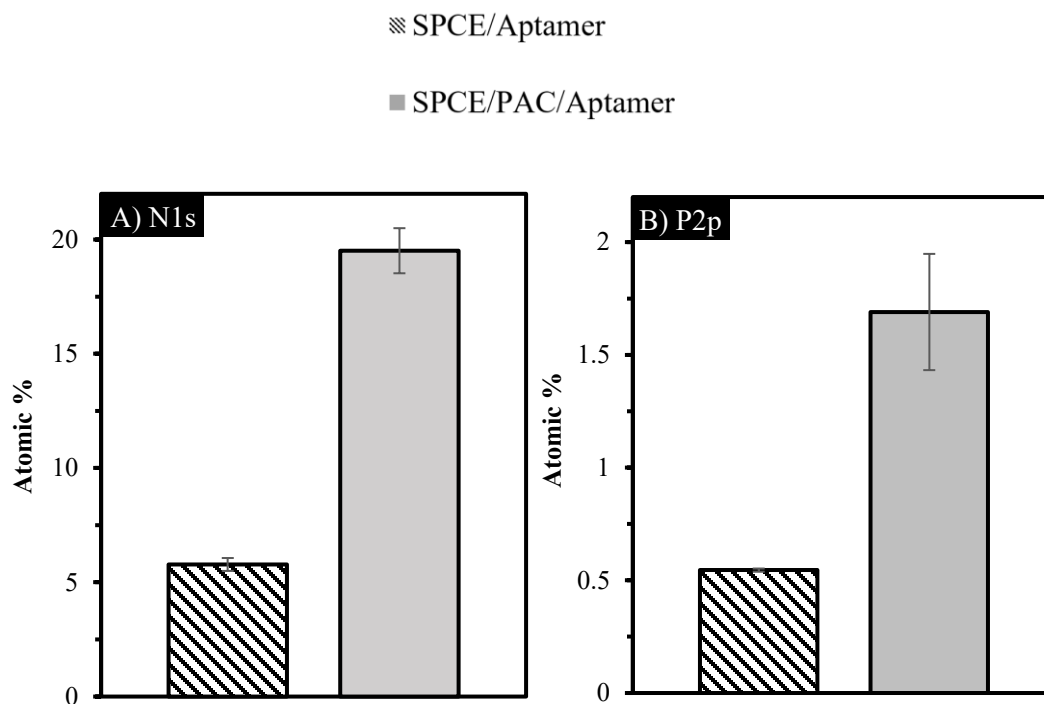


Figure 4.3. Bar chart comparing atomic percentage of aptamer-immobilized electrodes from XPS analysis; A) N1s: nitrogen and B) P2p: phosphorus of electrodes without and with PAC modification. Error bars are based on the XPS analysis of three individual SPCEs.

Additionally, the oxidation potential increased by 21.7%, while the reduction potential dropped by 80.0%, reflecting a reduced reversibility from an a $1e^-$ transfer in an ideal Nernstian system. PAC modification led to a notable improvement in electrochemical performance. Compared to the unmodified SPCE, the PAC-treated electrode showed a 16.8% increase in oxidation current and an 11.1% decrease in peak separation, indicating enhanced electron transfer due to the removal of surface contaminants and exposure of more electroactive sites. In contrast, the SPCE/PAC/Aptamer electrode exhibited 45.7% decrease in oxidation current, but only a 16.7% increase in peak separation. This suggests that while the aptamer layer on the PAC-treated surface is denser, it is more uniformly distributed and better integrated with the electrode's interface. With regards to the

SPCE/PAC/Aptamer sets of electrodes, the oxidation potential decreased slightly by 4.4%, and the reduction potential again dropped by 80.0%, indicating that the PAC surface maintains a relatively favorable electrochemical environment after aptamer immobilization. Overall, these relative changes suggest that PAC treatment improved the consistency and efficiency of aptamer immobilization while minimizing disruption to electron transfer.

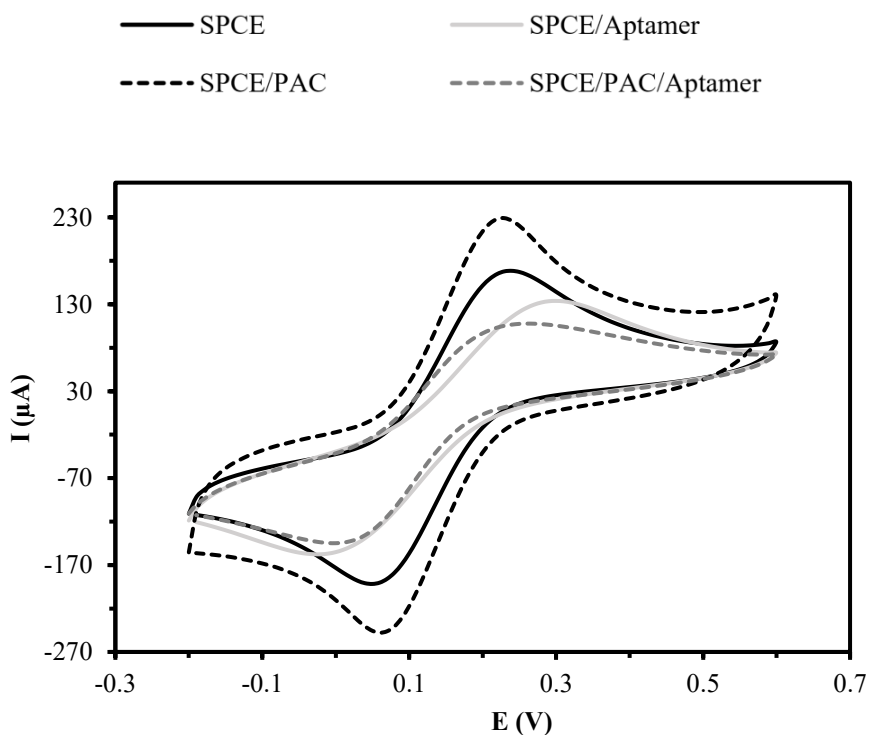


Figure 4.4. Cyclic voltammograms (CV) of SPCE with different surface modifications. The overlay demonstrates the enhancement of electrochemical response with PAC treatment and the subsequent decrease in peak currents following aptamer immobilization. Potential values are vs Ag/AgCl paste reference electrode in the measurement buffer solution (TBS 1X, 1 mM Mg^{2+} , and 2 mM $\text{Fe}(\text{CN})_6^{3-/4-}$).

Table 4.1. Peak characteristics in CV experiments conducted on electrodes that have undergone different surface treatments.

Parameters	SPCE	SPCE/Aptamer	SPCE/PAC	SPCE/PAC/Aptamer
$I_{\text{peak}_{\text{ox}}}$ (μA)	173	101	202	94
E_{ox} (V)	0.23	0.28	0.22	0.22
E_{red} (V)	0.05	0.01	0.06	0.01
ΔE_{peak} (V)	0.18	0.27	0.16	0.21

In PAC-treated electrodes, the electron transfer kinetics were significantly enhanced, making the electrode's impedance primarily controlled by mass transfer limitations. The results of electrochemical impedance spectroscopy (EIS) analysis of SPCEs with different modifications are provided in Table 4.2. In the PAC-modified electrodes, the semi-circle, which represents the charge transfer resistance, was nearly absent, indicating efficient electron transfer at the electrode surface.[37] However, upon aptamer immobilization, the PAC/Aptamer electrode exhibited a re-emergence of the semicircle in the Nyquist plot, with a charge transfer resistance of 118 Ω . This increase is due to the aptamer layer acting as a resistive barrier. The effective capacitance drops from 56.5 μF to 43.6 μF , indicating reduced electroactive surface area and increased thickness since $C \propto A/d$. In contrast, the unmodified SPCE showed a much higher baseline R_{ct} of 446 Ω and a smaller relative change in the R_{ct} after aptamer immobilization to 910 Ω . The capacitance dropped from 101.05 μF to 17.93 μF , indicating a significant reduction in accessible surface area due to the randomly attached aptamers on the electrode's surface (Table 4.2).

Table 4.2. EIS parameters of SPCE at different modification stages.

Electrode	R_u (Ω)	R_{ct} (Ω)	Q (μT)	n	C (μF)
SPCE	101.1	446.5	48.4	0.673	101.05
SPCE/Aptamer	94.19	910.4	11.5	0.713	17.93
SPCE/PAC	99.8	25.7	14.6	0.81	56.5
SPCE/PAC/Aptamer	96.0	117.6	11.5	0.83	43.6

In PAC-treated electrodes, the kinetic of electron transfer is so facile that the impedance was solely governed by mass transfer limits and the peak phase diminished, as shown in Figure 4.5.[37] Upon aptamer immobilization, the phase peak re-emerges due to the aptamer behaving as a resistive element, thereby introducing a charge transfer resistance (Figure 4.5.A) that significantly induced a maximal phase shift (Figure 4.5.B).[46] A similar phenomenon was observed in unmodified electrodes; however, the change in phase shift was less pronounced compared to that observed in PAC-treated electrodes. Overall, these results show that PAC modification significantly reduces charge transfer resistance and enhances electron transfer kinetics.

4.4.3. Thrombin biosensing on the PAC-modified electrodes

The data in Table 4.3 reveal systematic changes in electrical parameters as the carbon electrodes were functionalized, providing insight into molecular interactions and electron transfer dynamics. R_{ct} increased from 26 Ω (baseline SPCE/PAC electrode) to 314 Ω after

thrombin binding—a ≈ 12 -fold rise—directly correlating with sequential addition of the aptamer, BSA blocking agent, and thrombin.

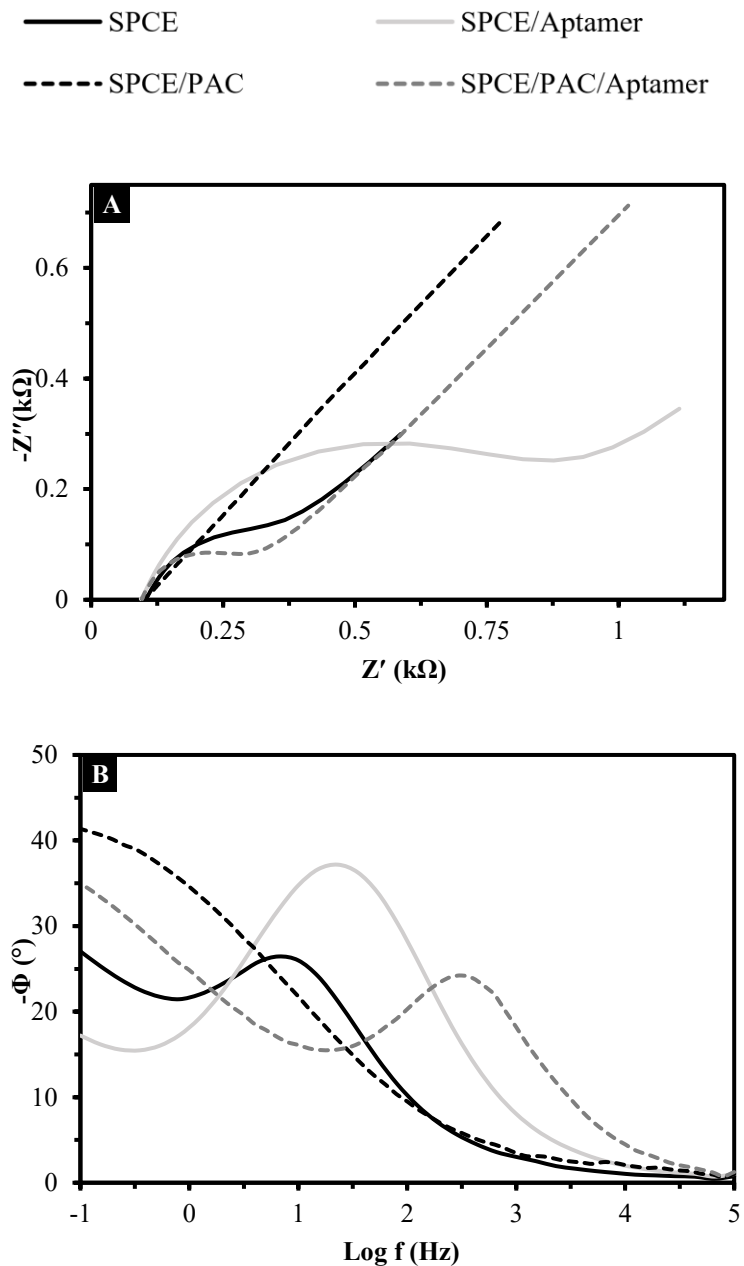


Figure 4.5. EIS analysis of SPCE electrodes at different modification stages. (A) Nyquist plots and (B) Bode phase angle plots of PAC-treated electrodes.

The resulting Nyquist and Bode plots are depicted in Figure 4.6 which shows that each biomolecular layer acted as an insulating barrier, progressively hindering electron transfer at the electrode–electrolyte interface. Capacitance decreased from 56.5 μF (baseline) to 34.3 μF post-thrombin, reflecting reduced charge storage due to the insulating biomolecular layers. The sensor’s response to thrombin is quantified by a 19% increase in R_{ct} compared to the BSA-only control, highlighting efficient aptamer–thrombin binding, and a 17% decrease in capacitance, indicating thrombin-induced changes in the dielectric properties at the interface. The progressive insulation from aptamer and thrombin layers supports a “signal-off” detection strategy, where target binding restricts electron flow. At 50 nM thrombin, the 19% R_{ct} shift can be used as the sensor signal for detecting physiologically relevant thrombin levels.

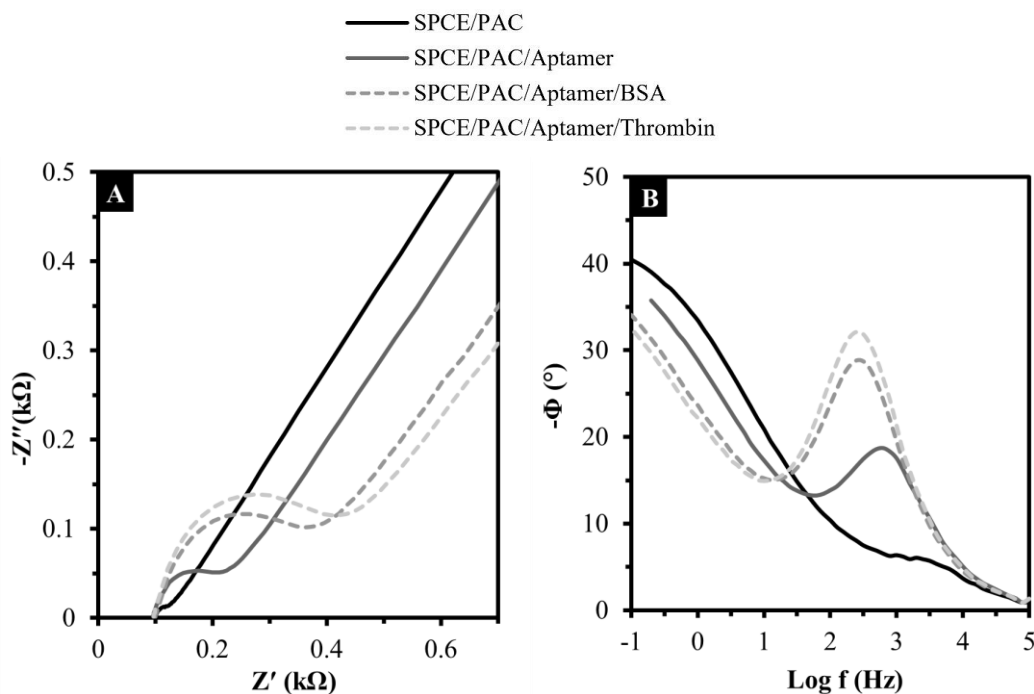


Figure 4.6. The resulted (A) Nyquist plot and (B) Bode plot faradaic EIS detection of thrombin using immobilized aptamer on PAC modified SPCE.

Table 4.3. Electrochemical impedance spectroscopy parameters of PAC-modified SPCE-based thrombin biosensor at different modification stages.

Electrode	R_u (Ω)	R_{ct} (Ω)	C (μF)
SPCE/PAC/Aptamer/BSA	101.0	263.6	41.4
SPCE/PAC/Aptamer/Thrombin	97.6	313.6	34.3
Capacitance Signal to Blank (50 nM Thrombin/5 μ M BSA)		-17%	
R _{ct} Signal to Blank (50 nM Thrombin/5 μ M BSA)		19%	

4.5. Conclusion

PAC treatment of carbon electrodes significantly enhanced the immobilization of ssDNA aptamers, as confirmed by a \approx 6-fold increase in XPS phosphorus signal (P2p). This surface modification improved electron transfer kinetics, evidenced by increased oxidation current and reduced peak separation in electrochemical measurements, while maintaining a facile kinetics of electron transfer after aptamer attachment. EIS revealed that PAC-treated electrodes exhibited lower baseline charge transfer resistance compared to unmodified SPCEs. Upon aptamer and thrombin binding, the charge transfer resistance increased, while capacitance decreased, reflecting the formation of insulating biomolecular layers that hinder electron flow and increase double layer capacitance thickness—a mechanism that supports sensitive, label-free “signal-off” biosensing. Overall, PAC modification enabled efficient, high-density aptamer immobilization without additional wet chemistry, offering a biosensing platform for electrochemical detection of clinically relevant targets such as thrombin. However, wet immobilization chemistry techniques are still well-developed and do not require specific instrumentation. The downside is the consumption of chemical

reagents, which are often expensive and produce biochemical waste. Plasma coating techniques do not require a linker or wet immobilization chemistry but do require specialized instrumentation and high power. For instance, in this study, the PAC coating required 10 minutes of 50 W RF power and a -500 V pulsed bias in a highly vacuumed condition.

4.6. Study limitations

The stability of PAC treatment on carbon electrodes was not studied, nor was the change in electrochemical and surface chemistry of PAC-treated electrodes over time. Moreover, a calibration curve to determine the correlation between the concentration of the thrombin and the sensor signal was not determined. Additionally, complex matrices or clinical samples, such as plasma, were not tested; instead, the experiments were conducted using isolated and purified proteins.

4.7. Future work

The validation of aptamer density must follow the well-established protocol for the electrochemical determination of attached DNA, originally developed by Tarlov et al[158]. A study must be conducted to determine the correlation between aptamer density and thrombin binding. A more established protocol based on methylene-blue or ferrocene-tagged aptamers may enhance the noise ratio of aptasensing. The enzymatic activity of thrombin after its binding must be determined to evaluate the effect of the PAC-modified electrode on thrombin's function. A fast scan electrochemical methodology must be developed to measure the binding kinetics of thrombin to the immobilized aptamer. The current method uses EIS in a wide frequency range, taking more than 3 minutes. The

relatively slow measurement might not be able to provide the kinetics of binding and unbinding, as aptamer binding is shown to be quick (≈ 10 seconds)[159].

4.8. Author contributions

All authors contributed to the preparation of this manuscript. Specific contributions are as follows: S.A. conceived of the original idea. S.A. planned the experiments. S.A., C.T., analyzed the data. S.A. conducted the experiments and wrote the manuscript. S.A., C.T., S.F., M.B., and A.I. edited the manuscript. S.A. and A.I. supervised and acquired funding for the project. All authors discussed the results and contributed to the final manuscript.

4.9. Acknowledgements

This work was carried out with financial support of the New Brunswick Innovation Foundation NBIF (Project No. EP-0000000155) & New Brunswick Health Research Fund NBHRF (Project No. 0000000045) and MITACS Globalink Research Award Application Ref. IT36728. We thank Kostadinos Tsoutas (University of Sydney) for his advice.

4.10. Conflict of interest

The authors declare no conflict of interest.

5. Revisiting a classical aptamer-based biosensor for electrochemical enzymatic detection of thrombin

S. Ardalan, A. Ignaszak. Submitted to ChemElectroChem, manuscript number 8993652, Jan 16, 2026.

5.1. Abstract

Thrombin-binding aptamers (TBA) are widely employed in electrochemical aptasensors; however, the selectivity and sensitivity of label-free detection methods require critical reassessment. In this work, an electrochemical aptasensor was fabricated by immobilizing thiol-modified TBA on a gold screen-printed electrode, followed by blocking with mercaptohexanol (MCH). When exposed to 1 μ M thrombin in a measurement buffer containing the ferro/ferricyanide redox couple, an \approx 80% increase in charge transfer resistance (R_{ct}) was observed by Electrochemical Impedance Spectroscopy (EIS). To further analyze the enzymatic activity of the captured thrombin, its enzymatic cleavage activity was measured electrochemically. The enzymatic assay utilizes an electrogenic substrate, H-D-Phe-Pip-Arg-para-nitroanilide, which can be cleaved by thrombin to generate para-nitroaniline (pNA). Square-wave voltammetry enabled detection of the liberated pNA at 0.12 V, producing \approx 90-fold greater signal than EIS under identical conditions. However, further control studies revealed that the enzymatic cleavage activity of thrombin on an MCH-blocked electrode without the aptamer produces an identical signal gain. These results indicate that R_{ct} increase in the label-free EIS could stem from nonspecific adsorption or SAM restructuring rather than true aptamer–protein binding, especially for disulfide-rich proteins such as thrombin.

5.2. Introduction

Thrombin is a serine protease that cleaves Arg–Gly bonds in fibrinogen to form fibrin and release fibrinopeptides A and B.[160, 161] In the body, thrombin is generated from its inactive precursor, prothrombin (factor II), a liver-produced glycoprotein found in plasma at 5–10 mg/dL with ~12% glycan content. Activated factor X (Xa) cleaves prothrombin into catalytically active α -thrombin, composed of a light chain (~6 kDa) and a heavy chain (~31 kDa) linked by a disulfide bond.[162]

Prothrombin Time (PT) and Partial Thromboplastin Time (PTT) are routinely used to assess coagulation but have limited value in predicting thrombotic or bleeding risk in complex clinical scenarios.[163] In contrast, Thrombin Generation Assays (TGAs) provide a more comprehensive evaluation of hemostasis by measuring both procoagulant and anticoagulant activity across all phases of coagulation: initiation, propagation, and termination.[164] Key TGA parameters include lag time, peak thrombin, endogenous thrombin potential, and termination time—offering valuable insights for guiding transfusion and coagulation factor replacement, particularly in hemophilia.[165]

Similarly, the International Normalized Ratio (INR) is a standardized measure derived from PT that primarily reflects activity in the extrinsic pathway and is commonly used for warfarin monitoring.[166, 167] Both TGA and INR ultimately assess thrombin enzymatic activity, often via substrate cleavage. For example, the Roche CoaguChek INR device employs an amperometric detection method using the substrate Tos-Gly-Pro-Arg-4-amino-2-chlorophenol acetate (Pentapharm; US Patent 6495336).[166, 168] This substrate includes a central tripeptide (Gly-Pro-Arg), a tosyl protecting group at the N-terminus, and an electroactive leaving group at the C-terminus, which is oxidized at 0.3 V vs Ag/AgCl to

generate a measurable current. A few well-recognized systems have been summarized in Table 5.1.

Table 5.1. Commercial Thrombin enzymatic substrates used in TGA or PT-INR instruments.

System	Substrate	Substrate Type	k_{cat} (s^{-1})	K_m (μM)
Technoclone – Technothrombin Diagnostica - Stago ST Genesia	Z-Gly-Gly-Arg-AMC	Fluorogenic	1.86	310
Siemens Healthcare - Innovance ETP BCS XP System	H- β -Ala-Gly-Arg- pNA	Chromogenic	1.91	1950
Enzyme Research Laboratories – ThrombinChrom	H-D-Phe-Pip-Arg- pNA	Chromogenic	100	10
Roche Diagnostics - CoaguChek XS PT/INR	Tos-Gly-Pro-Arg-4- Amino-2- chlorophenol	Amperogenic (electrogenic)		NA

5.3. Literature review

Decades of extensive research have been conducted on thrombin measurement and biosensing.[164, 166, 167, 169, 170] Herein, the most relevant electrochemical thrombin detection methods are reviewed.

Early electrochemical thrombin generation assays (TGAs) used Tos-Gly-Pro-Arg-ACP (4-amino-2-chlorophenol) on palladium sensor strips with Ag/AgCl reference/counter electrodes.[168] Upon plasma rehydration, thrombin cleaved the substrate, producing an

electroactive product detected at 0.3 V (0.4–50 U/mL). However, kinetic parameters and inhibitor effects were not reported. Anne et al. developed a ferrocene-labeled heptapeptide (Fc-[Arg-Phe-Ser-Arg-Pro-Gln-Leu]) immobilized on gold electrodes. Thrombin cleaved the Ser-Arg site, reducing the redox signal at ~0.15 V (CV). The system showed 80% cleavage yield, $k_{\text{cat}} = (1.0 \pm 0.2) \times 10^{-2} \text{ s}^{-1}$, $K_M = 10 \pm 2 \text{ nM}$, and a detection range of 1–1000 nM. However, the developed substrate by Horiba Medical, is not commercially available.[171] A chronocoulometric biosensor using ITO electrodes and freeze-dried filter paper embedded with Val-Pro-Arg-AN, glucose, and glucose dehydrogenase enabled thrombin detection via redox cycling of 4-amino-1-naphthol.[172] Measurements at 0 V showed a linear range of 100 pg/mL to 10 µg/mL. Enzyme kinetics and cross-reactivity were not assessed. Mruthunjaya et al. designed a disposable sensor with co-facing gold electrodes to monitor dabigatran via thrombin cleavage of Tos-Gly-Pro-Arg-ACP. ACP was detected at 0.4 V, with 0.22 µM thrombin and 0.3 mM substrate in diluted plasma.[173] The sensor achieved a 9.6 ng/mL detection limit and 11.5–140 ng/mL quantification range, offering rapid results (< 20 s) at physiological pH.

The literature review on aptamer-based thrombin biosensing is as follows: The first thrombin-binding aptamer (15-mer, $K_d = 100 \text{ nM}$) targets the fibrinogen-recognition exosite[16]; a later 29-mer ($K_d = 0.5 \text{ nM}$) binds the heparin-binding exosite.[130] Both form stable antiparallel G-quadruplexes. Early efforts to integrate aptamers with thrombin enzymatic biosensing introduced three electrochemical aptasensor configurations using a 15-mer thrombin-binding aptamer.[174] 1) Substrate Cleavage Assay: A thiolated aptamer immobilized on a gold electrode captured thrombin, which cleaved β -Ala-Gly-Arg-p-nitroaniline. The released p-nitroaniline (5 mM) was detected via DPV at -0.7 V vs.

Ag/AgCl. 2) Aptamer-Based Sandwich Assay: Mimicking ELISA, this setup used HRP-labeled secondary aptamers and a redox mediator ($[\text{Os}(\text{bpy})_2(\text{pyr-CH}_2\text{-NH}_2)]\text{Cl}$) to generate catalytic current. Direct Adsorption: Thrombin was adsorbed onto a modified gold electrode and detected using an HRP-labeled aptamer, achieving the lowest detection limit (3.5 nM). A separate study developed a label-free impedance biosensor with a 15-mer aptamer on gold.[175] Thrombin binding increased R_{ct} , further amplified by guanidine hydrochloride-induced denaturation, enhancing steric hindrance. This enabled detection from 10 to 100 fM, though the denaturation step added complexity and risk of non-specific signal drift. Another approach used split aptamers (15-mer and 29-mer) in a label-free sandwich format.[176] The 15-mer was immobilized, while the 29-mer bound thrombin in solution. Exonuclease I selectively cleaved unbound aptamers, reducing charge transfer resistance. This method achieved a 32 fM detection limit across a 1.35 pM–1.35 nM range.

5.4. Study novelties

This work provides three primary novelties in the field of thrombin biosensing as follows:

1. The first report of analyzing the binding affinity of the 29-mer thrombin binding aptamer on a screen-printed gold electrode by faradaic and non-faradaic EIS.
 - a. Studying the effect of a disulfide reduction agent, Tris(2-chloroethyl)phosphate (TCEP), on the immobilization efficiency of thiol-modified aptamers on a screen-printed gold electrode.
 - b. Characterizing the diffusion coefficient and kinetics of electron transfer of the aptasensor by analyzing the Warburg impedance and the Randles–Sevcik equation via cyclic voltammetry.

- c. Evaluating experimental conditions of thiol-modified aptamer immobilization on the gold electrode, including MCH co-immobilization, electrode pre-treatment, and the effect of solvents.
 - d. Measuring thrombin chemisorption on unmodified and MCH-modified gold electrodes.
 - e. Selectivity studies including interfering proteins (albumin, fibrinogen, prothrombin) on the MCH-modified aptasensor.
2. Novel electrochemical detection mechanism based on a thrombin electrogenic assay
- a. Monitoring the enzymatic activity of the thrombin to catalytically cleave a peptide-based substrate, H-D-Phe-Pip-Arg-pNA, by measuring the oxidation peak of the liberated para-nitroaniline (pNA) using square wave voltammetry (SWV)
 - b. Providing Michaelis-Menten kinetics parameters of H-D-Phe-Pip-Arg-pNA with the developed SWV protocol
 - c. Designing an electrochemical immunosorbent assay based on thrombin capture by the aptamer-modified gold electrode and enzymatic amplification via the peptide-based substrate
 - d. Comparing the sensing performance of the label-free thrombin aptasensor with the enzymatic assay.

The enzymatic electrochemical sensor produced ≈ 90 -fold increase in signal response for $1 \mu\text{M}$ thrombin compared to a control containing $50 \mu\text{M}$ human serum albumin (HSA). This response was significantly higher than that obtained from label-free impedance measurements at the same thrombin concentration, indicating greater signal amplification through the enzymatic approach.

5.5. Materials and methods

5.5.1. Chemicals and buffers

Potassium hexacyanoferrate(II) trihydrate ($\text{Fe}(\text{CN})_6^{4-}$; 98.5%), potassium hexacyanoferrate(III) ($\text{Fe}(\text{CN})_6^{3-}$; 99%), tris(hydroxymethyl)aminomethane hydrochloride (Tris.HCl; >99%), magnesium chloride hexahydrate ($\text{MgCl}_2 \cdot 6\text{H}_2\text{O}$ > 99%) calcium chloride hexahydrate ($\text{CaCl}_2 \cdot 6\text{H}_2\text{O}$ > 95%), mercaptohexanol (MCH; 99%) potassium chloride (KCl; 99%), sulfuric acid (H_2SO_4 ; 96%, p.a.), sodium hydroxide (98%, pellets), tris(2-carboxyethyl)phosphine hydrochloride (TCEP), hexa ammine ruthenium(III) chloride ($\text{Ru}(\text{NH}_3)_6\text{Cl}_3$, RuHex, 98%) were purchased from Sigma-Aldrich® (Canada). Folding buffer solution: tris-buffered saline, TBS 1X, MgCl_2 1 mM, CaCl_2 1 mM, buffered at pH 7.4. Measurement buffer solution: Folding buffer solution with 2 mM $[\text{Fe}(\text{CN})_6]^{4-}$ and 2 mM $[\text{Fe}(\text{CN})_6]^{3-}$ buffered at pH = 7.4. RuHex was dissolved in water to form a 1 mM concentration stock solution, then degassed for 15 min with N_2 and stored in the fridge. 25 mL of 25 mM TCEP stock solution was prepared by dissolving TCEP in \approx 15 mL water. The pH was adjusted by adding 1 M NaOH dropwise to reach pH = 7.0, then the solution was transferred to a 25 mL flask to reach the desired volume. 1 mM TCEP aliquots were prepared in MilliQ water. 20 μL of the 1 mM TCEP solution was transferred into small tubes and stored in a -20 °C freezer for long-term preservation. A 25 mM MCH stock solution was prepared by diluting MCH in water, aliquoted and stored at -20 °C.

All solutions were prepared with Milli-Q water. All solutions were filtered using 0.2 μm sterile filter. Aptamer and protein solutions were stored in low-binding tubes to reduce stickiness to the walls of the microtubes (DNA/Protein LoBind Tubes, Eppendorf). Low-

retention pipette tips (ART, Thermo Fisher Scientific) were used for pipetting to minimize DNA/protein binding to pipette tips.

5.5.2. Thrombin binding aptamer preparation

Desalted lyophilized aptamer with dithiol modification with six carbon spacers at 5' end (5'-C6-S-S-AGTCCGTGGTAGGGCAGGTTGGGGTGACT-3') was purchased from Integrated DNA Technologies (IDT, USA). Aliquots of 100 μ M aptamer solutions were prepared in LoBind DNA microtubes, diluted with the folding buffer, and stored at -80 °C.

5.5.3. Protein solutions preparation

Human alpha thrombin (9.2 mg/mL, 50% glycerol/water v/v, $E^{1\%}_{1\text{cm}, 280\text{nm}} = 18.3$, molecular weight (Mw) 36.7 kDa) was purchased from Prolytix (USA). To calculate protein concentration, the equation $\mu\text{M} = (\mu\text{g/mL}) / \text{Mw (kDa)}$ was used. The undiluted aliquots were transferred to LoBind protein microtubes (in ice) and stored at -80 °C. Prothrombin (9.26 mg/mL) and fibrinogen (44.2 mg/mL) were purchased from Enzyme Research Laboratories (USA). Human serum albumin (HSA, lyophilized powder, $\geq 97\%$) was purchased from Sigma (Canada).

5.5.4. Thrombin substrate preparation

Thrombin chromogenic substrate (H-D-Phe-Pip-Arg-pNA.2HCl) was purchased from Enzyme Research Laboratories (USA). A 4 mM stock solution of the substrate was prepared in TBS 1X (pH = 7.4), aliquoted and stored at -20 °C.

5.5.5. Screen-printed gold electrode preparation

ItalSens screen-printed gold electrode (gold SPE; \varnothing 3 mm working electrode) was purchased from Palmsens (Netherlands). Electrodes were pre-treated by three cyclic

voltammetry (CV) scans in 0.5 M H₂SO₄ at a scan rate of 0.1 V/s and referred to as electropolishing (E-polish).

5.5.6. Electrochemical measurement unit

Electrochemical measurements were performed at ambient conditions using a PalmSens4 potentiostat connected to a desktop PC. The data were collected through PSTrace, a software package that controls PalmSens potentiostats.

5.5.7. Scanning Electron Microscopy (SEM)

SEM Images were collected with a ThermoFisher Scientific Scios 2 electron microscope with an Oxford Ultim Max 170 EDS detector and Aztec software.

5.5.8. Aptasensing procedure

First, a 10 μ L of frozen aptamer (\approx 100 μ M, 850 ng/ μ L) was diluted in 90 μ L folding buffer, annealed at 85 $^{\circ}$ C for 5 min, and cooled to room temperature over 30 min. Then, 90 μ L of the annealed aptamer was mixed with 10 μ L of 1 mM thawed TCEP and incubated in the dark for 1 hour. The solution was diluted to \approx 10 ng/ μ L (confirmed via Nanodrop), and 10 μ L was incubated on the gold SPE electrode in a humidity chamber. Electrodes were rinsed, dried with N₂, and re-incubated in folding buffer for 1 hour. Next, 10 μ L of thawed 1 mM MCH was drop-casted onto the electrode for 1 hour, followed by the same rinsing procedure. Thrombin stock solution (\approx 250 μ M) was thawed at 37 $^{\circ}$ C, diluted in folding buffer, and 10 μ L was incubated on the electrode for 30 min. Then, the electrode was washed three times with 10 μ L folding buffer. Finally, 100 μ L of measurement buffer was added and incubated for 2 min before EIS measurement ($E_{dc} = E_{ocp}$, $E_{ac} = 10$ mV, 100

kHz–0.1 Hz, 10 points/decade, 61 points total). Data was analyzed via PSTrace using equivalent circuit fitting.

5.5.9. Enzymatic sensing procedure

The substrate stock solution was thawed rapidly at a 37 °C dry heat bath, followed by dilution in the folding buffer. Then, 90 µL of the substrate was pipetted on the gold SPE, and 10 µL of the sample containing thrombin or interfering proteins was mixed with the substrate on the electrode. Immediately afterward, repeated cycles of Square Wave Voltammetry (SWV) scans were applied to the electrode using the following parameters: a 1-second reduction potential at -0.85 V, a scanning window from -0.25 to 0.40 V with a step potential of 5 mV, an amplitude of 10 mV, and a frequency of 10 Hz. Peak oxidation currents at ≈ 0.12 V were determined by extracting the raw data from PSTrace to an Excel (Microsoft 365) file.

5.5.10. Data analysis

Minitab 18.1 and Excel (Microsoft 365) were used to generate graphs, determine statistical significance, and calculate analytical figures of merit. P-values were calculated using a two-sided t-test for independent samples assuming equal variances.

5.6. Results and discussion

5.6.1. Electroactive surface area calculations

Pre-treatment of a gold electrode is commonly done by cyclic voltammetry (CV) in 0.5 M H₂SO₄, providing a reduced state of gold atoms. This process is known as electropolishing (E-polish) and is shown in Figure 5.1. Several parameters can be calculated from the cathodic peak of gold, including electrode real surface area (S_{true}) and roughness factor (r).

The integral from 0.5 V to 0.7 V of the cathodic (reduction) peak, which is the reduction of Au^{3+} to Au, is used to calculate the total charge (Q).^[132] The integral from a current-potential (i-E) curve is the power ($i \times E$), and it needs to be divided by the scan rate (ν) to get the charge (Equation 5.1).^[133]

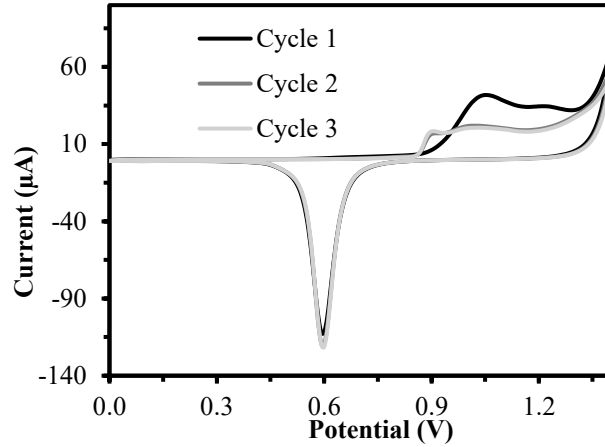


Figure 5.1. Electropolishing gold SPE in 0.5 M sulfuric acid provides a sharp gold reduction peak at ≈ 0.6 V which is used to calculate true surface area and roughness factor.

$$Q = \frac{\int_{E_1}^{E_2} I \cdot dE}{\nu} \quad 5.1$$

The working electrode roughness factor (r) was estimated based on a well-developed protocol for calculating the electrode's true surface from the charge in the range of oxygen reductive desorption.^[133] The true electrode surface (S_{true}) is the actual reactive area, while the geometrical surface (S_{geom}) is based on the electrode surface area (πr^2). The charge (Q_{red}) for oxygen electro-desorption is divided by $400 \mu\text{C}/\text{cm}^2$, the charge needed to desorb an oxygen monolayer from 1 cm^2 (Equation 5.2).^[134] Roughness factor (r) is calculated based on the ratio of true electrode surface to its geometrical area (Equation 5.3).^[134] Table 5.2 provides the surface area characteristics calculated from the reduction peak of

gold SPEs., which were calculated from Equation 5.1 to 5.3. Figure 5.2 presents the SEM image of the gold SPE, which shows micrometre-sized granular gold particles, providing a rough surface area ($r = 2.97$)

$$S_{true} = \frac{Q_{red}(\mu C)}{400 (\mu C \cdot cm^{-2})} \quad 5.2$$

$$r = \frac{S_{true}}{S_{geom}} \quad 5.3$$

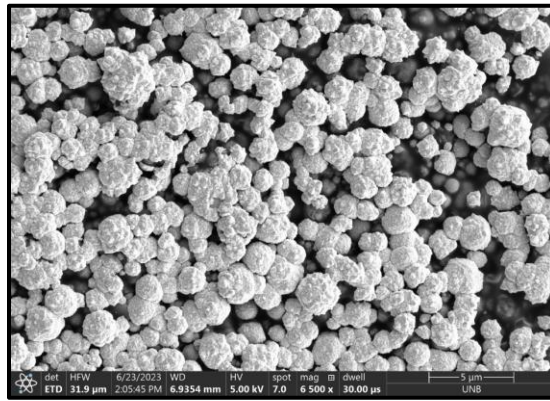


Figure 5.2. SEM image of an electropolished Italsens screen printed gold electrode showing micron-sized gold particles.

Table 5.2. Gold surface characteristics calculated from reduction peak of in 0.5 M sulfuric acid. RSD is provided based on the voltammogram data of three individual gold SPEs.

Average Q_{red} (μC)	84.1
S_{geom} (cm^2)	0.0707
S_{true} (cm^2)	0.210
RSD%	1.3
Roughness (f)	2.97

5.6.2. Electrode characterization by electrochemical impedance spectroscopy

In EIS characterization of an electrochemical sensor, the working electrode is perturbed by applying a small amplitude excitation alternating voltage along with a fixed direct potential, commonly open circuit potential (OCP), which is approximately at the formal potential (E^0) of the over a wide range of frequencies.[37] The Randles circuit is the most frequently used model, as it effectively represents uncompensated resistance (R_u), charge transfer resistance (R_{ct}), Warburg impedance (Z_w), and a non-ideal double layer capacitance, known as constant phase element (CPE), as shown in Figure 5.3.A.[37] The Randles circuit is simplified to an R_u in series with CPE in the absence of redox-active molecules and is shown in Figure 5.3.B.[136]

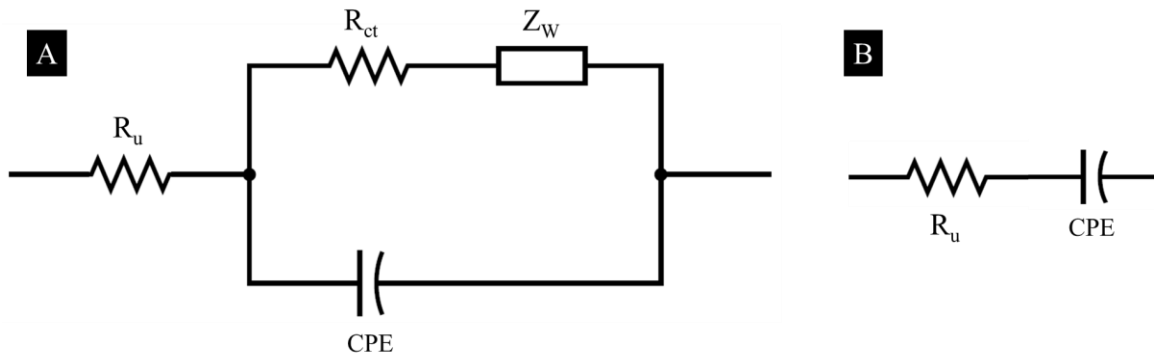


Figure 5.3. A) Modified Randles circuit for faradaic EIS modeling. B) Simplified equivalent circuit of a non-faradaic EIS test.

By fitting the impedance data to this equivalent circuit using appropriate modeling software, the values of each electrical component can be accurately calculated. The capacitance (C) can be explained by Equation 5.4.

$$C = \epsilon\epsilon_0\left(\frac{A}{d}\right) \quad 5.4$$

Where ϵ is the dielectric constant of the medium at the electrode/electrolyte interface, ϵ_0 is the permittivity of free space, A , is the electrode's surface area and d is the thickness of attached layers on the electrode's surface.[177] In a non-ideal behavior of capacitance, the term Q_0 is used to define the constant phase element. Q_0 has the numerical value of the admittance ($1/|Z|$) at $\omega = 1$ rad/s. In the case of an ideal capacitor where $n = 1$, $C = Q_0$ but most capacitance elements in Randles circuit of electrochemical sensors are drifted from the ideal capacitance.[177] In a Randles circuit with semi-finite diffusion, the effective capacitance is given by Equation 5.5.[135, 136]

$$C = Q_0^{\frac{1}{n}} \left(\frac{1}{R_u} + \frac{1}{R_{ct}} \right)^{\frac{n-1}{n}} \quad 5.5$$

In the absence of redox-active molecules, as shown in the Figure 5.3.B, the effective capacitance is simplified to the Equation 5.6.[136]

$$C = \frac{(Q_0 \cdot R_u)^{\frac{1}{n}}}{R_u} \quad 5.6$$

5.6.3. Effect of repeated EIS scans on the charge transfer and capacitance

Repeated EIS scans were conducted in a pre-bubbled N_2 purged cell on a freshly prepared gold SPE. The results reveal the reduction in R_{ct} and increase in effective C presumably caused by $[Fe(CN)_6]^{4-/3-}$ etching (Figure 5.4).[54] Thus, repeated measurement was avoided in the aptasensor to avoid the etching of the gold electrode and any possible interference with aptamer immobilization and functionality. The increase in capacitance was observed as etching of gold leading to more effective surface area.

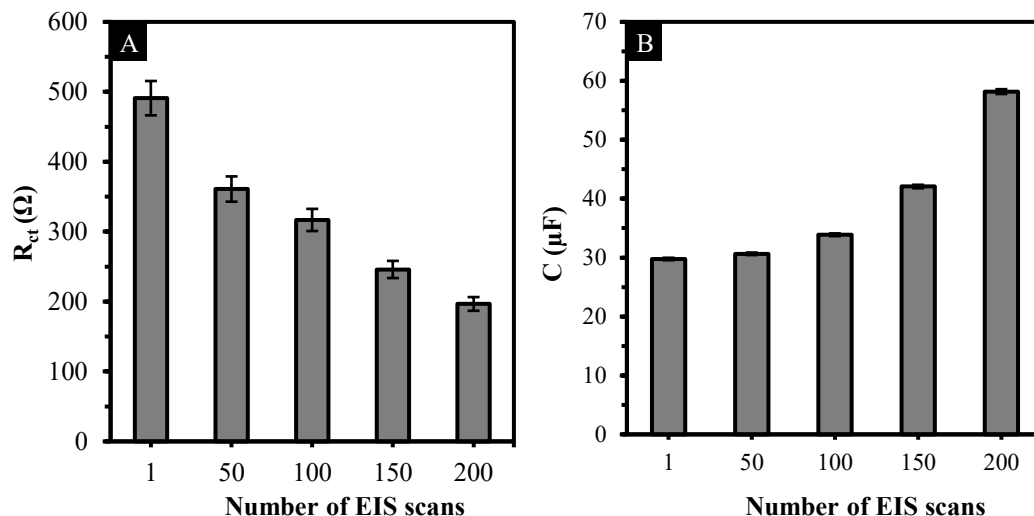


Figure 5.4. A) Decrease in R_{ct} and B) increase in effective capacitance of bare gold electrodes caused by $[\text{Fe}(\text{CN})_6]^{4-/3-}$ surface etching during repeated faradaic EIS scans. Error bars are included to represent the variability in the data collected from three different gold SPEs for each condition.

5.6.4. Effect of $[\text{Fe}(\text{CN})_6]^{4-/3-}$ on gold voltammogram

After pre-treatment if the electrode is analyzed by either CV or EIS in the measurement buffer, the anodic peak of gold changes significantly, showing the $[\text{Fe}(\text{CN})_6]^{4-/3-}$ interacts with the gold and causes a change in its electrochemical characteristics (Figure 5.5) Meanwhile, characterizing the electrode in folding buffer, resulting in non-faradaic EIS minimizes this change in the electrochemical oxidation peak characteristic of the gold electrode. Thus, characterization with measurement buffer is avoided prior to immobilization of thiol-modified self-assembled monolayers (SAMs).

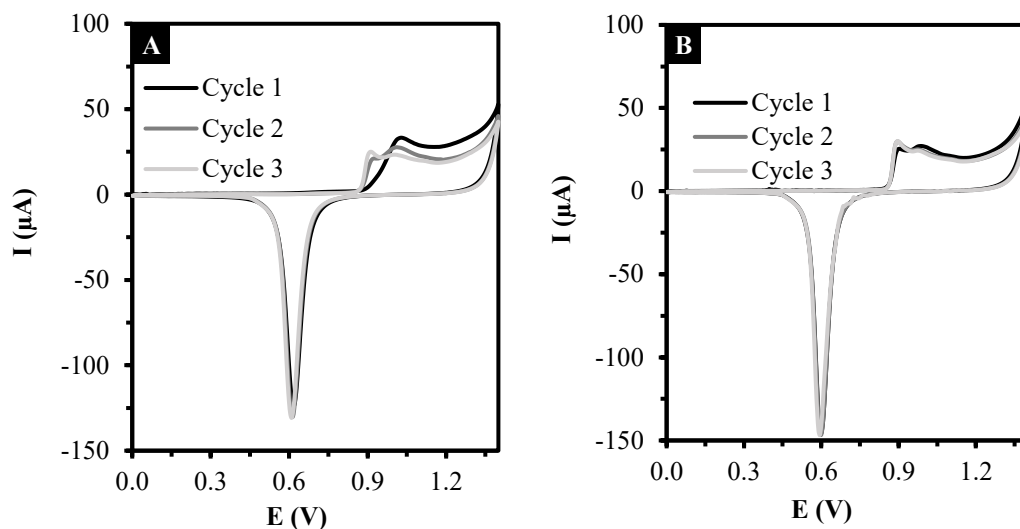


Figure 5.5. A) Treatment of the electrode with the redox-active buffer. B) Treatment of the electrode with the folding buffer.

5.6.5. Effect of experimental variables on immobilization of thiolated aptamers

Another impeding factor to an efficient and reproducible immobilization is the delay between electrode pre-treatment and SAM immobilization and the data are shown in a bar chart (Figure 5.6). The conducted experiment was based on incubating 10 ng/ μ L aptamer for 1 h on the gold SPE. Both delayed and immediate immobilization included the presence of 1 mM Mg^{2+} . The results indicate that immediately after pre-treatment of gold SPE, drop-casting the thiol-modified aptamer produces consistent monolayers with higher immobilization efficiency ≈ 4 k Ω of resistance vs ≈ 2 k Ω in delayed aptamer immobilization (1 h delay between E-polishing and immobilization) Moreover, for the selected thrombin binding aptamer, Mg^{2+} ions play a crucial role for proper aptamer folding since the optimized folding structure and binding was originally studied in the presence of 1 mM $MgCl_2$. [130]

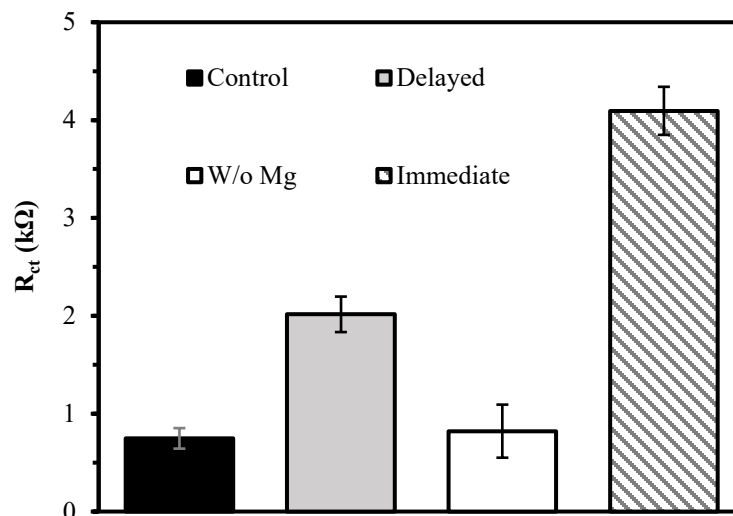


Figure 5.6. The effect of experimental conditions of thiol-modified aptamer SAMs on gold SPE. Control sample is related to electrodes without any aptamer modification (bare electrode). Error bars are included to represent the variability in the data collected from three different gold SPEs for each condition.

5.6.6. Effect of glycerin as solvent on gold

Glycerine is commonly used for long-term storage of protein solution aliquots to prevent the formation of ice and disturbing the protein structure. However, the interaction of glycerine and the electrode used in this work was unknown. To evaluate whether the glycerin attached strongly to the working electrode or its organic binders, the electropolished electrodes, without any aptamer modification, were incubated with a 50% glycerine/water mix for 30 min. The control group consisted of pf bare electrodes incubated with only water for 30 min (without any glycerol). Compared to the control group, there was no significant change in R_{ct} ($n=3$, p -value > 0.05). Thus, the protein aliquots for this work were stored in 50% glycerin for long term storage at -80 °C freezer.

5.6.7. Thrombin and human serum albumin (HSA) adsorption on gold

It is crucial to distinguish between aptamer-protein target binding and nonspecific protein adsorption on the electrode since in both cases R_{ct} could increase. Proteins can be chemisorbed on gold.[178] For instance, Thrombin is a α/β heterodimer composed of a 36 amino acid A chain and 259 amino acid B chain connected by a disulfide bridge between Cys1 and Cys122, in addition to 3 other intrachain disulfide bonds.[131] Disulfides strongly bond to gold via chemisorption.[179] MCH is an effective alkanethiol that has shown to significantly reduce biofouling.[27] To cross-verify, the electropolished gold SPEs were modified with 1 mM MCH in water for 1 h at 20 °C in a humidity chamber. MCH saturated the gold surface, significantly exceeding that of other thiolated biomolecules. Consequently, even though thrombin and other proteins contain sulfide and disulfide bonds, this is not a significant concern as the surface is already fully saturated with thiol-gold bonds as shown in the Nyquist plot and complex capacitance plot of EIS analysis in Figure 5.7.

More specifically, the complex capacitance plot shown in Figure 5.7.B provides a visual representation of the effective capacitance of the sensors with different modifications. The complex capacitance plot emphasizes capacitance values at high frequencies because, at these frequencies, faradaic processes are essentially blocked, and all current passes through the double-layer capacitance.[180] The semi-circle diameter observed on the complex capacitance is a visual representation of how the effective capacitance of the sensor changed due to each step of modifications.

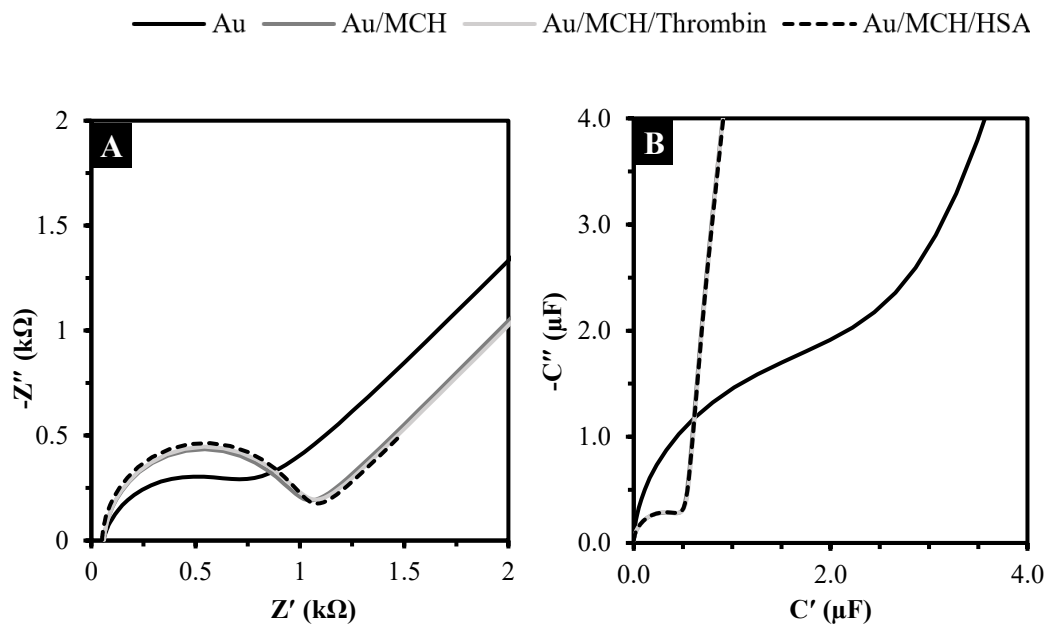


Figure 5.7. A) Nyquist plot and B) complex capacitance plot of gold electrode anti-biofouling by MCH.

In another experiment, solutions of 1 μM thrombin and 50 μM HSA were individually incubated for 30 minutes on MCH-modified electrodes and on a control group of electropolished electrodes without MCH (Table 5.3). The protein adsorption signal on electrodes was calculated using Equation 5.7.

$$\text{Relative protein adsorption \%} = \frac{R_{ct} \text{ protein} - R_{ct} \text{ electrode}}{R_{ct} \text{ electrode}} \times 100 \quad 5.7$$

Figure 5.8 shows the interactions between thrombin and gold electrodes. Thrombin exhibited strong adsorption on gold via the formation SAM through chemisorption of dithiol bonds, which increased the R_{ct} by 630%. Once thrombin is adsorbed onto the gold surface, it remained firmly attached even after washing or rinsing, indicating the stability of the adsorbate. However, it was noted that washing with Tween20 is not suitable for screen-printed electrodes, as this surfactant led to the detachment of the printed gold layer

Table 5.3. Effect of different electrode modifications on charge transfer resistance (R_{ct}). The RSD is provided to represent the variability in the data collected from three individual gold SPEs for each condition.

Electrode	Average R_{ct}	RSD%
Au	690	4.3
Au/Thrombin	3900	2.5
Au/HSA	2100	5.5
Au/MCH	900	0.3
Au/MCH/Thrombin	910	0.9
Au/MCH/HSA	825	2.7
Au/Aptamer/MCH	4240	2.5
Aptamer/MCH/Buffer_Stabilized	4340	0.9
Au/Aptamer/MCH/HSA	4560	2.7
Au/Aptamer_TCEP/MCH	9780	1.5
Au/Aptamer_TCEP/MCH/Buffer_Stabilized	9590	0.7
Au/Aptamer_TCEP/MCH/Buffer_Stabilized/HSA	9520	3.0

causing significant drift in the R_{ct} (Figure 5.8.A). The complex plane representation of thrombin adsorption (Figure 5.8.B) showed a decrease in capacitance, which can be attributed to the chemisorption of thrombin and the subsequent formation of the SAM and increasing the thickness of the double layer capacitance.

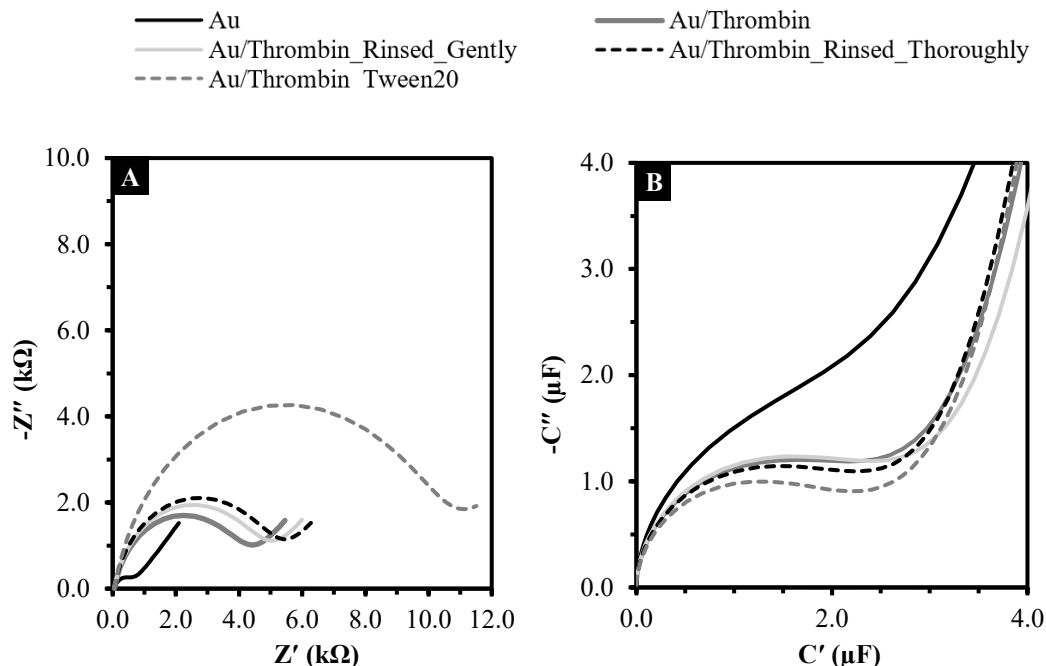


Figure 5.8. A) Nyquist plot and B) complex plane of thrombin adsorption on the gold SPE.

Table 5.4 summarizes the relative protein adsorption percentage on bare gold electrodes and MCH-modified gold electrodes. Adsorbed thrombin increased R_{ct} by $\approx 630\%$, indicating strong binding of thrombin to the gold electrode. Meanwhile, the albumin showed less adsorption at 270%, which showed a weaker adsorption even at 50 times higher concentration than thrombin. MCH decreased the adsorption below 2%.

5.6.8. DNA quantification by chronocoulometry

Historically, Fred C. Anson presented innovations in chronocoulometry (CC) for detecting adsorbed electroactive species on mercury electrodes.[181] Traditional CC measurements are influenced by double-layer capacitance, making it difficult to distinguish between capacitive and faradaic currents. Anson introduced two refined approaches to eliminate the double-layer charge: (1) a double potential-step CC technique, which returns the electrode

Table 5.4. Relative nonspecific protein adsorption on gold electrodes. The RSD is provided to represent the variability in the data collected from three individual gold SPEs.

Electrode	Average relative adsorption%	RSD
Au/Thrombin	630	2.5
Au/HSA	270	5.5
Au/MCH/Thrombin	1.4	0.9
Au/Aptamer/MCH/HSA	-0.7	2.7

to its initial potential to cancel out net double-layer charging, and (2) a drop extrusion - method where the charge on freshly extruded mercury drops is used to measure double-layer charge under different conditions directly. These methods enhance the precision in identifying whether adsorption of a reactant occurs, and they enable the accurate quantification of adsorbed species.

Later on, Tarlov et al. developed this method for direct DNA quantification using Anson methodology, specifically to determine the number of nucleotide phosphate residues that electrostatically adsorb a cationic redox marker, hexa-ammine-ruthenium (III) chloride ($\text{Ru}(\text{NH}_3)_6^{3+}$ or RuHex).[182] The quantity of charge-compensating redox marker that saturates the DNA monolayer, measured through CC, is directly related to the number of phosphate groups present, which in turn reflects the surface density of the DNA. A widely recognized, detailed protocol published in Nature Protocol explains the details and nuances of determining probe density on gold nanoparticles.[183] In summary, The DNA-modified electrode is first placed in a low ionic strength electrolyte (10 mM Tris-HCl buffer, pH

7.4) purged with N₂ for 10 min and kept under an N₂ atmosphere throughout. A two-step CC technique is applied on the electrode with the potential step from 200 mV to -500 mV and then to 200 mV again versus Ag/AgCl for 250 ms for each pulse (sample interval 2 ms, sensitivity (C or A/V): 5⁻⁵ A/V). Next, the electrode was immersed in a 50 μM RuHex in the same buffer, being purged with N₂ for 10 min and kept under an N₂ atmosphere throughout.

In the low ionic strength buffer, RuHex replaces the native monovalent DNA counterions, binding electrostatically to DNA phosphates in a 1:3 ratio. At the initial potential (200 mV), reduction is minimal if not absent, whereas at -500 mV, it ensures complete reduction of surface-bound RuHex and enables a diffusion-limited current. The total charge (Q_{tot}) measured after the potential step includes contributions from: (1) RuHex diffusing from solution (Q_{dif}), (2) the double layer capacitance (Q_{dl}), and (3) surface-confined RuHex in ssDNA (Q_{ss}). [184] This is modeled by the integrated Cottrell equation (Equation 5.8),

$$Q_{tot} = \frac{2nFD_0^{\frac{1}{2}}C_0^*}{\pi^{\frac{1}{2}}} t^{\frac{1}{2}} + Q_{dl} + nFA\Gamma_{ss} \quad 5.8$$

incorporating terms for the number of electrons transferred (n), the Faraday constant (F), electrode area (A), diffusion coefficient (D_0), bulk concentration (C_0^*), capacitive charge (Q_{dl}), and surface-bound species (Γ_{ss}). [184] CC data is plotted as charge (Q) versus the square root of time ($t^{1/2}$) in an Anson plot. By extrapolating the linear region to time zero, the intercept gives the charge associated with ion diffusion and Q_{dl} in the absence of RuHex. Since ion diffusion is a constant term in all solutions, we assume in the absence of RuHex, $Q_{tot} = Q_{dl}$ for simplicity. In the presence of RuHex $Q_{tot} = Q_{dl} + nFA\Gamma_{ss}$ or $Q_{tot} = Q_{dl}$

+ Q_{ss} . Assuming Q_{dl} remains unchanged between the two conditions, the surface-bound charge ($nF\Gamma_0$) is calculated from the difference between the two intercepts (Equation 5.9).

$$Q_{ss} = Q_{tot} - Q_{dl} \quad 5.9$$

Rearranging the Cottrell equation provides the total number of bound species given by Equation 5.10.

$$\Gamma_{ss} = \left(\frac{Q_{ss} N_A}{nFS} \right) \left(\frac{z}{m} \right) \quad 5.10$$

Where n is the number of electrons in the reaction (1 e^- from reduction of $\text{Ru}(\text{NH}_3)_6^{3+}$ to $\text{Ru}(\text{NH}_3)_6^{2+}$), S is the area of the working electrode ($S_{true} = 0.21 \text{ cm}^2$), m is the number of nucleotides in the DNA (29 NT), z is the charge of the redox molecules (+3), N_A is Avogadro's number (6.022×10^{23}), and F is the Faraday's constant (96485 C.mol^{-1}). Initially, the electrode is charged for 0.25 seconds with a constant potential of -0.5 V. In the presence of RuHex, a significant increase in charge is observed, attributed to the electrostatic binding between RuHex and DNA (Figure 5.9). Conversely, in the absence of RuHex, the minimal increase in charge is primarily associated with the adsorption of ions on the electrode surface, much smaller than the charged Ru^{3+} electrostatic attraction to the negative phosphate backbone of the aptamer. The difference in charge intercepts provides the adsorbed charge to calculate the number of immobilized DNA. 29-mer ssDNA thrombin binding aptamer (10 ng/ μL) incubated for 1 h on the electrode and backfilled with 1 mM MCH for 1 h provides 4.3×10^{12} ssDNA per cm^2 of the gold electrode (Table 5.5) Xiao et al. provided a comprehensive protocol and overview of ssDNA aptamer density on gold electrodes, finding that the optimal concentration is between 30 pmol. cm^2

to 3 nmol. cm². [115] Our results of 4.3×10^{12} ssDNA per cm² are converted to amounts of pmol per cm², which is ≈ 7.1 pmol. cm² within the range of previously reported probe density on gold electrodes. Another report by White et al showed that the probe density of the thrombin aptamer was approximately ≈ 6.7 pmol. cm² for optimized aptasensing. [185] The limitation of this part of our experiment was that we did not conduct protocols to optimize the packing density of the aptamer. Instead, we aimed to provide further proof of aptamer immobilization and to demonstrate the packing density we used throughout the aptasensing of thrombin.

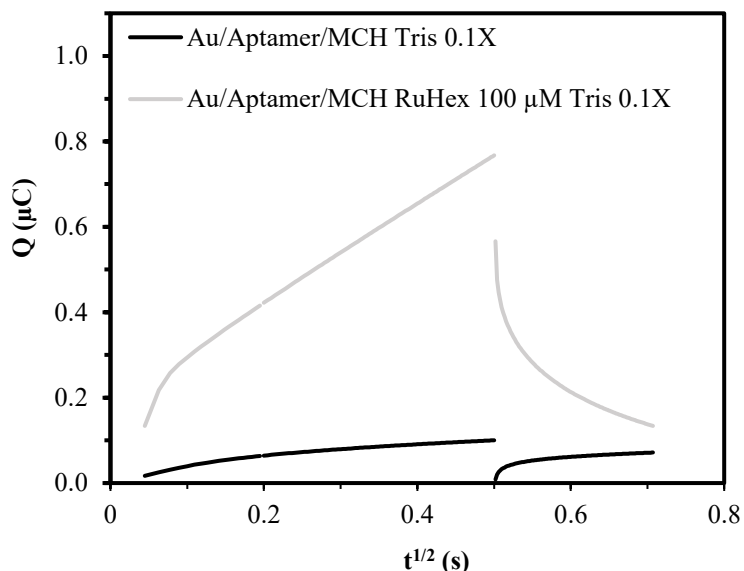


Figure 5.9. Anson plot response of aptasensors in absence (black curve) and presence (grey curve) of RuHex. A constant potential of -0.5 V is applied for 0.25 seconds, resulting in a significant charge increase with RuHex due to electrostatic binding, while the absence of RuHex shows minimal charge increase from ion adsorption. From 0.5 to 0.7 seconds, when the potential changes to +0.2 V, a drop in charge occurs if Ru³⁺ was present, as they detach from the negatively charged aptamer.

Table 5.5. CC results to measure the amount of aptamer per cm² (Γ) of the electrode.

Q	μC
Double layer (dl)	0.044
Total (tot)	0.19
Surface bound RuHex (ss)	0.15
Γ (cm⁻²)	4.3×10^{12}

5.6.9. Diffusion and kinetics of electron transfer

Two types of electrochemical tests were used to measure the diffusion coefficient. The first method is based on Randle-Sevcik method. In processes involving electrochemically reversible electron transfer with freely diffusing redox species, the Randles–Sevcik equation illustrates how the peak current (i_p) correlates linearly with the square root of the scan rate ν (V. s⁻¹). [137] In this equation, n represents the number of electrons involved in the redox reaction, A (cm²) denotes the electrode's surface area (typically regarded as the geometric area), D_o (cm².s⁻¹) indicates the diffusion coefficient of the oxidized species, and C^0 (in mol.cm⁻³) refers to the bulk concentration of the analyte. [137] Equation 5.11 was used to calculate diffusion coefficient.

$$i_p = 0.446nFAC^0 \left(\frac{nF\nu D_0}{RT} \right)^{\frac{1}{2}} \quad 5.11$$

Re-writing this equation based on plotting the i_p vs ν gives the Equation 5.12.

$$D_0 = \left(\frac{\text{Slope}}{0.446nFAC^0} \right)^2 \frac{RT}{nF} \quad 5.12$$

The second method of measuring the diffusion coefficient is based on the faradaic electrochemical impedance spectroscopy and measuring Warburg impedance.[37] The Warburg impedance, denoted as Z_w , characterizes the challenges associated with the mass transport of redox species to the electrode surface, considering a semi-infinite linear diffusion. Z_w acts like a series circuit composed of a resistance (R_w) and a capacitance (C_w), both of which vary with frequency as is defined by Equation 5.13.

$$Z_w = R_w + C_w = \left[\sigma \omega^{-\frac{1}{2}} - j \left(\sigma \omega^{-\frac{1}{2}} \right) \right] \quad 5.13$$

Where Warburg coefficient σ is defined by Equation 5.14.

$$\sigma = \frac{2RT}{n^2 F^2 A \sqrt{2} \sqrt{D_0} C_0} \quad 5.14$$

Rewriting to calculate D_0 by Equation 5.15.

$$D_0 = \left(\frac{2RT}{\sigma n^2 F^2 A \sqrt{2} C_0} \right)^2 \quad 5.15$$

The D_0 of the redox couple is assumed to be equal for both the oxidized (D_{ox}) and reduced (D_{red}) forms. The other symbols retain their previously defined meanings. Moreover, the kinetic of electron transfer is measured by defining the charge transfer resistance by the Equation 5.16.[37]

$$R_{ct} = \frac{RT}{k^0 n^2 F^2 AC} \quad 5.16$$

The only variable is k^0 heterogeneous electron transfer that is changing in each modification step. Although both CV and EIS can be used to estimate the D_0 of electroactive species, the values they yield often differ due to fundamental differences in the measurement principles. In CV, D_0 is derived from the peak current using the Randles–Sevcik equation, which reflects the transient diffusion of species toward the electrode surface during a dynamic potential sweep.[186] This method captures diffusion under relatively strong perturbations and evolving concentration gradients. In contrast, EIS estimates D_0 by analyzing the frequency-dependent impedance response, particularly the Warburg impedance at low frequencies, where diffusion is the dominant mass transport mechanism.[187] This approach probes the system under small-amplitude, steady-state sinusoidal perturbations and is more sensitive to surface heterogeneities, electrode roughness, and finite-length diffusion effects.[187] In this part of the experiment, the diffusion coefficient obtained from CV was approximately three times higher than that from EIS, a difference within acceptable limits and attributable to the distinct physical regimes each technique probes. The diffusion coefficients obtained by CV and EIS, along with the heterogeneous electron transfer rate constants, show clear trends depending on the surface modification of the electrode. The bare electrode exhibited the highest diffusion coefficients in both techniques. As the surface becomes increasingly modified with aptamer, MCH, and finally thrombin, a progressive decrease in both D_0 and k^0 is observed (Table 5.6). This suggests that surface modifications introduced physical and electrostatic barriers to mass transport and electron exchange, consistent with increasing steric

hindrance and reduced active area. The Warburg coefficient (σ) value was calculated by plotting the imaginary impedance $-Z''$ vs $\omega^{-1/2}$ depicted in Figure 5.10. The slope of this graph provided σ .

Table 5.6. Calculated diffusion coefficient (D_0) using the Randles-Sevick equation with the CV technique, Warburg impedance analysis via the EIS technique, and the resulting heterogeneous electron transfer rates (k^0) for each stage of the fabrication process.

Modification	$D_0 \text{ cm}^2 \text{ s}^{-1}$ (CV)	$D \text{ cm}^2 \text{ s}^{-1}$ (EIS)	$k^0 \text{ s}^{-1}$
Au	4.04×10^{-6}	6.84×10^{-7}	2.82×10^{-3}
Au/Aptamer	2.38×10^{-6}	6.51×10^{-7}	7.03×10^{-4}
Au/Aptamer/MCH	1.56×10^{-6}	6.19×10^{-7}	1.94×10^{-4}
Au/Aptamer/MCH/Thrombin	1.52×10^{-6}	6.02×10^{-7}	1.71×10^{-4}

5.6.10. Aptasensor fabrication and characterization

The goal is to fabricate a thrombin binding aptamer (TBA) on a gold SPE with MCH blocking agent. According to previous research, oxidized thiolated compounds can bind to gold,[188] thus, it may not be critical to use a reducing agent such as TCEP to reduce the S-S bond of modified aptamer to S-H. To study the effect of TCEP, first a control test using a fixed concentration of aptamer (10 ng/ μL), MCH (1 mM), and thrombin 25 U/ μL (\approx 225 nM) without TCEP was used to fabricate the electrochemical aptasensor.

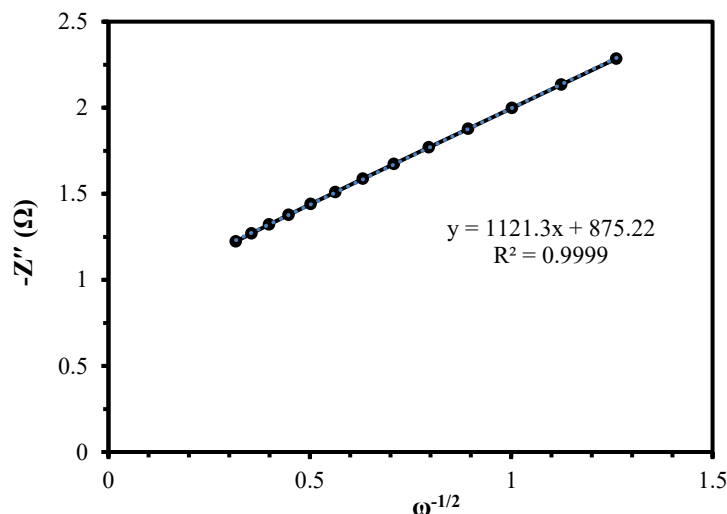


Figure 5.10. The slope of the $-Z''$ vs $\omega^{-1/2}$ provides the fitted σ value.

The aptasensor response was evaluated by measuring the change in R_{ct} using faradaic EIS. Steel et al. have shown that the behavior of hydroxythiol monolayers on gold is well described by an ideal parallel plate capacitor.[182] In the absence of MCH treatment, the DNA-modified electrode capacitance is slightly smaller than that of a bare gold electrode (3.54 vs 4.23 μF). Comparison of the mixed DNA/MCH capacitances to pure MCH monolayer values shows that the mixed systems have solvent and ionic permeabilities that are quite similar to those of a pure MCH monolayer. The slight increase (0.617 μF in mixed aptamer-MCH vs 0.560 μF in MCH-only) in the mixed system capacitances compared to the pure MCH values indicates a slightly enhanced ionic permeability in the mixed system. The capacitance data for DNA samples with and without treatment with MCH support the contention that the MCH treatment largely reorganizes the DNA from the surface to a conformation where each probe is immobilized solely through the thiolate end.

To reduce the effect of cyanides on gold, EIS in measurement buffer was not done before the thrombin test to make the surface suitable for thiol-SAM formation. To regenerate the

aptamer from the bound thrombin, the electrode was incubated with 3 M KCl at 37 °C, impairing the electrostatic forces and affinity between the aptamer and protein and releasing the bound thrombin.[129] The negative control (incubation with human serum albumin without thrombin) and buffer stability (incubation in folding buffer without any protein) in similar conditions were conducted, and the results are reported in Table 5.8. Compared to the sensor response (9.4%), the nonspecific response is much lower (-0.72%). KCl incubation at 37 °C effectively regenerates the aptasensor (95% signal recovery). Sensor response was calculated using Equation 5.17 where R_{ct} thrombin is the charge transfer resistance after incubating thrombin on the aptamer and MCH-modified electrode, and R_{ct} aptasensor is the charge transfer resistance of the electrode after aptamer and MCH immobilization.

$$\text{Sensor response \%} = \frac{R_{ct} \text{ thrombin} - R_{ct} \text{ aptasensor}}{R_{ct} \text{ aptasensor}} \times 100 \quad 5.17$$

Table 5.7. Fitted average R_{ct} and C values for thrombin aptasensor without TCEP reduction (n = 3) on gold SPE and its regeneration by KCl 3M incubation. Thrombin binding increases R_{ct} but does not change C significantly.

Electrode	Average R_{ct} (Ω)	RSD%	Average C (μ F)	RSD%
Au/Aptamer/MCH	6735	5.5	0.542	14
Au/Aptamer/MCH/Thrombin	7760	4	0.546	14
KCl_Regeneration	7090	6	0.512	0.31
Sensor response %	15	6.6	0.76	20
KCl recovery %	95	8.3	106	14

Table 5.8. The effect of buffer stability and negative control test (50 μ M HSA) on Aptamer/MCH modified gold SPE show minimal nonspecific response.

Electrode	R_{ct} (Ω)	C (μ F)
Au/Aptamer	23940	0.891
Au/Aptamer/MCH	9780	0.985
Au/Aptamer/MCH_Buffer_Stability	9590	0.985
Au/Aptamer/MCH_HSA_Negative_Control	9520	0.983
Biofouling/Nonspecific response		-0.72%

5.6.11. Effect of TCEP on immobilization efficiency and aptasensor performance

The goal is to evaluate the effect of the reducing agent, TCEP, on the immobilization efficiency of TBA on gold electrodes. A 10 μ L of TCEP-reduced aptamer was drop-casted on the electrode and incubated for 12 h in a humidity chamber in room temperature. The drop was pipetted out, and 10 μ L of folding buffer was pipetted onto the electrode twice. Then, the electrode was rinsed twice with 100 μ L of measurement buffer each time. Then the impedance was recorded by the EIS technique. TCEP-reduced aptamer increased R_{ct} significantly to \approx 24 k Ω . After MCH immobilization, R_{ct} decreased to \approx 8 k Ω due to aptamer reorganization. Buffer stability was assessed by incubating the aptasensor in folding buffer for 30 minutes and then measuring EIS again, which showed minimal changes in the impedance spectra. A negative control test was performed by incubating the electrode with 100 μ g/mL human serum albumin (HSA) for 30 minutes, which showed minimal change in impedance, indicating selectivity of the aptamer and anti-biofouling characteristics of MCH. The prepared thrombin solution was incubated with the aptasensor

for 5 minutes and 30 minutes at room temperature. No significant difference was observed between 5 minutes and 30 minutes of incubation time, as both incubation times increased the R_{ct} consistently by $\approx 600 \Omega$. The sensor was rinsed thoroughly with water and incubated in folding buffer for 30 minutes. The R_{ct} did not change significantly. Thrombin was incubated again on the sensor for 5 minutes. The R_{ct} increased consistently by an additional 600Ω . The aptamer-thrombin complex affinity was found to be strong since, after washing the electrode for 5 minutes with 37°C KCl 3M, it did not reduce the R_{ct} significantly; thus, the washing with KCl was further increased to 30 minutes in a 37°C water bath, which reduced the R_{ct} by $\approx 500 \Omega$. The sensor responses on the aforementioned conditions were calculated and shown in Table 5.9.

Table 5.9. Effect of experimental variables, TCEP reduction and thrombin pipetting on sensor response. The RSD is provided to represent the variability in the data collected from three different gold SPEs for each condition.

Modification	Sensor response (%)	RSD (%)
TCEP_Aptamer_MCH2h_Thrombin	15	23
NonTCEP_Aptamer_MCH4h_Thrombin	33	28
NonTCEP_Aptamer_MCH2h_Thrombin	15	23
NonTCEP_Aptamer_MCH4h_Thrombin_Pipetted	46	22

More experiments were conducted to investigate the effect of MCH time of incubation and the mode of thrombin incubation for a fixed amount of aptamer ($10 \text{ ng}/\mu\text{L}$), MCH (1 mM), and thrombin ($25 \text{ U}/\text{mL}$). Even though both non-TCEP and TCEP-treated aptasensor responses were significantly different from the negative control (p-values 0.026 and 0.024,

respectively). However, the sensor response of TCEP-treated aptasensors is not substantially different from the sensor response of a non-TCEP-treated aptasensor (p-value 0.996). A significant difference was found between the 4-hour MCH incubation and the 2-hour MCH incubation, indicating that more prolonged incubation leads to better organization of aptamers, resulting in a higher sensor response (p-value = 0.024). Moreover, instead of one-time direct pipetting on the working electrode, the thrombin solution was pipetted in and out several times to facilitate flow and binding. It was observed that this process caused a significant increase in binding compared to the control group, which involved pipetting once (p-value 0.006).

Another trial was conducted based on the idea that dispersed aptamers could yield a higher sensor response. The target is a large, charged protein molecule, much bigger than the aptamer. The affinity between the aptamer binding site and thrombin requires sufficient space to minimize spatial hindrance. Assuming the aptamer-protein is a complex 1:1 ratio and considering the maximum significantly meaningful thrombin concentration is not more than 1 μM in a normal Thrombin Generation Assay (TGA) and usually within the range of 1 nM to 1 μM , a 1 μM fixed thrombin concentration was chosen to study the sensor response to the upper limit. After TCEP reduction of the aptamer, it was incubated for 1 hour on E-polished gold SPE at room temperature. After 1 hour, the aptamer droplet was pipetted out. $3 \times 10 \mu\text{L}$ of the folding buffer was drop-casted and pipetted out from the working electrode, and then the electrode was rinsed with $3 \times 200 \mu\text{L}$ of folding buffer. The EIS test was conducted, and the resulting Nyquist and complex capacitance plots are shown in Figure 5.11. Buffer stability in the folding buffer was evaluated regarding SAM stability. If the Nyquist plot did not show overlap, buffer stability was repeated. After

stabilizing the aptamer SAM, 10 μL MCH 1 mM was incubated on the working electrode for 1 hour at room temperature. The same washing step and buffer stability test were done. Then, a 250 μM thrombin stock solution was rapidly thawed at 37 $^{\circ}\text{C}$ using a dry bath and diluted to 1 μM in folding buffer. It was then immediately cast onto the Aptamer-MCH modified electrode, 10 μL for 30 minutes. Then the washing and stability test was conducted again. A sensor response of $\approx 80\%$ was measured for the upper limit of thrombin. In a similar test for a control (HSA 100 μM), the sensor response is $\approx 7\%$. Thrombin 5 μM did not attach to an MCH-modified surface with a response of -15% . The mean R_{ct} value of three electrodes with their respective RSDs is shown in Table 5.10.

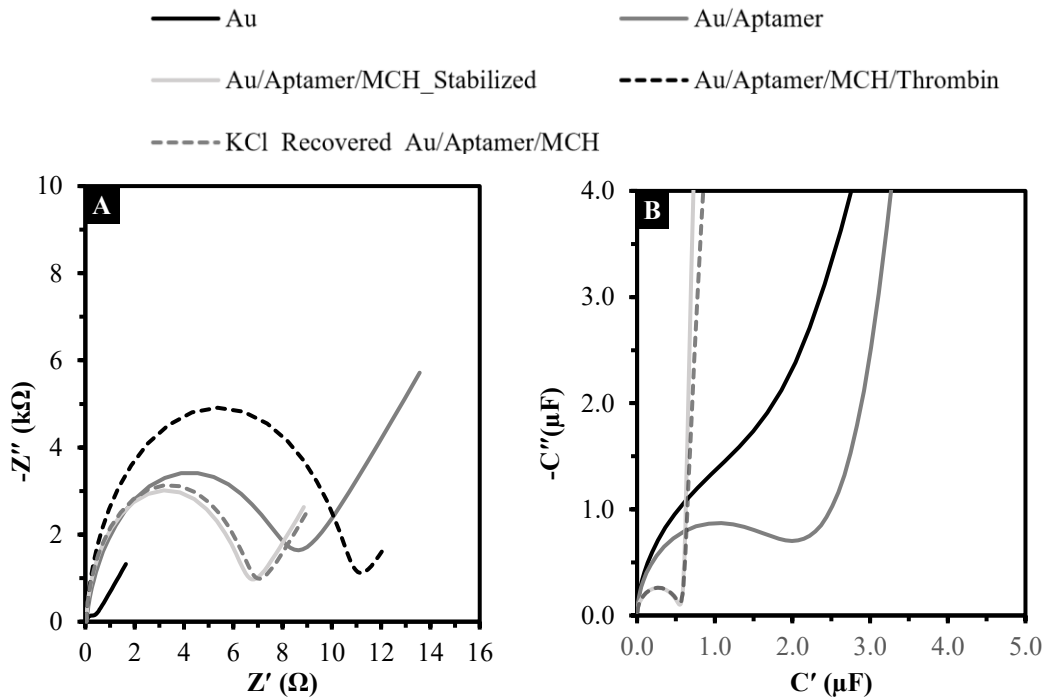


Figure 5.11. A) Nyquist plot and B) complex capacitance plot of a TCEP-reduced aptasensor.

Table 5.10. Aptasensor binding analysis by faradaic EIS. R_{ct} increases in each step of modification and further increases by thrombin-aptamer binding due to steric hindrance of charge transfer and electrostatic repulsion of the redox couple.

Modification	R_{ct}	RSD
E-polished	350	7%
Aptamer	6660	27%
MCH	8550	21%
Buffer stability	6450	13%
Thrombin_1 μ M_30min	11390	12%
Sensor Response	81%	19%

Our developed protocol to fabricate and regenerate the aptasensor included the following steps:

- Electrodes were incubated with 10 ng/ μ L TCEP-reduced aptamer for 1 hour.
- Electrodes were rinsed three times with 500 μ L folding buffer.
- Electrodes were incubated with 1 mM MCH for 1 hour.
- Electrodes were rinsed three times with 500 μ L folding buffer, followed by incubation in the folding buffer for 1 hour.
- Thrombin testing was performed at room temperature with a 30- minutes incubation.
- Electrodes were rinsed gently by pipetting three times with 10 μ L folding buffer.

- 100 μL of measurement buffer was incubated on the electrode for 5 minutes, followed by EIS measurement.
- To regenerate the electrodes, 10 μL of 3M KCl was incubated on the working electrode for 30 minutes at 37 $^{\circ}\text{C}$ followed by rinsing three times with 500 μL folding buffer

The sensor response for 1 μM thrombin is $\approx 80\%$ compared to the control group. The fabricated aptasensor exhibited antibiofouling properties, as MCH modification helps minimized thrombin and HSA biofouling, with a slight increase in sensor response of 0.5-5%. Unmodified electrodes strongly adsorb thrombin due to disulfide bonds, thus MCH modification was essential for reducing non-specific binding. The aptasensor was regenerated by incubating in 3 M KCl for 1 hour, followed by 1 hour buffer stabilization at room temperature.

5.6.12. MCH:aptamer co-immobilization

The potential role of MCH as a reducing agent in place of an aptamer was investigated. Ellman's reagent test showed a colour change from clear to yellow when MCH interacts with 5,5'-dithio-bis-(2-nitrobenzoic acid) (DTNB), which indicates that MCH can break the disulphide bonds in DTNB.[179] This raises the possibility that MCH could also break disulfide bonds in a di-thiol modified aptamer when they are mixed. However, our findings showed that the aptamer did not tether to the gold surface during this process (Figure 5.12). This is mainly because the high concentration of MCH (1 mM) saturated the surface and competes with the lower concentration of the aptamer (1 μM) for binding. Additionally, the Nyquist plot confirms that co-immobilization did not happen, as there was no significant change in R_{ct} or C in the mixed system compared to a pure MCH setup or layer-by-layer assembly.

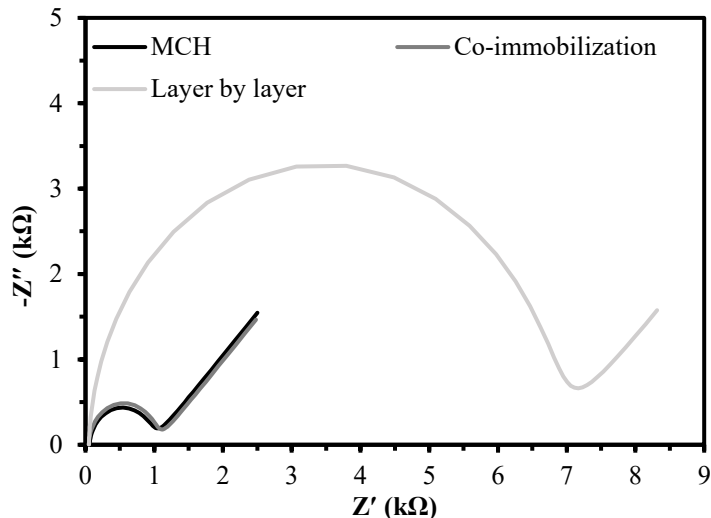


Figure 5.12. Nyquist plot of aptamer:MCH co-immobilization.

5.6.13. Sandwich aptamer assay

In 1992, a 15-mer thrombin-binding aptamer (TBA-15) was discovered that binds to the fibrinogen-binding exosite of thrombin.[16] In contrast, a 29-mer variant (TBA-29) binds to the heparin site on thrombin.[130] Theoretically, mixing TBA-15 with thrombin and TBA-29 could create a "sandwich" format. This would potentially enhance the entrapment of the thrombin-aptamer complex, leading to a higher hindrance of charge transfer. However, in our experiments, the observed change in the sensing signal was smaller than that of the TBA-29 immobilized aptamer alone. Specifically, while TBA-29 demonstrated an 80% increase in sensor response based on charge transfer resistance (R_{ct}) changes, the sandwich assay only showed a 3% improvement (Figure 5.13). This suggests that the sandwich approach may not be as effective as initially speculated.

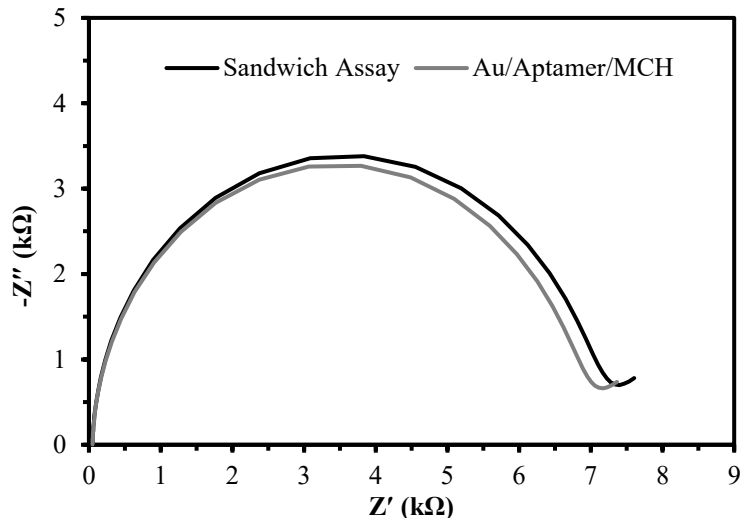


Figure 5.13. Sandwich assay using TBA15 as the homogenous assay pre-mixed with thrombin and incubated with TBA29 as the immobilized aptamer

5.6.14. Capacitive/non-faradaic EIS analysis of the aptasensor

A purely capacitive system, utilizing a non-redox electrochemical measurement buffer, can be employed in the fabrication of a biosensor.[189, 190] In the absence of redox species, the circuit is simplified to an uncompensated resistance (R_u) in series with CPE (Figure 5.3.B). The increase in layer thickness attributable to target binding may lead to a decrease in capacitance, which correlates with target concentration. We developed a similar approach based on non-faradaic EIS in the folding buffer. The fitted values based on the simplified circuit are provided in Table 5.11. According to Table 5.11, the R_u remained relatively constant ($\approx 40 \Omega$) regardless of the modifications made to the electrode. This stability in R_u is primarily due to the constant electrolyte concentration during the experiments. The constant phase element value (Q_0) first partially decreased from a clean (bare) gold electrode ($6.64 \mu\text{F}\cdot\text{s}^{n-1}$ to $3.91 \mu\text{F}\cdot\text{s}^{n-1}$) due to aptamer immobilization. Aptamer immobilization resulted in a decrease in capacitance since the aptamer monolayers increased the distance between the electrode and the double-layer ($C \propto 1/d$).[182] The slight

drop in n (0.895) suggests increased surface irregularity due to the flexible aptamer layer, resulting in less-ideal capacitance behaviour. However, after MCH immobilization the aptamer and MCH molecules rearranged during self assemble monolayer (SAM) formation forming a near-ideal capacitance behaviour ($n \approx 1$) as observed by the straight line in the Nyquist plot (Figure 5.14.A) The effective capacitance significantly dropped to 0.8 μF since MCH diminished any capacitive charging, as an organic layer with low ionic permeabilities[182]. The decrease in the capacitance was observed clearly in the complex capacitance plot, as shown Figure 5.14.B. The complex capacitance representation emphasizes values at high frequency since almost all faradaic current is blocked at high frequencies and all current passes through the electrode/electrolyte double-layer capacitance.[180] However, the target binding (thrombin) did not cause a change in the sensor response, resulting in a negligible change in capacitance. This limitation indicated that the system may not possess sufficient sensitivity for capacitive sensing.

Table 5.11. Quantitative fitted circuit analysis of non-faradaic EIS of aptasensors.

Electrode	R_u (Ω)	Q_0 ($\mu\text{F} \cdot \text{s}^{-n}$)	n	C (μF)
Au	40.48	6.643	0.911	11.5
Au/Aptamer	36.82	3.908	0.895	7.00
Au/Aptamer/MCH	39.13	0.776	0.985	0.817
Au/Aptamer/MCH/Thrombin	37.51	0.781	0.984	0.825

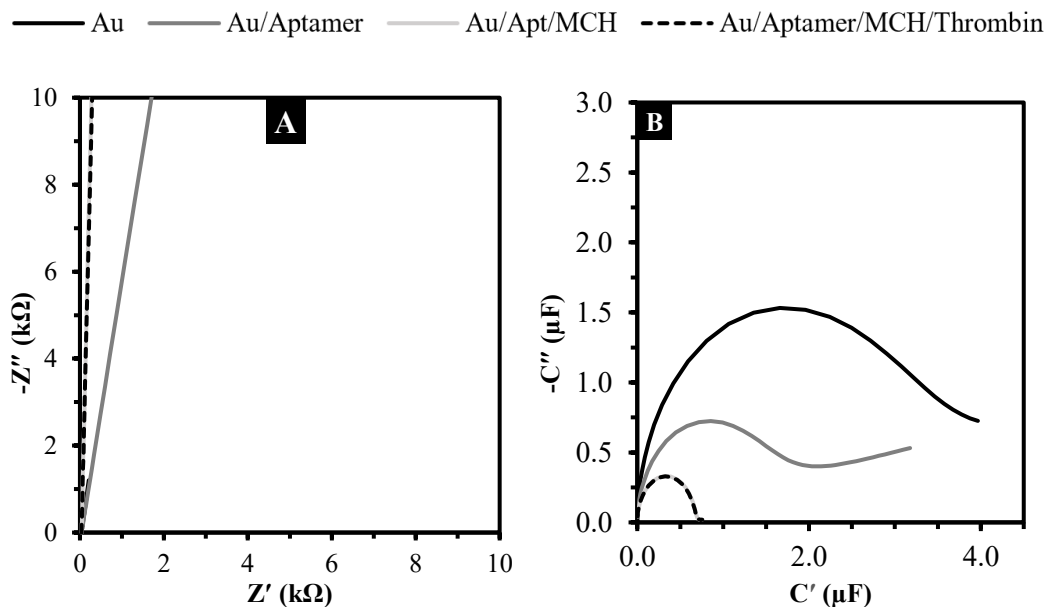


Figure 5.14. Non-faradaic EIS A) Nyquist plot and B) complex capacitance plot of a thrombin aptasensor.

5.6.15. Chromogenic and amperogenic thrombin assays

A commercial chromogenic thrombin substrate, H-D-Phe-Pip-Arg-pNA, was utilized in the enzymatic assay. Thrombin cleaved the Arg-nitroanilide bond, releasing pNA, which exhibits dual properties: it produces a yellow color with maximum absorption at 405 nm, which also can be electrochemically reduced at -0.8 V vs Ag/AgCl. Herein, the electrochemical properties of pNA (in 4.5 % DMSO) were evaluated by CV, indicating a distinct oxidation peak at ≈ 0.1 V and a reduction peak at ≈ -0.8 V (Figure 5.15.A). Increasing pNA concentrations amplified the reduction peak (Figure 5.15.B) and chronoamperometric tests at -0.85 V showed a proportional trend between current and pNA concentration (Figure 5.15.C). [11, 55] The CV of a 100 μM peptide-based substrate, combined with 1 μM thrombin and a control of 50 μM human serum albumin (HSA), is presented in Figure 5.15.D. After a 5-minute incubation at room temperature in the

presence of thrombin, both the reduction and oxidation peaks were observed to be higher than in the control test. This increase indicates that thrombin cleaves pNA from the amino acid arginine (Arg).

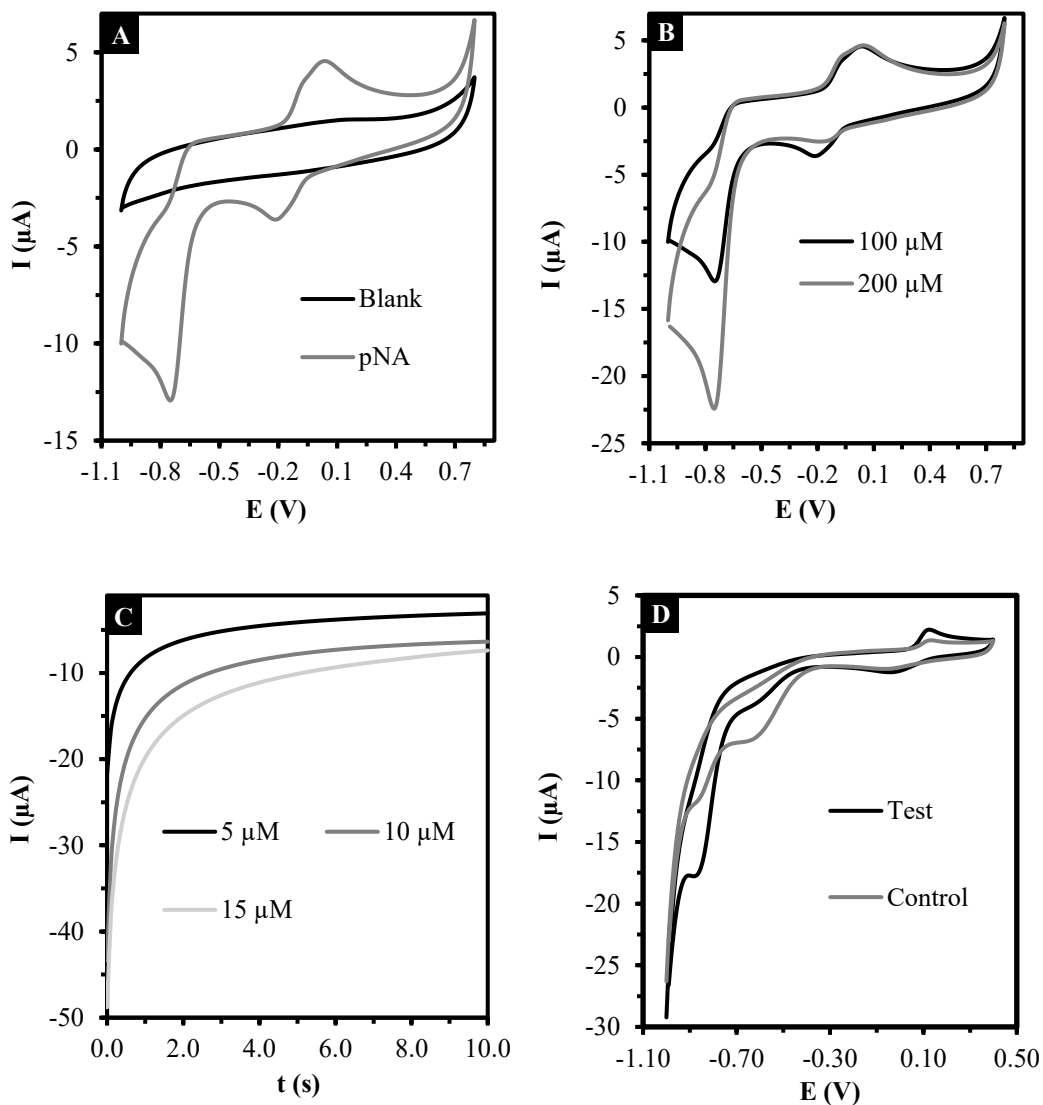


Figure 5.15. A) CV of pNA (100 μM in 4.5% DMSO) and blank (without pNA) on an GCE. B) CV of pNA 100 and 200 μM . C) Chronoamperometry (CA) response of varied concentration of pNA at -0.85 V for 10 s. D) CV of substrate with thrombin (1 μM) and HSA control (50 μM).

5.6.16. Square Wave Voltammetry (SWV) monitoring of thrombin enzymatic cleavage activity

An alternative approach using square wave voltammetry (SWV) was conducted to address the possibility that prolonged negative potentials during CV could lead to bilayer desorption, resulting in an oxidation peak at approximately 0.12 V after a shorter applied potential time. To further evaluate the necessity of reducing the nitro group of liberated pNA, a -0.3 V reduction potential (instead of -0.85 V vs Ag/AgCl) was applied for 1 s before the SWV scan, which did not produce any oxidation peaks, providing the necessity of nitro reduction before its oxidation (Figure 5.16.A). Another experiment involved capturing thrombin with the aptasensor to measure its enzymatic activity. After incubating various thrombin concentrations on an Aptamer/MCH-modified gold electrode, the substrate (100 μ M) was added and incubated, followed by an electrochemical reduction step at -0.85 V for 1 s and a SWV scan of the oxidation peak, demonstrating that the enzymatic cleavage of the substrate was proportional to thrombin concentration (Figure 5.16.B). Both CV and SWV showed that the oxidation and reduction potentials were directly proportional to thrombin concentration and significantly surpassed the control group (Figure 5.16.C). To cross-verify the cleavage activity of thrombin, UV-Vis absorption spectrophotometry was conducted to scan the absorption of uncleaned and cleaved substrate.

Compared to the control group (50 μ M HSA), peak absorption at 405 nm is observed, proportional to thrombin's concentration (Figure 5.16.D). Enzymatic activity measured via SWV exhibited greater sensitivity, with \approx 90-fold increase in the sensing response compared to the faradaic EIS technique (Table 5.12).

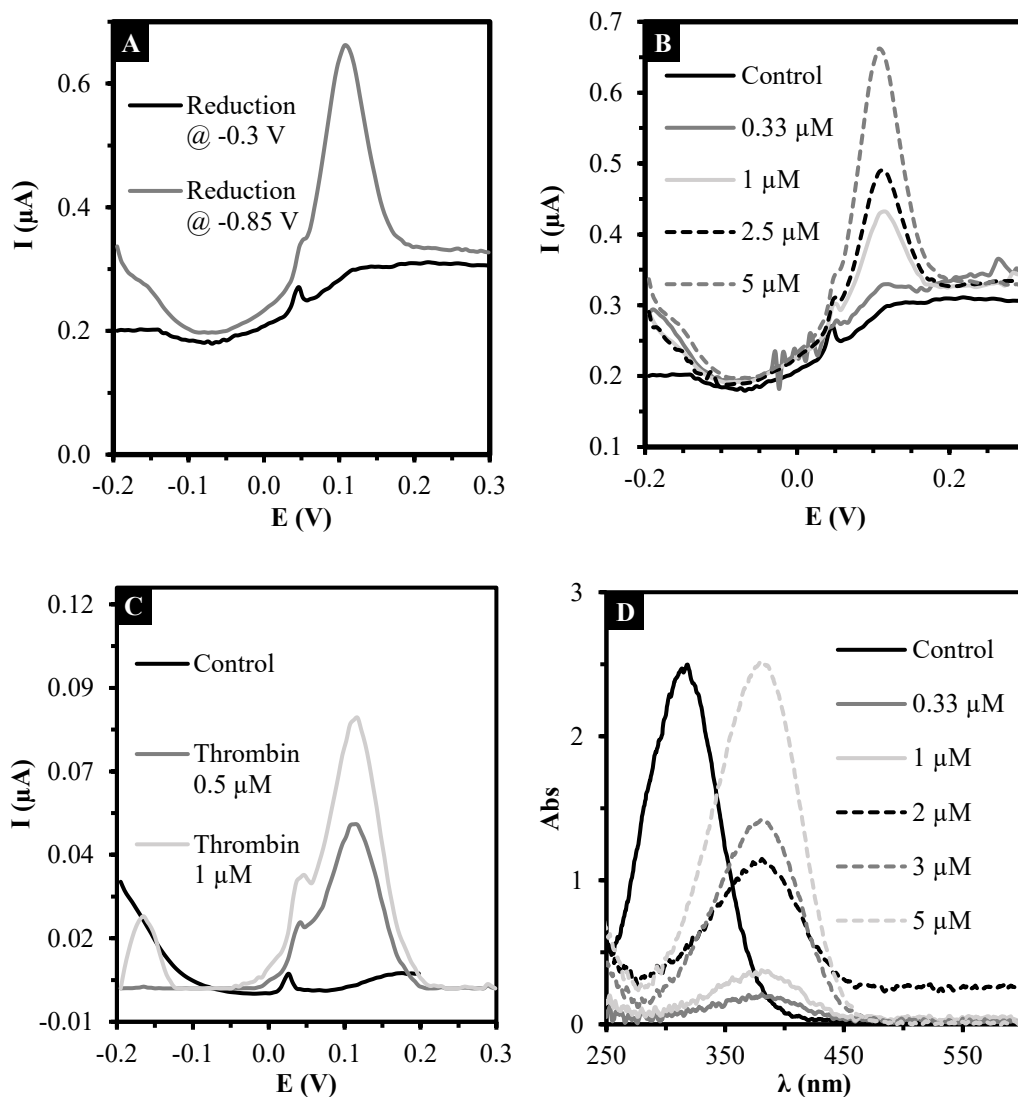


Figure 5.16. A) Effect of reduction potential on signal generation. B) Direct enzymatic reaction measurement by SWV in the presence of varied amounts of thrombin (without aptamer). C) Aptasensor coupled with thrombin substrate for enhanced detection of thrombin by detecting the oxidative current of cleaved substrate. D) UV-Vis spectrophotometry of varied concentrations of thrombin in the presence of 100 μM substrate vs control (50 μM HSA).

Table 5.12. Peak current SWV of thrombin aptasensing coupled with enzymatic reaction shows high sensitivity attributed to the cleaved pNA oxidation.

Enzymatic Thrombin Aptasensing			
	Control	Thrombin 0.5 μM	Thrombin 1 μM
Current at 0.12 V (μA)	0.0010	0.048	0.081
Relative sensor response (%)	0	4410	7370

5.6.17. Enzymatic activity of immobilized thrombin on gold

Thrombin contains multiple disulfide bonds and can be chemisorbed onto electrodes through thiol-gold bonds. We evaluated the enzymatic cleavage activity of the tethered thrombin and found that it retained its activity after a short incubation period of 30 minutes. This was indicated by an oxidation current of 0.249 μA (Figure 5.17.A). Notably, this current was significantly higher than the 0.81 μA oxidation current observed for thrombin captured by an aptasensor as shown in Figure 5.17.A. In the aptasensor design, MCH functions as a backfilling and anti-fouling agent, effectively reducing non-specific binding. Although changes in R_{ct} by non-specific adsorption were minimal, would it be possible to observe the small amount of randomly attached thrombin on the MCH-saturated surface? To address this, a 1 mM MCH backfilled gold electrode was incubated with 1 μM thrombin for 30 minutes.

While no significant R_{ct} change occurred with thrombin or HSA, the enzymatic assay revealed that thrombin does attach to the MCH-modified gold, albeit at a lower level compared to an unmodified gold electrode, with current readings of 0.11 μA for MCH-

modified gold versus 0.249 μA for bare gold (Figure 5.17.A). Moreover, the reproducibility of the generated signal was evaluated through repeated SWV measurement, and the RSD was found to be 15% across five independent measurements (Figure 5.17.B). Furthermore, the un-cleaved tripeptide substrate is not entirely resistant to oxidation. This oxidation occurs at a potential of 0.037 and 0.4 V, resulting in a slight peak current of 0.038 and 0.031 μA as depicted in Figure 5.17.C. Meanwhile, the release of pNA from a thrombin substrate $\beta\text{-Ala-Gly-Arg-p-nitroanilide}$ during hydrolysis was monitored using differential pulse voltammetry (DPV) in a previous study.[191] The peak potentials for free pNA and peptide-bound para-nitroaniline were recorded at pH 7.5, yielding values of -0.77 V vs. Ag/AgCl.[174] It is essential to note that utilizing such negative scan potentials can lead to the detachment of aptamers, as well as the potential oxidation of proteins or the modification of gold surfaces. In our experiment, with thrombin and substrate concentrations of 1 μM and 100 μM , respectively, the reduction current exhibited peak responses at two distinct potentials: first at -0.3 V and subsequently at -0.6 V. When we compared the reduction potential of the nitro group to its amine counterpart at -0.6 V, and its subsequent oxidation back to nitro at 0.2 V, we observed that the reduction peak signal was ≈ 2.5 times greater than the oxidation peak signal (Figure 5.17.D). However, the reduction current monitoring technique was no further evaluated due to its potential to interfere with the aptamer structure, the electrochemical overlap with the oxygen reduction reaction, and other side reactions that may occur at such negative potentials.[55]

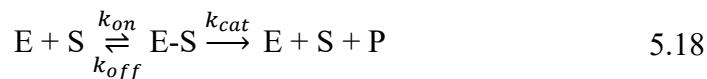
Two primary performance comparisons have been concluded from these experiments: 1) EIS vs enzymatic assay (both with aptamer-modified gold electrodes): Under similar conditions, the enzymatic assay yielded ≈ 90 -fold higher signal relative to its control

compared to the label-free EIS method, demonstrating the superior amplification achievable via enzymatic readout. 2) Enzymatic assay with different electrode configurations:

Using (I) aptamer and MCH-modified electrode produced 0.081 μA oxidation current, (II) MCH-modified electrode without the aptamer produced 0.110 μA , and (III) bare gold electrode produced 0.249 μA . This counterintuitively shows that aptamer incorporation in this assay format actually reduced the current signal relative to MCH-only and bare gold conditions. Taken together, these results indicate that in the current configuration, performance is limited more by aptamer–target affinity and immobilization effects than by the electrochemical detection method itself. Direct enzymatic activity measurements remain a robust detection route.

5.6.18. Kinetics of thrombin enzymatic cleavage of pNA from H-D-Phe-Pip-Arg-pNA

Cleavage of the electrogenic substrate by thrombin was kinetically studied by the following two-step reaction, where E is the thrombin (enzyme), S is the substrate (H-D-Phe-Pip-Arg-pNA), E-S is the thrombin-substrate complex, and P is the cleaved pNA, as shown in Equation 5.18;



where the magnitude of the forward rate constant k_{on} determines the collision rate of E and S and the backward rate constant k_{off} determines how readily the complex will fall apart in enzyme and substrate. The catalytic rate constant k_{cat} determines how readily the complex will produce a product (pNA).

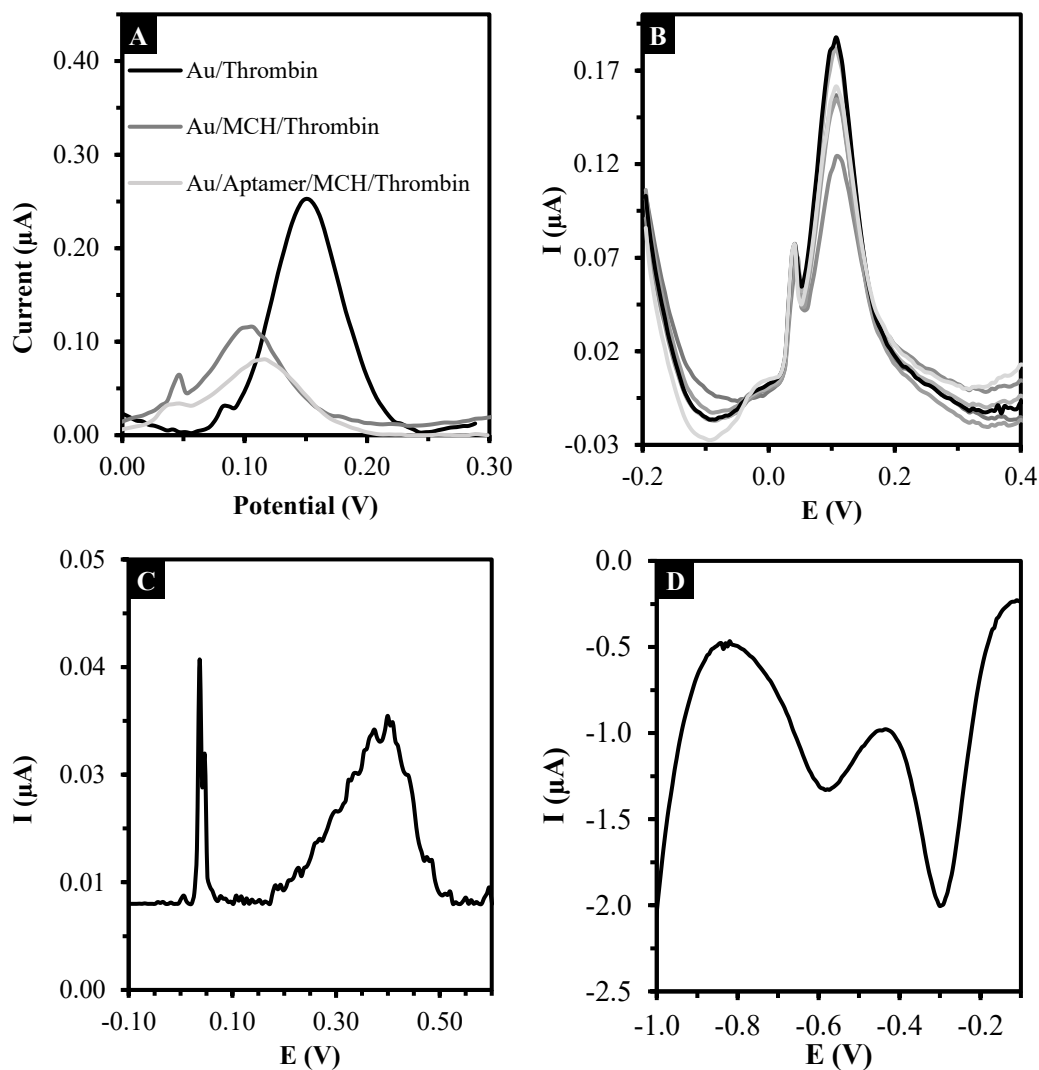


Figure 5.17. A) Oxidation current of 1 μM tethered thrombin on gold electrode with or without MCH after 20 min in presence of 100 μM substrate. B) The reproducibility of peak oxidation current was assessed through five repeated measurements of the same concentration of thrombin (1 μM). C) Oxidation of substrate in absence of thrombin. D) SWV of pNA release from thrombin substrate in the presence of 1 μM thrombin shows two-step reduction at -0.3 and -0.6 volts due to nitro to amine reduction.

To calculate the kinetic parameter, the general equation for enzymatic reaction rates known as the Michaelis-Menten formula was applied as shown in Equation 5.19;

$$v = \frac{V_{max} [S]}{K_m + [S]} \quad 5.19$$

where V_{max} is the maximum reaction rate and K_m is the Michaelis-Menten constant. Our method for determining K_m is based on the Lineweaver–Burk transformation. To provide the Lineweaver–Burk plot, the inverse of reaction rate ($1/v$) is plotted against the inverse of substrate concentration ($1/[S]$). The reaction rate (v) was based on the slope of pNA oxidation current over the first 60 seconds of enzymatic reaction. Given the Lineweaver–Burk, Michaelis-Menten constant (K_m) and maximum reaction rate (V_{max}) is derived from Equation 5.20.

$$\frac{1}{v} = \frac{K_m}{V_{max}} \frac{1}{[S]} + \frac{1}{V_{max}} \quad 5.20$$

Equation 5.20 reveals a linear relationship between $1/v$ and $1/[S]$ where $\frac{K_m}{V_{max}}$ is the slope and $\frac{1}{V_{max}}$ is the intercept. To determine the reaction rate (v) in $\mu\text{A}\cdot\text{s}^{-1}$ for each substrate concentration, the slope of the generated oxidation peak versus time was plotted. This slope was calculated by measuring the change in current over a 60-second interval. From the linear regression equation derived from the Lineweaver-Burk plot (Figure 5.18), K_m was found to be $174 \mu\text{M} \pm 10 \mu\text{M}$.

5.6.19. Analytical performance of electrochemical enzymatic thrombin sensing and aptasensing

To determine the linear range, limit of detection (LOD), and linear correlation coefficient between thrombin concentration and sensor signal, varying amounts of thrombin were analyzed using the two developed biosensors. In the enzymatic sensor, a fixed substrate

concentration (200 μM) was mixed with varied concentrations of thrombin. The calibration curve is based on the reaction rate (v in $\text{nA}\cdot\text{s}^{-1}$) in the first 60 seconds of thrombin introduction (Figure 5.19.A). In the aptasensor, fixed concentrations of TCEP-reduced aptamer (10 $\text{ng}/\mu\text{L}$) and MCH (1 mM) were immobilized on the gold SPE for 1 hour at room temperature in a humidity chamber and varied concentrations of thrombin were incubated on the aptasensor for 30 minutes (Figure 5.19.B). The analytical figures of merit for thrombin detection using the developed electrochemical sensors are presented in Table 5.13.

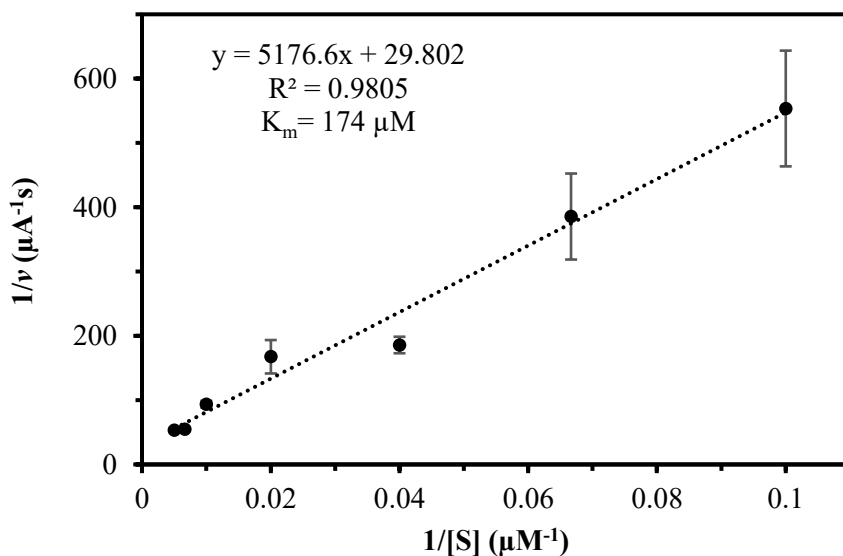


Figure 5.18. Lineweaver–Burk plot of the enzymatic thrombin activity (100 nM) monitoring on Italsens gold SPE using varied amounts of H-D-Phe-Pip-Arg-pNA substrate. Reaction rate (v) was the slope of the pNA oxidation peak current in the first 60 seconds of thrombin introduction. Error bars shown for each point were based on the three replicates of each thrombin concentration on freshly prepared gold SPEs. RSD of calculated K_m found to be 5.7%.

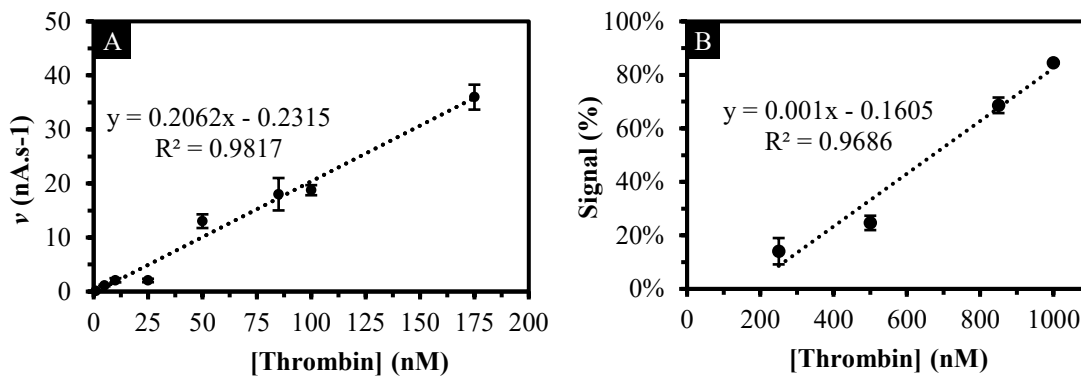


Figure 5.19. Calibration plots of thrombin biosensing on Italsens gold SPE; A) Enzymatic electrochemical thrombin assay: Substrate concentration was kept constant (200 μ M) in all experiments. Reaction rate (v) was the slope of the pNA oxidation peak current in the first 60 seconds of thrombin introduction. B) Thrombin aptasensing using 10 ng/ μ L aptamer and 1 mM MCH, both incubated for 1 hour. Error bars shown for each point were based on the three replicates of each thrombin concentration.

Table 5.13. Analytical figures of merit for thrombin detection using the developed aptasensor and enzymatic sensor.

Figures of merit	Label-free aptasensing	Enzymatic sensing
Linear range (nM)	250 – 1000	1 – 175
Correlation coefficient (r)	0.984	0.991
Limit of detection (nM)	165	0.24 nM
RSD of calibration slope	11%	5.5%

5.6.20. Selectivity tests

The selectivity of the developed enzymatic sensor and aptasensor was evaluated in the presence of three interfering proteins: human serum albumin (HSA), prothrombin, and fibrinogen. HSA was selected as a non-specific protein since it is the most abundant circulating protein found in plasma.[192] Fibrinogen and prothrombin were also included as interfering proteins because of their direct involvement with thrombin. Thrombin is generated through the enzymatic breakdown of prothrombin by factor Xa, making them structurally similar, and thrombin selectively cleaves fibrinogen to form fibrin clots.[161] The results of the selectivity test for enzymatic thrombin sensing are presented in Figure 5.20.A. The reaction solution was prepared with a fixed concentration of substrate (200 μM), thrombin (100 nM), prothrombin (0.7 μM), and fibrinogen (4.5 μM).

The results for the enzymatic reaction rates involving isolated interfering proteins, HSA, prothrombin, and fibrinogen, are not shown due to their minimal effect on the enzymatic reaction rate (less than $0.05 \text{ nA}\cdot\text{s}^{-1}$). In the presence of both fibrinogen and thrombin, a visible, sticky white clot formed that adhered firmly to the gold electrode. The clot resulted in a significant reduction in the enzymatic reaction rate ($\approx 16 \text{ nA}\cdot\text{s}^{-1}$ compared to $28 \text{ nA}\cdot\text{s}^{-1}$, $p\text{-value} < 0.05$) and a notable increase in the charge transfer resistance signal for aptasensing ($\approx 80\%$ compared to 12% for pure thrombin, $p\text{-value} < 0.05$). The results of the selectivity test for thrombin aptasensing are presented in Figure 5.20.B. The presence of fibrinogen without thrombin resulted in a reduction in the aptasensing signal ($\approx -28\%$), which could be due to the reorganization of SAMs. The presence of prothrombin and HSA did not lead to a significant change in the reaction rate ($p\text{-value} 0.07$) or the aptasensing signal ($p\text{-value} 0.09$).

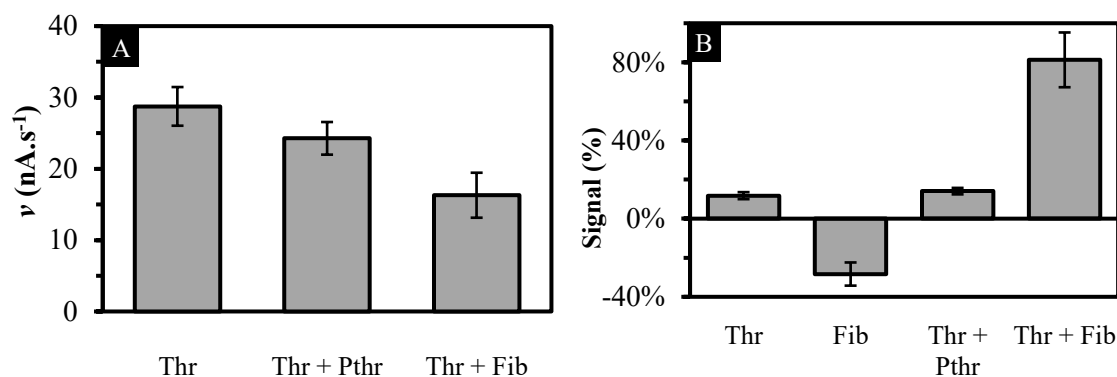


Figure 5.20. Selectivity tests of the developed biosensors for thrombin detection (Thr 100 nM) in the presence of interfering proteins, including prothrombin (Pthr, 0.7 μ M) and fibrinogen (Fib 4.5 μ M); A) Enzymatic sensor response, and B) aptasensor sensor response. Error bars are provided based on three replicates on Italsens gold SPE-based sensors.

5.7. Conclusion

This study evaluated thrombin detection via electrochemical aptasensing and enzymatic sensing strategies on screen-printed gold electrodes.

Aptasensing using faradaic Electrochemical Impedance Spectroscopy (EIS)

demonstrated sensitivity only at high thrombin concentrations (250–1000 μ M), with a maximum signal change of \approx 80%. The observed increase in R_{ct} was attributed to electrostatic repulsion of the redox probe $[\text{Fe}(\text{CN})_6]^{3-/4-}$ and steric hindrance caused by aptamer-thrombin binding at the electrode surface.

Non-faradaic EIS capacitance measurements were highly sensitive to self-assembled monolayer (SAM) formation and showed effective capacitance reduction from unmodified electrode (4.23 μ F) to aptamer and MCH modified electrode (0.56 μ F) but showed no significant change upon thrombin-aptamer binding.

Antibiofouling effect of MCH using faradaic and non-Faradaic EIS measurements showed no significant change upon thrombin incubation on MCH-blocked electrodes, suggesting effective suppression of nonspecific adsorption. However, enzymatic amplification revealed a previously unobserved phenomenon: thrombin retained catalytic activity even on MCH-blocked surfaces, producing an oxidation current of $\approx 0.11 \mu\text{A}$ compared to $\approx 0.25 \mu\text{A}$ on non-MCH-modified electrodes. This indicates that while MCH reduces biofouling, it does not eliminate it entirely.

Thrombin substrate H-D-Phe-Pip-Arg-pNA was found to possess dual chromogenic and electrogenic properties. Upon thrombin cleavage, para-nitroaniline (pNA) was released, exhibiting redox activity. pNA reduces at -0.85 V and oxidizes at 0.12 V versus Ag/AgCl on a gold SPE. Enzymatic kinetics followed Michaelis-Menten model ($K_m = 174 \pm 10 \mu\text{M}$), and a sensitive linear response was achieved for thrombin concentrations ranging from 1 to 175 nM.

Comparative analysis of detection strategies under identical aptamer-modified conditions revealed that the enzymatic assay produced approximately 90-fold higher signal relative to its control than the EIS-based method which showed the superior amplification capability and sensitivity of enzymatic readouts for thrombin detection.

The enzymatic electrochemical sensor developed in this study holds promise for integration into thrombin generation assays (TGA) and international normalized ratio (INR) prothrombin time (PT) tests, offering a potential tool for monitoring anticoagulant therapy and evaluating coagulation status and thrombotic risk.

5.8. Study limitations

This study utilized isolated human alpha-thrombin and interfering protein mixtures to evaluate biosensor performance. While these models offer controlled conditions for initial assay validation, they do not fully replicate the complexity of clinical matrices such as plasma or whole blood. Consequently, the sensor's behavior in a clinical setting remains unverified. Future work should incorporate clinical samples to assess biosensor robustness, specificity, and diagnostic relevance under physiologically relevant conditions. Furthermore, thrombin activity measurements obtained via the developed biosensors were not cross-validated against a gold-standard thrombin analyzer. Incorporating parallel measurements with a thrombin analyzer in future studies will be essential to confirm analytical validity and support clinical translation.

5.9. Future work

Further investigation and experiments are necessary for developing a sensitive and rapid electrochemical point-of-care thrombin generation assay.

1. **Preventing sensor blockage via clot inhibition:** Sensor fouling due to clot formation remains a challenge in whole blood applications. Future designs should incorporate anticoagulant strategies or surface modifications that inhibit fibrin deposition.
2. **Validation in real clinical samples and complex matrices:** Sensor performance must be evaluated in physiologically relevant samples, including citrated plasma, platelet-rich and platelet-poor plasma, and whole blood. Specificity testing in the presence of anticoagulants such as heparin and warfarin will be essential to confirm diagnostic reliability across diverse clinical contexts.

3. **Assessing aptamer influence on enzymatic activity:** The aptamer's binding to thrombin may modulate its catalytic behavior. Investigating this interaction will clarify mechanistic aspects of the sensing platform and guide optimization of both sensitivity and kinetic response.
4. **Quantifying and mitigating sensor drift:** Future work should characterize sensor drift under various operational conditions and explore calibration protocols or algorithmic corrections to maintain analytical consistency.
5. **Electrode type:** Comparative electrochemical studies using carbon, indium tin oxide, platinum, will identify optimal substrates for sensitivity, reproducibility, and integration into portable diagnostic platforms.

5.10. Authorship contribution

S.A.: Conceptualization, Data curation, Formal analysis, Investigation, Methodology, Project administration, Software, Supervision, Validation, Visualization, Writing – original draft Writing, Review and Editing. A.I.: Supervision, Funding acquisition, Resources, Project administration, Review and Editing

5.11. Acknowledgements

This work was carried out with financial support from the New Brunswick Innovation Foundation NBIF, Project No. EP-0000000155) & New Brunswick Health Research Fund NBHRF, Project No. 0000000045).

5.12. Conflict of interest

The authors declare no conflict of interest.

6. Summary and future work

6.1. Summary

This thesis investigated strategies for detecting protein targets with bioanalytical electrochemistry techniques. One particular focus of this thesis was on aptamer-based biorecognition elements immobilized on screen-printed gold electrodes. Electrochemical characterization methodologies were conducted to investigate the electron transfer processes at the electrode-aptamer interfaces. Faradaic and non-faradaic electrochemical impedance spectroscopy provided information regarding the charge transfer resistance, capacitance, and diffusion of redox species at the electrode-aptamer interface. Moreover, the effect of a blocking agent, mercaptohexanol, on electron transfer and capacitive properties of aptasensors was investigated.

In the first project described in Chapter 2, the binding between an ssDNA aptamer and SARS-CoV-2 spike protein was investigated. The pre-assumption behind the mechanism of binding affinity between aptamer and target was based on the reduction in electron transfer rate when the aptamer binds to its protein target. Thus, the affinity of large molecules such as proteins could be measured via faradaic electrochemical impedance spectroscopy in a measurement solution containing buffers and a common redox-active couple, namely ferro/ferricyanide. The previous research and our hypothesis were based on the assumption that the affinity between the aptamer and its protein targets would hinder the electron transfer from the bulk (measurement buffer) to the electrode. The reduction in the electron transfer rate was quantified by measuring the charge transfer resistance via the electrochemical impedance spectroscopy technique. The steric hindrance due to the captured protein being bound to the aptamer, as well as the charge repulsion by the

negatively charged redox ligands (cyanide-iron) and negatively charged captured protein residues increased the interfacial impedance. In other words, this mixed effect “impeded” charge transfer of redox, thus increasing charge transfer resistance, which was observed in the Nyquist plots of impedance spectra. The immobilized aptamer and blocking agent, mercaptohexanol, increased the charge transfer resistance of the gold electrode from ≈ 1.5 k Ω to 9 k Ω . Incubation of SARS-CoV-2 spike protein further increases the charge transfer resistance to ≈ 12 k Ω . Compared to control groups of non-specific proteins such as immunoglobulin A, serum albumin, and thrombin, SARS-CoV-2 spike protein increased the relative charge transfer resistance, i.e. sensor signal, by ≈ 3 -fold, showing a semi-selective response. This work provided a proof-of-concept framework of an impedance-based aptasensor for qualitative protein detection.

The limitation of our first work was that COVID-19 was not as prominent a topic in 2022-2023 as it was in early 2020 and 2021, due to global vaccine deployment and care measures that reduced costs and prevented further spread. Also, the emergence of highly sensitive lateral flow assays developed by major companies reduced the need for a specialized electrochemical platform to detect SARS-CoV-2. More importantly, SARS-CoV-2 has undergone rapid mutations, so the designed sensor must be updated each time with a new sequence of aptamer to measure the mutated spike protein.

Amid our projects on SARS-CoV-2 and thrombin detection, we used a massive number of screen-printed electrodes. Though we did not discuss using other types of electrodes, such as disc-shaped electrodes, in this thesis, we could not successfully fabricate aptasensors on them due to the lack of reproducibility and the challenges associated with their preparation. The significant cost of such electrodes raises the question of whether it is possible to

recycle them for reuse. For instance, one box of screen-printed gold electrodes, including 75 electrodes from Metrohm, costs about 700 CAD. Fabricating an aptasensor faced several challenges that led to significant electrode consumption. Many tests failed due to the lack of observable change in charge transfer resistance after aptamer incubation. Other issues include leakage between the counter and reference electrodes, optimizing the volume of the drop-cast solution, and experimenting with different concentrations of aptamer, protein, and blocking agents (data were not shown).

We found we need to run each test at least five times (five individual electrodes) to get statistically meaningful results because most of the time at least two sensors failed (significant drift, no observed change in impedance plot, high noise background). For instance, a test of measuring four proteins such as the one provided in Figure 2.10 at a fixed concentration required using $5 \times 4 = 20$ electrodes. The challenge of calibration is even higher if we want to calibrate an electrode using only 3 points (lower end, mid range, higher end) of the target's concentration. Optimizing other variables such as probe density, blocking agent density, etc., would increase these numbers even further.

The first project conducted at the University of Sydney was based on saving the cost of electrode consumption by recovering them through air plasma cleaning. As mentioned above biosensor development requires numerous trials and experiments, leading to overconsumption of expensive gold SPE. This motivated the research to evaluate the possibility of cleaning the gold SPEs rather than using them once and disposing of them after each use. It was shown that air plasma cleaning is a non-invasive and green surface treatment that effectively regenerates the used electrodes. It also resulted in much higher hydrophilicity (water contact angle of 33° compared to 100° new electrode), increased

surface area by ≈ 1.24 -fold, and a ≈ 2 -fold increase in thiol-terminated aptamer immobilization. The surface chemistry and electrochemical properties of such recovered electrode were studied, and it was observed that the charge transfer resistance decreases significantly after plasma regeneration, providing a highly conductive gold substrate with lower carbon-based sources of contamination, as observed by X-ray photo electron spectroscopy.

The second project at the University of Sydney was motivated by an interest in exploring alternative and cost-effective electrode substrates (carbon rather than gold) and evaluating a novel plasma-enhanced chemical vapour deposition to treat the carbon surface for capture probe immobilization. Immobilization of capture molecules such as aptamers has been dominated by self-assembled monolayer formation of thiol-terminated compounds or by carbodiimide crosslinker chemistry, streptavidin/biotin affinity, or gel membranes. This attempt was an alternative method based on plasma-activated coating, which had been shown to generate long-lived radicals on various surfaces such as glass and polymers for optical assays and cell cultures. This project aimed to investigate how plasma-activated coating affects the electrochemical properties of carbon electrode surfaces for electrochemical sensor fabrication. A significant improvement in the immobilization of thrombin-binding aptamer on plasma-activated electrode was verified by X-ray photoelectron spectroscopy. Compared to a control group of electrodes incubated with aptamer (without plasma treatment), we observed \approx a 3-fold increase in surface phosphorus of the group that was modified by plasma-activated coating. Moreover, the plasma-activated electrode showed near-zero charge transfer resistance. The sensor response to the

target thrombin, based on the relative change in charge transfer resistance, was $\approx 19\%$ compared to a control group of a non-specific protein, albumin.

Recently in our latest project outlined in Chapter 5, by going deeper into the biosensing mechanism, it was observed that this sensing mechanism of increased charge transfer is not solely due to the confined effect of steric hindrance and/or charge repulsion. We demonstrated that the affinity of the thrombin binding aptamer in an electrochemical format of self-assembled monolayers of immobilized thiol-terminated aptamer on a gold electrode, is only sensitive at thrombin concentrations above 100 nM. Even though at first it was observed in an optimized condition, charge transfer resistance increased by ≈ 1.8 -fold upon 1 μM thrombin incubation, but this change in charge transfer resistance did not necessarily relate to the aptamer-thrombin binding, but a mixed effect of thrombin non-specific absorption on the gold electrode due to its dithiol bonds and possibly due to aptamer/mercaptohexanol monolayer rearrangements. To prove this hypothesis, a gold electrode was only backfilled with blocking agent mercaptohexanol, and thrombin could still be detected by means of chromogenic/electrogenic substrate cleavage, leading to the release of electrogenic/chromogenic para-nitroaniline. The current peak detected by the square wave voltammetry method established that using aptamer or just mercaptohexanol without any aptamer does not significantly change the square wave voltammetry current peak of incubated thrombin.

The enzymatic activity of thrombin was further investigated using an electrochemical Micheles-Menten kinetic analysis. It was shown that thrombin rapidly cleaved its peptide-based substrate in seconds, which led to the detection of the cleaved product, para-

nitroaniline by square wave voltammetry technique. The enzymatic activity of thrombin showed a linear response from 1 to 175 nM with the detection limit of 0.24 nM.

6.2. Future work

This thesis focused on screen-printed gold electrodes as a primary material for sensor development. Alternative materials, which are more cost-effective and less susceptible to biofouling, demand further investigation. Building upon the current findings, expanding the range of electrode materials beyond commercially available screen-printed gold electrodes is imperative; this expansion should include carbon, indium tin oxide, and platinum electrodes.[97, 193]

In terms of aptasensing, the relationship between aptamer density and affinity signal remains unexplored, yet it appears to be crucial for sensor performance.[185] The label-free method examined in this work concentrated solely on homogeneous ferro/ferricyanide; however, recent literature and numerous commercial products emphasize the advantages of labeled methods (such as methylene blue or ferrocene tagged aptamers), which provide enhanced reproducibility and sensitivity.[194]

We did not investigate the performance of the aptasensor in a flow-based system that uses a rapid, ideally real-time, detection method. Our method was based on a fixed time analysis (usually after 30 minutes of target incubation in a steady, unstirred state) and full-spectra impedance analysis. Implementing a flow-based system with the capability for real-time detection, (such as a fixed frequency impedance method) allows for the continuous monitoring of interactions between the aptamer and its target.[195]

Future research should examine the effects of various plasma cleaning treatments, including pure nitrogen, argon, and oxygen, or mixtures of these gases, on the surface treatment and fabrication of electrochemical biosensors.[196] Our research provided the recycling of screen-printed gold electrodes up to three cycles. However, in future attempts, proper experiments need to be conducted to evaluate how many times the electrodes can undergo plasma treatment until failure. Also, the analytical figures of merit of plasma-recycled electrodes versus non-modified electrodes need to be compared, such as sensitivity, linear range, and detection limit.

In terms of plasma-activated coating treatment the surface characteristics of various carbon-based substrates, such as multi-walled carbon nanotubes, glassy carbon, and graphite, should be evaluated to establish proof-of-concept reagent-free biosensor fabrication. The long-term stability of plasma-treated electrodes necessitates assessment, particularly regarding the changes in electrochemical behavior (charge transfer resistance, capacitance) and surface chemistry (surface elemental composition) over time. The plasma activated coating modification method developed in this study will also be applied to other electrode surfaces, aiming to fabricate biosensors capable of continuous thrombin sensing, which holds significant market potential given the existence of innovative prothrombin time and activated clotting time sensors developed by Roche diagnostics and Abbot.[169]

To address biofouling challenges in whole blood applications, future sensor designs should consider the incorporation of anticoagulant coatings or surface modifications, such as zwitterionic polymers, which may inhibit fibrin deposition and maintain electrode accessibility during extended usage.[197, 198] Finally, clinical validation of the sensor

must encompass testing in physiologically relevant matrices, including citrated plasma, platelet-rich plasma, and whole blood.[168]

Last but not least, one of the important limitations of fabricating electrochemical sensors is the high cost and labour-intensive nature of sample analysis. Compared to an optical enzyme-linked immunosorbent assay (ELISA), which utilizes relatively inexpensive substrates and can accommodate multiple reaction zones—such as 96-well plates made of polystyrene—our method is limited to analyzing one electrode at a time. While ELISA can measure 96 reactions simultaneously, our output is slow, tedious, and costly due to the expensive materials involved, such as gold, platinum, and silver. It would be beneficial to develop inexpensive multi-electrode array substrates connected to a potentiostat with multiple readouts, enabling several tests to be conducted simultaneously, especially for binding analysis and calibration curves.

Bibliography

- [1] L.C. Clark, S. Kaplan, E.C. Matthews, P.K. Edwards, J.A. Helmsworth, Monitor and Control of Blood Oxygen Tension And pH During Total Body Perfusion, *Journal of Thoracic Surgery*, **1958**, 36 (4), 488-496.
- [2] L.C. Clark Jr., C. Lyons, Electrode Systems for Continuous Monitoring in Cardiovascular Surgery, *Annals of the New York Academy of Sciences*, **1962**, 102 (1), 29-45.
- [3] S.J. Updike, G.P. Hicks, The Enzyme Electrode, *Nature*, **1967**, 214 (5092), 986-988.
- [4] World Health Organization, Diabetes, Retrieved July 16, 2025. <https://www.who.int/health-topics/diabetes>.
- [5] S.A. Pullano, M. Greco, M.G. Bianco, D. Foti, A. Brunetti, A.S. Fiorillo, Glucose biosensors in clinical practice: principles, limits and perspectives of currently used devices, *Theranostics*, **2022**, 12 (2), 493-511.
- [6] A.H.B. Wu, A selected history and future of immunoassay development and applications in clinical chemistry, *Clinica Chimica Acta*, **2006**, 369 (2), 119-124.
- [7] H.R. Boehringer, B.J. O'Farrell, Lateral Flow Assays in Infectious Disease Diagnosis, *Clinical Chemistry*, **2021**, 68 (1), 52-58.
- [8] Katarzyna M. Koczula, A. Gallotta, Lateral flow assays, *Essays in Biochemistry*, **2016**, 60 (1), 111-120.
- [9] T. Naghdi, S. Ardalan, Z.A. Adib, A.R. Sharifi, H. Golmohammadi, Moving toward smart biomedical sensing, *Biosensors and Bioelectronics*, **2023**, 223, 115009.
- [10] S. Ardalan, A. Ignaszak, Innovations and Challenges in Electroanalytical Tools for Rapid Biosurveillance of SARS-CoV-2, *Advanced Materials Technologies*, **2022**, n/a (n/a), 2200208.
- [11] S. Ardalan, A. Ignaszak, Can Electrochemical Aptasensors Achieve the Commercial Success of Glucose Biosensors?, *Advanced Sensor Research*, **2023**, 3 (4), 2300132.
- [12] M.A. Morales, J.M. Halpern, Guide to Selecting a Biorecognition Element for Biosensors, *Bioconjugate Chem.*, **2018**, 29 (10), 3231-3239.
- [13] R.-M. Lu, Y.-C. Hwang, I.J. Liu, C.-C. Lee, H.-Z. Tsai, H.-J. Li, H.-C. Wu, Development of therapeutic antibodies for the treatment of diseases, *Journal of Biomedical Science*, **2020**, 27 (1), 1.
- [14] J.T.W. Tong, P.W.R. Harris, M.A. Brimble, I. Kavianinia, An Insight into FDA Approved Antibody-Drug Conjugates for Cancer Therapy, *Molecules*, **2021**, 26 (19), 5847.
- [15] A.D. Ellington, J.W. Szostak, In vitro selection of RNA molecules that bind specific ligands, *Nature*, **1990**, 346 (6287), 818-822.
- [16] L.C. Bock, L.C. Griffin, J.A. Latham, E.H. Vermaas, J.J. Toole, Selection of single-stranded DNA molecules that bind and inhibit human thrombin, *Nature*, **1992**, 355 (6360), 564-566.

- [17] A.D. Keefe, S. Pai, A. Ellington, Aptamers as therapeutics, *Nature Reviews Drug Discovery*, **2010**, 9 (7), 537-550.
- [18] E.J. Cho, J.-W. Lee, A.D. Ellington, Applications of Aptamers as Sensors, *Annual Review of Analytical Chemistry*, **2009**, 2 (Volume 2, 2009), 241-264.
- [19] D.S. Rijkers, S.J.H. Wienders, G.I. Tesser, H.C. Hemker, Design and synthesis of thrombin substrates with modified kinetic parameters, *Thrombosis Research*, **1995**, 79 (5), 491-499.
- [20] X. Pang, C. Cui, S. Wan, Y. Jiang, L. Zhang, L. Xia, L. Li, X. Li, W. Tan, Bioapplications of Cell-SELEX-Generated Aptamers in Cancer Diagnostics, Therapeutics, Theranostics and Biomarker Discovery: A Comprehensive Review, *Cancers (Basel)*, **2018**, 10 (2), 47.
- [21] K.B. Mullis, F.A. Faloona, Specific synthesis of DNA in vitro via a polymerase-catalyzed chain reaction, *Methods in Enzymology*, Academic Press, **1987**, pp. 335-350.
- [22] B.P. Biotechnologies, What is an Aptamer? – Aptamers and SELEX, Retrieved **2025-02-15**. <https://basepairbio.com/what-is-an-aptamer/>.
- [23] A.M. Downs, K.W. Plaxco, Real-Time, in Vivo Molecular Monitoring Using Electrochemical Aptamer Based Sensors: Opportunities and Challenges, *ACS Sensors*, **2022**, 7 (10), 2823-2832.
- [24] D. Voet, J.G. Voet, C.W. Pratt, *Fundamentals of Biochemistry: Life at the Molecular Level*, Wiley, **2016**.
- [25] P.V. Iyer, L. Ananthanarayan, Enzyme stability and stabilization—Aqueous and non-aqueous environment, *Process Biochemistry*, **2008**, 43 (10), 1019-1032.
- [26] E. Miller, H.D. Sikes, Addressing Barriers to the Development and Adoption of Rapid Diagnostic Tests in Global Health, *Nanobiomedicine*, **2015**, 2, 6.
- [27] Z. Watkins, A. Karajic, T. Young, R. White, J. Heikenfeld, Week-Long Operation of Electrochemical Aptamer Sensors: New Insights into Self-Assembled Monolayer Degradation Mechanisms and Solutions for Stability in Serum at Body Temperature, *ACS Sensors*, **2023**, 8 (3), 1119-1131.
- [28] S. Arshavsky-Graham, C. Heuer, X. Jiang, E. Segal, Aptasensors versus immunosensors—Which will prevail?, *Engineering in Life Sciences*, **2022**, 22 (3-4), 319-333.
- [29] H. Hasegawa, N. Savory, K. Abe, K. Ikebukuro, Methods for Improving Aptamer Binding Affinity, *Molecules*, **2016**, 21 (4), 421.
- [30] T. Adachi, Y. Nakamura, Aptamers: A Review of Their Chemical Properties and Modifications for Therapeutic Application, *Molecules*, **2019**, 24 (23), 4229.
- [31] H.P. Erickson, Size and Shape of Protein Molecules at the Nanometer Level Determined by Sedimentation, Gel Filtration, and Electron Microscopy, *Biological Procedures Online*, **2009**, 11 (1), 32.

- [32] V. Crivianu-Gaita, M. Thompson, Aptamers, antibody scFv, and antibody Fab' fragments: An overview and comparison of three of the most versatile biosensor biorecognition elements, *Biosensors and Bioelectronics*, **2016**, 85, 32-45.
- [33] S.B. Bankar, M.V. Bule, R.S. Singhal, L. Ananthanarayan, Glucose oxidase — An overview, *Biotechnology Advances*, **2009**, 27 (4), 489-501.
- [34] V. Vogiazzi, A. De La Cruz, W.R. Heineman, R.J. White, D.D. Dionysiou, Effects of Experimental Conditions on the Signaling Fidelity of Impedance-Based Nucleic Acid Sensors, *Analytical Chemistry*, **2021**, 93 (2), 812-819.
- [35] Z. Zhang, R. Pandey, J. Li, J. Gu, D. White, H.D. Stacey, J.C. Ang, C.-J. Steinberg, A. Capretta, C.D.M. Filipe, K. Mossman, C. Balion, M.S. Miller, B.J. Salena, D. Yamamura, L. Soleymani, J.D. Brennan, Y. Li, High-Affinity Dimeric Aptamers Enable the Rapid Electrochemical Detection of Wild-Type and B.1.1.7 SARS-CoV-2 in Unprocessed Saliva, *Angewandte Chemie International Edition*, **2021**, 60 (45), 24266-24274.
- [36] N. Arroyo-Curras, K. Scida, K.L. Ploense, T.E. Kippin, K.W. Plaxco, High Surface Area Electrodes Generated via Electrochemical Roughening Improve the Signaling of Electrochemical Aptamer-Based Biosensors, *Anal Chem*, **2017**, 89 (22), 12185-12191.
- [37] A.C. Lazanas, M.I. Prodromidis, Electrochemical Impedance Spectroscopy—A Tutorial, *ACS Measurement Science Au*, **2023**, 3 (3), 162-193.
- [38] W.H. Mulder, J.H. Sluyters, T. Pajkossy, L. Nyikos, Tafel current at fractal electrodes: Connection with admittance spectra, *Journal of Electroanalytical Chemistry and Interfacial Electrochemistry*, **1990**, 285 (1), 103-115.
- [39] C.-H. Kim, S.-I. Pyun, J.-H. Kim, An investigation of the capacitance dispersion on the fractal carbon electrode with edge and basal orientations, *Electrochimica Acta*, **2003**, 48 (23), 3455-3463.
- [40] B.-Y. Chang, S.-M. Park, Electrochemical Impedance Spectroscopy, *Annual Review of Analytical Chemistry*, **2010**, 3 (Volume 3, 2010), 207-229.
- [41] S. Wang, J. Zhang, O. Gharbi, V. Vivier, M. Gao, M.E. Orazem, Electrochemical impedance spectroscopy, *Nature Reviews Methods Primers*, **2021**, 1 (1), 41.
- [42] A.-E. Radi, J.L. Acero Sánchez, E. Baldrich, C.K. O'Sullivan, Reagentless, Reusable, Ultrasensitive Electrochemical Molecular Beacon Aptasensor, *Journal of the American Chemical Society*, **2006**, 128 (1), 117-124.
- [43] H. Cai, T.M.-H. Lee, I.M. Hsing, Label-free protein recognition using an aptamer-based impedance measurement assay, *Sensors and Actuators B: Chemical*, **2006**, 114 (1), 433-437.
- [44] D. Xu, D. Xu, X. Yu, Z. Liu, W. He, Z. Ma, Label-Free Electrochemical Detection for Aptamer-Based Array Electrodes, *Analytical Chemistry*, **2005**, 77 (16), 5107-5113.
- [45] A.E. Radi, J.L. Acero Sanchez, E. Baldrich, C.K. O'Sullivan, Reusable impedimetric aptasensor, *Anal Chem*, **2005**, 77 (19), 6320-3.

- [46] M.C. Rodriguez, A.-N. Kawde, J. Wang, Aptamer biosensor for label-free impedance spectroscopy detection of proteins based on recognition-induced switching of the surface charge, *Chemical Communications*, **2005**, (34), 4267-4269.
- [47] L.M. Fischer, M. Tenje, A.R. Heiskanen, N. Masuda, J. Castillo, A. Bentien, J. Émneus, M.H. Jakobsen, A. Boisen, Gold cleaning methods for electrochemical detection applications, *Microelectronic Engineering*, **2009**, 86 (4), 1282-1285.
- [48] J.-B.D. Green, E. Clarke, M.D. Porter, C.A. McDermott, M.T. McDermott, C.-J. Zhong, A.J. Bergren, On the Counter-intuitive Heterogeneous Electron Transfer Barrier Properties of Alkanethiolate Monolayers on Gold: Smooth versus Rough Surfaces, *Electroanalysis*, **2022**, 34 (12), 1936-1952.
- [49] X. Xu, A. Makaraviciute, J. Pettersson, S.-L. Zhang, L. Nyholm, Z. Zhang, Revisiting the factors influencing gold electrodes prepared using cyclic voltammetry, *Sensors and Actuators B: Chemical*, **2019**, 283, 146-153.
- [50] G. Feng, T. Niu, X. You, Z. Wan, Q. Kong, S. Bi, Studies on the effect of electrode pretreatment on the coverage of self-assembled monolayers of dodecanethiol on gold by electrochemical reductive desorption determination, *Analyst*, **2011**, 136 (23), 5058-5063.
- [51] X. Hua, H.L. Xia, Y.T. Long, Revisiting a classical redox process on a gold electrode by operando ToF-SIMS: where does the gold go?, *Chem Sci*, **2019**, 10 (24), 6215-6219.
- [52] S. Lee, W.J. Kim, M. Chung, Enhanced electrochemical biosensing on gold electrodes with a ferri/ferrocyanide redox couple, *Analyst*, **2021**, 146 (17), 5236-5244.
- [53] S. Vogt, Q. Su, C. Gutiérrez-Sánchez, G. Nöll, Critical View on Electrochemical Impedance Spectroscopy Using the Ferri/Ferrocyanide Redox Couple at Gold Electrodes, *Analytical Chemistry*, **2016**, 88 (8), 4383-4390.
- [54] J. Lazar, C. Schnelting, E. Slavcheva, U. Schnakenberg, Hampering of the Stability of Gold Electrodes by Ferri-/Ferrocyanide Redox Couple Electrolytes during Electrochemical Impedance Spectroscopy, *Analytical Chemistry*, **2016**, 88 (1), 682-687.
- [55] K.K. Leung, A.M. Downs, G. Ortega, M. Kurnik, K.W. Plaxco, Elucidating the Mechanisms Underlying the Signal Drift of Electrochemical Aptamer-Based Sensors in Whole Blood, *ACS Sensors*, **2021**, 6 (9), 3340-3347.
- [56] T. Ma, D. Bizzotto, Improved Thermal Stability and Homogeneity of Low Probe Density DNA SAMs Using Potential-Assisted Thiol-Exchange Assembly Methods, *Analytical Chemistry*, **2021**, 93 (48), 15973-15981.
- [57] T. Ma, I. Martens, D. Bizzotto, Thermal Stability of Thiolated DNA SAMs in Buffer: Revealing the Influence of Surface Crystallography and DNA Coverage via In Situ Combinatorial Surface Analysis, *Langmuir*, **2020**, 36 (48), 14495-14506.
- [58] V. Bhalla, S. Carrara, C. Stagni, B. Samori, Chip cleaning and regeneration for electrochemical sensor arrays, *Thin Solid Films*, **2010**, 518 (12), 3360-3366.
- [59] J. Kang, P.A. Rowntree, Gold film surface preparation for self-assembled monolayer studies, *Langmuir*, **2007**, 23 (2), 509-516.

- [60] A. Makaraviciute, X. Xu, L. Nyholm, Z. Zhang, Systematic Approach to the Development of Microfabricated Biosensors: Relationship between Gold Surface Pretreatment and Thiolated Molecule Binding, *ACS Applied Materials & Interfaces*, **2017**, 9 (31), 26610-26621.
- [61] C.M. Pharr, P.R. Griffiths, Infrared Spectroelectrochemical Analysis of Adsorbed Hexacyanoferrate Species Formed during Potential Cycling in the Ferrocyanide/Ferricyanide Redox Couple, *Analytical Chemistry*, **1997**, 69 (22), 4673-4679.
- [62] J. Das, S. Gomis, J.B. Chen, H. Yousefi, S. Ahmed, A. Mahmud, W. Zhou, E.H. Sargent, S.O. Kelley, Reagentless biomolecular analysis using a molecular pendulum, *Nature Chemistry*, **2021**, 13 (5), 428-434.
- [63] K. Raiber, A. Terfort, C. Benndorf, N. Krings, H.H. Strehblow, Removal of self-assembled monolayers of alkanethiolates on gold by plasma cleaning, *Surface Science*, **2005**, 595 (1-3), 56-63.
- [64] J.D. Schrottenecker, R. Heer, E. Melnik, T. Maier, G. Fafilek, R. Hainberger, Hexaammineruthenium (II)/(III) as alternative redox-probe to Hexacyanoferrat (II)/(III) for stable impedimetric biosensing with gold electrodes, *Biosensors and Bioelectronics*, **2019**, 127, 25-30.
- [65] A. Shaver, S.D. Curtis, N. Arroyo-Currás, Alkanethiol Monolayer End Groups Affect the Long-Term Operational Stability and Signaling of Electrochemical, Aptamer-Based Sensors in Biological Fluids, *ACS Applied Materials & Interfaces*, **2020**, 12 (9), 11214-11223.
- [66] N. Arroyo-Currás, P. Dauphin-Ducharme, K. Scida, J.L. Chávez, From the beaker to the body: translational challenges for electrochemical, aptamer-based sensors, *Analytical Methods*, **2020**, 12 (10), 1288-1310.
- [67] J. Sabaté del Río, O.Y.F. Henry, P. Jolly, D.E. Ingber, An antifouling coating that enables affinity-based electrochemical biosensing in complex biological fluids, *Nature Nanotechnology*, **2019**, 14 (12), 1143-1149.
- [68] Report from the Canadian Chronic Disease Surveillance System: Heart Disease in Canada, **2018**. <https://www.canada.ca/en/public-health/services/publications/diseases-conditions/report-heart-disease-Canada-2018.html>.
- [69] Ischemic heart disease in New Brunswick, **2016**. <https://www2.gnb.ca/content/dam/gnb/Departments/h-s/pdf/en/Publications/Profiles/ProfilesHealthHeartDisease.pdf>.
- [70] Demographic estimates by age and sex, provinces and territories, **2022**. <https://www150.statcan.gc.ca/n1/pub/71-607-x/71-607-x2020018-eng.htm>.
- [71] S. Obradovic, B. Dzudovic, B. Subotic, J. Matijasevic, Z. Mladenovic, A. Bokan, J. Trobok, S. Pekovic, S. Salinger-Martinovic, L. Jovanovic, L. Kos, T. Kovacevic-Preradovic, M. Nikolic, V. Miloradovic, A. Kovacevic-Kuzmanovic, N. Zec, N. Markovic-Nikolic, I. Srdanovic, Z. Gluovic, S. Kafedzic, S. Pancevacki, A. Neskovic, S. Konstantinides, Predictive value of heart failure with reduced versus preserved ejection fraction for outcome in pulmonary embolism, *ESC Heart Failure*, **2020**, 7 (6), 4061-4070.

- [72] C. Hofmann, M. Völkers, H.A. Katus, Targeting coagulation in heart failure with preserved ejection fraction and cardiac fibrosis, *European Heart Journal*, **2019**, 40 (40), 3333-3335.
- [73] Retrieved July 17, 2025. <https://researchnb.ca/researchers/thomas-pulinilkunnil/>.
- [74] B. Udugama, P. Kadhiresan, H.N. Kozlowski, A. Malekjahani, M. Osborne, V.Y.C. Li, H. Chen, S. Mubareka, J.B. Gubbay, W.C.W. Chan, Diagnosing COVID-19: The Disease and Tools for Detection, *ACS Nano*, **2020**, 14 (4), 3822-3835.
- [75] H. Yousefi, A. Mahmud, D. Chang, J. Das, S. Gomis, J.B. Chen, H. Wang, T. Been, L. Yip, E. Coomes, Z. Li, S. Mubareka, A. McGeer, N. Christie, S. Gray-Owen, A. Cochrane, J.M. Rini, E.H. Sargent, S.O. Kelley, Detection of SARS-CoV-2 Viral Particles Using Direct, Reagent-Free Electrochemical Sensing, *J Am Chem Soc*, **2021**, 143 (4), 1722-1727.
- [76] K.J. Land, D.I. Boeras, X.-S. Chen, A.R. Ramsay, R.W. Peeling, REASSURED diagnostics to inform disease control strategies, strengthen health systems and improve patient outcomes, *Nature Microbiology*, **2019**, 4 (1), 46-54.
- [77] M. Yu, X. Zhang, X. Zhang, Q.U.A. Zahra, Z. Huang, Y. Chen, C. Song, M. Song, H. Jiang, Z. Luo, Y. Lu, An electrochemical aptasensor with N protein binding aptamer-complementary oligonucleotide as probe for ultra-sensitive detection of COVID-19, *Biosens Bioelectron*, **2022**, 213, 114436.
- [78] P. Pokhrel, C. Hu, H. Mao, Detecting the Coronavirus (COVID-19), *ACS Sens*, **2020**, 5 (8), 2283-2296.
- [79] J. Kim, M. Park, Recent Progress in Electrochemical Immunosensors, *Biosensors*, **2021**, 11 (10), 360.
- [80] J. Leva-Bueno, S.A. Peyman, P.A. Millner, A review on impedimetric immunosensors for pathogen and biomarker detection, *Medical Microbiology and Immunology*, **2020**, 209 (3), 343-362.
- [81] T.A.P. Rocha-Santos, Sensors and biosensors based on magnetic nanoparticles, *TrAC Trends in Analytical Chemistry*, **2014**, 62, 28-36.
- [82] H.H. Nguyen, S.H. Lee, U.J. Lee, C.D. Fermin, M. Kim, Immobilized Enzymes in Biosensor Applications, *Materials*, **2019**, 12 (1), 121.
- [83] C. Singhal, J.G. Bruno, A. Kaushal, T.K. Sharma, Recent Advances and a Roadmap to Aptamer-Based Sensors for Bloodstream Infections, *ACS Applied Bio Materials*, **2021**, 4 (5), 3962-3984.
- [84] A.D. Gelinias, T.K. Tan, S. Liu, J.G. Jaramillo, J. Chadwick, A.C. Harding, C. Zhang, B.E. Ream, C.N. Chase, M.R. Otis, T. Lee, D.J. Schneider, W.S. James, N. Janjic, Broadly neutralizing aptamers to SARS-CoV-2: A diverse panel of modified DNA antiviral agents, *Mol Ther Nucleic Acids*, **2023**, 31, 370-382.
- [85] Y. Zhang, B.S. Lai, M. Juhas, Recent Advances in Aptamer Discovery and Applications, *Molecules*, **2019**, 24 (5), 941.

- [86] Y. Dai, C.C. Liu, Recent Advances on Electrochemical Biosensing Strategies toward Universal Point-of-Care Systems, *Angewandte Chemie International Edition*, **2019**, 58 (36), 12355-12368.
- [87] A. De Girolamo, M. McKeague, M. Pascale, M. Cortese, M.C. DeRosa, Immobilization of Aptamers on Substrates, *Aptamers for Analytical Applications* **2018**, pp. 85-126.
- [88] M. Alafeef, K. Dighe, P. Moitra, D. Pan, Rapid, Ultrasensitive, and Quantitative Detection of SARS-CoV-2 Using Antisense Oligonucleotides Directed Electrochemical Biosensor Chip, *ACS Nano*, **2020**, 14 (12), 17028-17045.
- [89] Y. Li, R. Han, M. Chen, L. Zhang, G. Wang, X. Luo, Bovine Serum Albumin-Cross-Linked Polyaniline Nanowires for Ultralow Fouling and Highly Sensitive Electrochemical Protein Quantification in Human Serum Samples, *Anal Chem*, **2021**, 93 (9), 4326-4333.
- [90] ePlex System | GenMark Diagnostics.
<https://www.genmarkdx.com/education/technology/>.
- [91] K. Resman Rus, M. Korva, N. Knap, T. Avsic Zupanc, M. Poljak, Performance of the rapid high-throughput automated electrochemiluminescence immunoassay targeting total antibodies to the SARS-CoV-2 spike protein receptor binding domain in comparison to the neutralization assay, *J Clin Virol*, **2021**, 139, 104820.
- [92] In Vitro Diagnostics EUAs - Serology and Other Adaptive Immune Response Tests for SARS-CoV-2. <https://www.fda.gov/medical-devices/coronavirus-disease-2019-covid-19-emergency-use-authorizations-medical-devices/in-vitro-diagnostics-euas-serology-and-other-adaptive-immune-response-tests-sars-cov-2>.
- [93] N. Kacherovsky, L.F. Yang, H.V. Dang, E.L. Cheng, I.I. Cardle, A.C. Walls, M. McCallum, D.L. Sellers, F. DiMaio, S.J. Salipante, D. Corti, D. Veessler, S.H. Pun, Discovery and Characterization of Spike N-Terminal Domain-Binding Aptamers for Rapid SARS-CoV-2 Detection, *Angewandte Chemie International Edition*, **2021**, 60 (39), 21211-21215.
- [94] R.F. Carvalhal, R.S. Freire, L.T. Kubota, Polycrystalline gold electrodes: A comparative study of pretreatment procedures used for cleaning and thiol self-assembly monolayer formation, *Electroanalysis*, **2005**, 17 (14), 1251-1259.
- [95] Metrohm DropSens gold electrodes.
https://www.dropsens.com/en/pdfs_products/new_brochures/gold_electrodes.pdf.
- [96] PalmSens4 Electrochemical Analyzer.
<https://www.palmsens.com/product/palmsens4/>.
- [97] M. Zamani, V. Yang, L. Maziashvili, G. Fan, C.M. Klapperich, A.L. Furst, Surface Requirements for Optimal Biosensing with Disposable Gold Electrodes, *ACS Meas Sci Au*, **2022**, 2 (2), 91-95.
- [98] X. Xu, A. Makaraviciute, S. Kumar, C. Wen, M. Sjödin, E. Abdurakhmanov, U.H. Danielson, L. Nyholm, Z. Zhang, Structural Changes of Mercaptohexanol Self-Assembled Monolayers on Gold and Their Influence on Impedimetric Aptamer Sensors, *Analytical Chemistry*, **2019**, 91 (22), 14697-14704.

- [99] U. Chadha, P. Bhardwaj, R. Agarwal, P. Rawat, R. Agarwal, I. Gupta, M. Panjwani, S. Singh, C. Ahuja, S.K. Selvaraj, M. Banavoth, P. Sonar, B. Badoni, A. Chakravorty, Recent progress and growth in biosensors technology: A critical review, *Journal of Industrial and Engineering Chemistry*, **2022**, 109, 21-51.
- [100] G. Paimard, E. Ghasali, M. Baeza, Screen-Printed Electrodes: Fabrication, Modification, and Biosensing Applications, *Chemosensors*, **2023**, 11 (2), 113.
- [101] Global Screen-printed Electrodes Market 2024–2033, **May 2024**. <https://www.custommarketinsights.com/report/screen-printed-electrodes-market/>.
- [102] Scopus search results for “screen printed electrode” in Article Title and Abstract Accessed June 11, 2024.
- [103] A. Villalonga, A.M. Pérez-Calabuig, R. Villalonga, Electrochemical biosensors based on nucleic acid aptamers, *Analytical and Bioanalytical Chemistry*, **2020**, 412 (1), 55-72.
- [104] S. Hassani, M.R. Akmal, A. Salek-Maghsoudi, S. Rahmani, M.R. Ganjali, P. Norouzi, M. Abdollahi, Novel label-free electrochemical aptasensor for determination of Diazinon using gold nanoparticles-modified screen-printed gold electrode, *Biosensors and Bioelectronics*, **2018**, 120, 122-128.
- [105] A. Mahmud, D. Chang, J. Das, S. Gomis, F. Foroutan, J.B. Chen, L. Pandey, C.D. Flynn, H. Yousefi, A. Geraili, H.J. Ross, E.H. Sargent, S.O. Kelley, Monitoring Cardiac Biomarkers with Aptamer-Based Molecular Pendulum Sensors, *Angewandte Chemie International Edition*, **2023**, 62 (20), e202213567.
- [106] Y. Yang, X. Gao, B. Widdicombe, X. Zhang, J.L. Zielinski, T. Cheng, A. Gunatilaka, K.K. Leung, K.W. Plaxco, R. Rajasekharan Unnithan, A.G. Stewart, Dual-Purpose Aptamer-Based Sensors for Real-Time, Multiplexable Monitoring of Metabolites in Cell Culture Media, *ACS Nano*, **2024**, 18 (38), 26127-26139.
- [107] S.W. Abeykoon, R.J. White, Single Voltammetric Sweep Calibration-Free Interrogation of Electrochemical Aptamer-Based Sensors Employing Continuous Square Wave Voltammetry, *Analytical Chemistry*, **2024**, 96 (18), 6958-6967.
- [108] Y.-H. Chang, C.-L. Hsu, C.-J. Yuan, S.-F. Tang, H.-J. Chiang, H.-D. Jang, K.-S. Chang, Improvement of the inter-electrode reproducibility of screen-printed carbon electrodes by oxygen plasma etching and an image color level method for quality control, *Materials Science and Engineering: C*, **2011**, 31 (7), 1265-1270.
- [109] D. Stan, A.-C. Mirica, R. Iosub, D. Stan, N.B. Mincu, M. Gheorghe, M. Avram, B. Adiaconita, G. Craciun, A.L. Bocancia Mateescu, What Is the Optimal Method for Cleaning Screen-Printed Electrodes?, *Processes*, **2022**, 10 (4), 723.
- [110] N.A.F. Roslan, R.A. Rahim, A.A.M. Ralib, N.F. Za’bah, A.N. Nordin, M.S.R. Bashri, M.I. Suhaimi, Z. Samsudin, L.L. Ming, G. Sugandi, Performance Analysis of Optimized Screen-Printed Electrodes for Electrochemical Sensing, *International Journal of Integrated Engineering*, **2022**, 14 (3), 250-261.

- [111] S.C. Wang, K.S. Chang, C.J. Yuan, Enhancement of electrochemical properties of screen-printed carbon electrodes by oxygen plasma treatment, *Electrochimica Acta*, **2009**, 54 (21), 4937-4943.
- [112] G. Cui, Y. Jae Hyun, L. Joung Su, J. Yoo, U. Jung Hee, C. Geun Sig, H. Nam, Effect of pre-treatment on the surface and electrochemical properties of screen-printed carbon paste electrodes, *Analyst*, **2001**, 126 (8), 1399-1403.
- [113] F. Ghamouss, E. Luais, C. Thobie-Gautier, P.Y. Tessier, M. Boujtita, Argon plasma treatment to enhance the electrochemical reactivity of screen-printed carbon surfaces, *Electrochimica Acta*, **2009**, 54 (11), 3026-3032.
- [114] Y. Koç, U. Moralı, S. Erol, H. Avci, Electrochemical Investigation of Gold Based Screen Printed Electrodes: An Application for a Seafood Toxin Detection, *Electroanalysis*, **2021**, 33 (4), 1033-1048.
- [115] Y. Xiao, R.Y. Lai, K.W. Plaxco, Preparation of electrode-immobilized, redox-modified oligonucleotides for electrochemical DNA and aptamer-based sensing, *Nat Protoc*, **2007**, 2 (11), 2875-80.
- [116] M. Yuan, S. Zhan, X. Zhou, Y. Liu, L. Feng, Y. Lin, Z. Zhang, J. Hu, A Method for Removing Self-Assembled Monolayers on Gold, *Langmuir*, **2008**, 24 (16), 8707-8710.
- [117] J. Enomoto, T. Kageyama, D. Myasnikova, K. Onishi, Y. Kobayashi, Y. Taruno, T. Kanai, J. Fukuda, Gold cleaning methods for preparation of cell culture surfaces for self-assembled monolayers of zwitterionic oligopeptides, *Journal of Bioscience and Bioengineering*, **2018**, 125 (5), 606-612.
- [118] L.S.J. Ho, J.L. Limson, R. Fogel, Certain Methods of Electrode Pretreatment Create Misleading Responses in Impedimetric Aptamer Biosensors, *ACS Omega*, **2019**, 4 (3), 5839-5847.
- [119] H.T.N. Le, L.M.T. Phan, S. Cho, Removal of Thiol-SAM on a Gold Surface for Re-Use of an Interdigitated Chain-Shaped Electrode, *Materials*, **2022**, 15 (6), 2218.
- [120] A. Piper, D.K. Corrigan, A.R. Mount, An electrochemical comparison of thiolated self-assembled monolayer (SAM) formation and stability in solution on macro- and nanoelectrodes, *Electrochemical Science Advances*, **2022**, 2 (6), e2100077.
- [121] J. Lee, H.N. Suh, H.-b. Park, Y.M. Park, H.J. Kim, S. Kim, Regenerative Strategy of Gold Electrodes for Long-Term Reuse of Electrochemical Biosensors, *ACS Omega*, **2023**, 8 (1), 1389-1400.
- [122] Z. Li, L. Zhang, S. Zeng, M. Zhang, E. Du, B. Li, Effect of surface pretreatment on self-assembly of thiol-modified DNA monolayers on gold electrode, *Journal of Electroanalytical Chemistry*, **2014**, 722-723, 131-140.
- [123] T.C. Isabell, P.E. Fischione, Applications of Plasma Cleaning for Electron Microscopy of Semiconducting Materials, *MRS Online Proceedings Library*, **1998**, 523 (1), 31-38.
- [124] J. Sun, Y. Yu, J. Tang, Y. Zeng, J. Chen, Plasma Cleaning Technology: Mechanisms, Influencing Factors, and Applications, *IEEE Access*, **2025**, 13, 37221-37242.

- [125] T. Sun, P.-Y. Blanchard, M.V. Mirkin, Cleaning Nanoelectrodes with Air Plasma, *Analytical Chemistry*, **2015**, 87 (8), 4092-4095.
- [126] T.C. Isabell, P.E. Fischione, C. O'Keefe, M.U. Guruz, V.P. Dravid, Plasma Cleaning and Its Applications for Electron Microscopy, *Microscopy and Microanalysis*, **1999**, 5 (2), 126-135.
- [127] Y. Li, Q. Bai, Y. Guan, H. Liu, P. Zhang, B. Batelbieke, R. Shen, L. Lu, X. Yuan, X. Miao, W. Han, C. Yao, The mechanism study of low-pressure air plasma cleaning on large-aperture optical surface unraveled by experiment and reactive molecular dynamics simulation, *Plasma Science and Technology*, **2022**, 24 (6), 064012.
- [128] J.C. Love, L.A. Estroff, J.K. Kriebel, R.G. Nuzzo, G.M. Whitesides, Self-Assembled Monolayers of Thiolates on Metals as a Form of Nanotechnology, *Chemical Reviews*, **2005**, 105 (4), 1103-1170.
- [129] A.-E. Radi, J.L. Acero Sánchez, E. Baldrich, C.K. O'Sullivan, Reusable Impedimetric Aptasensor, *Analytical Chemistry*, **2005**, 77 (19), 6320-6323.
- [130] D.M. Tasset, M.F. Kubik, W. Steiner, Oligonucleotide inhibitors of human thrombin that bind distinct epitopes | Edited by R. Huber, *Journal of Molecular Biology*, **1997**, 272 (5), 688-698.
- [131] Thrombin from human plasma_Product information. <https://www.sigmaaldrich.com/deepweb/assets/sigmaaldrich/product/documents/599/516/t6884pis.pdf>.
- [132] K. Ogura, S. Haruyama, K. Nagasaki, The Electrochemical Oxidation and Reduction of Gold, *Journal of The Electrochemical Society*, **1971**, 118 (4), 531.
- [133] V.M. Andoralov, M.R. Tarasevich, O.V. Tripachev, Oxygen reduction reaction on polycrystalline gold. Pathways of hydrogen peroxide transformation in the acidic medium, *Russian Journal of Electrochemistry*, **2011**, 47 (12), 1327-1336.
- [134] S.N. Ovchinnikova, A.Z. Medvedev, Desorption of octanethiol from gold electrode surface during its electrochemical cleaning, *Russian Journal of Electrochemistry*, **2015**, 51 (4), 287-293.
- [135] B.-Y. Chang, Conversion of a Constant Phase Element to an Equivalent Capacitor, *J. Electrochem. Sci. Technol*, **2020**, 11 (3), 318-321.
- [136] B.-Y. Chang, The Effective Capacitance of a Constant Phase Element with Resistors in Series, *J. Electrochem. Sci. Technol*, **2022**, 13 (4), 479-485.
- [137] N. Elgrishi, K.J. Rountree, B.D. McCarthy, E.S. Rountree, T.T. Eisenhart, J.L. Dempsey, A Practical Beginner's Guide to Cyclic Voltammetry, *Journal of Chemical Education*, **2018**, 95 (2), 197-206.
- [138] T. Tichter, A. Tichter, D. Andrae, C. Roth, Simulating cyclic voltammetry at rough electrodes by the digital-simulation–deconvolution–convolution algorithm, *Electrochimica Acta*, **2024**, 508, 145175.
- [139] Y. Xue, X. Li, H. Li, W. Zhang, Quantifying thiol–gold interactions towards the efficient strength control, *Nature Communications*, **2014**, 5 (1), 4348.

- [140] F. Vitale, I. Fratoddi, C. Battocchio, E. Piscopiello, L. Tapfer, M.V. Russo, G. Polzonetti, C. Giannini, Mono- and bi-functional arenethiols as surfactants for gold nanoparticles: synthesis and characterization, *Nanoscale Res. Lett.*, **2011**, 6 (1), 103.
- [141] K. Juodkazis, J. Juodkazyte, V. Jasulaitiene, A. Lukinskas, B. Sebek, XPS studies on the gold oxide surface layer formation, *Electrochemistry Communications*, **2000**, 2 (7), 503-507.
- [142] K. Tamargo-Martínez, S. Villar-Rodil, A. Martínez-Alonso, J.M.D. Tascón, Surface modification of high-surface area graphites by oxygen plasma treatments, *Applied Surface Science*, **2022**, 575, 151675.
- [143] K. Barman, S. Luhar, R. Rane, D.N. Srivastava, S.K. Nema, S. Bhattacharjee, Improving electrochemical sensitivity of screen-printed carbon electrodes by atmospheric pressure plasma jet treatment and electrochemical detection of dopamine, *Plasma Processes and Polymers*, **2023**, 20 (3), 2200161.
- [144] R. Voicu, T.H. Ellis, H. Ju, D. Leech, Adsorption and desorption of electroactive self-assembled thiolate monolayers on gold, *Langmuir*, **1999**, 15 (23), 8170-8177.
- [145] M. Asal, Ö. Özen, M. Şahinler, H.T. Baysal, İ. Polatoğlu, An overview of biomolecules, immobilization methods and support materials of biosensors, *Sensor Review*, **2019**, 39 (3), 377-386.
- [146] S. Gao, J.M. Guisán, J. Rocha-Martin, Oriented immobilization of antibodies onto sensing platforms - A critical review, *Analytica Chimica Acta*, **2022**, 1189, 338907.
- [147] W. Putzbach, N.J. Ronkainen, Immobilization Techniques in the Fabrication of Nanomaterial-Based Electrochemical Biosensors: A Review, *Sensors*, **2013**, 13 (4), 4811-4840.
- [148] M.S. Inkpen, Z.F. Liu, H. Li, L.M. Campos, J.B. Neaton, L. Venkataraman, Non-chemisorbed gold-sulfur binding prevails in self-assembled monolayers, *Nature Chemistry*, **2019**, 11 (4), 351-358.
- [149] S. Liébana, Guido A. Drago, Bioconjugation and stabilisation of biomolecules in biosensors, *Essays in Biochemistry*, **2016**, 60 (1), 59-68.
- [150] X. Meng, D. O'Hare, S. Ladame, Surface immobilization strategies for the development of electrochemical nucleic acid sensors, *Biosensors and Bioelectronics*, **2023**, 237, 115440.
- [151] K. Coffi Dit Gleize, C.T.H. Tran, A. Waterhouse, M.M.M. Bilek, S.F.J. Wickham, Plasma Activation of Microplates Optimized for One-Step Reagent-Free Immobilization of DNA and Protein, *Langmuir*, **2023**, 39 (1), 343-356.
- [152] D. Ashok, J. Singh, S. Jiang, A. Waterhouse, M. Bilek, Reagent-Free Covalent Immobilization of Biomolecules in a Microfluidic Organ-On-A-Chip, *Advanced Functional Materials*, **2024**, 34 (30), 2313664.
- [153] C.T.H. Tran, A.D. Gilmour, B.B. Boumelhem, S.T. Fraser, M.M.M. Bilek, Plasma-Activated Coated Glass: A Novel Platform for Optimal Optical Performance and Cell Culture Substrate Customization, *Small Science*, **2024**, 4 (4), 2300228.

- [154] B. Akhavan, M. Croes, S.G. Wise, C. Zhai, J. Hung, C. Stewart, M. Ionescu, H. Weinans, Y. Gan, S. Amin Yavari, M.M.M. Bilek, Radical-functionalized plasma polymers: Stable biomimetic interfaces for bone implant applications, *Applied Materials Today*, **2019**, 16, 456-473.
- [155] C.T.H. Tran, M. Craggs, L.M. Smith, K. Stanley, A. Kondyurin, M.M. Bilek, D.R. McKenzie, Covalent linker-free immobilization of conjugatable oligonucleotides on polypropylene surfaces, *RSC Advances*, **2016**, 6 (86), 83328-83336.
- [156] C.-Y. Lee, G.M. Harbers, D.W. Grainger, L.J. Gamble, D.G. Castner, Fluorescence, XPS, and TOF-SIMS Surface Chemical State Image Analysis of DNA Microarrays, *Journal of the American Chemical Society*, **2007**, 129 (30), 9429-9438.
- [157] M. Ramstedt, A. Shchukarev, XPS spectra from nucleobases, DNA, and RNA, *Surface Science Spectra*, **2023**, 30 (1), 014011.
- [158] D.Y. Petrovykh, H. Kimura-Suda, L.J. Whitman, M.J. Tarlov, Quantitative Analysis and Characterization of DNA Immobilized on Gold, *Journal of the American Chemical Society*, **2003**, 125 (17), 5219-5226.
- [159] A.M. Downs, J. Gerson, K.L. Ploense, K.W. Plaxco, P. Dauphin-Ducharme, Subsecond-Resolved Molecular Measurements Using Electrochemical Phase Interrogation of Aptamer-Based Sensors, *Analytical Chemistry*, **2020**, 92 (20), 14063-14068.
- [160] D.L. Higgins, S.D. Lewis, J.A. Shafer, Steady state kinetic parameters for the thrombin-catalyzed conversion of human fibrinogen to fibrin, *Journal of Biological Chemistry*, **1983**, 258 (15), 9276-9282.
- [161] J.Y. Chang, S.S. Alkan, N. Hilschmann, D.G. Braun, Thrombin specificity. Selective cleavage of antibody light chains at the joints of variable with joining regions and joining with constant regions, *Eur J Biochem*, **1985**, 151 (2), 225-30.
- [162] I. Russo Krauss, A. Merlino, A. Randazzo, L. Mazzarella, F. Sica, Crystallization and preliminary X-ray analysis of the complex of human alpha-thrombin with a modified thrombin-binding aptamer, *Acta crystallographica. Section F, Structural biology and crystallization communications*, **2010**, 66, 961-3.
- [163] M.B. Pagano, W.L. Chandler, Thrombin Generation Assay: Are We Ready for Prime Time?, *The Journal of Applied Laboratory Medicine*, **2017**, 2 (2), 135-137.
- [164] F. Depasse, N.B. Binder, J. Mueller, T. Wissel, S. Schwerts, M. Germer, B. Hermes, P.L. Turecek, Thrombin generation assays are versatile tools in blood coagulation analysis: A review of technical features, and applications from research to laboratory routine, *Journal of Thrombosis and Haemostasis*, **2021**, 19 (12), 2907-2917.
- [165] W.L. Chandler, Coagulation activation during extracorporeal membrane oxygenation (ECMO), *Thrombosis Research*, **2022**, 211, 154-160.
- [166] L.F. Harris, V. Castro-López, A.J. Killard, Coagulation monitoring devices: Past, present, and future at the point of care, *TrAC Trends in Analytical Chemistry*, **2013**, 50, 85-95.
- [167] A.K.V. Mruthunjaya, A.A.J. Torriero, Electrochemical Monitoring in Anticoagulation Therapy, *Molecules*, **2024**, 29 (7), 1453-1458.

- [168] C. Thuerlemann, A. Haeberli, L. Alberio, Monitoring Thrombin Generation by Electrochemistry: Development of an Amperometric Biosensor Screening Test for Plasma and Whole Blood, *Clinical Chemistry*, **2009**, 55 (3), 505-512.
- [169] J. Kintigh, P. Monagle, V. Ignjatovic, A review of commercially available thrombin generation assays, *Research and Practice in Thrombosis and Haemostasis*, **2018**, 2 (1), 42-48.
- [170] Z. Oushyani Roudsari, H. Ghasemi, S.H. Khatami, M. Khorsand, F. Rahdan, D. Chehri, O. Sheydaei, S. Aiiashi, R. Mahmoudi, A. Movahedpour, Aptamer biosensors for thrombin, *Clin Chim Acta*, **2025**, 565, 119976.
- [171] J. Adjémian, A. Anne, G. Cauet, C. Demaille, Cleavage-Sensing Redox Peptide Monolayers for the Rapid Measurement of the Proteolytic Activity of Trypsin and α -Thrombin Enzymes, *Langmuir*, **2010**, 26 (12), 10347-10356.
- [172] S. Park, G. Kim, H. Yang, Proteolytic reaction-based versatile electrochemical biosensor chip for simple and quantitative point-of-care testing, *Sensors and Actuators B: Chemical*, **2024**, 414, 135934.
- [173] A.K.V. Mruthunjaya, R.C. Chatelier, A.A.J. Torriero, Electrochemical Disposable Biosensor to Monitor Dabigatran in Point-of-Care Anticoagulation Therapy, *Molecules*, **2023**, 28 (13), 4953.
- [174] M. Mir, M. Vreeke, I. Katakis, Different strategies to develop an electrochemical thrombin aptasensor, *Electrochemistry Communications*, **2006**, 8 (3), 505-511.
- [175] Y. Xu, L. Yang, X. Ye, P. He, Y. Fang, An aptamer-based protein biosensor by detecting the amplified impedance signal, *Electroanalysis*, **2006**, 18 (15), 1449-1456.
- [176] K. Fan, J. Zhu, X. Wu, X. Zhang, S. Wang, W. Wen, A flexible label-free electrochemical aptasensor based on target-induced conjunction of two split aptamers and enzyme amplification, *Sensors and Actuators B: Chemical*, **2022**, 363, 131766.
- [177] C.H. Hsu, F. Mansfeld, Technical Note: Concerning the Conversion of the Constant Phase Element Parameter Y_0 into a Capacitance, *Corrosion*, **2001**, 57 (9), 747-748.
- [178] M. Mrksich, G.B. Sigal, G.M. Whitesides, Surface Plasmon Resonance Permits in Situ Measurement of Protein Adsorption on Self-Assembled Monolayers of Alkanethiolates on Gold, *Langmuir*, **1995**, 11 (11), 4383-4385.
- [179] G.M. Whitesides, J.E. Lilburn, R.P. Szajewski, Rates of thiol-disulfide interchange reactions between mono- and dithiols and Ellman's reagent, *The Journal of Organic Chemistry*, **1977**, 42 (2), 332-338.
- [180] M.E. Orazem, B. Tribollet, *Electrochemical Impedance Spectroscopy*, John Wiley & Sons, Inc., **2008**, pp. 324-333.
- [181] F.C. Anson, Innovations in the Study of Adsorbed Reactants by Chronocoulometry, *Analytical Chemistry*, **1966**, 38 (1), 54-57.
- [182] A.B. Steel, T.M. Herne, M.J. Tarlov, Electrochemical quantitation of DNA immobilized on gold, *Analytical Chemistry*, **1998**, 70 (22), 4670-4677.

- [183] J. Zhang, S. Song, L. Wang, D. Pan, C. Fan, A gold nanoparticle-based chronocoulometric DNA sensor for amplified detection of DNA, *Nature Protocols*, **2007**, 2 (11), 2888-2895.
- [184] S.D. Keighley, P. Li, P. Estrela, P. Migliorato, Optimization of DNA immobilization on gold electrodes for label-free detection by electrochemical impedance spectroscopy, *Biosensors and Bioelectronics*, **2008**, 23 (8), 1291-1297.
- [185] R.J. White, N. Phares, A.A. Lubin, Y. Xiao, K.W. Plaxco, Optimization of Electrochemical Aptamer-Based Sensors via Optimization of Probe Packing Density and Surface Chemistry, *Langmuir*, **2008**, 24 (18), 10513-10518.
- [186] S. Mehra, S.S. Jadaun, A. Kumar, A.K. Panwar, Study of Lithium-Ion Diffusion Coefficients Through Analysis of CV and EIS for Ni₂MnO₄ Alternate Anode Material in Lithium-Ion Batteries, *Journal of Electronic Materials*, **2025**, 54 (10), 8439-8447.
- [187] T.Q. Nguyen, C. Breitkopf, Determination of Diffusion Coefficients Using Impedance Spectroscopy Data, *Journal of The Electrochemical Society*, **2018**, 165 (14), E826-E831.
- [188] C.D. Bain, H.A. Biebuyck, G.M. Whitesides, Comparison of self-assembled monolayers on gold: coadsorption of thiols and disulfides, *Langmuir*, **1989**, 5 (3), 723-727.
- [189] P. Zhuravski, S.K. Arya, P. Jolly, C. Tiede, D.C. Tomlinson, P. Ko Ferrigno, P. Estrela, Sensitive and selective Affimer-functionalised interdigitated electrode-based capacitive biosensor for Her4 protein tumour biomarker detection, *Biosensors and Bioelectronics*, **2018**, 108, 1-8.
- [190] H.-J. Chen, R.L.C. Chen, B.-C. Hsieh, H.-Y. Hsiao, Y. Kung, Y.-T. Hou, T.-J. Cheng, Label-free and reagentless capacitive aptasensor for thrombin, *Biosensors and Bioelectronics*, **2019**, 131, 53-59.
- [191] P. Heiduschka, J. Dittrich, Electrochemical investigation of enzyme catalysed hydrolysis and synthesis of peptides using peptidyl-4-nitroanilides as substrates, *Bioelectrochemistry and Bioenergetics*, **1990**, 24 (2), 231-239.
- [192] H. Olsen, A. Andersen, A. Nordbo, U.E. Kongsgaard, O.P. Borner, Pharmaceutical-grade albumin: impaired drug-binding capacity in vitro, *BMC Clin Pharmacol*, **2004**, 4 (1), 4-8.
- [193] E. Kerr, R. Alexander, P.S. Francis, R.M. Guijt, G.J. Barbante, E.H. Doeven, A Comparison of Commercially Available Screen-Printed Electrodes for Electrogenated Chemiluminescence Applications, *Front Chem*, **2020**, 8, 628483.
- [194] E.M. Dief, W. Tang, L.R. Carroll, T. Breton, J.J. Gooding, Preparation of electrochemical aptamer-based sensors: a direct aryl diazonium grafting approach, *Chemical Communications*, **2025**, 61 (42), 7648-7651.
- [195] C.D. Flynn, M. Sandomierski, K. Kim, J. Lewis, V. Lloyd, A. Ignaszak, Electrochemical Detection of *Borrelia burgdorferi* Using a Biomimetic Flow Cell System, *ACS Measurement Science Au*, **2023**, 3 (3), 208-216.

- [196] S. Cheunkar, S. Oaew, A. Parnsubsakul, P. Asanithi, Reactive argon-plasma activation of screen-printed carbon electrodes for highly selective dopamine determination, *Analytical Methods*, **2022**, 14 (42), 4193-4201.
- [197] T. Kilic, I. Gessner, Y.K. Cho, N. Jeong, J. Quintana, R. Weissleder, H. Lee, Zwitterionic Polymer Electroplating Facilitates the Preparation of Electrode Surfaces for Biosensing, *Adv Mater*, **2022**, 34 (8), e2107892.
- [198] J.J. Gooding, Finally, a simple solution to biofouling, *Nature Nanotechnology*, **2019**, 14 (12), 1089-1090.

Curriculum Vitae

Candidate's full name: Sina Ardalan

University attended:

- Chemistry and Chemical Engineering Research Center of Iran, MSc, 2020
- Sharif University of Technology, BSc, 2017

Publications:

- S. Ardalan, C. Tran, S. Fraser, M. Bilek, A. Ignaszak, Sustainable air plasma regeneration of screen-printed gold electrodes with enhanced electroactive surface area and biosensing performance, Submitted to RSC Sustainability, manuscript number SU-ART-02-2026-000113, Feb 23, **2026**.
- S. Ardalan, A. Ignaszak, Rapid Electrochemical Monitoring of Thrombin Activity Using an Electrogenic Substrate: Toward Real-time Coagulation Monitoring, Submitted to ChemElectroChem, manuscript number 8993652, Jan 16, **2026**.
- C. O'Brien, C.K. Khor, S. Ardalan, A. Ignaszak, Multiplex electrochemical sensing platforms for the detection of breast cancer biomarkers, *Frontiers in Medical Technology*, **2024**, 6, 1360510.
- S. Ardalan, A. Ignaszak, Can Electrochemical Aptasensors Achieve the Commercial Success of Glucose Biosensors? *Advanced Sensor Research*, **2024**, 3(4), 2300132.
- A.R. Sharifi, S. Ardalan, R.S. Tabatabaee, S. Soleimani Gorgani, H. Yousefi, K. Omidfar, M.A. Kiani, C. Dincer, T. Naghdi, H. Golmohammadi, Smart wearable

- nanopaper patch for continuous multiplexed optical monitoring of sweat parameters, *Analytical Chemistry*, **2023**, 95(44), 16098-16106.
- T. Naghdi, S. Ardalan, Z.A. Adib, A.R. Sharifi, H. Golmohammadi, Moving toward smart biomedical sensing, *Biosensors and Bioelectronics*, **2023**, 223, 115009.
 - S. Ardalan, A. Ignaszak, Innovations and Challenges in Electroanalytical Tools for Rapid Biosurveillance of SARS-CoV-2, *Advanced Materials Technologies*, **2022**, 7(12), 2200208.
 - S. Ardalan, Hamed Golmohammadi Ghane, Fluorescence sensor for detecting biomarkers in a sweat sample, US Patent, **2021**, US 20210310953 A1.
 - S. Ardalan, M. Hosseinifard, M. Vosough, H. Golmohammadi, Towards smart personalized perspiration analysis: An IoT-integrated cellulose-based microfluidic wearable patch for smartphone fluorimetric multi-sensing of sweat biomarkers, *Biosensors and Bioelectronics*, **2020**, 168, 112450.

Conference presentations:

- Ardalan, S.; Ignaszak, A. Electrochemical Thrombin Biosensor: Towards Monitoring Coagulation Disorders, ResearchNB Health Research Symposium, Fredericton, NB, **Nov 20, 2025**, (Poster).
- Ardalan, S.; Ignaszak, A. Electrochemical Thrombin Biosensor: Towards Monitoring Coagulation Disorders, Faculty of Mathematics and Science (FMS) grad seminar, Brock University, Saint Catharines, ON, **Oct 3, 2025**, (Oral).

- Ardalan, S.; Tran, C. T. H.; Fraser, S. T.; Bilek, M.; Ignaszak, A. Regeneration of Screen-Printed Gold Electrodes by Air Plasma Cleaning, 248th ECS meeting, Montreal, QC, **May 21, 2025**, (Oral).
- Ardalan, S.; Tran, C. T. H.; Fraser, S. T.; Bilek, M.; Ignaszak, A. Regeneration of Screen-Printed Gold Electrodes by Air Plasma Cleaning, 6th International congress on biosensors, Konya, Turkey, **Sept 5, 2024**, (Oral).
- Ardalan, S.; Ignaszak, A. Detection of SARS-CoV-2 via an Aptamer Modified Electrochemical Sensor. ChemCon, Dalhousie University, Poster fair, **May 26, 2023**, (Poster).

Scholarships and awards:

- Frank J. and Norah Toole Graduate Scholarship, University of New Brunswick, 2025
- NSERC Catalyst, 2025
- Knowledge Translation Grant, ResearchNB, 2024
- School of Graduate Studies Travel Award, University of New Brunswick, 2024
- Globalink Research Award, MITACS, 2023
- Dr. William S. Lewis Doctoral Fellowship, University of New Brunswick, 2021-2025
- Subsidy award for international differential charges, University of New Brunswick, 2021-2025